

Alma Mater Studiorum – Università di Bologna

**DOTTORATO DI RICERCA IN
CHIMICA**

Ciclo XXIX

Settore Concorsuale di afferenza: 03/C1

Settore Scientifico disciplinare: CHIM/06

**SYNTHESIS OF SELF-ASSEMBLING MOLECULES FOR FUNCTIONAL
MATERIALS**

Presentata da: Marilena Campitiello

Coordinatore Dottorato

Prof. Aldo Roda

Relatore

Prof. Stefano Masiero

Esame finale anno 2017

Abstract

The research carried out during these three years was developed as part of the MolArNet Project, supported by the European Commission, which aims at giving a first demonstration of molecular Quantum-dot Cellular Automata (QCA) elementary devices as a feasible approach to unconventional computation. QCA represent a smart model of alternative nanoscale logic devices and consist of an organized array of cells, each containing quantum-dots. Binary information can be encoded, without current flow, in the molecular charge configuration of a cell and propagated to the next neighbor cell within the array.

Here we describe the design and synthesis of novel alkyl substituted guanosine-ferrocene derivatives, and their self-assembly at the solid/liquid interface on highly oriented pyrolytic graphite (HOPG). Supramolecular self-assembly of these derivatives has been accomplished in solutions by NMR and CD spectroscopy and on surface by STM and AFM techniques.

We have shown that supramolecular structures formed by ferrocene-exposing guanosines in solutions and at surfaces can be tuned by introducing sterically demanding substituents, ranging from *G*-ribbons to *G₄* cation-free architectures. This self-assembly is governed by the formation of H-bonds between guanosines that dictates the spatial localization of ferrocenes, ultimately forming 1D conjugated arrays that may be employed as prototypes of supramolecular nanowires. In this thesis we also explored the possibility of using porphyrin derivatives carrying ferrocene residues directly connected to the porphin core, as alternative approach to QCA implementation. Preliminary electrochemical studies using cyclic voltammetry show that porphyrins can be used as a two/four dots cells.

During the period at the University of Maryland, in the Prof. Jeffery Davis' research group, I worked on the synthesis and characterization of specific dyes, containing azobenzene groups, in order to insert them in the guanosine hydrogels. These dyes are capable, in principle, to change their conformation in a reversible way, through an external light stimulus. Thus, it could be possible to obtain photoresponsive hydrophilic gels, able to break and reform themselves in a controlled manner.

Table of contents

Chapter I. Nanotechnology.....	1
1.1 Introduction	1
1.2 Top-down and bottom-up approaches	2
1.3 Nanomaterials.....	4
1.4 Self-assembly of nanoparticles.....	7
1.5 QCA	7
1.6 Molecular quantum-dot cellular automata.....	10
1.7 Ferrocene fragments for molecular QCA cells	12
Bibliography	14
Chapter II. Supramolecular chemistry.....	16
2.1 Introduction	16
2.2 Self-assembly in supramolecular system.....	17
2.3 Guanine and G-quartet	19
2.4 G-quadruplex.....	20
2.5 Structure and behaviour of lipophilic guanosines	22
2.5.1 Self-assembly in presence of metal ions.....	22
2.5.2 Self-assembly in absence of metal ions	25
2.6 Methods for studying G-quadruplexes	26
Bibliography	33
Chapter III. Porphyrins.....	35
3.1 Introduction	35
3.2 Nomenclature of porphyrins.....	36
3.3 Biological role of porphyrins.....	36
3.4 Reactivity of porphyrins.....	39
3.5 Porphyrin synthesis	40

3.6 Aggregation of porphyrins	44
Bibliography	46
Chapter IV. Guanosine-ferrocene derivatives	48
4.1 Introduction	48
4.2 Previous studies.....	49
4.3 Synthetic approaches	51
4.3.1 G1 (1 5'-O-ferrocenoyl-3'-O-octadecanoyl-2'-deoxyguanosine)	51
4.3.2 G2 (8-bromo-5'-O-ferrocenoyl-3'-O-octadecanoyl-2'-deoxyguanosine)	52
4.3.3 G3 (8-phenoxy-5'-O-ferrocenoyl-3'-O-octadecanoyl-2'-deoxyguanosine).....	53
4.4 Supramolecular studies.....	53
4.4.1 G1	53
4.4.2 G2	56
4.4.3 G3	60
4.4.4 DFT.....	64
4.5 Metal free G4 wires	66
4.5.1 Synthesis of G4 (G_8Ph_5Fc_23C10)	67
4.5.2 Synthesis of G5 (G_8Fc_235C10)	68
4.5.3 Supramolecular studies of G4 and G5.....	68
4.5.4 Solid-state characterization of the aggregates	74
4.6 Conclusions	75
Bibliography	77
Chapter V. Porphyrin-ferrocene hybrids	79
5.1 Introduction	79
5.2 Project.....	79
5.3 Synthetic approaches	81
5.3.1 P1 (5,10,15,20-tetra ferrocenyl porphyrin).....	81
5.3.2 P2 (Porf_COOEt)	83
5.3.3 P3 (Porf_COOBz)	84
5.3.4 P4 (Porf_NHFc).....	85
5.3.5 P5 (Porf_NHC ₁₀)	86
5.4 Electrochemical studies	87

5.5 Organization on surfaces	88
Bibliography	90
Chapter VI. Supramolecular photoswitchable hydrogels	91
6.1 Introduction	91
6.2 Project.....	92
6.3 Synthesis of AD dye.....	93
6.4 Studies in solution	93
6.5 GB hydrogels.....	96
Bibliography	101
Chapter VII. Experimental part	102

“Je suis de ceux qui pensent que la science est d’une grande beauté. Un scientifique dans son laboratoire est non seulement un technicien: il est aussi un enfant placé devant des phénomènes naturels qui l’impressionnent comme des contes de fées.”

“Io sono tra quelli che pensano che la scienza abbia una grande bellezza. Uno scienziato nel suo laboratorio non è solo un tecnico: è anche un bambino posto di fronte a fenomeni naturali che lo impressionano come un racconto di fiabe.”

Marie Curie

I. Nanotechnology

1.1 Introduction

“What I want to talk about is the problem of manipulating and controlling things on a small scale. As soon as I mention this, people tell me about miniaturization, and how far it has progressed today. [...] But that's nothing; that's the most primitive, halting step in the direction I intend to discuss. It is a staggeringly small world that is below”.

On December 29, 1959 at the annual meeting of the American Physical Society¹, the physicist Richard Feynman gave a lecture *“There's Plenty of Room at the Bottom”*, in which he suggested the possibility of direct manipulation of individual atoms and molecules as a more powerful form of synthetic chemistry in order to create devices and materials without violating the laws of physics. He regarded microtechnology as a frontier to be overcome by the development of a new technology able to produce assembly and replicate small components. He focused on complex, active, nanoscale biological mechanisms as an inspiration for nanoscale technology. Feynman was the first to outline a world of technologies that would work and build at the ultimate, atomic scale. He viewed this world from a top-down perspective, as the ultimate frontier for miniaturization.

The term “nanotechnology” was coined a decade later, by professor Norio Taniguchi, during his explorations of ultraprecision machining. It wasn't until 1981, with the development of the scanning tunneling microscope that could "see" individual atoms, that modern nanotechnology began. Thanks to the development of new techniques and instruments, nanotechnology has spread into different fields, including chemistry, physics, material science, engineering, and biology.

Today nanotechnology is one of the most active research areas, that has changed and will continue to change vision, expectations and abilities to control the material world. These developments will definitely have an impact on the construction industry, particularly the field of construction materials.

Figure 1 illustrates typical biological objects, whose sizes belong to the significant range between 1 to 100 nm (made of 10 to 10^6 atoms).

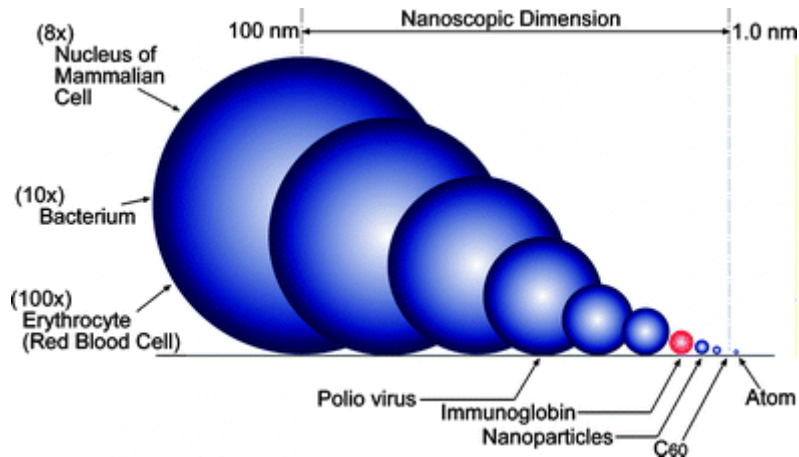


Figure 1 The size window of nanoparticles in comparison to other familiar bodies.

The interest in nanoparticles of these typical sizes is due to the fact that the magnetic, optical and electronic behavior of bulk materials can change when their size approaches the nanometer scale.

1.2 Top-down and bottom-up approaches

Top-down and bottom-up models are both strategies of information processing, used in a variety of fields from computer science to humanistic and scientific theories. The top-down approach plans to start with a bulk material and then break it into nanoparticles by mechanical attrition, chemical or other form of energy and etching techniques.² This strategy often uses the traditional workshop or microfabrication methods, where externally controlled tools are used to cut, mill, and shape materials into the desired shape and order. Techniques such as photolithography and inkjet printing belong to this category.

One of the earlier definitions of nanotechnology, given by Drexler³, was referred to a bottom-up approach: “the control of matter based on molecule-by-molecule control of products and by-products through high-precision systems as well as the products and processes of molecular manufacturing, including molecular machinery.”. Here, organic and inorganic structures are constructed atom-by-atom or molecule-by-molecule. In the bottom-up approach, materials and devices are built from molecular components, which assemble themselves via molecular recognition. Both approaches can be followed in either gas, liquid, supercritical fluids, solid state, or in vacuo. Scientists are interested in the ability to control: a) particle size b) particle shape c) size distribution d) particle composition e) degree of particle agglomeration (Figure 1.2).

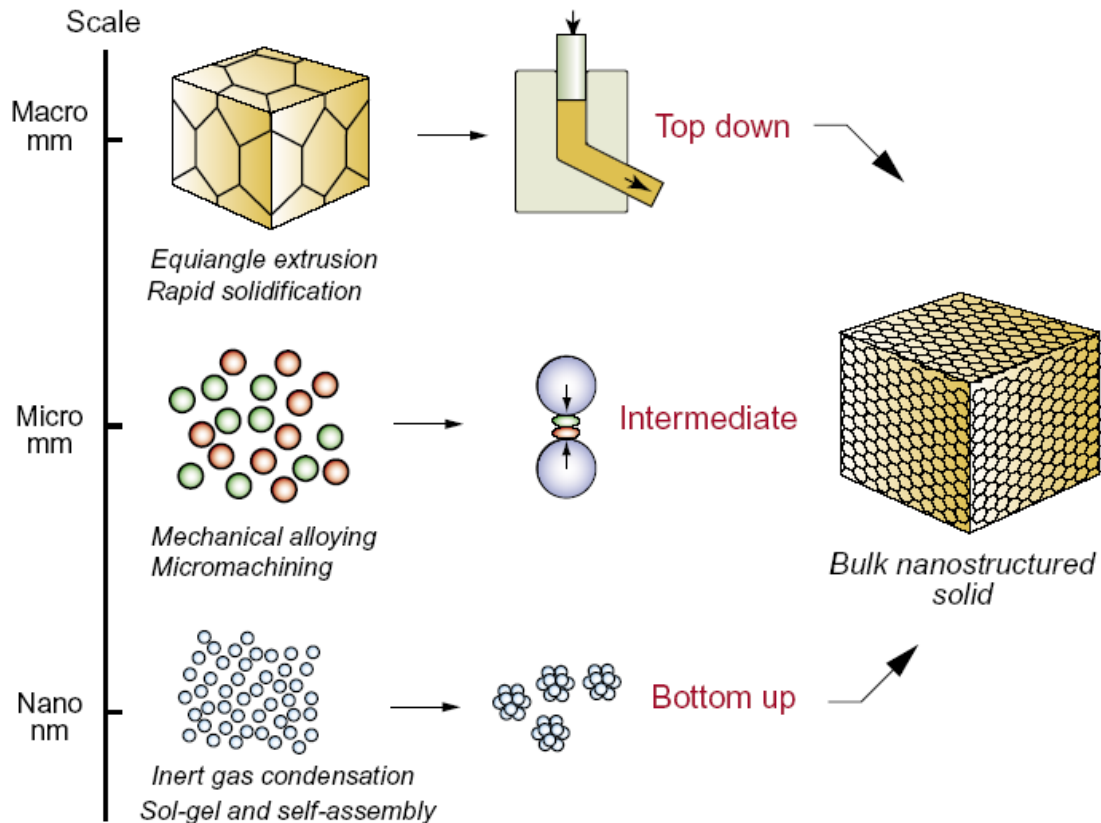


Figure 1.2 Schematic nanostructure synthesis and assembly approaches.

One of the most direct effects of reducing the size of materials to the nanometer range is that several phenomena become significant, for example statistical mechanical effects or quantum mechanical effects. In the "quantum size effect"⁴ the electronic properties of solids are altered with great reductions in particle size. This effect does not come into play on going from macro to micro dimensions, but can become important when the nanometer size range is reached, typically at distances of 100 nanometers or less (or at very low temperature), the so-called quantum scale. Once the effect is originated on the nanometer scale, it can operate on a macro level, generating some paradoxes like in the Schrödinger's cat experiment or electron tunneling experiment. Most fundamental processes in molecular electronics, organic electronics and organic semiconductors also originate in the quantum realm.

In addition, materials reduced to the nanoscale can show different properties compared to those they exhibit on macroscale. For instance, opaque substances can become transparent (copper); stable materials can turn combustible (aluminium); insoluble materials may become soluble (gold). A material such as gold, which is chemically inert at normal scales, can be a potent chemical catalyst at nanoscales. Much of the fascination with nanotechnology stems from these quantum and surface phenomena that matter exhibits at the nanoscale.⁵

1.3 Nanomaterials

The concept of nanomaterials could be summarized in the following definition: “Nanomaterials represent nanoindustry products in the form of materials containing structural nanoelements that substantially improve or cause qualitatively new mechanical, chemical, physical, biological, and other properties”⁶.

Nanomaterials could be categorized with different methods of classification⁷: according to their origin (natural or artificial), according to dimensions (from zero to three-dimensional nanomaterials) or on their structural configuration (based on the different nature of structural nanoelements). In this last classification, nanomaterials can be divided into four categories:

- *Carbon Based Materials*
- *Metal Based Materials*
- *Dendrimers*
- *Composites*

Carbon Based Materials: composed mostly of carbon in several allotropic forms, including crystalline, three-dimensional (diamond, graphite and lonsdaleite); two dimensional (graphene), one-dimensional (nanotubes, cylindrical form), zero dimensional (fullerene, spherical and ellipsoidal forms). These materials demonstrate unique physical and chemical properties such as high strength, excellent resistance to corrosion and exceptional electrical and thermal conduction and stability. Thanks to these features, they have many potential applications, including improved films and coatings, stronger and lighter materials, and applications in electronics (Figure 1.3).

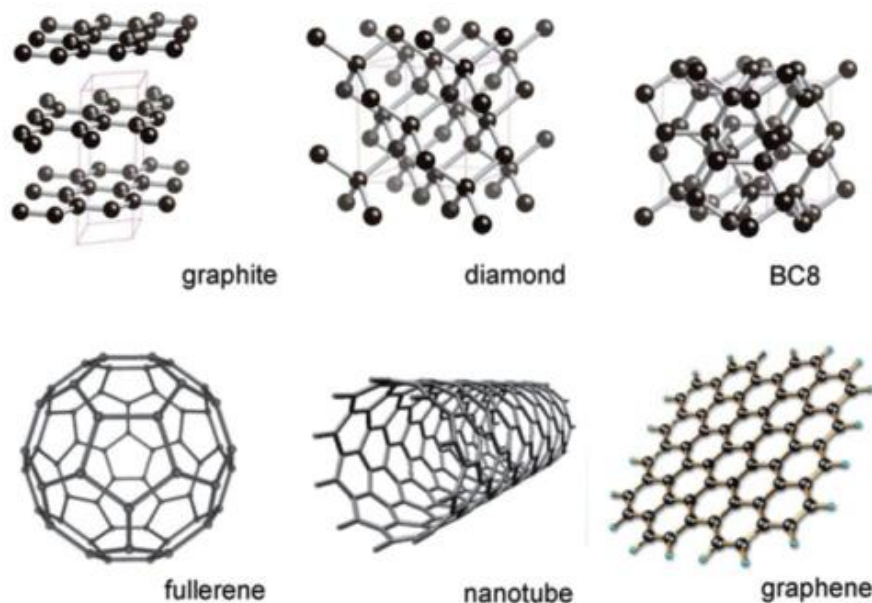


Figure 1.3 The common allotropes of carbon occur in different crystallographic forms (Reviews in mineralogy and geochemistry; 2013, 75(1), 4).

Metal Based Materials: The power of these nanoparticles is in the chemical binding and conjugated properties. These nanomaterials include nanogold, nanosilver, oxides with metal bases (such as titanium dioxide, TiO_2) and quantum dots (Figure 1.4). A quantum dot is a small semiconductor crystal, comprised of hundreds or thousands of atoms, and whose size is on the order of a few to a few hundred nanometers. Changing the size of quantum dots changes their optical and electronic properties.

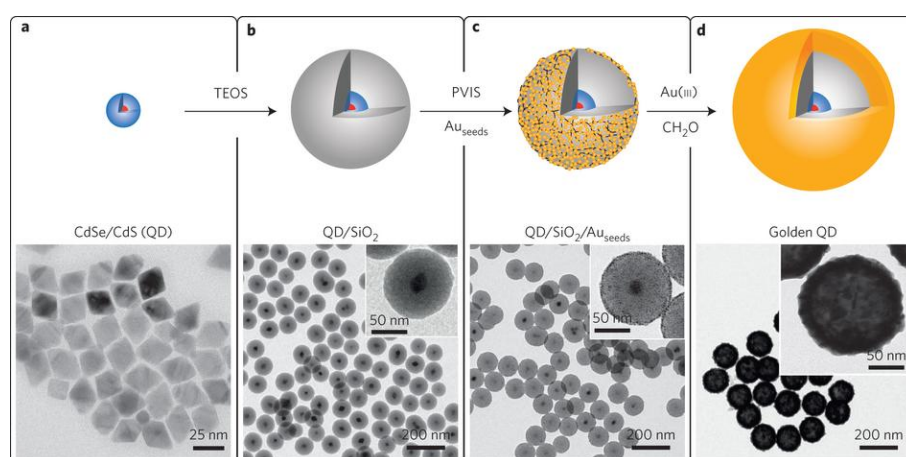


Figure 1.4 Schematic representations of the different stages during golden QD synthesis (top), and corresponding TEM images (bottom). (Reviews: Nature Nanotechnology 10, 170–175 (2015).

Dendrimers: nanosized polymers⁸ built from highly branched units, representing a half step between molecular chemistry and polymer chemistry. The surface of a dendrimer possesses numerous chain ends, which can be tailored to perform specific chemical functions (Figure 1.5). Dendrimers are combinable to create hollow cavities where other molecules could be placed (useful for biomedical applications, as drug delivery systems) or used as sensors⁹.

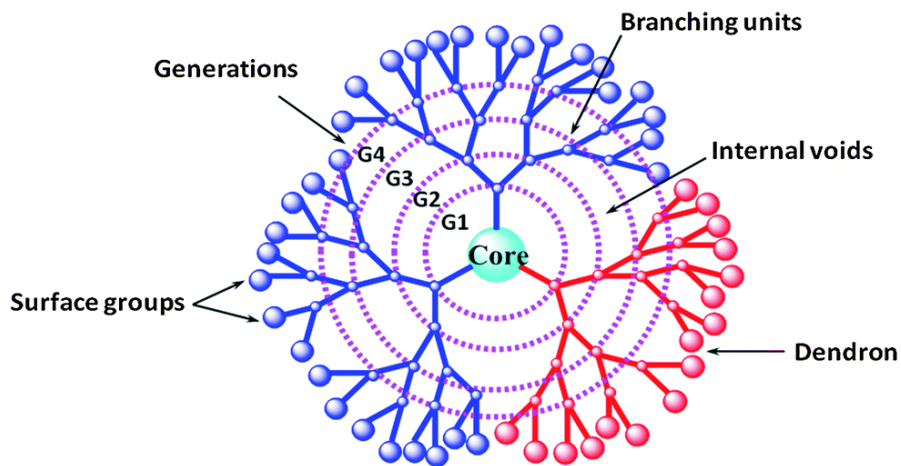


Figure 1.5 Basic dendrimer components (Nanoscale, 2014,6, 2476-2501).

Composites: multiphase solid material where nanoparticles can combine with other nanoparticles or with larger, bulk-type materials to form unique products¹⁰. Nanoparticles, such as nanosized clays, are today added to products ranging from auto parts to packaging materials, to enhance mechanical, thermal and flame-retardant properties. The most common examples of these materials are colloids, gels and copolymers (Figure 1.6).

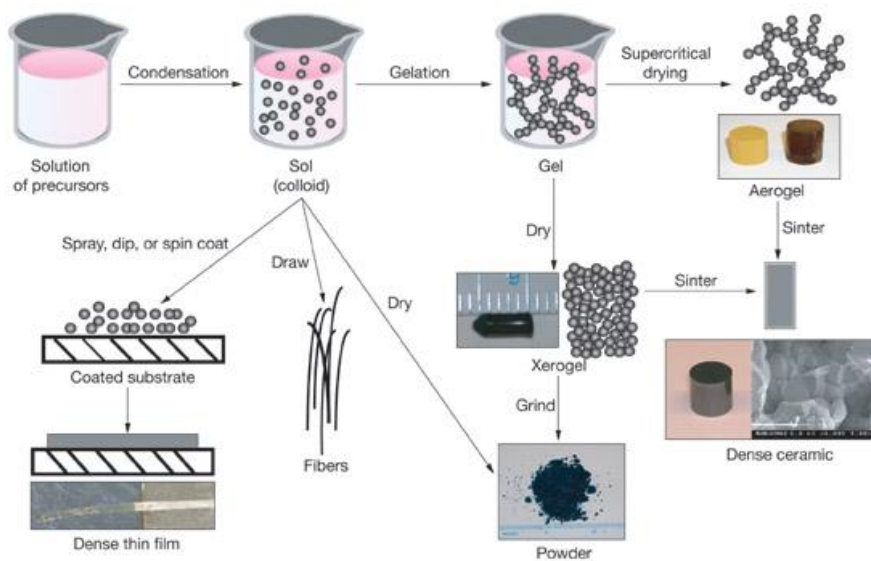


Figure 1.6 Sol-gel processing routes.

1.4 Self-assembly of nanoparticles

Materials science needs an accessible strategy to fabricate nanomaterials with the fine resolution of bottom-up methods and the arbitrary structure of top-down processes. Modern synthetic chemistry has reached the point where it is possible to prepare almost any type of molecules, from pharmaceuticals products to commercial polymers. In the bottom-up approach this ability is raised to the next level, in order to assemble molecules in a specific manner into a supramolecular entity. In the framework of nanofabrication by bottom-up synthetic chemistry, self-assembly has provided a powerful way of making materials and organizing them into functional constructs designed for a specific purpose.

The strategy of self-assembly allows structures synthesized with bottom-up method in the nanoscale to organize themselves into regular patterns or structures by using local forces to find the lowest energy configuration.

Self-assembly of nanoparticles could be useful for a variety of applications. For example, building sensors to detect chemical and biological molecules. In addition, it can also be exploited on creating computer chips with smaller component sizes, which can then allow more computing power to be stored on a chip. Moreover, it can be possible to attach molecules onto specific clusters and substrates, such as thiol (-SH) end group on the gold surface¹¹. These approaches utilize the concepts of molecular self-assembly and/or molecular recognition, which will be discussed in detail in the next chapter.

Despite the top-down methods, bottom-up approaches should be capable of producing devices in parallel and at a lower price, but could potentially be overwhelmed as the size and complexity of the desired assembly increases. Most useful structures require complex and thermodynamically unlikely arrangements of atoms. Nevertheless, there are many examples of self-assembly based on molecular recognition in biology, most notably Watson–Crick base pairing and enzyme-substrate interactions. The challenge for nanotechnology is whether these principles can be used to engineer new constructs in addition to natural ones.

1.5 QCA

In the electronic industry, common digital circuits have made extensive use of Field-effect transistor (FETs),¹² a semiconductor device used to amplify electronic signals or as electronic switch from “on” to “off” state due to encode binary information. Despite vast improvements in integrated circuit fabrication technology over the past three decades, the role played by the FETs has maintained acceptable performance as current switch.¹³ It is able to use much lower levels of current and, as a result, it has enabled far higher degrees of integration to be attained than would

have been possible by any other means. However, these advances are only partial, because also the most advanced chips use the same paradigms compared to their precursors. Additionally, the current levels of miniaturization are hardly improvable (Moore's Law). Further difficulties have arisen by approaching the quantum nanoscale, such as high power dissipation and short-channel effects, which lead to performance degradation. Achievement of ever higher levels of integration in microelectronics will require a shift from the FET based paradigm to a revolutionary approach to computing.¹⁴

In order to overcome these limits, new frontiers in nanoscale computing devices have been developed. In the '90s, Lent¹⁵ proposed an alternative computational model system, based on quantum-dot cellular automata (QCA). This new approach opens the door to applications in the fields of micro- and nano-electronics, most notably the construction of a new transistorless method for computation, where exchange of information between components no longer relies on moving particles along physical communication channels, but uses quantum interactions between elementary particles, with advantages in terms of energy consumption, miniaturization and performance.

Each device designed for the representation of data and to perform computational roles must have two fundamental properties: 1) kind of "barriers" which allow them to distinguish between two states (from state 0 to state 1 for example) and 2) the ability to switch from one state to another and vice versa. In digital electronic systems this "barrier" is created from the transistors, which base their operation on the state of the electric charge, the QCA instead bases its operation on the space disposition.

The concept of QCA does not refer to a particular technology but rather to a theoretical scheme. Devices are composed of cells, each containing quantum-dots. A dot, in this case, is simply a region in which charge is localized.¹⁶ Figure 1.7 illustrates a schematic four-dot QCA cell: a square of nanometric dimension where four corners are occupied by four quantum dots which act as charge containers. In the model presented by Lent, two electric charges try to occupy the farthest possible site with respect to each other in order to minimize their mutual Coulomb interaction.

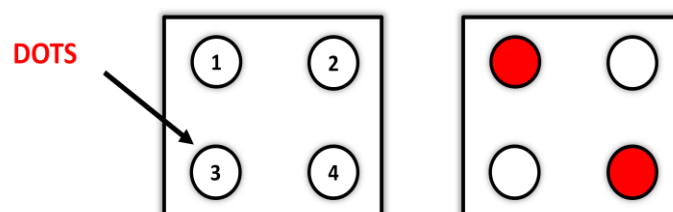


Figure 1.7 A cell with four quantum-dot. White ones are free, while red ones are occupied by electric charges.

Since diagonal is the largest distance in a square, there are two possible conditions, as shown in Figure 1.8: two degenerate ground states, corresponding to two different types of polarization, $P=-1$ and $P=+1$, which are associated with logic binary states “0” and “1”, respectively.

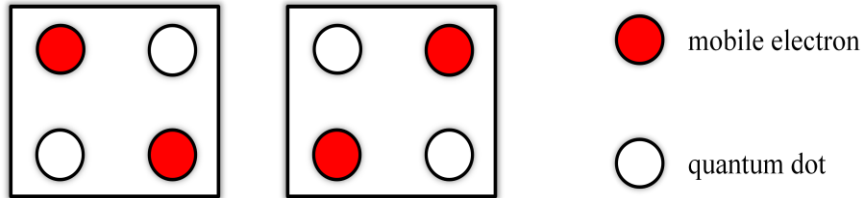


Figure 1.8 Two possible states of QCA: on the left state 0, on the right state 1.

The potential barrier existing between the dots makes it possible the movement of the charges from one dot to another only by tunnel effect. Furthermore, displacements from one cell to another are not permitted because potential barriers are high enough to prevent inter-cell tunneling.¹⁷ An electrostatic perturbation causes a sudden and highly non-linear switching between the two states of the cell.

The second requirement is the possibility of changing the charge configuration by means of an external signal (input), through electron tunneling between neighbouring sites (dots) of the cell. In a QCA binary wire (Figure 1.9) the left-most cell, called driver cell, is fixed with a polarization representing the ground state configuration. By an external input voltage, the polarization of driver cell can be switched and this configuration change propagates to other cells by coulomb interactions.

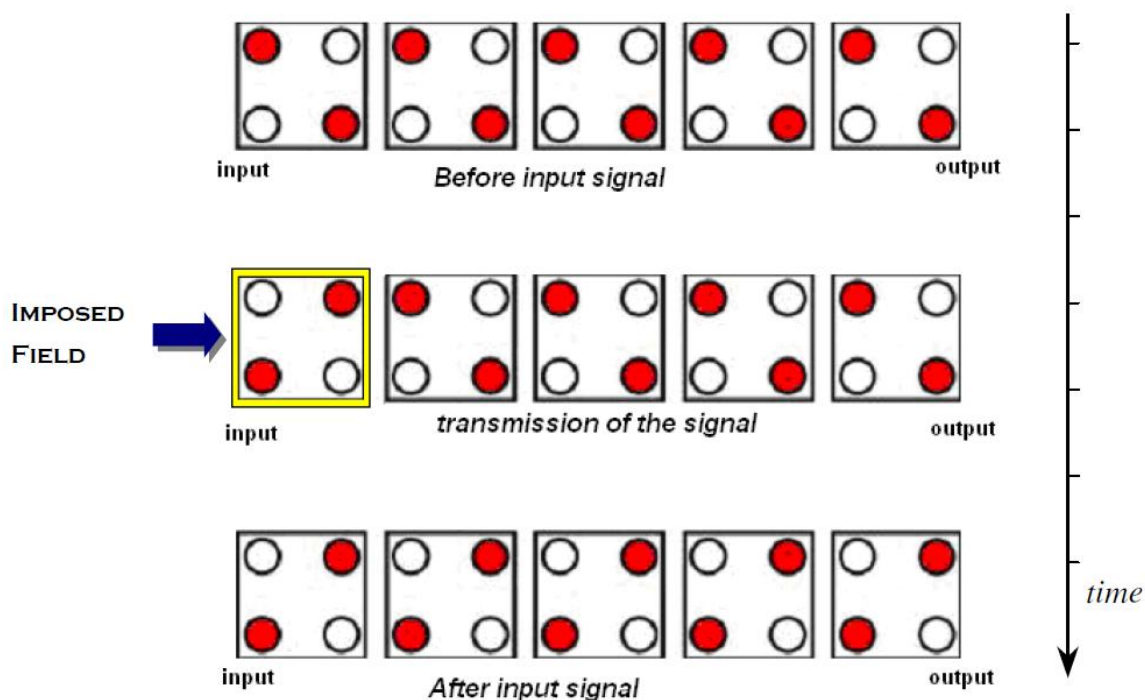


Figure 1.9 QCA binary wire. Cells arranged in a line all take on the same value.

This cell-cell interaction is the basis of QCA device operation and binary information can be encoded without current flow along the entire array, enhancing logic operations with ultra-low power dissipation.¹⁸ According to spatial organization of the cells different QCA structures can be obtained, each with a particular geometry, which can be employed to several computer applications. Despite the QCA theoretical model is well developed and several papers tried to explore possible candidate molecular systems, a practical implementation of the QCA model into a real molecular system is still far from being reality.

1.6 Molecular quantum-dot cellular automata

Since the dot size can ultimately be as small as a single molecule, the QCA architecture offers ultrahigh device density, and is predicted to be both faster and more energy efficient than conventional complementary metal–oxide–semiconductor technology. Furthermore, molecular QCA cells should have state energy difference of two polarizations greater than the thermal energy at room temperature. Indeed the energy difference scales inversely with size and at the molecular level.^{19,20} QCA devices can be contracted so that a single molecule can act as a QCA cell. Redox centers within the molecule can act as quantum dots while molecular bonds form tunneling paths. This alternative approach to realize QCA logic gates has many advantages. At first, molecules provide QCA cells of uniform size,²¹ with high device density (in the range of 10^{11} – 10^{14} devices cm^{-2}). Besides, the intrinsic bistability of the charge configuration results in dipole or quadrupole

fields which couple strongly to the state of neighboring molecules. In order to have a practical application at computational level, the presence of functional groups or linkers is necessary to ensure the anchoring and a proper orientation on a solid surface as well as to set the input signal and detect the output signal.

Several molecules have been investigated as candidates for construction of molecular QCAs. Initially, Lent focused on a simple molecular structure, shown in Figure 1.10, first proposed by Aviram²² and later studied by Hush et al.²³ The utility of the Aviram molecule is especially theoretical because of its instability and its too simple structure (for example, it doesn't possess groups which allow anchoring on surfaces). However, it is suitable to illustrate the basic features that molecular units suitable for QCA should possess.

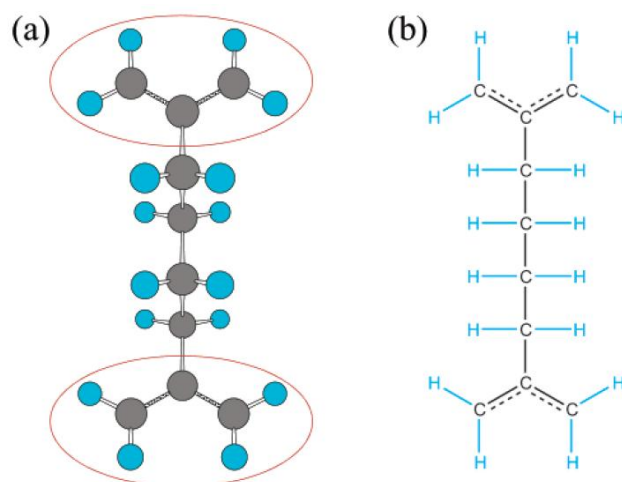


Figure 1.10 Two views of Aviram molecule.

Aviram molecule²⁴ (1,4-diallyl butane radical cation) consists of two allyl groups connected by a butyl bridge. Lent studies related in particular to the molecular cation for which one allyl group is a neutral radical and the other is cationic (the molecular anion behaves very similarly). The three-carbon π -system in the allyl group has a doubly occupied bonding level and a nonbonding level which is singly occupied in the neutral allyl radical and unoccupied in the allyl cation. The unpaired electron can flip between the nonbonding levels at the opposite allyl end-groups with little changes on the molecular geometry.

This system provides an example of localized states with nonbonding character which can play the role of dots for QCA. If the charge is resident in only one end but not the other, the molecule will develop a dipole moment, which changes sign when the electron tunnels from one end to the other. Because the charged end has one less electron than does the neutral end, it will be helpful to view this process as a hole tunneling from one allyl end-group to the other. QCA action is possible

because the dipole field from one molecule can cause the dipole moment of a neighboring molecule to change sign; this confirms the validity of Aviram molecule as a prototype of molecular QCA.

1.7 Ferrocene fragments for molecular QCA cells

Ferrocene (Figure 1.11) and its derivatives fit molecular QCA requirements and have been the subject of extensive study due to their unique structural, spectroscopic and electrochemical properties.²⁵ Ferrocene was first prepared in 1951 by Pauson and Kealy,²⁶ who reported the reaction of cyclopentadienyl magnesium bromide and ferric chloride. Ferrocene is part of the class of metallocenes in which interactions between the d-orbitals of the Fe (II) metal centre with the π -orbitals of the two planar cyclopentadienyl ligands ($C_5H_5^-$) form the metal-ligand bonds. Thus, all the carbon atoms in the cyclopentadienyl rings are bonded equally to the central Fe^{2+} ion.

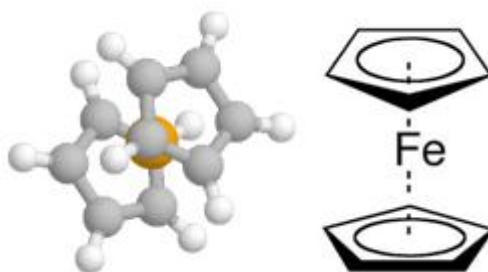


Figure 1.11 Ferrocene molecule.

Ferrocene exhibits aromatic properties and is thermally very stable. It is also resistant to acidic and basic reagents. Oxidation of ferrocene gives a stable cation called ferrocenium.²⁷ Substituents on the cyclopentadienyl ligands alter the redox potential. Ferrocene derivatives exhibiting multiple ferrocene groups, with the potential possibility of producing mixed-valent states, are being actively explored for application as molecular diodes.

From this perspective, another molecular four-dot cell²⁸ for the quantum cellular automata has been evaluated by Lent and coworkers. X-ray structure determination of this four-dot cell revealed four ferrocenes arranged in a square at the corners of a cyclobutadiene linker as shown in Figure 1.12. Each ferrocene group acts as a quantum dot, and a Co atom in the center of the square provides a bridging ligand which acts as a tunneling path. This molecule has two mobile electrons which occupy the antipodal sites due to Coulomb interaction, thus providing two stable charge configurations suitable for representing binary information.

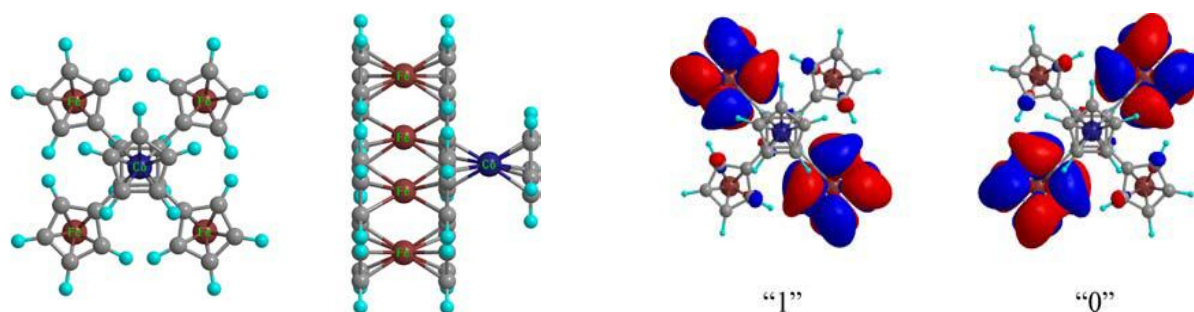


Figure 1.12 Left: Self-assembly of 4 quantum dots. Right: The HOMOs of the two stable states of the molecule.

In addition, Lent and coworkers constructed a two units supramolecular system, with the distance between two cell centers (Co atoms) fixed as two times of the square lateral length, in order to satisfy the second key requirement of a QCA molecule. The electronic charge configuration of one molecule responding to its neighboring molecule represents a quadrupole-quadrupole interaction.

The results support the hypothesis that Coulomb interactions between molecules can be exploited for binary information propagation from one molecule to another. The practical application of this molecule is not possible because of the absence of appropriate groups for anchoring on a surface, as in Aviram molecule. However, further progress in the study of molecular QCA is represented by the fact that the coupling between cells is obtained by self-assembly, combining the principles of quantum computation with supramolecular chemistry.

Lent and colleagues have also reported a functionalized molecule containing unsymmetrical mixed-valence complex (two different redox ferrocene units) and rutenocene.²⁹ The molecule was then supported in its corresponding oxidized form to a silicon surface through a binding linker, forcing the molecular orientation in a certain position. Under an electric field Fe(II)-Ru(III) and the Fe(III)-Ru(II) cations exchange an electron between the Fe and Ru sites at the potential where metal energies are equalized. A compound like this represents an advance toward the effective practical application of molecular quantum cells.

Despite the many challenges that remain, thus far all of the experimental results support the possible implementation of QCA at the molecular scale. The use of molecules in quantum computation is still developing, however it is clear as this new approach could offer many advantages: further size reduction and devices with increasing performance and density. This is accompanied by the possibility to operate at room temperature, while with metal dots is necessary to adopt cryogenic temperatures.

Bibliography

- ¹ R. Feymann, *There's Plenty of Room at the Bottom*, American Physical Society at the California Institute of Technology (Caltech), **December 29th 1959**.
- ² B. Bhushan (Ed.), *Handbook of Nanotechnology*. Springer, **2004**.
- ³ K.E. Drexler, C. Peterson and G. Pergamit, *Unbounding the Future. William Morrow*, New York, **1991**.
- ⁴ *Quantum size effects in nanostructures*, Lecture notes to the course Organic and Inorganic Nanostructures, Kjeld Pedersen, Aalborg, August **2006**.
- ⁵ Lubick N; Betts, Kellyn, *Environ Sci Technol.* **2008**, 42 (11): 3910.
- ⁶ *Proceedings of the Second International Forum on Nanotechnologies*, Moscow, Russia, **2009**.
- ⁷ *Introduction to nanomaterials*. Alagarasi.
- ⁸ Elham Abbasi et all., *Nanoscale Res Lett.* **2014**, 9(1): 247.
- ⁹ Balzani V, Ceroni P, Gestermann S, Kauffmann C, Gorka M, Vögtle F. *Chem Commun.* **2000**, 9, 853–854.
- ¹⁰ Janczak CM, Aspinwall CA., *Anal Bioanal Chem.* **2012 Jan**, 402(1):83-9.
- ¹¹ Thomas Bürgi, *Nanoscale* **2015**, 7, 15553-15567.
- ¹² Kahng, Dawon, *Electric Field Controlled Semiconductor Device*, U. S. Patent No. 3, 102, 230 (Filed 31 May 31, **1960**, issued August 27, **1963**).
- ¹³ I. Amlani, A. O. Orlov, G. Toth, G. H. Bernstein, C. S. Lent, G. L. Snider, *Science* **1999**, 284, 289.
- ¹⁴ A. O. Orlov, I. Amlani, G. H. Bernstein, C. S. Lent, G. L. Snider, *Science* **1997**, 277, 928.
- ¹⁵ C.S. Lent, P.D. Tougaw, W.Porod, G.H. Bernstein, *Nanotechnology* **1993**, 4, 49-57.
- ¹⁶ H. Qi, S. Sharma, Z. Li, G. L. Snider, A. O. Orlov, C. S. Lent, T. P. Fehlner, *J. Am. Chem. Soc.* **2003**, 125, 15250-15259.
- ¹⁷ P. D. Tougaw, C. S. Lent, *J. Appl. Phys.* **1994**, 75, 1818-1825.
- ¹⁸ C. S. Lent, M. Liu, Y. Lu, *Nanotech.* **2006**, 17, 4240.
- ¹⁹ C. S. Lent, B. Isaksen, M. Lieberman, *J. Am. Chem. Soc.* **2003**, 125, 1056.
- ²⁰ C. S. Lent, B. Isaksen, *IEEE Trans. Electron Devices* **2003**, 50, 1890.
- ²¹ C. S. Lent, *Science* **2000**, 288, 1597.
- ²² Aviram, A.J. , *Am. Chem. Soc.* **1988**, 110, 5687.
- ²³ Hush, N. S.; Wong, A. T.; Backskay, G. B.; Reimers, J. R. J. , *Am. Chem. Soc.* **1990**, 112, 4192.
- ²⁴ C. S. Lent, B. Isaksen, M. Lieberman, *J. Am. Chem. Soc.* **2003**, 125, 1056-1063.
- ²⁵ A. H. Schafer, C. Seidel, L. Chi, H. Fuchs, *Comm. Adv. Mater.* **1998**, 10, 839.

- ²⁶ T. J. Kealy, P. L. Pauson, *Nature* **1951**, 168, 1039.
- ²⁷ D. T. Gryko, F. Zhao, A. A. Yasseri, K. M. Roth, D. F. Bocian, W. G. Kuhr, J. S. Lindsey, *J. Org. Chem.* **2000**, 65, 7356-7362.
- ²⁸ Y. Lu, C. S. Lent, *Journal of Computational Electronics* **2005**, 4, 115-118.
- ²⁹ H. Qi, S. Sharma, Z. Li, G. L. Snider, A. O. Orlov, C. S. Lent, T. P. Fehlner, *J. Am. Chem. Soc.* **2003**, 125, 15250.

II. Supramolecular chemistry

2.1 Introduction

“The extraordinary and to some extent inexplicable production of urea without the assistance of vital functions, for which we are indebted to Wöhler, must be considered one of the discoveries with which a new era in science has commenced.”¹

In 1828, a German chemist Friedrich Wöhler was able to synthesize urea, an organic compound found in mammalian urine, by heating cyanic acid and ammonia in vitro.² The simple experiment of Wohler had a huge impact in the history of chemistry, overcoming definitely the line between organic and inorganic synthesis and consequently the "vitalism" concept³ on the functioning of living cells on which was based the whole chemistry of the XVIII century.

Over the years, chemical synthesis has developed different methods in order to build more complex molecular structures from smaller molecules, by creating and breaking covalent bonds between atoms. The progress of organic synthetic chemistry and polymer chemistry has led to a broad spectrum of low and high molecular weight molecules, from dyes to medicines. In all those cases, building atoms are linked to each other by covalent bonds. This type of interaction seemed the only possible way to synthesize complex organic compounds and for decades the synthetic activity moved to the refining of synthetic techniques.

By taking inspiration from biological systems, synthetic chemists can design new highly sophisticated artificial systems, able to respond to external stimuli. However, *“chemistry is not limited to systems found in biology, but is free to create unknown species and to invent novel processes. So the traditional chemistry is increasingly moving towards a new approach, a new perspective for the development of supramolecular chemistry.”*

The current definition of supramolecular chemistry was given by Jean-Marie Lehn, who was awarded the Nobel Prize in 1987⁴, together with D.J. Cram and C.J. Pedersen, for his studies on the chemical basis of “molecular recognition”. He wrote that: “beyond molecular chemistry, supramolecular chemistry aims at constructing highly complex, functional chemical systems from components held together by intermolecular forces.”⁵

Following this definition, a supermolecule is an organized, complex entity that is created from the association of two or more chemical species held together and organized by means of intermolecular binding interactions. Supramolecular structures are the result of both additive and cooperative interactions, including hydrogen bonding, π - π stacking interactions, electrostatic interactions (ion-ion, ion-dipole and dipole-dipole), dispersion and induction forces (van der Waals

forces) and hydrophobic/solvatophobic interactions. The resulting supramolecule shows properties which are different from the sum of the properties of each individual component.

Individually, the energies involved in the formation of supramolecular aggregates, with the exception of the coordination bond, are much weaker than those of covalent bonds. The weak nature of the interactions allows automatic adjustments during the assembly process due to its reversibility. The reproducibility of these interactions allows us to refer to such systems as self-organized.

2.2 Self-assembly in supramolecular systems

As defined by Lehn, self-assembly is the prerogative of those systems which are able to self-organize spontaneously, to generate a well-defined and ordered supramolecular architecture. The constituent units, led by molecular recognition and intermolecular non-covalent interactions, behave in a programmed manner, forming complex structures such as layers, membranes, micelles or liquid crystals. The importance of self-organization is such that Lehn defines it as “evolutionary drive towards more complex forms of matter”⁶ and molecular interactions through non-covalent bonds are the foundation of many biological processes: protein-substrate binding, enzymatic reactions, antigen-antibody recognition are just a few examples.

DNA (Figure 2.1) is a typical example of a biological macromolecule. Base pairing via either double or triple hydrogen bonds allow the formation of the famous double helix from individual strands, and provide the means to read out and to replicate the genetic information stored in it.

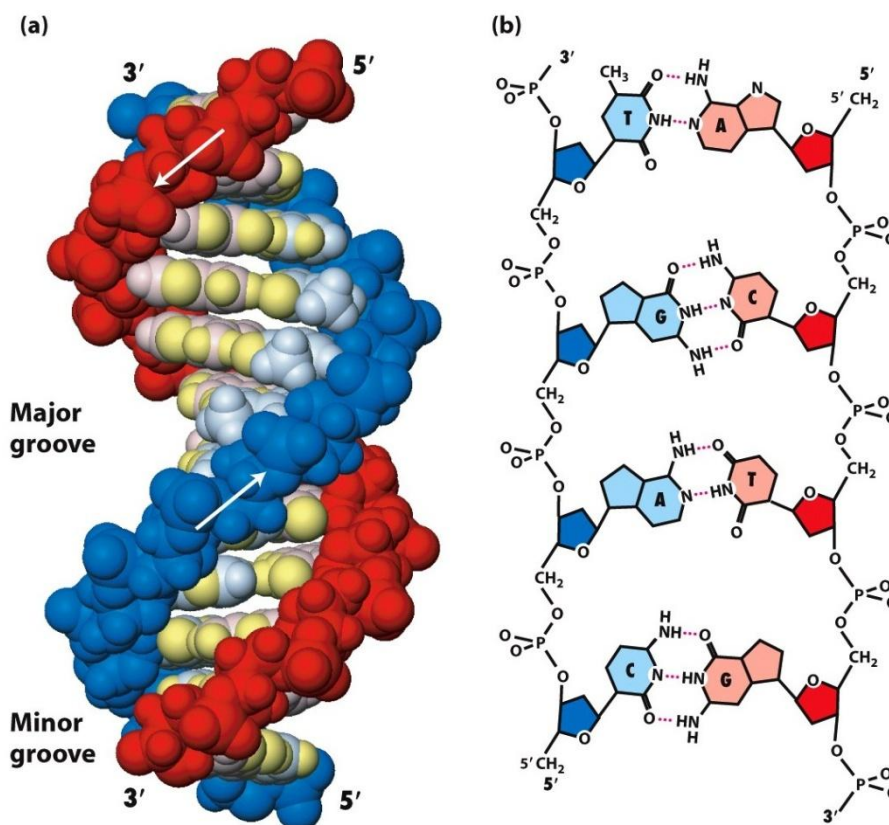


Figure 2.1 DNA double helix and nucleobases coupling through hydrogen bonding interactions.

The canonical Watson and Crick base pairing is crucial in the formation of DNA double helix and in the storage of genetic information. It comprises two of the most common geometries involving the pairing of deoxyadenosine (dA) with deoxythymidine (dT) and deoxyguanosine (dG) with deoxycytidine (dC) through the formation of two and three hydrogen bonds, respectively.

The process of self-organization can be exploited to create also synthetic compounds. The desired supramolecular entity was designed storing the information in order to organize itself in a specific structure.

A self-organization process may be considered to involve three main stages :

- Molecular recognition for the selective binding of the basic components.
- Growth through sequential binding of multiple components in the correct relative disposition.
- Termination of the process, requiring a built-in feature, a stop signal, that specifies the end point.

Suitable encoding by manipulation of structural subunits and processing through interactional algorithms should give access to a variety of systems.

2.3 Guanine and G-quartet

Nucleobases are excellent building blocks for construction of supramolecular aggregates, due to their ability to form non-covalent interactions.⁷ They are well known to form complementary H-bonds between specific base pairs, according to Watson and Crick base pairing in DNA. Alternative hydrogen bonding patterns, such as the Hoogsteen base pairing can also occur, giving rise to complex and functional tertiary structures (Figure 2.2). This last mode of pairing implies the N⁷ position (as a hydrogen bond acceptor) and amino group (as a donor) of the purine base, which binds the Watson-Crick (N³-N⁴) edge of the pyrimidine base.

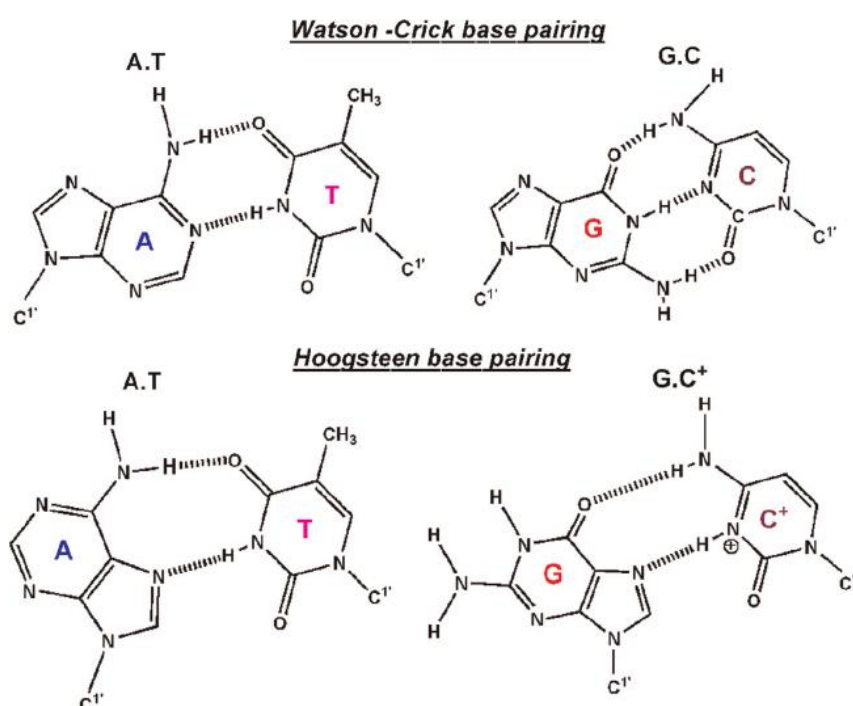


Figure 2.2 Watson-Crick edge and Hoogsteen base pairs.

Among DNA nucleobases, guanine (G) is the most versatile scaffold, containing both a Watson-Crick edge and an Hoogsteen edge⁸, and exhibits a very rich self-assembly behavior. The Watson-Crick edge has two hydrogen bond donors (N¹H, N²H) that can hydrogen bond with the two hydrogen bond acceptors (O⁶, N³ or N⁷) on the Hoogsteen edge. Depending on the environmental conditions, guanine can undergo different self-assembly pathways resulting in various well-distinct architectures including dimers, tetramers, ribbons, and helical structures. Among them, the best known is the so-called *G-quartet* which is a macrocyclic array of four guanines, hydrogen bonded through their self-complementary Watson-Crick (N¹H and N²H) and Hoogsten (O⁶ and N⁷) edges.⁹ Carbonyl oxygens point to the center of these quartets, creating a negative charge which is stabilized through coordination of O⁶ with a monovalent or divalent cation of suitable size (usually

Na^+ , K^+). The other important architecture is the ribbon-like structure, characterized by a different hydrogen-bonding pattern (Figure 2.3).

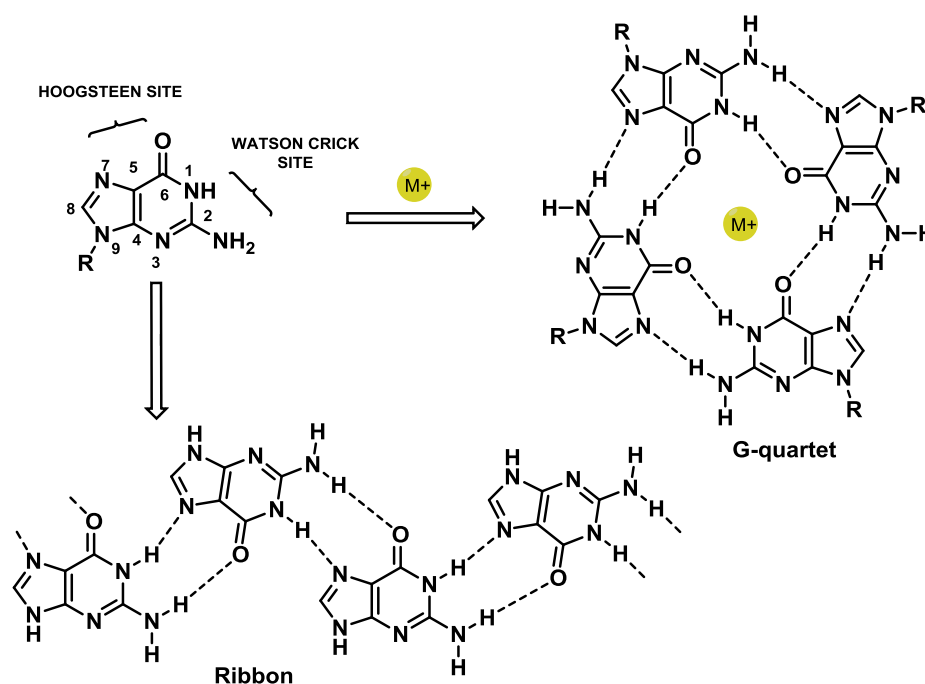


Figure 2.3 Guanine structure and possible linear and cyclic self-assembled structures.

2.4 G-quadruplex

The ability of guanine derivatives to form aggregates is known since 1910, when Bang¹⁰ reported gel formation of a highly concentrated solution of guanylic acid (Guanosine 5'-monophosphate, 5'-GMP). In 1962 Davies and coworkers¹¹ identified through X-ray diffraction the G-quartet structure as the structural unit behind hydrogels formed by 5'-guanosine monophosphate (5'-GMP). But, only several years later research activities in the field of G-quartet related molecular systems have grown exponentially, due to the existence of the G-quartet motif in many biologically important systems in DNA and RNA structures.¹² Now G-quartet structures can be found in many diverse areas such as molecular biology, medicinal chemistry and nanotechnology.

G-quadruplex¹³ structures can form in guanine-rich DNA or RNA strands and consist of guanine tetrads (G-quartets) stacked on each other and stabilized by central monovalent cations, which interact with the lone pairs on the O⁶ atoms surrounding the central core (Figure 2.4). In mammalian cells this role is mainly played by K^+ , which has a higher intracellular concentration (140 mM) than Na^+ (10 mM). G-quadruplexes can form spontaneously at sufficiently high concentrations of guanine. In particular, oligonucleotides with contiguous runs of guanine, such as d(TGGGT) can form stacked structures with the G-quartets linked by the sugar-phosphate backbone.

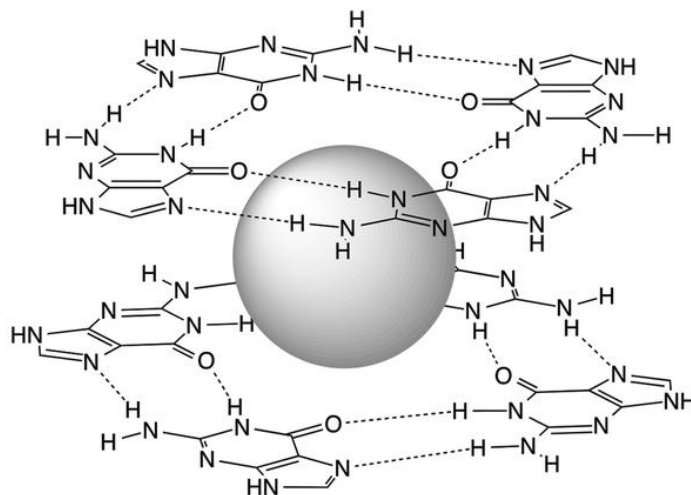


Figure 2.4 G-quadruplex structure.

There are different types of G-quadruplex structures, depending on the involvement of one or more strands, on the length and composition of G-rich sequences. They can form within a single strand of DNA or RNA (intramolecular G-quadruplex) or from the interaction of two or more strands (intermolecular G-quadruplex). These strands have a directionality described as from 5'-end to 3'-end and they can be parallel or antiparallel. At a molecular level, the different directionality of the strands relates to the conformational state of the glycosidic bond between the guanine base and the sugar. This may be either syn or anti. When all bases are in anti conformation the four strands are parallel, when the bases are in the syn all strands are antiparallel. This then affects the orientation of the backbone relative to the G-quartets, and hence results in grooves of different sizes.¹⁴ G-quadruplexes may be comprised of four separate strands, as in Figure 2.5, forming tetramolecular G-quadruplexes, which are always found in the all-anti parallel form. Alternatively, they may be formed from two strands, each with two sets of contiguous guanines, or just from one strand, folding back on itself to form an intramolecular structure. In either of these cases, there will be loops that serve to connect the strands of the structure together. Depending on which strands are connected, these loops may cross diagonally across the top of the structure, joining diagonally opposed antiparallel strands; go across a side, linking adjacent antiparallel strands; or may loop around the side of the structure linking parallel strands and forming a double-strand reversal loop.

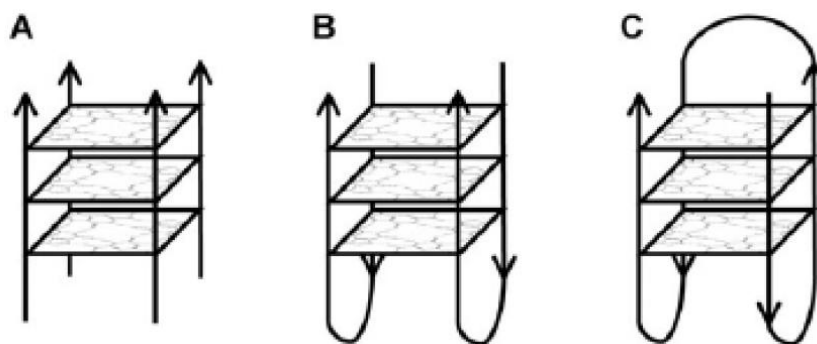


Figure 2.5 Different stoichiometries and folding patterns of G-quadruplexes. (A) Tetramolecular structure with all strands parallel; (B) bimolecular antiparallel structure with adjacent parallel strands; (C) unimolecular antiparallel structure with alternating parallel strands.

Computational studies demonstrate that G-rich regions are not randomly located *in vivo*: in human, yeast and bacterial genomes potential quadruplex sequences have been identified in eukaryotic telomeres,¹⁵ and more recently in non-telomeric genomic DNA, e.g. in nuclease-hypersensitive promoter regions. This specific distribution and the evolutionary conservation of these sequences suggests that G4-motifs have important functions in cells. The natural role and biological validation of these structures is starting to be explored, and there is particular interest in them as targets for therapeutic intervention.

2.5 Structure and behaviour of lipophilic guanosines

Guanine moiety is a versatile hydrogen bonding building block and guanosine derivatives have been studied for their application in supramolecular chemistry. Our group started the research on the supramolecular behavior of guanine-related compounds in late 80's with the observation of the lyotropic properties exhibited by 2'-deoxyguanylyl-(3'-5')-2'-deoxyguanosine (d(GpG)) sodium salt in water.¹⁶ In order to investigate guanosine behavior in absence of H-bonding competitors like water molecules, our group decided to synthesize lipophilic derivatives (LGs) which maintain the donor and acceptor groups in the nucleobase, but with long aliphatic chain in the sugar moiety that makes them readily soluble in apolar organic solvents.

2.5.1 Self-assembly in presence of metal ions

Lipophilic guanosines exhibit in the presence of cation different self-assembly pathways depending on experimental conditions. Our group showed¹⁷ that LipoGs, in particular 3',5'-O-didecanoyl-2'-deoxyguanosine derivative dG(C10)₂, extracts K⁺ picrate from water into chlorinated solvents giving rise to an octameric complex composed of two stacked G-quartets (Figure 2.6 a). The NMR

spectrum of the LG molecule before and after extraction was clearly different, depending on the effective amount of potassium picrate KPic (1:8 or 1:4 K^+/G ratio). In the 1:8 ratio case, a C_4 symmetric octamer was formed. In fact, the 1H NMR spectra,¹⁸ essentially temperature independent over more than $100^\circ C$, show two sets of signals in a 1:1 ratio corresponding each to nucleosides with different glycosidic conformation (*syn-like* and *anti-like*). With more potassium picrate, a 1:4 K^+/G structure (the pseudo-polymer) was produced (Figure 2.6 b).

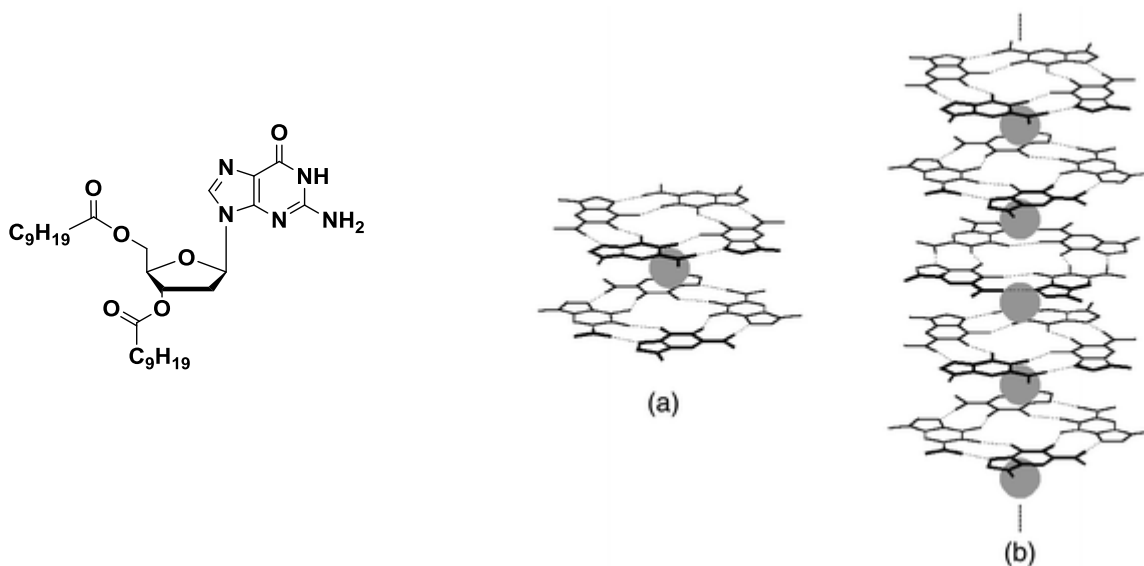


Figure 2.6 The cation-templated self-assembly of derivative dG(C10)₂ from the unassembled molecule to an octameric species (a) and to a pseudopolymeric aggregate (b), (the spheres represent the cation).

Another stereochemical consequence to the cation-templated self-assembly of guanosine derivatives is the mutual orientation between the two stacked quartets, which have diastereotopic faces, known as head (H) and tail (T). The two quartets in the octamer can be arranged in three different ways: H-to-T (C_4 symmetry, homopolar stacking), H-to-H and T-to-T (D_4 symmetry, heteropolar stacking) (Figure 2.7).

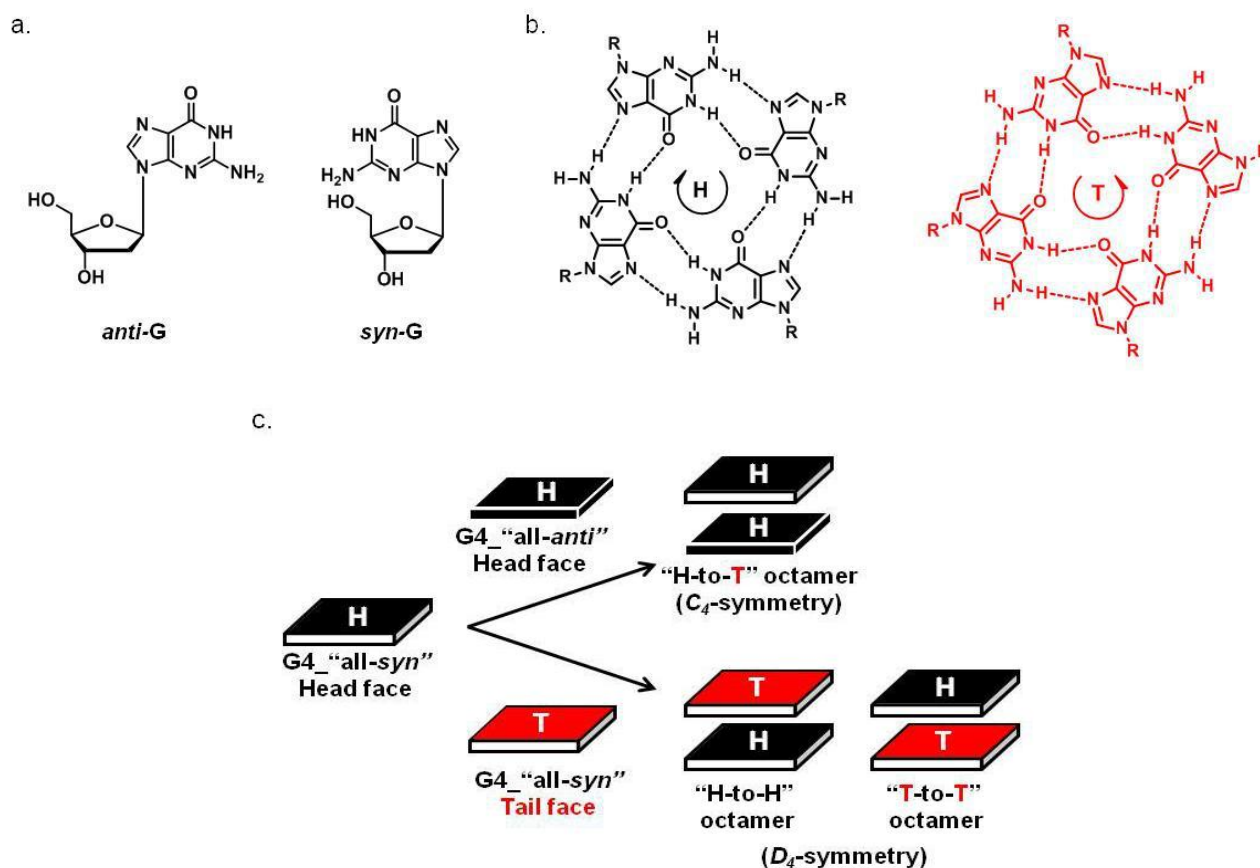


Figure 2.7 a. Glycosidic syn and anti conformations of guanosine; b. Two diastereotopic faces of guanosine; head (H) with a clockwise direction of hydrogen bonds from donor to acceptor and tail (T, anti-clockwise); c. Schematic drawing of a C_4 -symmetric octamer, with an all-syn G-quartet (white) stacking with its tail-side (T, red) on the head-side (H, black) of an all-anti (black) G-quartet, and a D_4 -symmetric octamer with two all-syn tail to tail G-quartet stack.

NMR data indicated a stereoselectivity for the octameric structure of $dG(C10)_2$: a single diastereomer of C_4 symmetry was formed and, in one G-quartet, all monomers had a *syn* conformation, while the other tetramer had an *all-anti* conformation. NOE interactions indicated a relative orientation with the head-side of the "all-anti" G-quartet facing the tail-side of the "all-syn" G-quartet. While this derivative forms the K^+ -templated C_4 -symmetric octamer structure or pseudopolymeric assembly in solution, other lipo-G derivatives (especially those with ribose, in place of deoxyribose, including 2',3'-di-O-isopropylidene-guanosine derivative (Figure 2.8) can give a different stereoregular octamer with a D_4 symmetry.^{19,20}

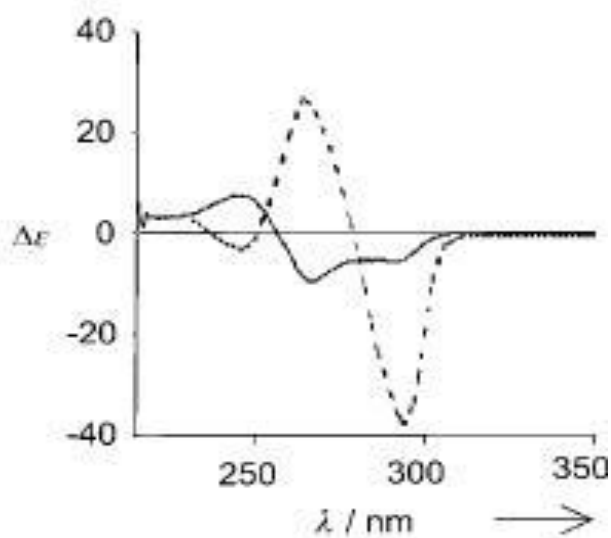


Figure 2.8 Comparison between CD spectra of C4- (solid line) and D4-symmetric (dashed line) octamers $G8 \cdot M^+$ obtained from **A** and **B**, respectively (Data from references 19-20).

Furthermore, the picrate anion is not passive, as it contributes to keep together the complex structure by means of hydrogen bonds with the exocyclic NHs of two different quartets: this binding contribution of the picrate anion was also evident from an ESI-MS study.²¹ The lipophilic G-quadruplex looks like a cation channel with an anionic belt wrapped around its middle.

2.5.2 Self-assembly in absence of metal ions

In the absence of metal cations, derivative $dG(C10)_2$ has been shown to undergo extensive self-assembly mediated by hydrogen bonding between guanine bases: ribbon-like aggregates²² of indefinite length were characterized these both in solution and in solid state. CD spectra, recorded in chloroform at different temperatures and concentrations, showed weak signals, without any exciton pattern, suggesting that no supramolecular chirality was originated by self-assembly of guanines under these conditions. ¹H-NMR spectra in $CDCl_3$ showed broad signals if compared to the ones recorded in the strongly competing solvent $DMSO-d_6$, as expected for largely associated molecules. The existence of oligomeric structures in $CDCl_3$ was supported by ESI mass spectrometry.

Moreover, when increasing guanosine concentration (or lowering temperature), progressive deshielding of both the imino N^1H and amino N^2H protons took place, indicating that the H-bond donor groups of the guanine bases are progressively involved in the self-assembly process. IR spectra led to the same conclusion.²³

Two different ribbon-like aggregates (Figure 2.9), with different patterns of hydrogen bonds, were identified in the solid state and in chloroform solution: when a couple of guanines exposes to the observer their opposite sides, an infinite H-bonded motif is obtained (“ribbon A”). Furthermore, a different homocoupling (ADDA) in which different H-bonding sites of the guanine are involved, leads to the formation of a further kind of H-bonded ribbon (“ribbon B”).

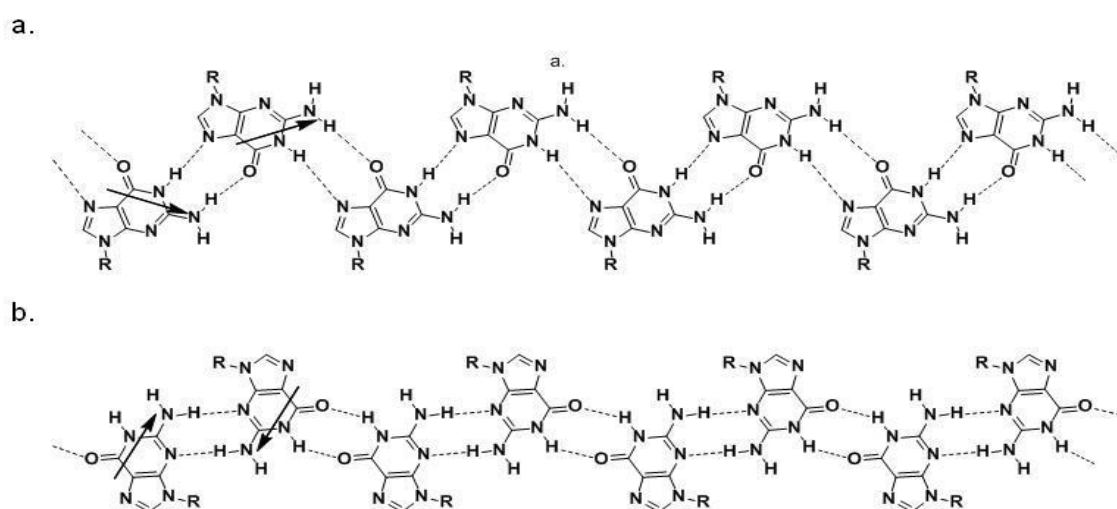


Figure 2.9 H-bond pattern of ribbon-like assemblies ribbon A (a.) and ribbon B (b.). Arrows indicate molecular dipoles.

2.6 Methods for studying G-quadruplexes

Several high- and low-resolution analytical techniques can be used to study and characterize the topology of G-quadruplexes, each examining different aspects of the structures, and hence reporting on different aspects of their formation. X-ray crystallography, NMR spectroscopy and molecular modelling give access to atomic-scale structure information and have revealed over the last decades an impressive structural polymorphism among G-quadruplexes. Other techniques such as UV spectroscopy, electronic circular dichroism spectroscopy, mass spectrometry and chromatography are employed to determine strand orientations, stoichiometry and molecular sizes. Each of these methods gives different types of information so it is important to combine different result in order to have a complete characterization.

The first method used was X-ray crystallography²⁴: obtaining a single crystal is still a slow and uncertain procedure, but with this technique it has been achieved a high resolution (sometimes

below 1 Å) that has allowed the determination of more than 50 crystal structures of G-quadruplexes. X-ray crystallography provides admission to atomic-scale resolution structures of DNA, RNA or LNA G-quadruplex, including the cations, water molecules and binders. A good number of structures containing alkali cations have been solved using this method so crystallography is considered very powerful to characterize cation coordination and more generally ligand binding. It also provides better defined structures than NMR in cases of mixtures of conformations. The limit with this technique is that only the structure adopted in solid state is reported: G-quadruplex structures are frequently highly polymorphic and the crystal structure obtained represents the form that crystallizes more easily, not the favoured one in solution.

NMR spectroscopy is a very useful method²⁵ to collect information about G-quadruplex structures and their dynamics in solution. This high-resolution technique requires much less sample preparation than crystallography, but does require very pure and high-concentrated samples. At the simplest level, it is possible to gain much information even from a 1-D ¹H NMR spectrum, as there are a relatively small number of protons in nucleic acids and the guanine NH1 imino protons have a characteristic shift when hydrogen bonded. In addition, they exchange relatively slowly with the deuterated solvent when compared to non-hydrogen-bonded protons. This may therefore be used to show G-quadruplex formation. In order to provide a more detailed analysis, multi-dimensional techniques are needed, which allow the complete assignment of resonances to the sequence being studied.^{26,27}

The most common low-resolution technique to study G-quadruplex is circular dichroism (CD). CD is a spectroscopic method that measures the difference in absorption of left- and right-circularly polarized light by chiral compounds. In the presence of chiral species, circularly polarized light will generally interact asymmetrically with chiral molecules, and the asymmetry varies with wavelength; the main aim of this method is to assign the absolute configuration of a chiral molecule, but it is very often used for studying conformational changes and supramolecular interactions.

Although the topology of the folding of G4-DNA strands is very complex, only two basic types of CD spectra, which have been associated with the relative orientation of the strands parallel and antiparallel (Figure 2.10), are investigated.

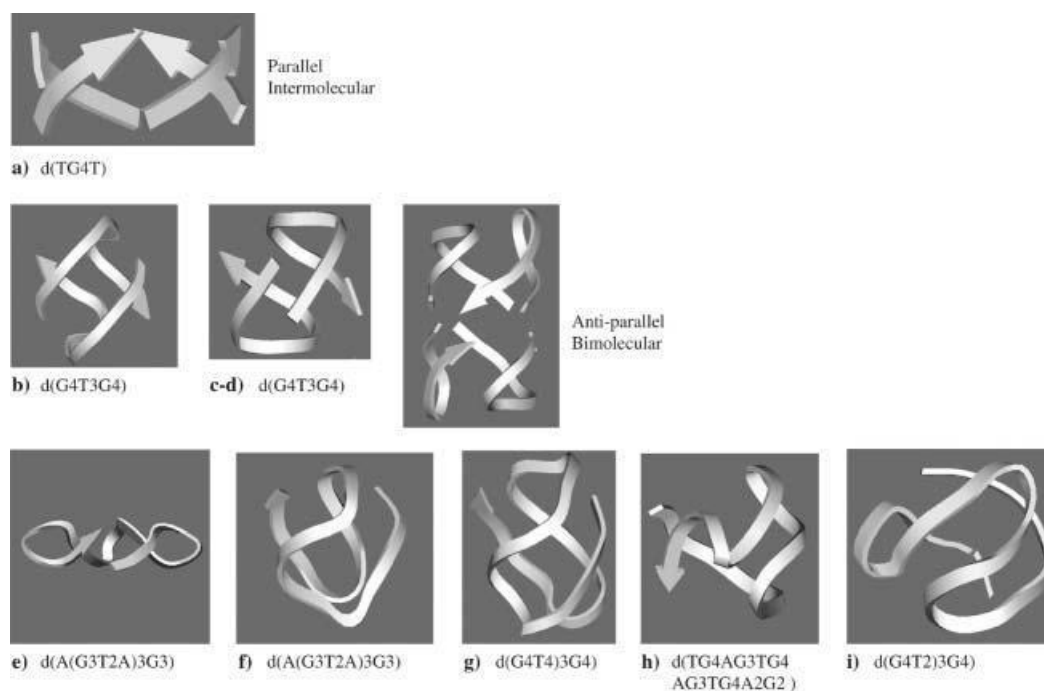


Fig 2.10 Typical folding topologies of G4-DNA forming sequences: a parallel intermolecular structure (a), bimolecular antiparallel structural motifs (b–d), intramolecular parallel (e) and antiparallel (f–i) monomolecular structures. Arrows represent backbones running from 5' to 3' end.

Typically G-quadruplex are characterized by their bands in the UV area, from 210 to 300 nm, because of electronic transitions of the guanine chromophore.

The spectra of parallel quadruplexes, in which four strands with all glycosidic bonds in *anti* have a dominant positive band at 260 nm, and a negative band at 240 nm while the spectra of antiparallel quadruplexes (where guanines alternate *syn* and *anti* glycosidic conformations along each strands) have a negative band at 260 nm and a positive band at 290 nm (Figure 2.11). Although this empirical relationship often works in the interpretation for most CD spectra of G4-DNA, it cannot be considered of general validity.

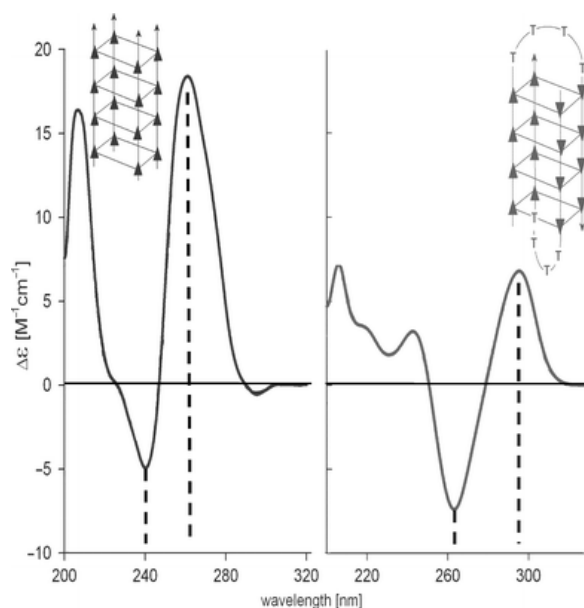


Fig 2.11 CD spectra of guanine quadruplexes. Left side: the parallel stranded quadruplex $[d(G_4)]_4$ stabilized by 16 mM K^+ ; right side: Na^+ -induced antiparallel bimolecular quadruplex of $[d(G_4T_4G_4)]_2$.

However starting from the chromophore it is possible to explain how the different folding patterns affect the CD. The guanine moiety chromophore has two absorption bands, corresponding to π - π^* transitions at ca. 279 nm (short axis polarized) and 248 nm (long axis polarized).

In G4-DNA, G-quartets are stacked one on the top of the other and they are rotated one with respect to the adjacent one: this rotation causes a chiral exciton coupling between transition dipole moments located in near-neighbour guanines. The first non-empirical interpretation of CD of G4 DNA has been reported by Spada et al. 29 By an exciton calculation considering only near-neighbour interactions between the guanine transitions of two stacked G-quartets, it has been possible to reproduce the spectrum of polyguanilic acid, which shows the typical features of “parallel” G4-DNA. The two faces of a G-quartet are diastereotopic so when the G-tetrads are piled, each quartet can stack onto the adjacent one through the same (head-to-head or tail-to tail) or the opposite (head to tail) face leading to a heteropolar or homopolar stacking respectively (Figure 2.12).

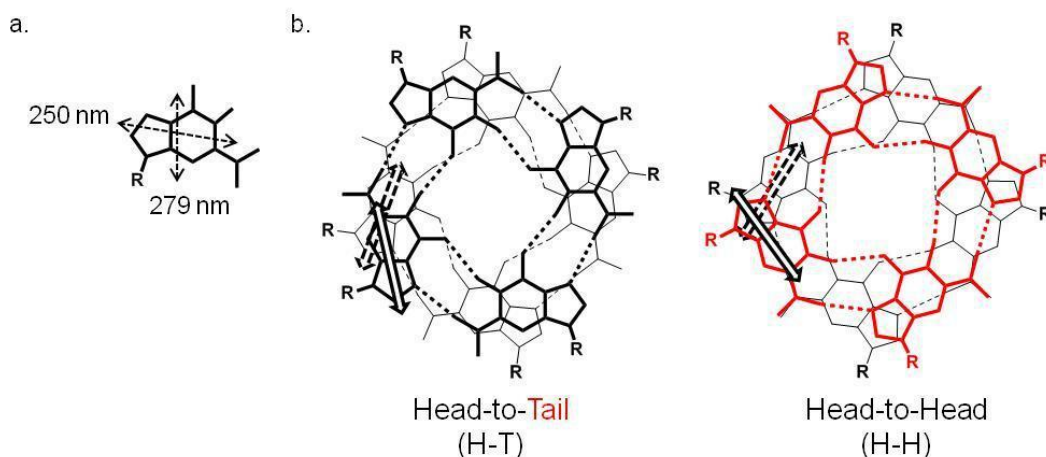


Fig 2.12 a. Representation of π - π^* axis polarized transitions in guanine structure; b. Two possible stacking modes of guanine octamers.

Considering the case of parallel G4-DNA, the disposition of two adjacent G-quartets in a H-to-T orientation is that reported in the Figure 2.12 where the electric moments of a couple of near neighbour guanines are shown. Applying the simplified model of the exciton coupling it emerges that this chiral arrangement is expected to exhibit a positive exciton centered at 250 nm (Figure 2.13). When the glycosidic bonds of the guanines alternate in syn and anti conformations along each strand (antiparallel strands) the G-quartet polarity also alternates, while quadruplexes with parallel strands and all anti glycosidic bonds have a non-alternating G-quartet polarity. CD spectra in these two cases are expected to be different. Indeed, in the heteropolar H-to-H stacking of two quartets, the relative orientation of the closest dipole moments is different from the case described above. Using the qualitative approach of exciton coupling, the chiral arrangement is expected to give a negative couplet centered at 250 nm

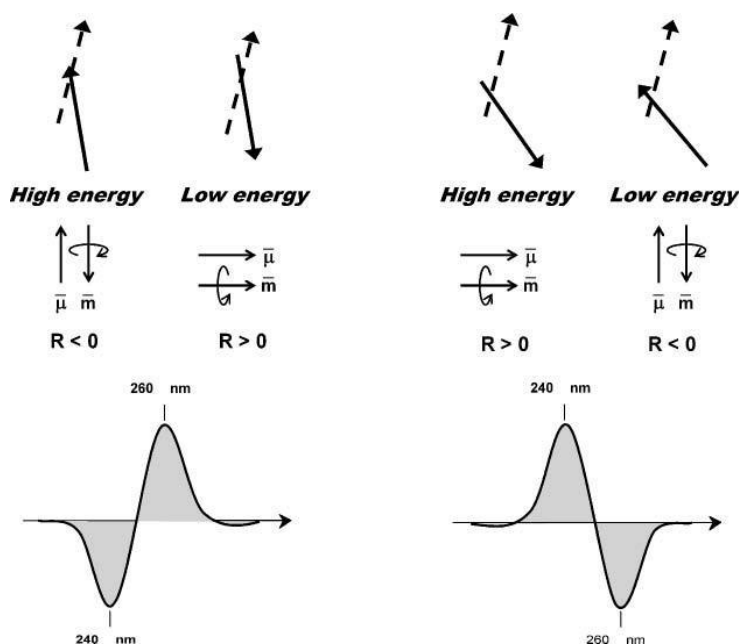


Fig 2.13 A simplified model for the origin of the positive (left side) and negative (right side) exciton couplets for the head-to-tail (H-to-T) and head-to-head (H-to-H) G-quartet stacking, respectively. Top: the arrangement of two 250 nm electric transition moments (full line: front vector; dashed line: rear vector) located in two closest guanines. Middle: the magnetic (\mathbf{m}) and electric (\mathbf{l}) moments generated by the coupling of the two guanine chromophore (more in details, in the high energy coupling of the left-side panel, the two electric transition moments—top—sum to a total electric vector pointing upward—middle—and generate a charge rotation with a resulting magnetic moments pointing downward, that is antiparallel). Bottom: the predicted CD spectra.

CD spectra calculations with the dipole approximation of the two G-quartet stacked with the same or the opposite polarity have been performed by Gray *et al.* (fig. 1.17) and their results are in agreement with the computations by Spada *et al.* on the homopolar stacked system and show how heteropolar stacking explains the emergence of a positive CD signals at 290 nm. The kind of CD spectrum is actually not directly related to the relative strands orientation: the stacking orientation of G tetrads obviously depends on the folding of the strands, however no direct relationship can be established between the two topological features.

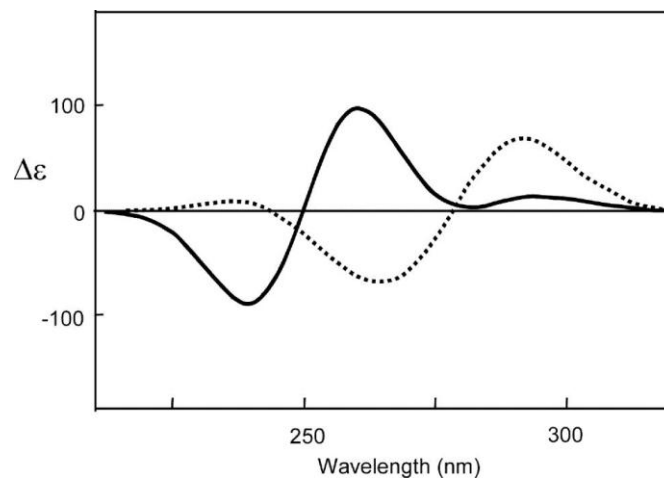


Fig 2.14 Superimposed calculated CD spectra of two G-quartets stacked in the H-to-T (solid line) or H-to-H (dashed line) orientation as shown in Fig. 2.12. The relative orientation of the G-quartets for the calculation were extracted from the solution structure of d(G3T4G3) that present mixed polarities of stacked G-quartets.

Bibliography

- ¹ Cohen P. S.; Cohen S. M., *J. Chem. Educ.* **1996**, 73, 883–886.
- ² Wöhler F., *Ann Phys Chem* **1828**;12:253–256.
- ³ Kinne-Saffran E1, Kinne RK. *Vitalism and synthesis of urea.*, From Friedrich Wöhler to Hans A. Krebs. *Am J Nephrol.* **1999**;19(2):290-4.
- ⁴ Schmeck, Harold M. Jr., Chemistry and Physics Nobels Hail Discoveries on Life and Superconductors; Three Share Prize for Synthesis of Vital Enzymes, *New York Times*.
- ⁵ Lehn J. M., *Chem Soc Rev.* **2007 Feb**; 36(2):151-60. *Epub 2006 Dec 15*.
- ⁶ J. M. Lehn, *Angew. Chem. Int. Ed.* **2013**, 52, 2836-2850.
- ⁷ S. Sivakova, S. J. Rowan, *Chem. Soc. Rev.* **2005**, 34, 9.
- ⁸ W Saenger, *Principles of Nucleic Acid Structure*, Springer-Verlag: New York, **1984**.
- ⁹ G.P.Spada et al., *Chem. Eur. J.* **2009**, 15, 7792-77806.
- ¹⁰ Bang, I., *Biochem. Z.* **1910**, 26, 293.
- ¹¹ Gellert, M.; Lipsett, M. N.; Davies, D. R., *Proc. Natl Acad. Sci. Usa* **1962**, 48, 2013.
- ¹² D. Rhodes, R. Giraldo, *Curr. Opin. Struct. Biol.* **1995**, 5, 311–322
- ¹³ S. Burge, G. N. Parkinson, P. Hazel, A. K. Todd and S. Neidle, *Nucleic Acids Res.* **2006**, 34, 5402.
- ¹⁴ J. L. Huppert, *Chem. Soc. Rev.* **2008**, 37, 1375–1384.
- ¹⁵ Huppert, J.; Balasubramanian, S., *Nucleic Acids Research* **2005**, 33 (9), 2908-2916.
- ¹⁶ Spada, G.; Carcuro, A.; Colonna, F.; Garbesi, A.; Gottarelli, G. *Liquid Crystals* **1988**, 3, 651.
- ¹⁷ G. Gottarelli, S. Masiero, G. P. Spada, *J. Chem. Soc.-Chem. Commun.* **1995**, 2555.
- ¹⁸ S. Lena, S. Masiero, S. Pieraccini and G. P. Spada *Chem. Eur. J.* **2009**, 15, 7792-7806.
- ¹⁹ M. S. Kaucher, Y.-F. Lam, S. Pieraccini, G. Gottarelli, J. T. Davis, *Chem. Eur. J.* **2005**, 11, 164.
- ²⁰ G. P. Spada, S. Lena, S. Masiero, S. Pieraccini, M. Surin, P. Samorì, *Adv. Mater.* **2008**, 20, 2433.
- ²¹ Manet, I.; Francini, L.; Masiero, S.; Pieraccini, S.; Spada, G.; Gottarelli, G. *Helvetica Chimica Acta* **2001**, 84, 2096.
- ²² R. S. Cahn, C. Ingold and V. Prelog, *Angew. Chem., Int. Ed. Engl.* **1966**, 5, 385.
- ²³ Gottarelli, G.; Masiero, S.; Mezzina, E.; Spada, G.; Mariani, P.; Recanatini, M. *Helvetica Chimica Acta* **1998**, 81, 2078.
- ²⁴ Campbell, N.; Parkinson, G., *Methods* **2007**, 43 (4), 252-263.
- ²⁵ Da Silva, M., *Methods* **2007**, 43 (4), 264-277.
- ²⁶ J. L. Huppert, *Chem. Soc. Rev.* **2008**, 37, 1375–1384.

²⁷ S. Masiero, R. Trotta, S. Pieraccini, S. De Tito, R. Perone, A. Randazzo, G. P. Spada, *Org. Biomol. Chem.* **2010**, 8, 2683–2692.

III. Porphyrins

"Vivid testimony to the continuing broad interest and deep impact of the chemistry of these Pigments of Life." - Jean-Marie Lehn, Nobel Laureate, Chemistry, College de France, France.

3.1 Introduction

Porphyrins are an important class of macrocyclic compounds which play leading roles in the metabolism of living organisms and in electron transport in biological systems. They are involved in a large variety of essential functions, as oxygen transport and storage, respiration, photosynthesis, electron transfer, catalysis, etc.

In the past decade, porphyrin systems have become very popular, being targets for commercial exploitation of several catalytic processes such as in the chemical functionalization of hydrocarbons, transportation of oxygen, etc. The porphyrin macrocycle also provides an excellent chelating ligand for a variety of metal ions, giving rise to a wealth of molecules with interesting new features for inorganic and organometallic chemistry, as well as for theoretical, physical, and spectroscopic investigations.

The word porphyrin is derived from the Greek word *porphyrá* which means purple. Indeed, pure porphyrins are crystalline fluorescent pigments intensely colored, of natural or synthetic source. The color is a consequence of the electronic spectra of porphyrins, which contain intense absorptions in the visible region, at 500 nm (called Q bands). Even more intense is the Soret band found in the near UV, from 400 to 450 nm, so named after its discoverer.¹

The first hypothesis on porphyrin structure was formulated in 1884 by Nencki², who suggested that the chemical structure of porphyrins is based on pyrroles. Many years later, Kuster³ specified that this macrocycle is made up of only four units of pyrroles. The final structure was confirmed in 1926, when Fischer⁴ synthesized the etioporphyrin. The porphyrin molecule is usually described as a union of four pyrrole rings linked by four methine bridges to form an aromatic macrocycle, called porphin (Figure 3.1).

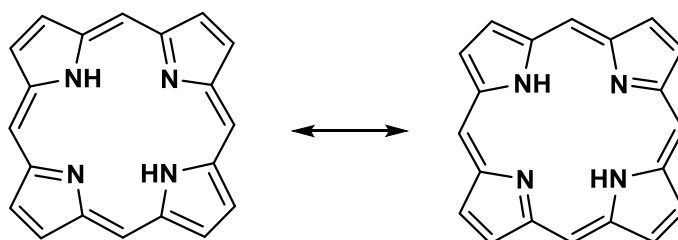


Figure 3.1 Porphin, the core structure of porphyrin.

3.2 Nomenclature of porphyrins

The Fischer system for nomenclature of porphyrins is shown in Figure 3.2. Fischer also created a host of trivial names for porphyrins and for chlorophyll derivatives and a “type” isomer system of nomenclature, which was used to define the nature of the substituents array in certain porphyrins. Despite the significant work done by Fischer, this method has been replaced by IUPAC system.

The official nomenclature system adopted by the IUPAC implies the numbering of all the ring carbons, including the nitrogen atoms, such that the two saturated nitrogens receive the numbers 21 and 23 (Figure 3.2). For a free base porphyrin, the positions at 1, 4, 6, 9, 11, 14, 16 and 19 are identified as alpha (α) positions. In a similar way, the 2, 3, 7, 8, 12, 13, 17 and 18 positions are called beta (β) positions. At last, the positions 5, 10, 15 and 20 are referred commonly as "meso-positions". Respectively, a proton bonded to a meso carbon is cited as H meso and that to a beta carbon as H β .

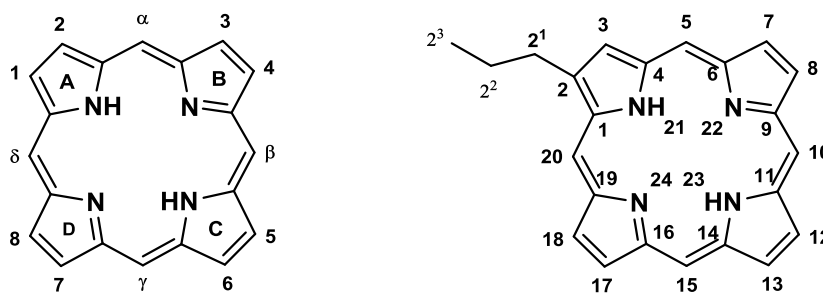


Figure 3.2 Fisher numeration (left) and IUPAC system (right).

Normally, porphyrin macrocycles are planar compounds⁵, but distortion of the macrocycle can be observed in many cases, for example due to the metallation of the porphyrin macrocycle or after a substitution of the macrocycle at beta or meso positions by bulky groups.

3.3 Biological role of porphyrins

Porphyrins derivatives take part in many biological metabolic processes, as the prosthetic groups in a wide variety of primary metabolites, such as hemoglobins, myoglobins, cytochromes, catalases, peroxidases, chlorophylls, and bacteriochlorophylls.

Cytochrome *c*⁶ is a small water-soluble protein (Figure 3.3), located in mitochondrial intermembrane-space and involved in two processes: oxidative phosphorylation and apoptosis. As an electron carrier in oxidative phosphorylation, cytochrome *c* shuttles four electrons, one at time, via its heme group from cytochrome *c* reductase (Complex III) to cytochrome *c* oxidase

(Complex IV). The transition of cytochrome c between the ferrous and ferric states within the cell, makes it an efficient biological electron-transporter and it plays a vital role in cellular oxidations in both plants and animals.

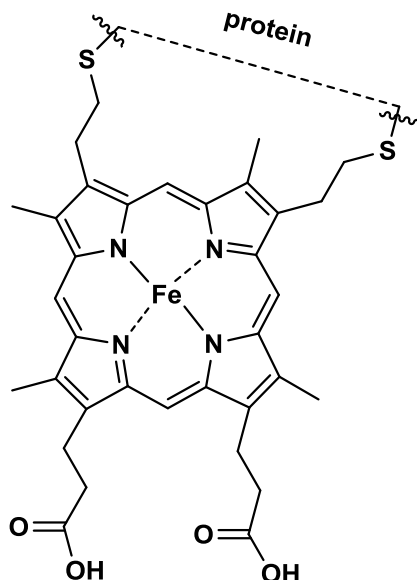


Figure 3.3 Chemical structure of cytochrome c.

More recently, cytochrome c has been identified as a crucial mediator in apoptosis⁷ (programmed cell death). When a cell receives an apoptotic stimulus, cytochrome c is released from mitochondria into the cytosol and triggers programmed cell death through apoptosis. Because cytochrome c leaves the apoptotic cell following induction of apoptosis it is being increasingly recognized as a potentially useful circulating extracellular diagnostic and prognostic biomarker for disease conditions in which apoptosis is involved.⁸

Hemoglobin⁹ (Hb) is a globular heme protein in vertebrate red blood cells and in the plasma of many invertebrates, formed by symmetric pairing of a dimer of polypeptide chains, the α - and β -globins, into a tetrameric structural and functional unit. These 4 polypeptides each have a large central space into which a heme b prosthetic group, an iron-protoporphyrin IX molecule, is bound by noncovalent forces (Figure 3.4). The reversible binding of gases by the heme group allows hemoglobin to transport oxygen, carbon monoxide, carbon dioxide and nitric oxide.

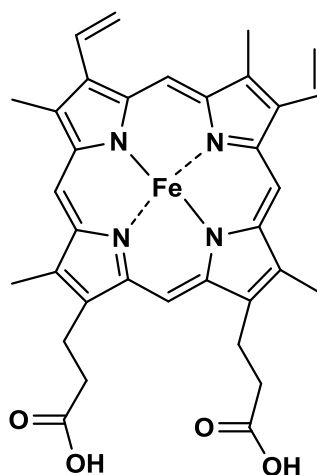


Figure 3.4 Chemical structure of heme b.

Myoglobin¹⁰ (Mb) is a small globular monomeric protein, expressed in cardiac myocytes and oxidative skeletal muscle fibers, that reversibly binds and stores O₂ by its heme residue and catalyzes NO oxidation. Myoglobin is also thought to buffer intracellular O₂ concentration when muscle activity increases and to facilitate intracellular O₂ diffusion by providing a parallel path that augments simple diffusion of dissolved O₂. The iron-ligand bond is broken by light; therefore, Mb has also been employed for exploring the first relaxation events after photodissociation by fast and ultra-fast kinetic methods.¹¹

The biological role of chlorophyll is well known, as it allows plants to absorb energy from light in the photosynthesis. Chlorophyll is a green pigment found in cyanobacteria and the chloroplasts of algae and plants, isolated and named for the first time by Joseph Bienaimé Caventou and Pierre Joseph Pelletier in 1817. The central ring structure is a chlorin, similar to porphyrin, which is produced through the same metabolic pathway as heme group, with three pyrroles and one pyrroline, instead four pyrroles as porphyrin, and a Mg²⁺ metal ion inside. The chlorin ring can have several different side chains, usually including a long phytol chain. There are a few different forms that occur naturally, but the most widely distributed forms in terrestrial plants are chlorophyll a and b (Figure 3.5).

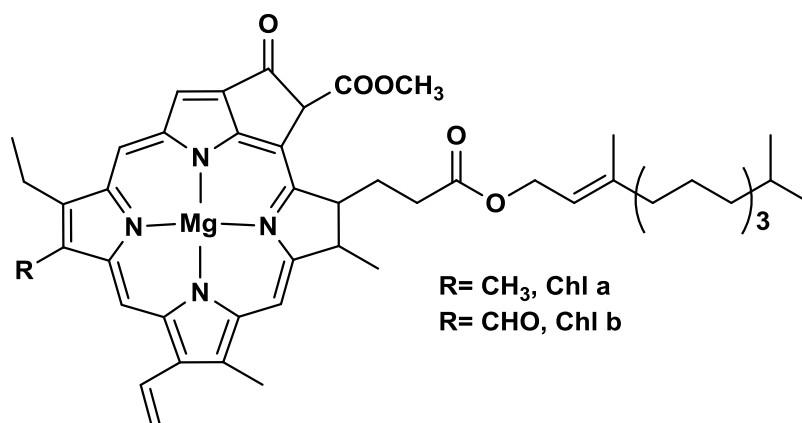


Figure 3.5 Chemical structures of chlorophyll a and b.

The difference between these two forms is in the composition of a sidechain (in a it is $-\text{CH}_3$, in b it is CHO). This small difference allows each type of chlorophyll to absorb light at slightly different wavelengths. However, chlorophyll absorbs light most strongly in the blue portion and in the red portion of the electromagnetic spectrum.

3.4 Reactivity of porphyrins

The porphyrin macrocycle contains 22 conjugated π -electrons, 18 of them are required for its conjugated aromatic network, according to Huckel's rule.¹² As a consequence, porphyrins maintain their aromaticity even after different type of reactions, as additions, substitution, cross-couplings, oxidations and reductions. In this way, it possible to synthesize a large variety of functionalized macrocycles, which are widely used in multiple applications in the fields of biology, medicine and materials science.

The meso and β -pyrrole positions are both involved in this kind of reactions, but with a different reactivity. The most electronically reactive positions are the *meso*-positions, and generally they are the preferential sites for electrophilic aromatic substitutions, additions and radical reactions. On the other hand, the β -pyrrolic positions are the most sterically accessible and can also undergo the same type of reactions. It is possible to protonate the inner pyrroline nitrogen atoms of porphyrins to give the corresponding mono- or di-cations. On the contrary, the NH groups are slightly acidic and can be deprotonated by bases to produce di-anions.

Porphyrins can also be readily metalated with a wide variety of metal ions; indeed the four nitrogens in the middle of the porphyrin molecule can grab and hold metal ions such as magnesium (Mg), iron (Fe), zinc (Zn), nickel (Ni), cobalt (Co), copper (Cu), and silver (Ag). The metal ions have an important inductive effect on the π -electron system and strongly influence chemical reactivity, photophysical properties and biological functions of porphyrin macrocycles.

Closed-shell configuration metals incapable of $d\pi$ - $p\pi$ back-bonding, such as Zn(II) and Cd(II), induce the highest negative charge onto the porphyrin periphery, conferring them the lowest one-electron oxidation potentials. On the other hand, metals capable of π -back-bonding decrease the electron density on the macrocycle, for example Cu(II) and Ni(II) with d^6 - d^9 configurations, and in particular metals with d^1 - d^5 configurations, such as Sn(IV) and Fe(III), strongly reduce the electron density at the porphyrin periphery.

3.5 Porphyrin Synthesis

Porphyrin systems have been the subject of many synthetic investigations over the past 70 years, involving different building blocks, like pyrroles, aldehydes, dipyrromethanes, dipyrromethenes, tripyrranes and linear tetrapyrroles.

The chemistry of meso-substituted porphyrins developed thanks to the intense work of Rothmund, who first in 1935 investigated the synthesis of tetramethylporphyrin by the condensation of acetaldehyde and pyrrole in methanol at different temperatures.¹³ Rothmund and Menotti¹⁴ proposed a synthesis of meso-tetraphenylporphyrin (5,10,15,20-tetraphenylporphyrin (TPP)⁴) in one step by reaction between benzaldehyde and pyrrole in pyridine in a sealed glass tube at 220 °C under nitrogen for 48 h to give blue needle- crystals. High concentrations of the reagents, higher temperatures and the absence of oxidising agents are the identifying characteristics of the so-called "Rothmund method ". (See Figure 3.6)

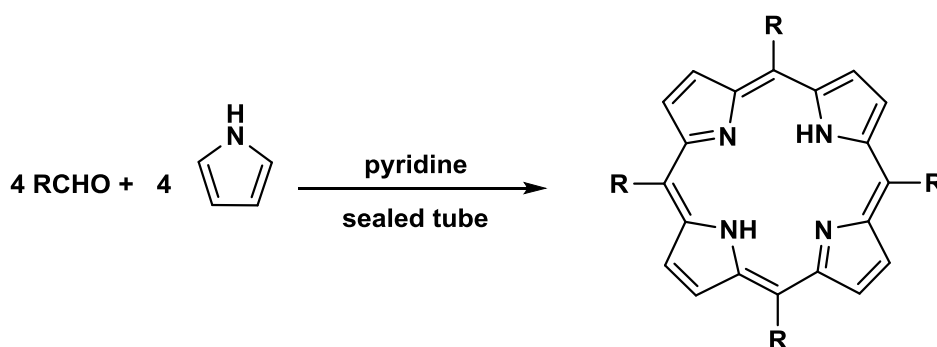


Figure 3.6 Rothmund method for the synthesis of meso-substituted porphyrins.

Unfortunately, the yield of these reactions remains very low, usually less than 5%. The reason for this low yield is due to the presence of a contaminant, the corresponding meso-substituted chlorin (17,18-dihydroporphyrin), which was studied and identified by Calvin and coworkers. In addition, Ball et al.¹⁵ also discovered that the addition of metal salts, like zinc acetate, to the reaction mixture of benzaldehyde and pyrrole increases the yield of TPP (as the zinc derivative) to 10% and decreases the amount of chlorin compound.

A modification by Adler, Longo and their colleagues¹⁶ came many years later, in the 1960s, with a method that involves an acid catalyzed condensation in glassware open to the atmosphere (Figure 3.7). By refluxing pyrrole and benzaldehyde in boiling propionic acid for about 30 minutes, they obtained yields of 20-25%, with chlorin yields of 1% to 3%.¹⁷ This by-product can be easily removed by oxidation with dichloro-dicyanobenzoquinone (DDQ), thereby eliminating the need for a separation procedure.¹⁸

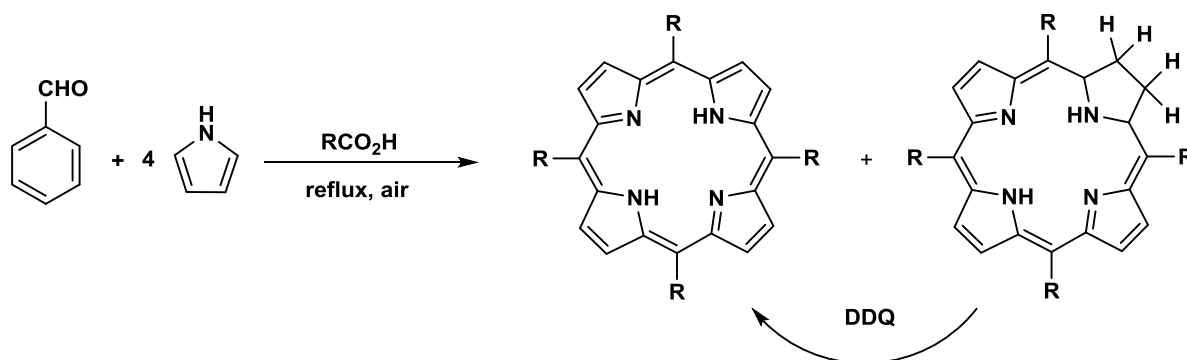
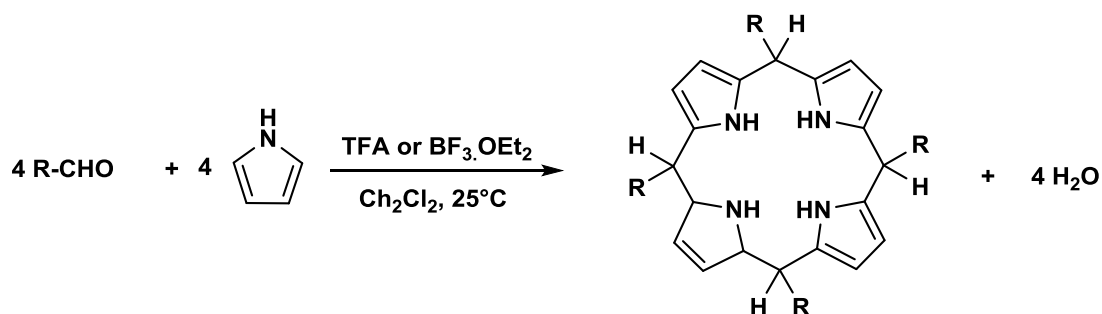


Figure 3.7 Adler-Longo method for preparing meso-substituted porphyrins.

The reaction also works with a limited number of substituted benzaldehydes that are able to survive to refluxing propionic acid. Yields of 35-40% were obtained in acetic acid, but purification was more difficult. Anaerobic conditions provided lower yields (about 5%), highlighting how the oxidation of the intermediate porphyrinogen by atmospheric oxygen was a critical step in the synthesis.¹⁹

Over the period 1979-1986, Lindsey's group^{20,21} developed a new and innovative method, called "two-step one-flask room temperature" to synthesize porphyrins, using a sequential process of condensation and oxidation under milder working conditions, thus expanding the number of aldehydes usable and hence the porphyrins available (Figure 3.8). The condensation of pyrrole and aldehyde was carried under argon, using a chlorinated solvent such as dichloromethane or chloroform, in the presence of a Lewis acid catalyst, usually $\text{BF}_3\cdot\text{OEt}_2$ or trifluoroacetic acid (TFA). In the second step of the reaction, the initial product (a colorless porphyrinogen) is oxidized to porphyrin using a stoichiometric amount of a quinone such as 2,3-dichloro-5,6-dicyanobenzoquinone (DDQ) or tetrachloro-1,4-benzoquinone (p-chloranil).

1. Condensation



2. Oxidation

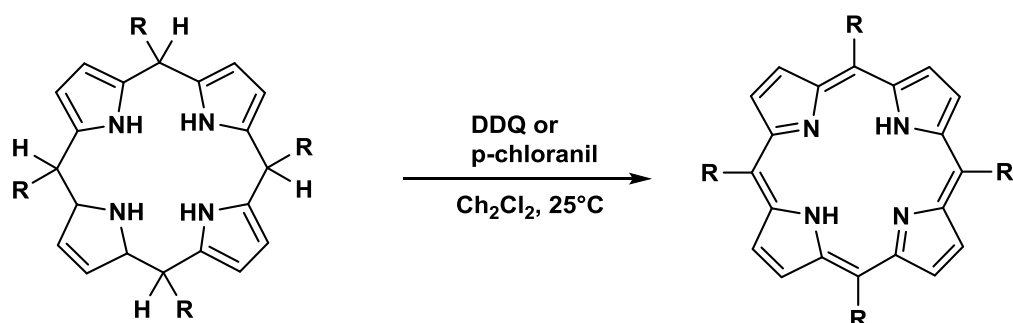


Figure 3.8 Lindsey method “Two-step one-flask room-temperature synthesis of porphyrins”.

Yields up to 50% are reported, although this percentage is influenced by parameters such as the type of catalyst and oxidant employed, the concentration of the reactants and the duration of the condensation phase. Optimal concentration of pyrrole and aldehyde is around 10^{-2}M ; that is to favor the cyclization over the polymerization.

The methods described above are suitable for the synthesis of porphyrins with four identical groups in the meso positions. Starting from a mixture of different aldehydes, the reaction leads to mixed condensation products, which require an heavy chromatographic work to obtain pure derivatives. Another strategy involves the use of dipyrromethanes, derivatives that consist of two pyrrole rings linked by a methine bridge. In most cases the meso position has either no substituted or a single aryl or dialkyl or aryl substituted. Dipyrromethanes allow the synthesis of trans- A_2 and trans- A_2B_2 systems (Figure 3.9) by condensation [2+2] with aldehydes, as proposed for the first time by MacDonald in 1960.²²

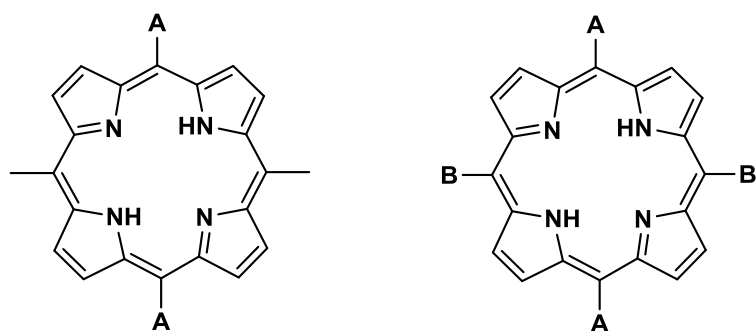


Figure 3.9 Structure of trans A_2 porphyrin (left) and trans A_2B_2 porphyrin (right).

In the following years, Lindsey applied the conditions of his method to MacDonald's reaction, in order to optimize the synthesis of this type of porphyrins (Figure 3.10).²³ Using dipyrromethanes as starting material, the synthesis is unambiguous if condensation takes place with a single aldehyde. This obviously requires the prior synthesis of the dipyrromethane intermediate.

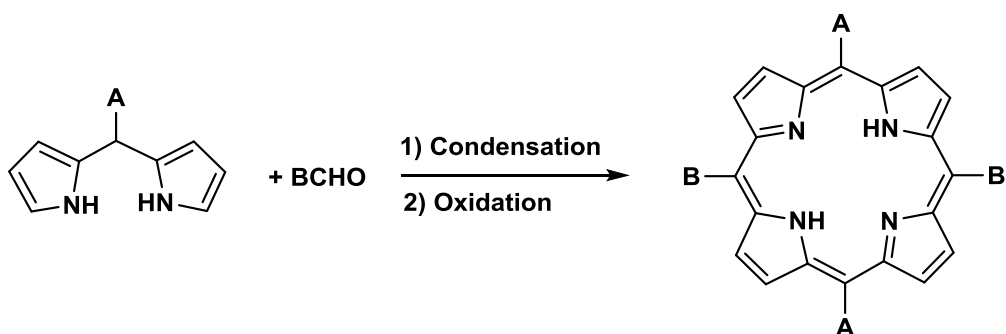


Figure 3.10 Lindsey's synthesis of trans- A_2B_2 porphyrins.

During the condensation between aldehyde and dipyrromethane, acid catalyzed sequence of fragmentations and rearrangements can occur, leading to the formation of by-products as –for example- cis- A_2B_2 isomer, hardly separable from trans form. This process²⁴, called scrambling²⁵ (Figure 3.11), could be minimized by properly controlling parameters like solvent, catalyst, temperature and concentration of the reagents. Another important factor in order to avoid scrambling is the location of the more hindered substituent: it has been noticed that when it is on dipyrromethane the scrambling doesn't occur or is minimized.

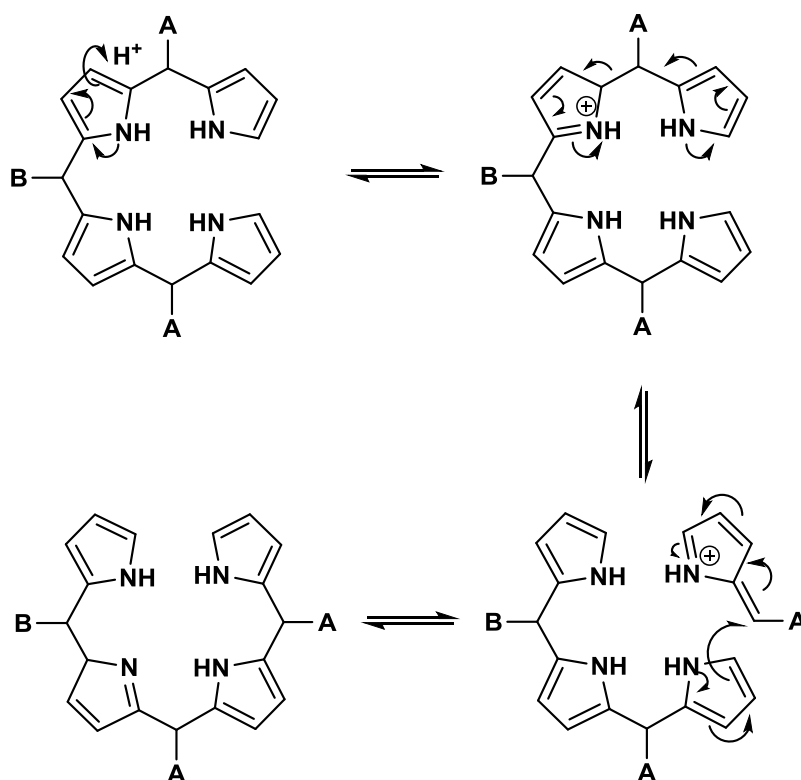


Figure 3.11 Mechanism of acid catalyzed scrambling.

3.6 Aggregation of Porphyrins

Aggregation of porphyrins has been deeply studied in solution: different aggregates can form depending on ionic strength, temperature, pH, peripheral substitution, etc.^{26,27}

Porphyrins and metalloporphyrins can form two types of supramolecular structures (Figure 3.12), due to strong π - π interactions establishing between the aromatic systems: “H-type”, characterized by a bathochromic shift of both B and Q bands with respect to those of the monomer; “J-type” showing blue-shift of B band and red-shift of Q band.

- The J-type or side-by-side aggregates were formed for transitions polarized parallel to the long axis of the aggregate.
- H-type or face-to-face aggregates for transitions polarized perpendicular to it.

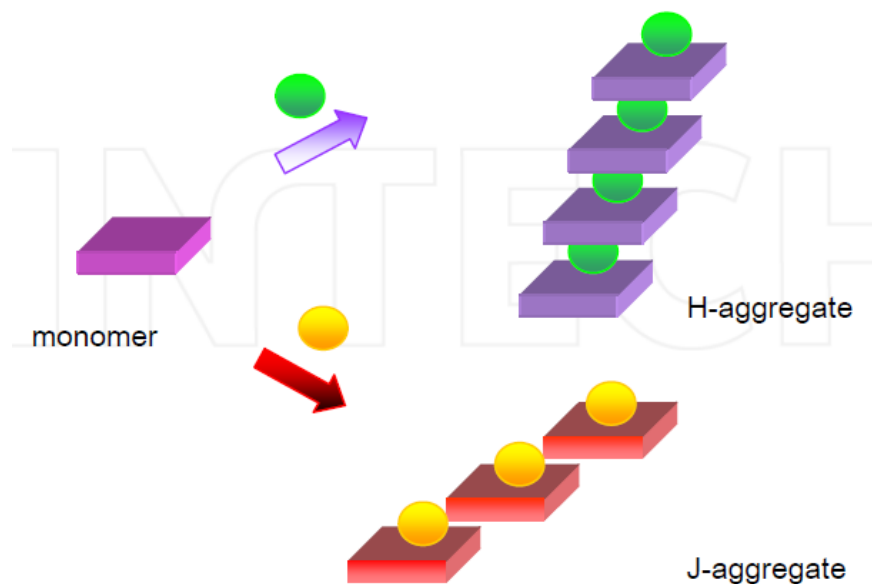


Figure 3.12 Schematic representation of H and J aggregates.¹²

H- and J-aggregates were formed by simply mixing aqueous solutions of two kinds of porphyrins with opposite charges.²⁸ In order to obtain deposition of an ordered monolayer, porphyrins can be functionalized with linkers which ensure the covalent anchoring to the surface. For example, porphyrins form a self-assembled monolayer (SAM) on gold via in situ cleavage of the thiol protecting group.²⁹ In this way it is possible to use porphyrins as molecular quantum devices, driving their assembly on a solid surface of gold or other electroactive material.

Bibliography

- ¹ Soret, J. L. *Compt. Rend.* **1883**, 97, 1267.
- ² Nencki, M., Sieber, N., *Arch. Expt. Path. Pharmacol* **1884**, 18, 401.
- ³ Kuster, W., *Physiol. Chem.* **1912**, 82, 463.
- ⁴ Fischer, H., Klarer, J. Justus Liebig's, *Ann. Chem.* **1926**, 450, 181.
- ⁵ Milgrom, L. R., *The Colours of Life: An Introduction to the Chemistry of Porphyrins and Related Compounds*, Oxford University Press, **1997**, 3.
- ⁶ David Dolphin, *The Porphyrins.*, Vol VII: *Bio Chemistry*, Part B.
- ⁷ Ow YP, Green DR, Hao Z, Mak TW, *Nat Rev Mol Cell Biol.* **2008** Jul;9(7):532-42.
- ⁸ T H Ward, J Cummings, E Dean, A Greystoke, J M Hou, I A Backen, M Ranson, and C Dive,* *Biomarkers of apoptosis, Br J Cancer.* **2008 Sep 16**; 99(6): 841-846.
- ⁹ Alan N. Schechter, *Blood.* **2008 Nov 15**; 112(10): 3927-3938.
- ¹⁰ George A. Ordway, Daniel J. Garry, *Journal of Experimental Biology* **2004**, 207, 3441-3446.
- ¹¹ Maurizio Brunori, Adriana E Miele, *Myoglobin*, **August 2015**.
- ¹² R. Giovannetti, *The Use of Spectrophotometry UV – Vis for the Study of Porphyrins, Macro to Nano Spectroscopy*, J. Uddin, Ed. InTech. **2012**, available from:
<http://www.intechopen.com/books/macro-to-nano-spectroscopy/the-use-of-spectrophotometry-uv-vis-for-the-study-of-porphyrins>
- ¹³ Rothemund P., *J. Am. Chem. Soc.* **1935**, 57, 2010-2011.
- ¹⁴ Rothemund P, Menotti AR., *J. Am. Chem. Soc.* **1941**, 63, 267-270.
- ¹⁵ Ball, R. H.; Dorough, G. D.; Calvin, M., *J. Am. Chem. Soc.* **1946**, 68, 2278.
- ¹⁶ A. D. Adler, F. R. Longo, and W. Shergalis, *Am. Chem. Soc.* **1964**, 86, 3145.
- ¹⁷ A. D. Adler, F. R. Longo, J. D. Finarelli, J. Goldmacher, J. Assour, L. Korsakoff, *J. Org. Chem.* **1967**, 32, 476.
- ¹⁸ Barnett GH, Hudson MF, Smith KM., *J. Chem. Soc. Perkin Trans.*, **1975**, 1, 1401-1403.
- ¹⁹ Adler, A. D.; Sklar, L.; Longo, F. R.; Finarelli, J. D.; Finarelli, M. G. J. *Heterocyclic Chem.* **1968**, 5, 669.
- ²⁰ Lindsey JS, Schreiman IC, Hsu HC, Kearney PC, Marguerettaz AM., *J. Org. Chem.* **1987**, 52, 827-836.
- ²¹ Lindsey JS. In: *The Porphyrin Handbook.*, Kadish KM, Smith KM, Guillard R, editors. Vol. 1. Academic Press; Boston, **1999**, 45-118.
- ²² G. P. Arsenault, E. Bullock, S. F. MacDonald, *J. Am. Chem. Soc.* **1960**, 82, 4384-4389.
- ²³ B. J. Littler, Y. Ciringh, J. S. Lindsey, *J. Org. Chem.* **1999**, 64, 2864-2872.

- ²⁴ Geier, G. R., III; Lindsey, J. S. J., *Chem. Soc., Perkin Trans. 2* **2001**, 677-718.
- ²⁵ Lindsey, J. S., *Acc. Chem. Res.* **2010**, 43, 300-311.
- ²⁶ Choi, M.-S. Aida, T. Luo, H. Araki, Y. Ito, O. *Angew. Chem., Int. Ed.* **2003**, 42, 4060.
- ²⁷ Siskova, K. Vlckova, B. Mojzes, P. *J. Mol. Struct.* **2005**, 744.
- ²⁸ Xiangqing Li, Line Zhang, Jin Mu, *Colloids and Surfaces A: Physicochem. Eng. Aspects* . **2007**, 311, 187.
- ²⁹ D. T. Gryko, F. Zhao, A. A. Yasseri, K. M. Roth, D. F. Bocian, W. G. Kuhr, J. S. Lindsey, *J. Org. Chem.* **2000**, 65, 7345-7362 .

IV. Guanosine-ferrocene derivatives

4.1 Introduction

As described in Chapter I, Quantum-dot Cellular Automata (QCA) is a revolutionary approach to computing and has been considered one of the most promising post-Moore alternatives. Implementation and miniaturization of QCA at the molecular level lead to severe challenges when addressing the single elementary units.

The research carried out during these three years was part of the MolarNet project, supported by the European Commission, which aims at giving a first demonstration of molecular QCA elementary devices.

In particular, the project specifically addressed the basic requirements to implement molecular QCA-inspired Networks, namely the measurement of the electrostatic interaction between a forced molecule (input) and its neighbour; the investigation of the propagation of a signal in a long row of molecules (binary line); the implementation and testing of a majority gate.

In order to obtain an organized array of cells as binary line, the MolArNet consortium followed two approaches: 1) the single cell is the outcome of the self-assembly of molecular sub-units, 2) a single molecule constitutes a single cell. In any case, iron complexes were used as quantum dots moieties.

In the first part of the project,¹ alkyl substituted guanosine derivatives equipped with a ferrocene moiety on the C(5') position of the sugar have been synthesized in order to study their self-assembly at the solid/liquid interface on highly oriented pyrolytic graphite (HOPG) with scanning tunneling microscopy (STM) or under ultra-high vacuum (UHV),² in collaboration with other partners of MolArNet project.

This technique has shown numerous advantages, for example it provides an excellent environment for *in situ* chemical modifications of adsorbed molecules.³ When guanosine derivatives are physisorbed at surfaces, thermodynamically stable supramolecular ribbons, characterized by N(2)-H \cdots O(6) and N(1)-H \cdots N(7) H-bonds, are observed. In the solid state, the ribbons, by bridging gold electrodes, were found to be photoconductive⁴ and also exhibited rectifying properties.⁵

Given the possibility to functionalize the guanosines in the sugar moiety, they appeared as ideal building blocks for the fabrication of conformationally rigid and structurally complex architectures, thus paving the way towards their use as scaffolds in QCA devices.⁶

Furthermore, the control over the self-assembly of ferrocene-based architectures through molecular engineering is crucial in order to control and improve their optical and electronic properties. For example, the assembly of ferrocenes on surfaces was directed by using H-bonding between carboxylic acids, leading to two-dimensional quasicrystals.⁷

4.2 Previous studies

Numerous guanosine ferrocene hybrids had already been synthesized and studied as prototypes for the realization of QCA. As a first approach, several molecules equipped with ferrocene have been synthesized: deoxyguanosine (dG), 2',3'-O-isopropylidenguanosine (GACE) and guanine derivatives, in order to obtain a first generation derivatives. Some examples are shown in Figure 4.1.

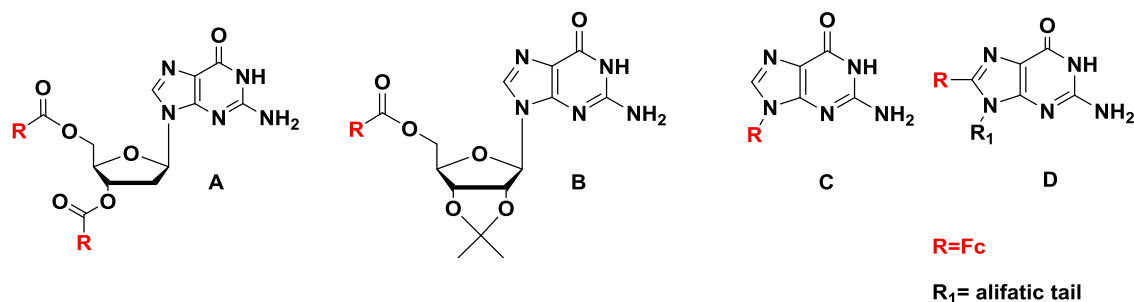


Figure 4.1 First generation derivatives.

In solution, these derivatives had shown the typical supramolecular behavior of lipophilic guanosines (lipo-Gs), both in the presence and in the absence of cations, suggesting the feasibility of the approach. Furthermore, it had been established that the presence of Fc units does not influence the self-assembly attitude of the nucleobase. On the other hand, these derivatives turned out to be unfit for the realization of QCA because of their very low solubility and difficulties to form ordered structures on surfaces. On the basis of these results, a second generation of ferrocene-LipoG hybrids has been synthesized (Figure 4.2).

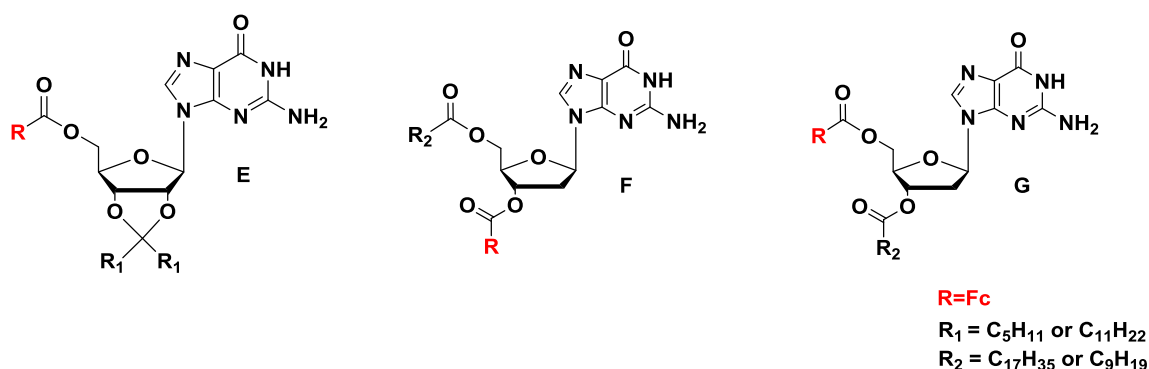


Figure 4.2 Second generation derivatives.

Derivative E: guanosine derivatives with 2' and 3' positions of the sugar protected as acetals and with long tails to confer a better solubility to the molecules.

Derivatives F and G: guanosine derivatives in which either 3' and 5' positions of the sugar were derivatized with ferrocene and long aliphatic tails (Chains C10 or C18).

Derivatives E showed a good solubility to be studied in solution, forming octameric structures in the presence of potassium, but did not organize into ordered structures on surfaces.

Electrochemical studies on the compound Ga (dG_5'Fc_3'C10) have instead shown that this molecule is suitable for QCA implementation.⁸ Furthermore, the introduction of a long alkyl chain (C18) in 3' and 5' positions (Gb) drives the formation of ribbon-like structures on the surface.

At the same time, the electrochemical behavior of two others derivatives A and Ga (Figure 4.3) was characterized by cyclic voltammetry. These studies have highlighted an interesting behavior: in CHCl_3 , the self-assembly of the guanine derivatives, driven by the formation of hydrogen bonds, induces the formation of layers on the surface of the electrodes. Some of these layers are again dissolved following the reduction of the Iron, this process is observable in the time scale of cyclic voltammetry experiments.

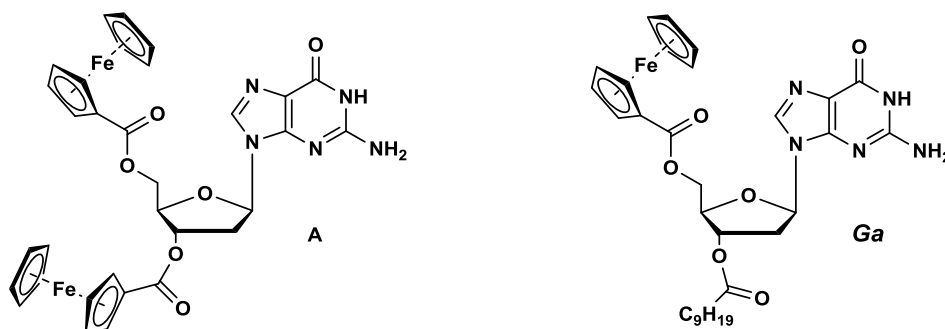


Figure 4.3 Guanosine derivatives A and Ga.

One of the potential problems in the use of G-quartets as scaffolds for QCA cells is the presence of the cation and the counterion, which may interfere with electrochemical processes. Although cations are normally necessary for the templation of G-quartets, there have been examples of G-quartets formed in the absence of cations. Studies carried out by the group of Prof. Sessler⁹ show a crystal structure of G10 (Figure 4.4) that revealed an “empty” G-quartet even without the assistance of a templating cation.

The presence of a sterically bulky group on the C8 position of the guanine core gave a conformationally constrained nucleoside that prefers to adopt a syn glycosidic bond conformation both in the solid state and in solution. This syn conformation prevents the nucleoside from any hydrogen-bonded ribbon formation (as already mentioned before) and thus favors formation of the macrocyclic G-quartet. Cation-free isolated G_4 have been also observed by MAS NMR in solid samples of derivatives devoid of substituents in C(8) position.¹⁰

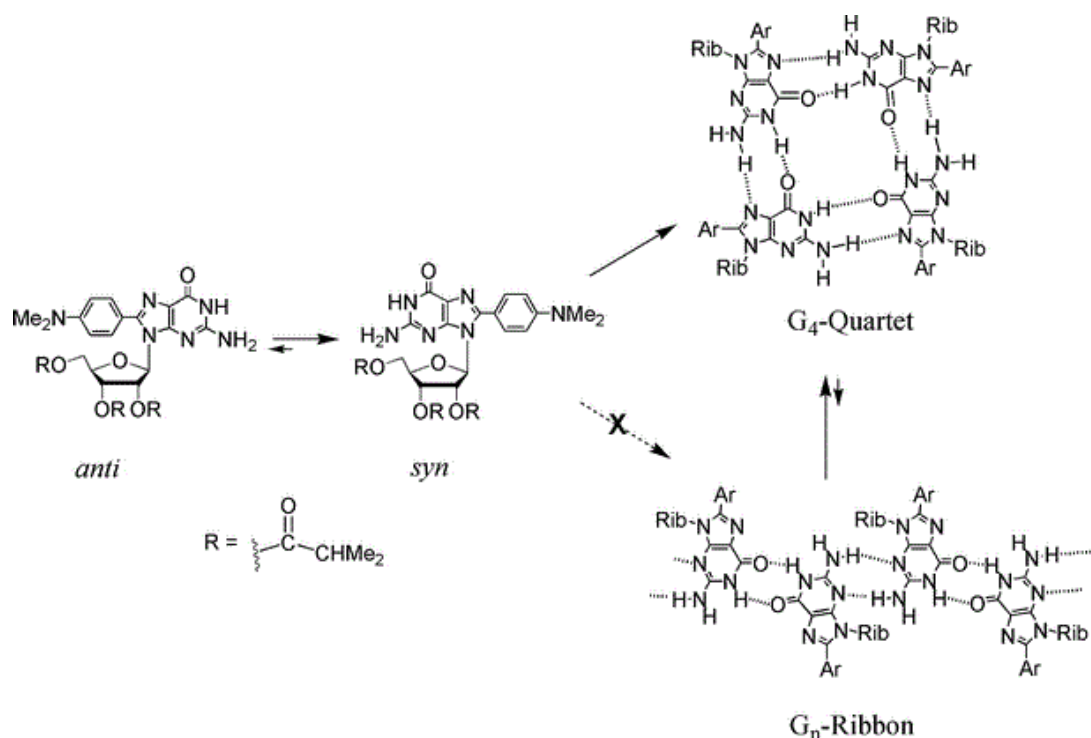


Figure 4.4 Conformationally constrained G 10 forms a G-quartet without presence of a templating cation.

On the basis of these considerations and thanks to the preliminary studies from previous molecules, we have designed and synthesized three lipophilic guanosine derivatives **G1-G3** exposing a ferrocene moiety on the C(5') position of the sugar (Figure 4.5), in order to study the effect of sterically demanding substituents covalently linked to the C(8) position on the self-assembly process at the solid/liquid interface on highly oriented pyrolytic graphite (HOPG).

The presence of a long stearate side chain in C(3') position of the sugar is expected to promote the molecular physisorption on HOPG.

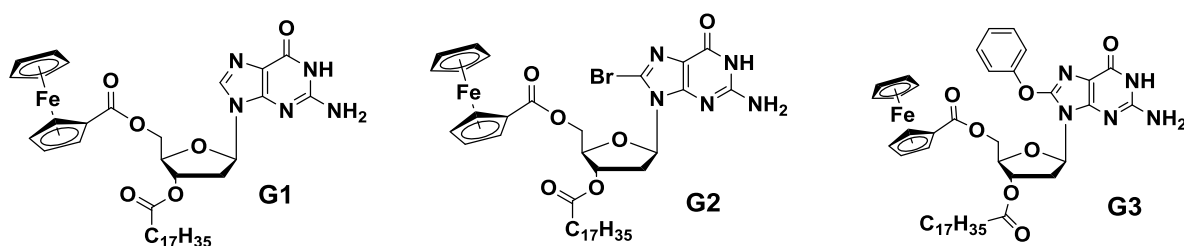


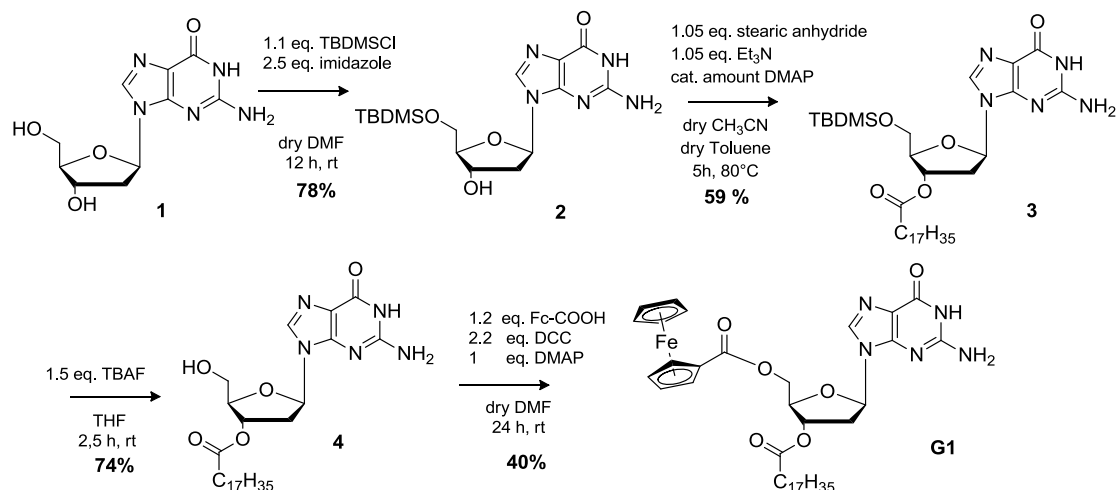
Figure 4.5 Derivatives **G1** (dG_{3'}C18_{5'}Fc), **G2** (dG_{8Br}_{3'}C18_{5'}Fc) and **G3** (dG_{8PhO}_{3'}C18_{5'}Fc).

4.3 Synthetic approaches

4.3.1 G1 (5'-O-ferrocenoyl-3'-O-octadecanoyl-2'-deoxyguanosine)

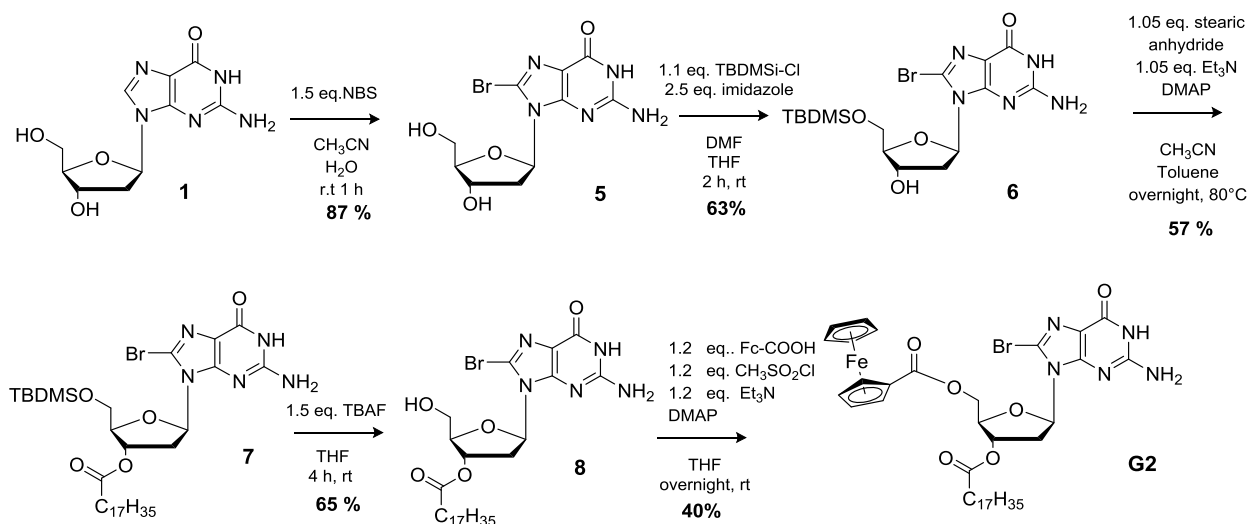
Derivative **G1** was prepared according to Scheme 4.1 Deoxyguanosine was first reacted with tert-Butyldimethylsilyl chloride (TBDMSiCl) to give 5'-O-silylated **2**. This compound, with free 3'-

hydroxyl, was then acylated with stearic anhydride at 70°C in toluene to afford **3**. Removal of 5'-silyl group with tetrabutylammonium fluoride (TBAF) followed by esterification with FcCOOH gave the desired product **G1**.

Scheme 4.1 Synthesis of **G1**.

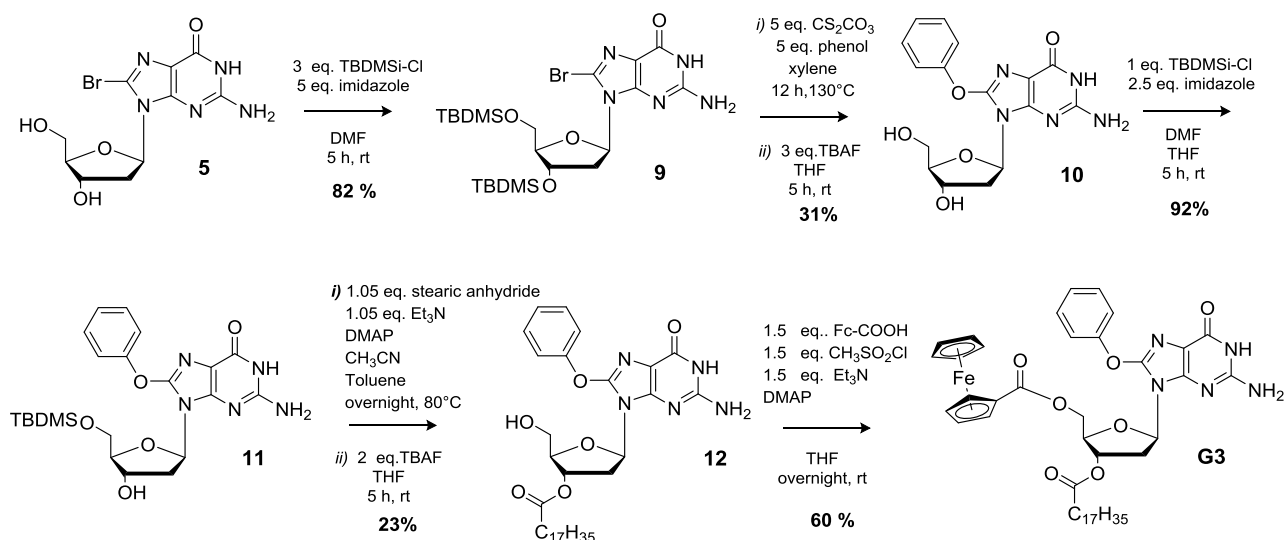
4.3.2 **G2** (8-bromo-5'-*O*-ferrocenoyl-3'-*O*-octadecanoyl-2'-deoxyguanosine)

The synthesis of derivative **G2** is practically the same as derivative **G1**, except for the insertion of bromine atom in C8 position in the first step with NBS and the last esterification performed with $\text{CH}_3\text{SO}_2\text{Cl}$ and Et_3N in THF (Scheme 4.2).

Scheme 4.2 Synthesis of **G2**.

4.3.3 G3 (8-phenoxy-5'-O-ferrocenoyl-3'-O-octadecanoyl-2'-deoxyguanosine)

In order to synthesize derivative **G3** we started from commercially available dG (Scheme 4.3), which is initially protected with TBDMSiCl. Subsequently, the hydrogen in the 8 position is replaced with bromine by reaction with NBS. The protected **9** was then used in the third step in order to replace bromine atom with phenoxy group, through a nucleophilic aromatic substitution on C8 position. At first, the nucleophilic aromatic substitution was attempted directly on 8-bromo deoxyguanosine with free hydroxy groups but, probably due to low solubility, we were not able to obtain derivative **10**. After deprotection of **9** with TBAF, a mono-protection was carried out with TBDMSiCl on five prime position. Position three prime was then esterified with stearic anhydride. The subsequent deprotection on the five prime position with TBAF allows the reaction with carboxylic acid of ferrocene with methanesulfonylchloride, through the formation of a mixed anhydride.

Scheme 4.3 Synthesis of **G3**.

4.4 Supramolecular studies

Several techniques were employed to study the self-assembly of guanine derivatives: NMR (monodimensional and bidimensional experiments) and CD (circular dichroism), STM (scanning tunneling microscopy) and AFM (atomic force microscopy).

4.4.1 G1

In the absence of metal ions, **G1** forms ribbon-like structures. ^1H NMR spectra in CDCl_3 show a progressive downfield shift for both N(1)-H and N(2)-H signals upon cooling, while considerable line broadening occurs (Figure 4.6).

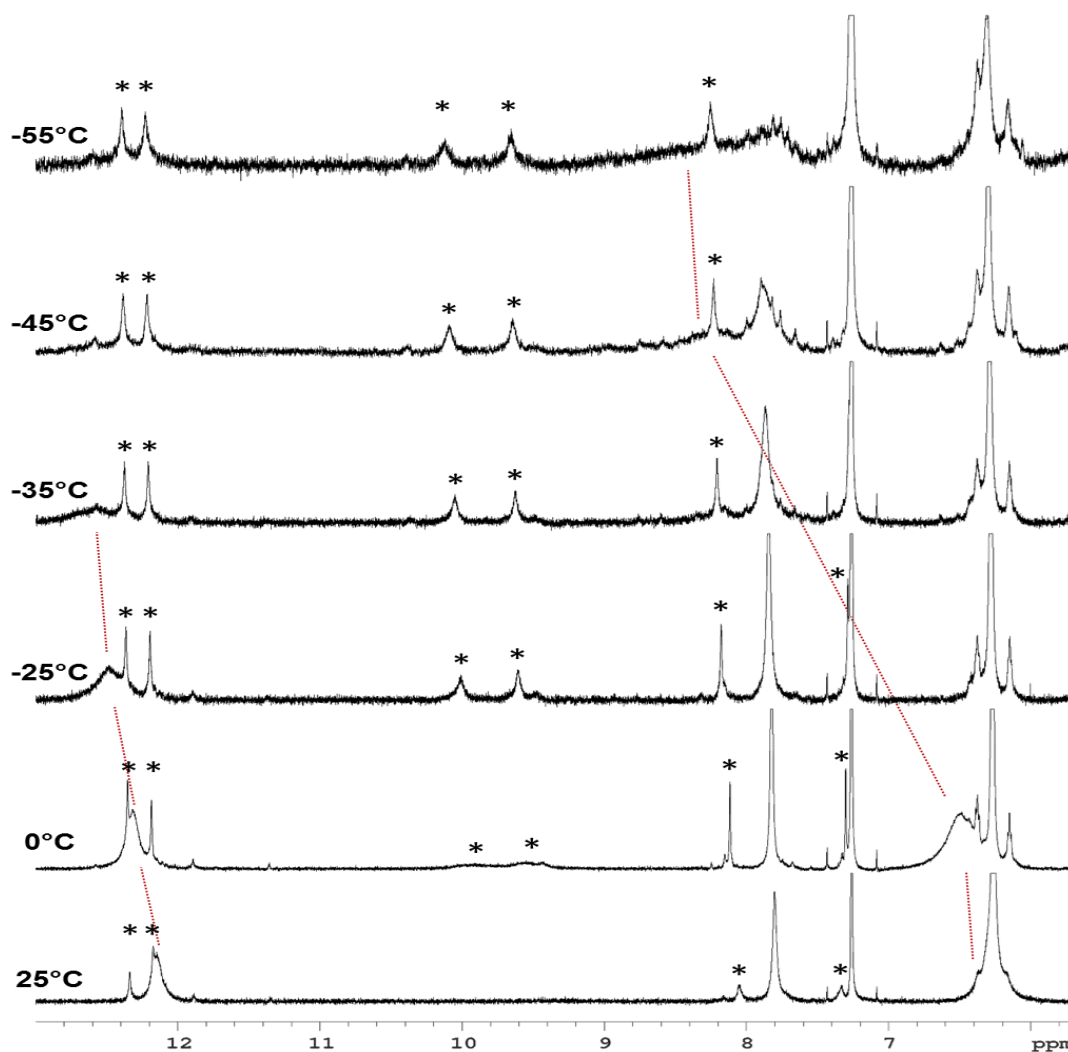


Figure 4.6 downfield portion of the ^1H -NMR spectrum of **G1** (16 mM) at different temperatures in CDCl_3 . Guidelines highlight imino and amino N-H shifts. Signals marked with stars belong to the C_4 -symmetric $\text{G1}_8\cdot\text{K}^+$ complex formed by addition of a small amount of KI to the sample.

G1 can complex alkali metal ions to form a C_4 symmetric octamer consisting of two stacked G1_4 , as indicated from the characteristic changes both in the ^1H NMR and in the CD spectrum¹¹ (Figure 4.7).

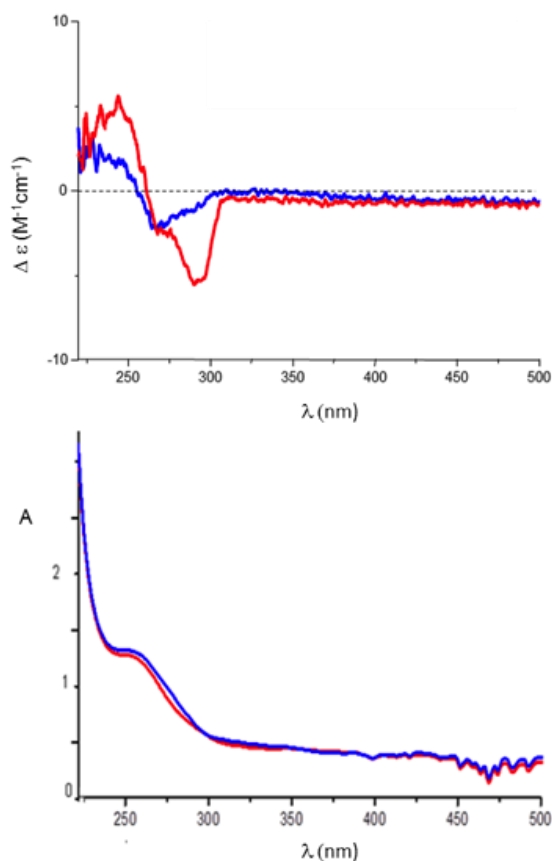


Figure 4.7 CD (top) and UV (bottom) spectra of **G1** (2.5 mM in CHCl_3) before (blue) and after (red) addition of potassium picrate (1/8 mol/mol).

We have then investigated the self-assembly of neat **G1** by applying a 4 μL drop of a (100 ± 2) μM solution of **G1** in 1-phenyloctane on the HOPG surface. The *in situ* STM image recorded at the solid-liquid interface showed a crystalline structure consisting of ribbon-like architectures forming a lamellar motif (Figure 4.8 left). In this 2D crystal, the stearate side chains are physisorbed flat on the basal plane of the surface and they are interdigitated between adjacent lamellae. The unit cell parameters amount to $a = (7.4 \pm 0.1)$ nm, $b = (1.0 \pm 0.1)$ nm, and $\alpha = (88 \pm 2)^\circ$, leading to an area $A = (7.4 \pm 0.2)$ nm², where each unit cell contains four molecules. Thus, the area occupied by a single molecule **G1** corresponds to (1.85 ± 0.10) nm². Given the size of the unit cell there is not enough space to accommodate the ferrocene units on the basal plane of the HOPG surface, therefore it is most likely that they are either back-folded into supernatant solution or physisorbed as second layer on the top of the guanosine first layer. Unfortunately, despite the high spatial resolution attained by STM imaging, we are unable to rule out any of these two scenarios. The monitored supramolecular motif can be well-described by the formation of a 1D hydrogen-bonded ribbon that involves the pairing $\text{N}(2)\text{-H}\cdots\text{O}(6)$ and $\text{N}(1)\text{-H}\cdots\text{N}(7)$. This self-assembly behavior is in good agreement with NMR solution data (see models in Figure 4.8 right and experimental part).

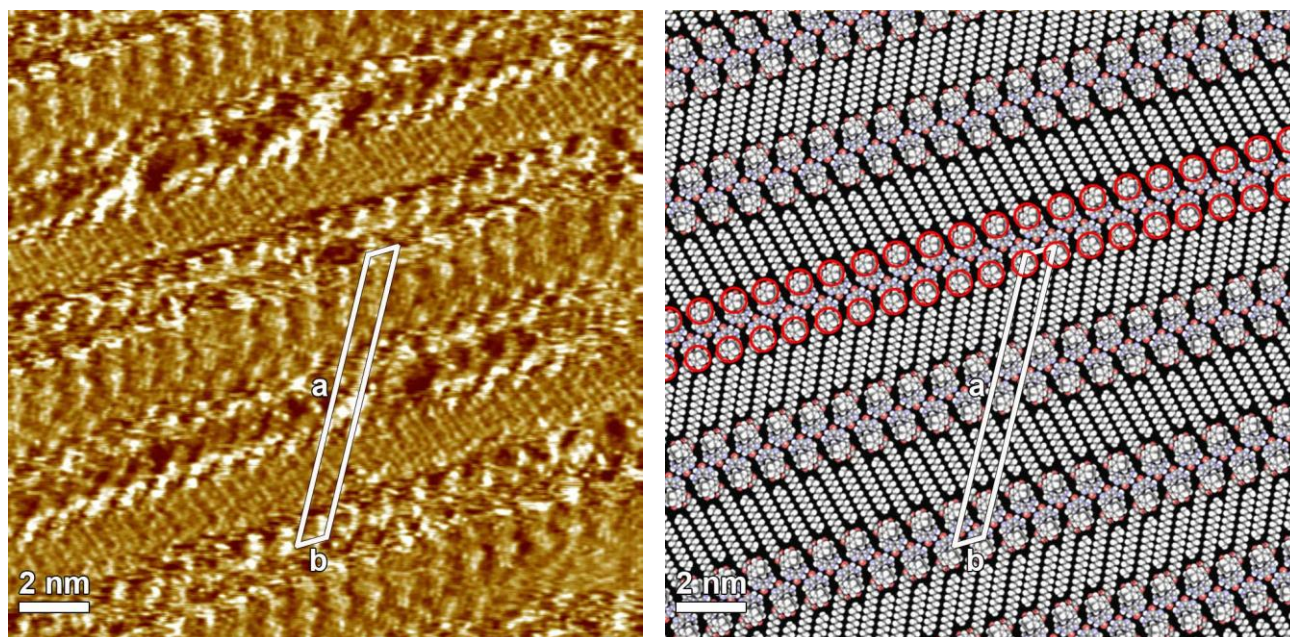


Figure 4.8 Left: STM current image of **G1** monolayer at the graphite-solution interface using 1-phenyloctane as a solvent. Right: Proposed molecular packing of **G1**. The image shows the supramolecular self-assembly forming ribbon-like structures of **G1**.

4.4.2 G2

We then extended our study to guanosine **G2**, functionalized in C(8) position with a Br atom. Its $^1\text{H-NMR}$ spectra recorded on cooling a solution in CDCl_3 (Figure 4.9) show a progressive splitting of the broad N(2)-H singlet at 6.1 ppm into two signals (bonded and free N(2)-H, at 8.7 and 5.7 ppm, respectively). The chemical shifts for the N(2)-H protons are close to those reported for a similar compound (8.50 and 5.44 ppm),¹² but differ from those of the two stacked G-quartets formed by **G1** in the presence of metal ions as well as from those of an isolated G-quartet (9.81 and 5.15 ppm). Moreover, the lack of substantial line broadening is indicative of small sized aggregates.¹³ CD spectra recorded before and after K^+ addition confirm the absence of stacked G-quartets (Figure 4.10).

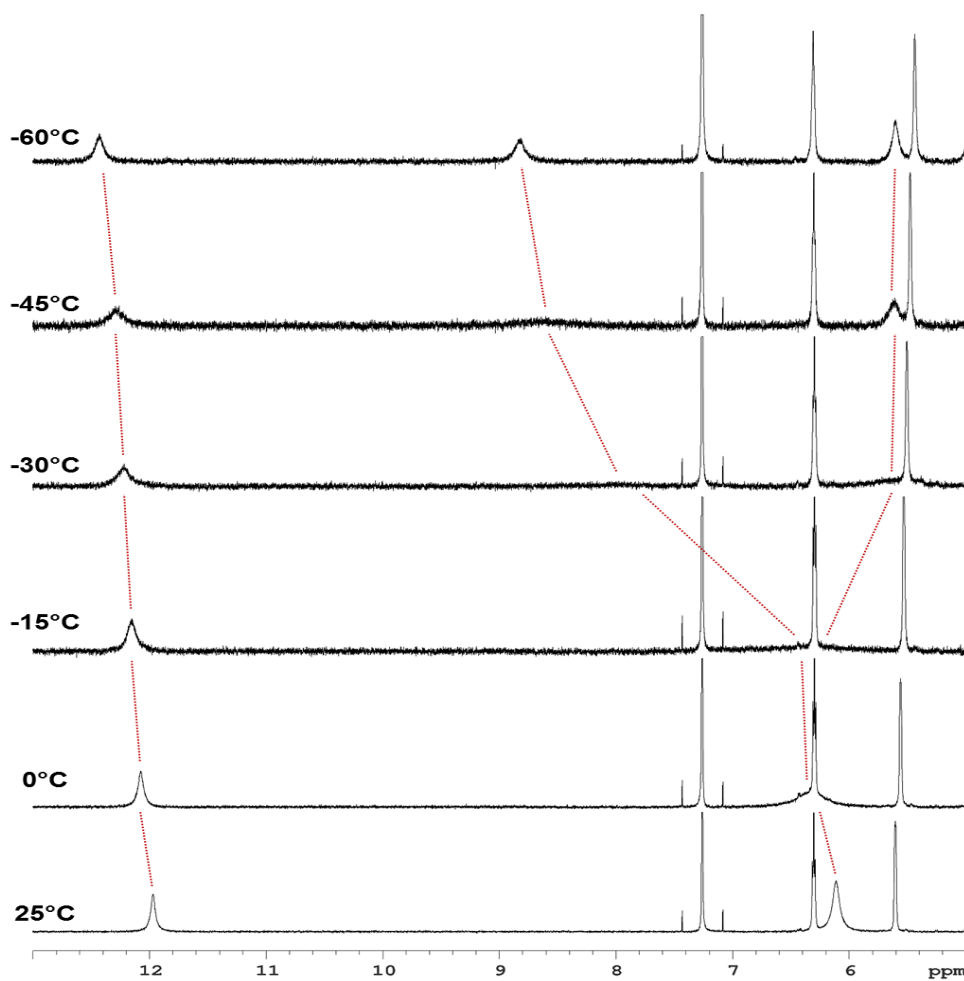


Figure 4.9 Downfield portion of the ¹H-NMR spectrum of **G2** (9 mM) at different temperatures in CDCl₃. Guidelines highlight imino and amino N-H shifts.

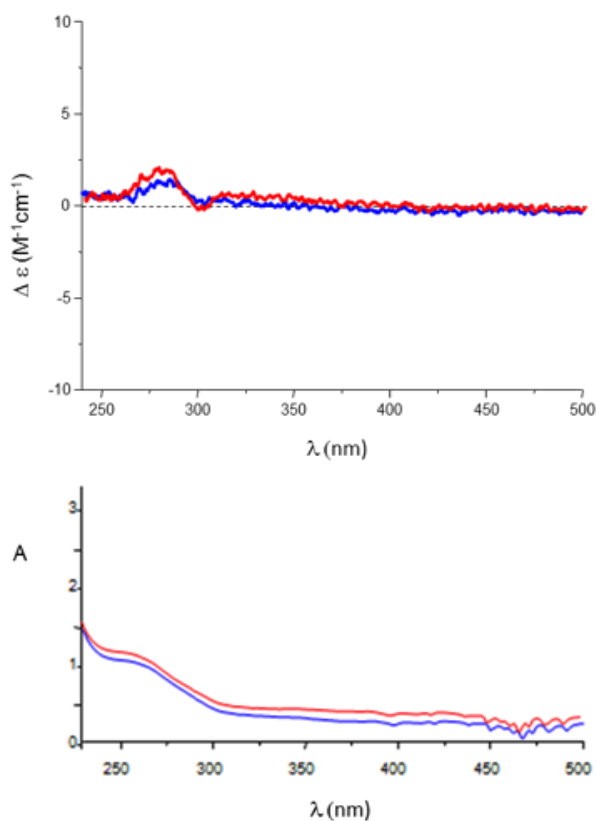


Figure 4.10 CD (top) and UV (bottom) spectra of **G2** (2.5 mM in CHCl_3) before (blue) and after (red) addition of potassium picrate (1/8 mol/mol).

Monolayers of **G2** have been generated by applying a 4 μL drop of a (100 ± 2) μM solution of **G2** in 1-phenyloctane on the HOPG surface. The STM image of the obtained monolayer (Figure 4.11 left) shows a crystalline lamellar structure consisting of ribbon-like architectures. In **G2**-based 2D crystal, the stearate side chains are physisorbed flat on the surface and are interdigitated between adjacent lamellae. The unit cell parameters, $a = (4.1 \pm 0.1)$ nm, $b = (0.9 \pm 0.1)$ nm, and $\alpha = (90 \pm 2)^\circ$, lead to an area $A = (3.7 \pm 0.1)$ nm^2 , where each unit cell contains two molecules. Thus, the area occupied by a single molecule **G2** corresponds to (1.85 ± 0.10) nm^2 . While the area occupied by single molecule **G2** is identical with the one of **G1**, their self-assembled patterns are markedly different. In particular, the appearance of hollow features within **G2** ribbon core as well as different orientation of stearate side chains vs. the main lamellar axis (60° and 90° for **G1** and **G2** patterns, respectively) provides unambiguous evidence for a different self-assembly motif. In fact, the **G2** supramolecular motif can be well-described by the formation of H-bonded dimers that involves the pairing $\text{N}(1)\text{-H}\dots\text{O}(6)$ (see models in Figures 4.11 right and experimental part). Each dimer interacts laterally with neighboring dimers via $\text{N}(2)\text{-H}\dots\text{Br}(8)$ bonding, resulting in the formation of 1D polymeric arrays. Similarly to the case of **G1** ribbons, ferrocene units are likely back-folded into

supernatant solution or adsorbed as a second layer. Formation of such structures highlights the role played by bulky bromine atoms in C(8) position of guanine core, that induces the derivative **G2** to organize themselves on the surface in a ribbon-like structure renamed ribbon C (see Figure 4.12), different from those (ribbon A and ribbon B) normally observed previously for lipoG. However, their presence in the molecular structure introduced N(2)-H...Br(8) bonding, which prevents the molecules from self-association into macrocyclic structures. We therefore decided to replace the Br atom with a more neutral group, which is also more sterically demanding, i.e. phenol (**G3**).

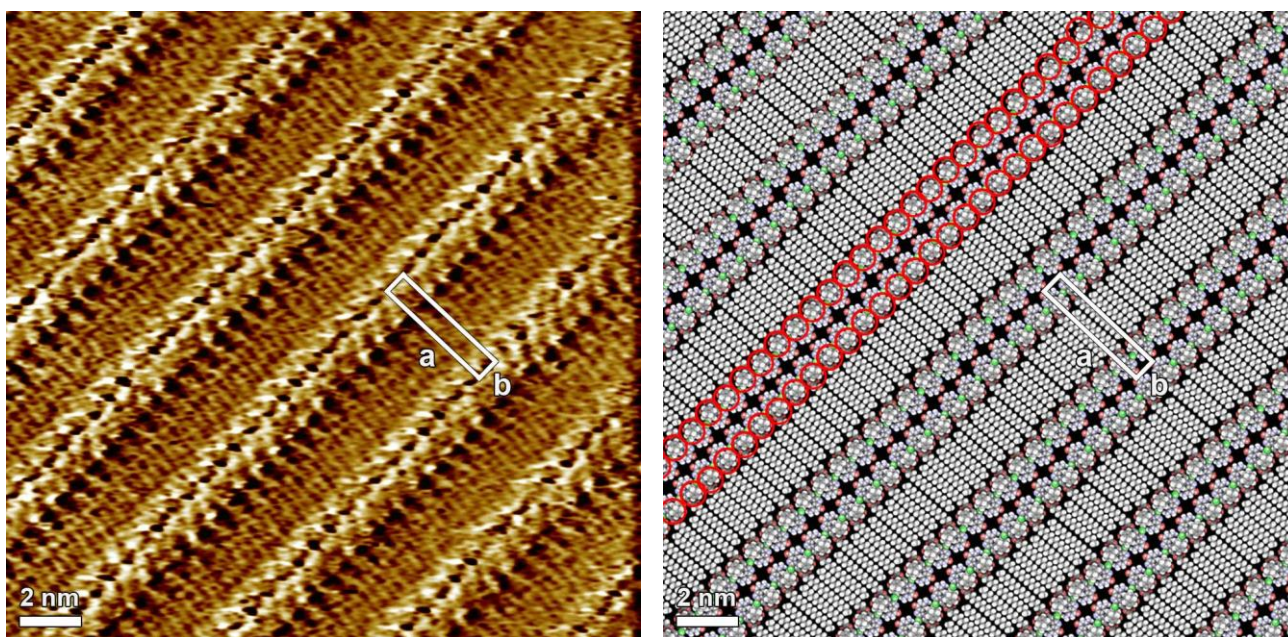


Figure 4.11 Left: STM current image of **G2** monolayer at the graphite-solution interface using 1-phenyloctane as a solvent. Right: Proposed molecular packing of **G2**. The image shows an unprecedented supramolecular motif, called ribbon-C.

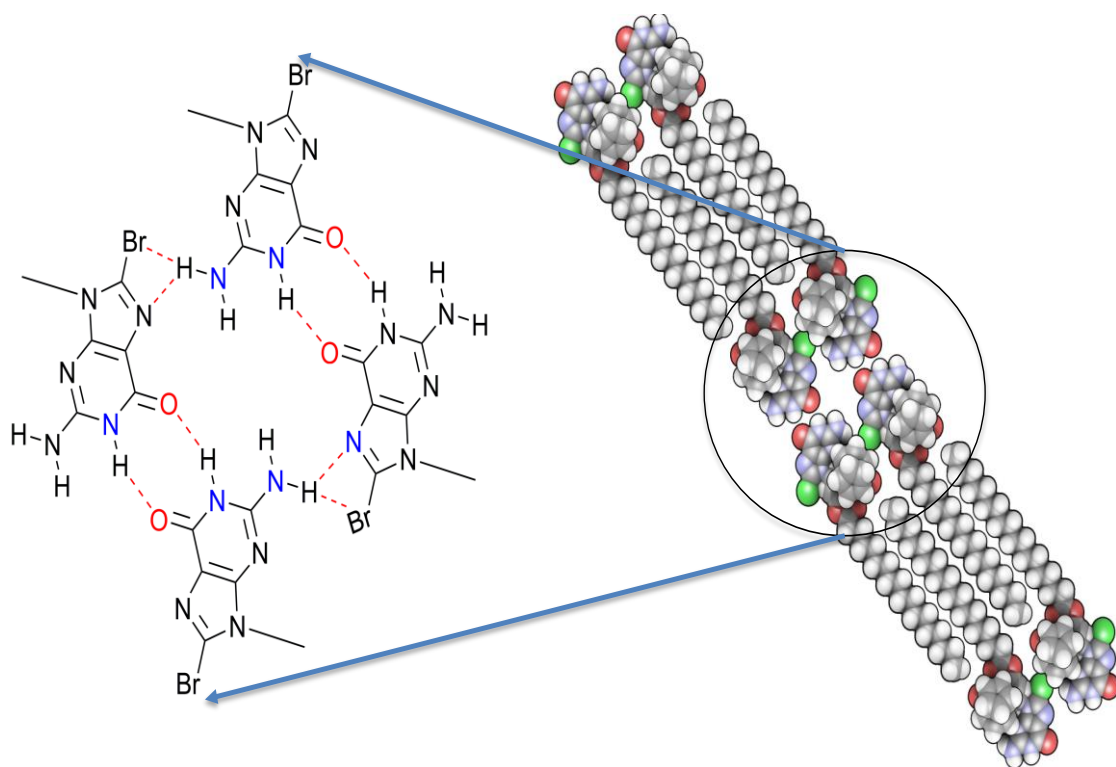


Figure 4.12 Ribbon C.

4.4.3 G3

The behaviour of **G3** in solution is very peculiar. In analogy to **G2**, the **G3** molecule is unable to complex metal ions to form G4 stacked structures, as no changes can be detected both on CD and on ^1H NMR spectra after the addition of K^+ (Figure 4.13).

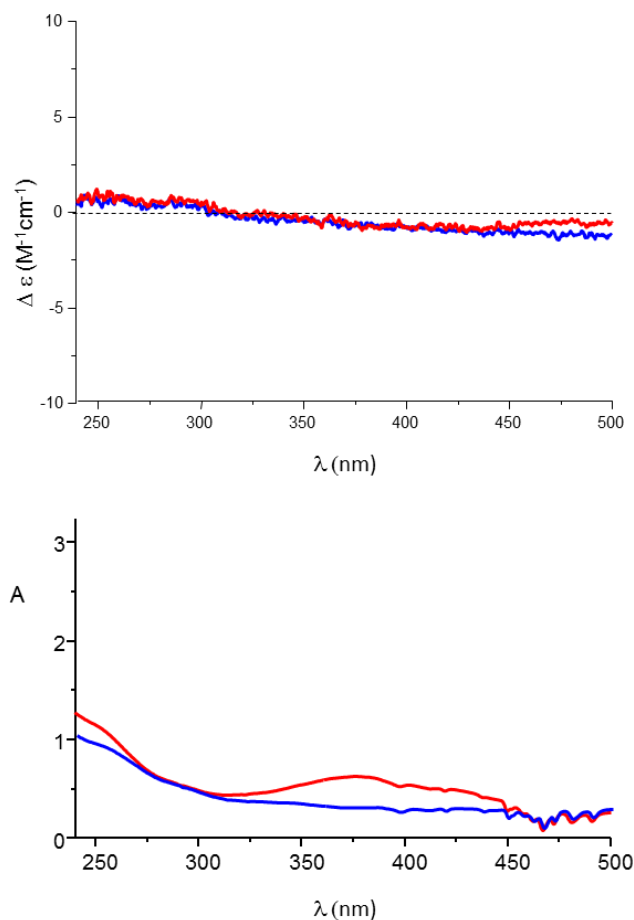


Figure 4.13 CD (top) and UV (bottom) spectra of **G3** (2.5 mM in CHCl_3) before (blue) and after (red) addition of potassium picrate (1/8 mol/mol).

Furthermore, in the absence of added ions, both N(1)-H and N(2)-H signals split upon cooling. In particular, the N(2)-H signal splits into two couples of new signals in a 2:1 ratio. A couple of signals resonate at about 8 ppm, and can be attributed to H-bonded N(2)-Hs, while the other couple of signals appearing at 3 ppm can be ascribed to free N(2)-Hs. The existence of two sets of resonances for both imino and amino protons in a 2:1 ratio points to the existence of two different supramolecular species (Figure 4.14).

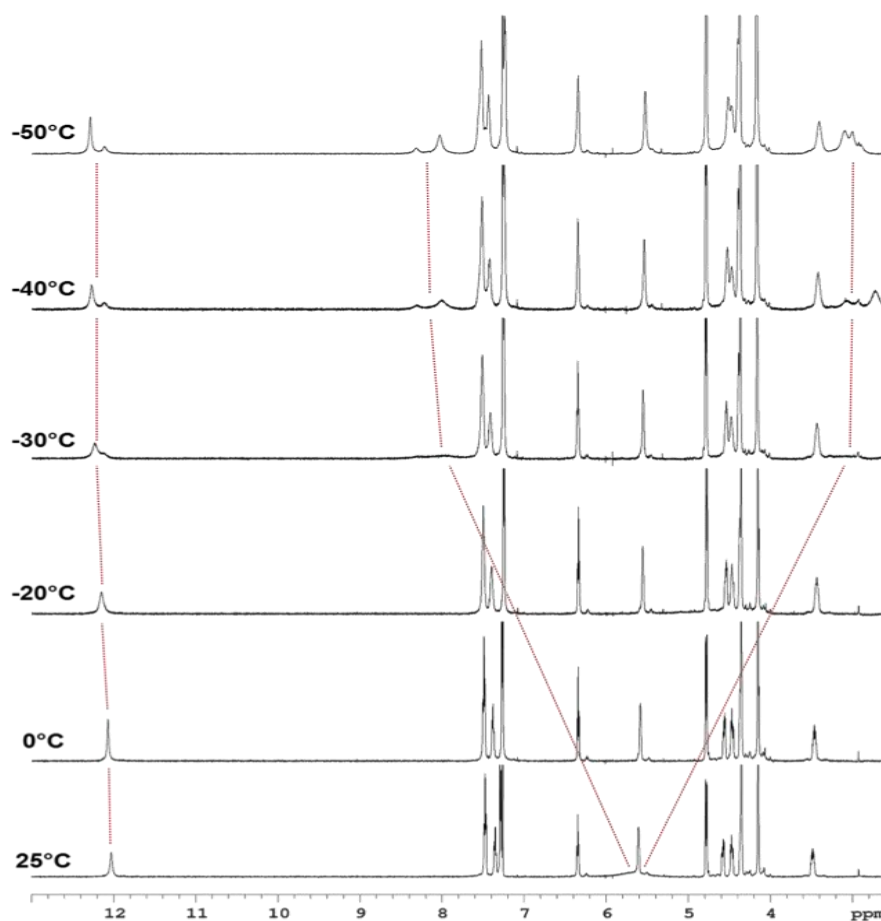


Figure 4.14 Downfield portion of the ^1H -NMR spectrum of **G3** (14 mM) at different temperatures in CDCl_3 . Guidelines highlight imino and amino N-H shifts.

Based on NOE analysis (Figures 4.15 and 4.16) the major species can be ascribed to the formation of all-syn isolated G3_4 . Although no direct and conclusive evidence could be gathered from the spectra, in depth inspection of the models suggests anti G3_4 or anti G3 -ribbons analogous to those found for **G2** on surfaces, as the possible structure for the minor species.

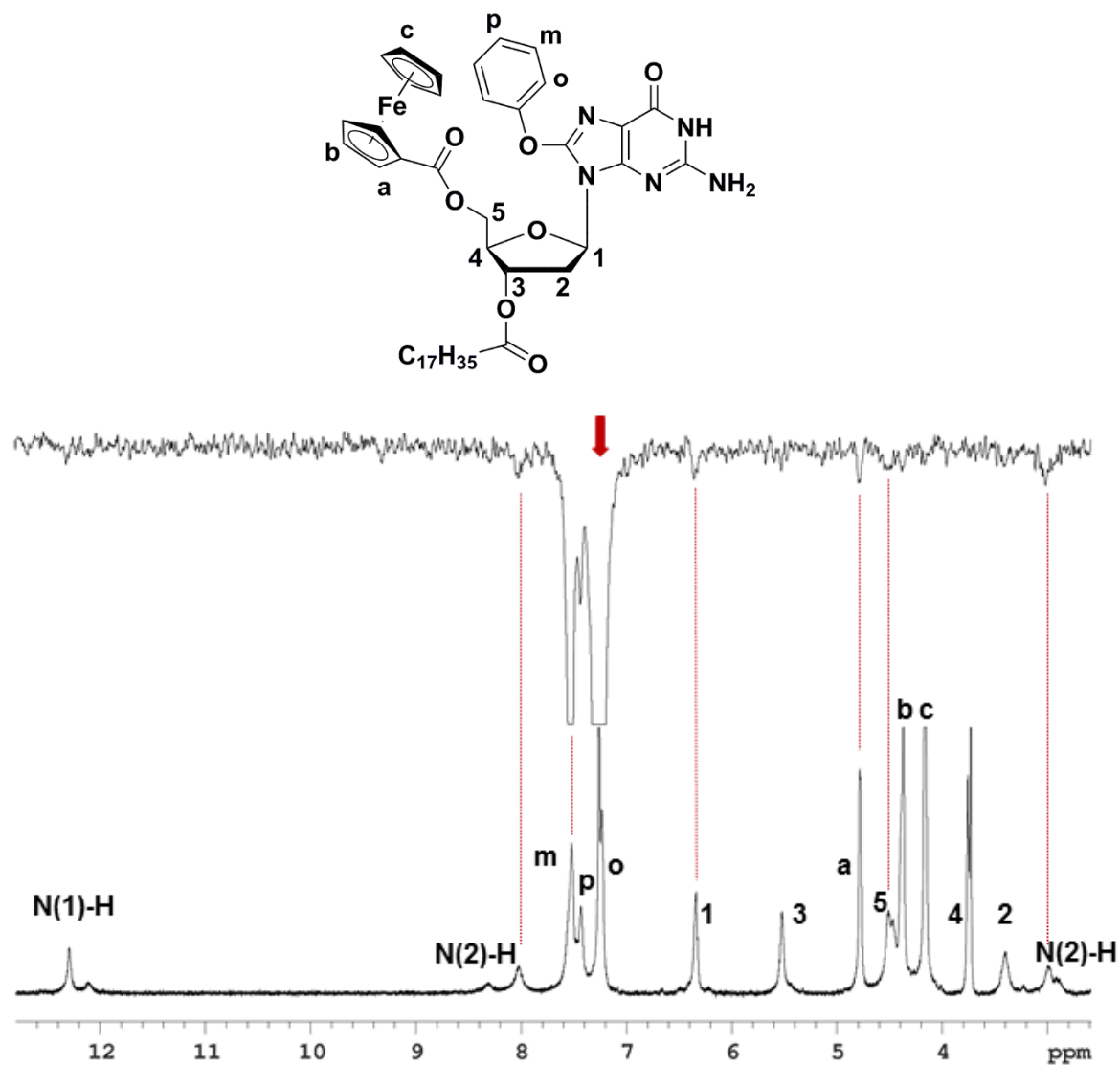


Figure 4.16. Bottom: $^1\text{H-NMR}$ spectrum of **G3** in CDCl_3 at -50°C . Signals were assigned on the basis of COSY, HSQC and HMBC experiments. Top: noesy1d spectrum of the same sample (irradiation of protons **o** – see formula above – with a 50 Hz shaped pulse, mixing time 300 ms).

NOE spectra (Figure 4.16) show weak contacts between ortho (**o**) and $\text{H}_{1'}$ as well as between **o** and $5'/5''$: according to calculations, the two conformers differ only slightly in energy. In addition, NOE intermolecular proximities can be observed between **o** and ferrocene **a** and between **o** and both free N(2)-H and bound N(2)-H (major specie).

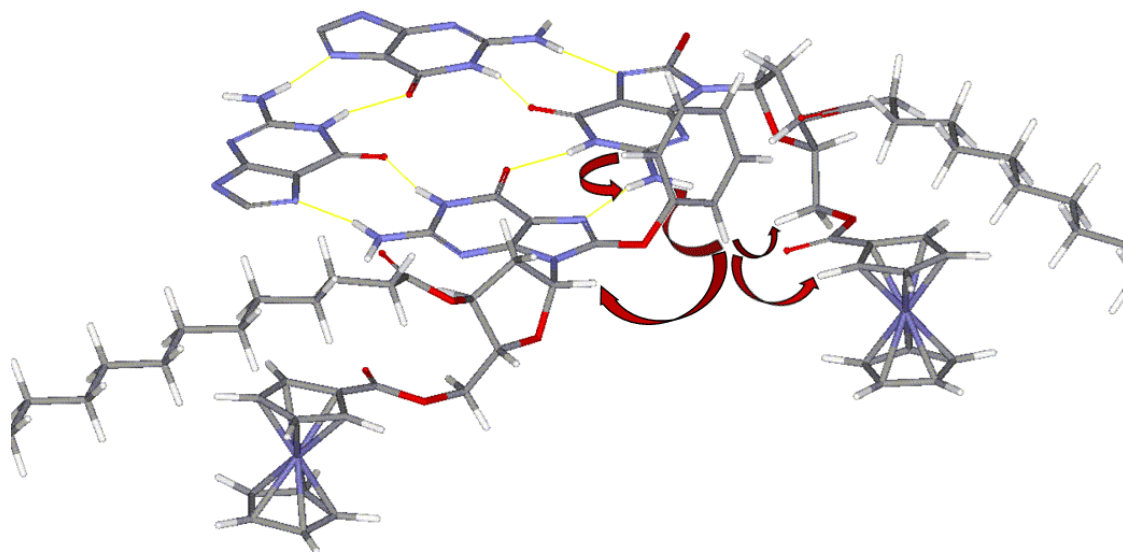


Figure 4.17. Model of an isolated G-quartet formed by *syn*-**G3** (some atoms are omitted for clarity). NOE contacts of Figure 4.16 are indicated by arrows.

STM investigation of sub-monolayer-thick films obtained from $(100 \pm 2) \mu\text{M}$ solution of **G3**, revealed the formation of a new type of pattern (Figure 4.18). In this 2D crystal, because of steric hindrance brought into play by the phenol unit, only three out of four stearate side chains are physisorbed flat on the surface. The unit cell parameters, $a = (4.5 \pm 0.1) \text{ nm}$, $b = (1.8 \pm 0.1) \text{ nm}$, and $\alpha = (90 \pm 2)^\circ$, lead to an area $A = (8.1 \pm 0.1) \text{ nm}^2$, where each unit cell contains two molecules. Thus, the area occupied by a single molecule **G3** corresponds to $(4.1 \pm 0.1) \text{ nm}^2$. The packing of **G3** molecules is very loose as evidenced by the large discrepancy between the areas occupied by single molecules **G1**, **G2** and **G3**. The STM inset in Figure 4.14 clearly shows the presence of macrocyclic bright features decorated with four small protrusions, which can be assigned to G3_4 and ferrocene groups (backfolded into the supernatant solution), respectively. Because of the presence of sterically demanding phenoxy substituent in the C(8) position of **G3**, the formation of ribbon-like structures is hindered, leading to the generation of cyclic tetrameric H-bonded structures characterized by the $\text{N}(1)\text{-H}\cdots\text{O}(6)$ and $\text{N}(2)\text{-H}\cdots\text{N}(7)$ motif, whose existence was also indicated by NOE. While NOE analysis suggests the presence of all-*syn* isolated G3_4 , as the main specie, once adsorbed on the surface both all-*syn* and all-*anti* G3_4 , will occupy the same areas, therefore we cannot unambiguously exclude the existence of the former over the latter. Noteworthy, some of G3_4 appear brighter in the STM image, which can be explained by the interference of the supramolecular lattice and the underling HOPG surface.

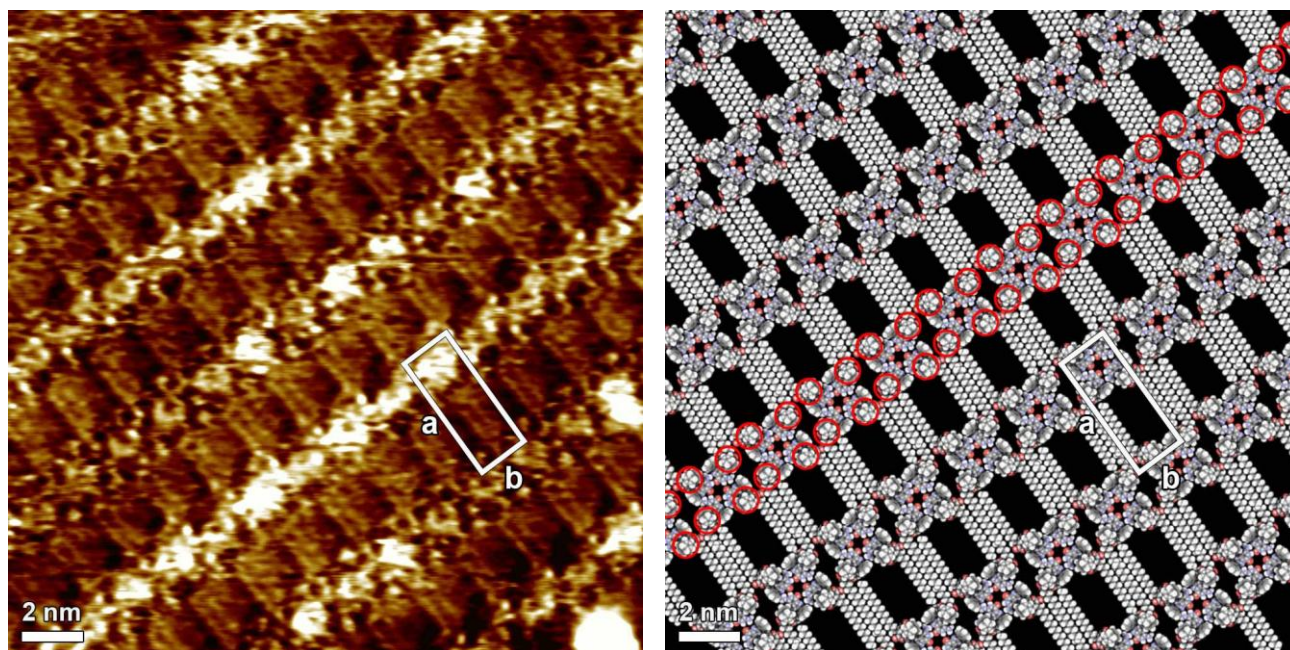


Figure 4.18 Left: STM current image of **G3** monolayer at the graphite-solution interface using 1-phenyloctane as a solvent. Right: Proposed molecular packing of **G3**. The image shows an array of metal-free guanosine quartets.

4.4.4 DFT

To provide a molecular understanding of the three G derivatives self-assembly in 2D and gain insight into the formation and stability of supramolecular structures, we have carried out density functional theory (DFT) calculations using the hybrid Gaussian and plane-wave method (GPW), implemented in the QUICKSTEP module of the CP2K package.¹⁴ We used the B3LYP hybrid exchange-correlation potential,¹⁵ whereas the Grimme's DFT-D2 method¹⁶ was employed for taking into account the dispersion forces. To bestow information onto the intermolecular binding mechanisms, we have focused our attention on unraveling the interplay between H-bonds, which hold the guanine cores together, and the effective metallic repulsion coming from the four iron cations present in the ferrocenes. Noteworthy, as can be seen in the suggested monolayer packing motifs, two types of intramolecular interactions can be distinguished, namely, the hydrogen-bonding (or $\text{NH}\cdots\text{Br}$ interactions in the case of the **G2** structure) between guanine cores, and the van der Waals interaction, resulting from the interdigitation of the stearate chains. In order to determine their contribution in the total cohesive energy, we calculated the intermolecular dissociation energy for each of the different four-molecule-based configurations exhibited in three G-based complexes (Figure 4.19).

According to E_{tot} values of three G derivatives, the ribbon structure of **G1** is greatly stabilized by four strong H-bonds. In the **G2** ribbon-like structure molecules are held together by two H-bonds to form dimers, which further self-assemble *via* two strong $\text{N}(2)\text{-H}\cdots\text{Br}$ bonds to form ribbons. As

expected the G₃₄ macrocycle is energetically unfavored, since the H-bonds involved in pairing are of the weakest nature. Our findings indicate that the formation of H-bonds between molecules guides the generation of self-assembled structures, since the interactions between the stearate chains are much weaker. In gas phase, the calculated electronic structure of the dimers and ribbons exhibits hybridization between the states stemming from the organic complex, namely the guanine backbone, and the metallic states associated to the ferrocene functional groups. The information given by the electronic structure of calculated complexes strengthens our initial idea where, mainly, these complexes are held together by H-bonds formation even in presence of the metallic repulsion coming from the occupied molecular orbitals with clear *d* symmetries.

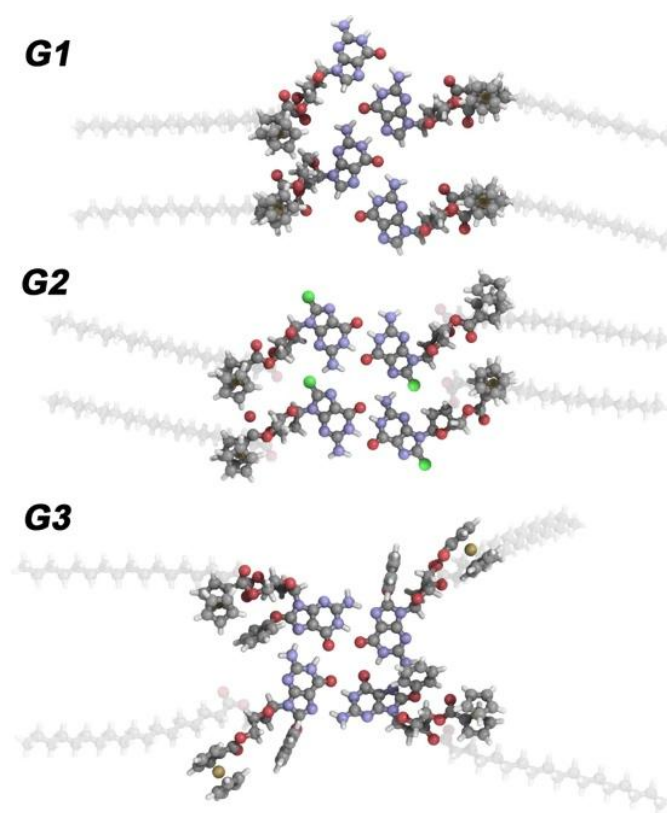
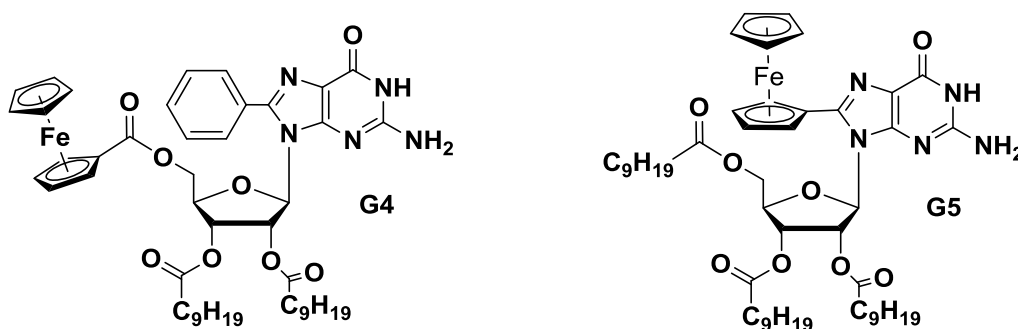


Figure 4.19 Calculated structure of *G1* and *G2* ribbons and *G3*₄ cation-free quartet structure.

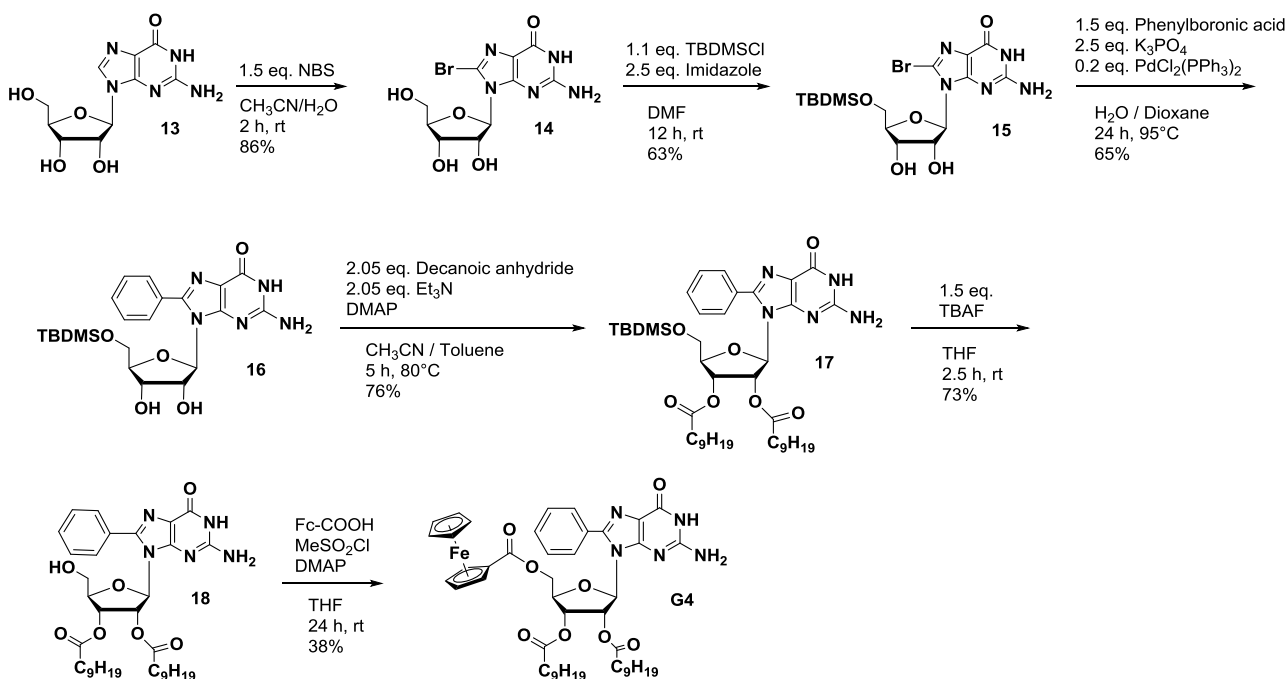
4.5 Metal free G₄ wires

The results obtained with **G3** led us to synthesize two other 8-substituted derivatives (Figure 4.20), using guanosine as the starting material in place of deoxyguanosine. This allows us to increase the lipophilic character of the compound. The first molecule is lipophilic guanosine derivative **G4**, with a phenyl group in C8 position. The second molecule is the analogous derivative **G5**, which carries a ferrocene residue in the 8-position. Both derivatives were expected to form metal free quartet-based assemblies.

Figure 4.20 Derivatives **G4** and **G5**.

4.5.1 Synthesis of **G4** (**G_8Ph_5Fc_23C₁₀**)

The synthesis of derivative **G4** was realized starting from commercial guanosine as described in Scheme 4.4. Bromination of the 8 position followed by selective protection of the primary alcoholic function led to derivative **15**. Suzuki coupling with phenylboronic acid produced the 8-phenylguanosine **16**. The two secondary alcoholic functions were then esterified at 80°C with decanoic anhydride in a mixture of toluene and acetonitrile: with this procedure it is not necessary to protect the nucleobase exocyclic amino function. The primary alcoholic function was then deprotected and esterified with ferrocene carboxylic acid *via* a mixed anhydride, to form the target guanosine **G4**.

Scheme 4.4 Synthesis of **G4**.

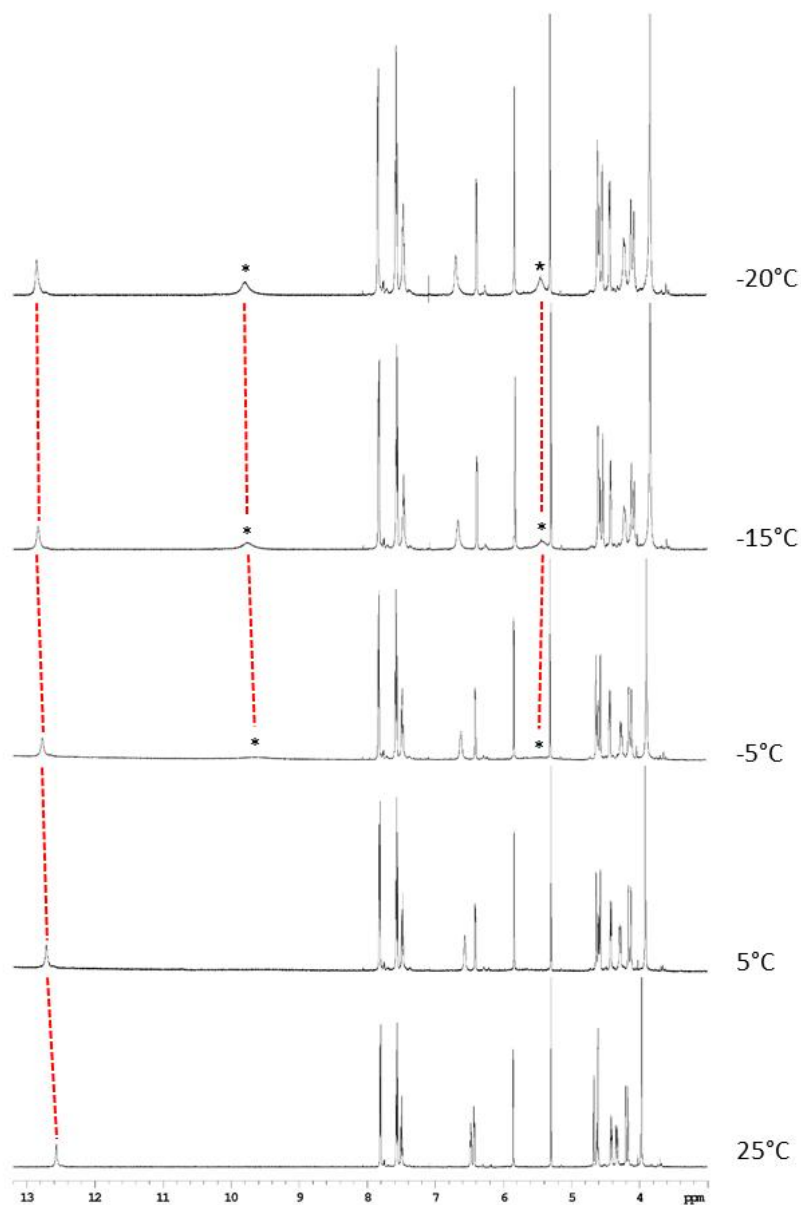


Figure 4.21 Downfield portion of the ^1H -NMR spectrum of pure **G4** at different temperatures in CD_2Cl_2 . Amino protons are marked with asterisks.

This is the behavior normally observed in the presence of G_4 s, although in this case no templating ions are present.

A further evidence of the existence and nature of self-assembled structures in solution is given by 2D-NOE spectra, where cross peaks have the same phase as the diagonal. This is characteristic of slow tumbling regime, implying that the objects in solution have a MW above 2000 Da, while the MW of **G4** is 879 Da. NOE experiments allow one to obtain a more detailed description of the species in solution and to confirm the existence of isolated G_4 s. Figure 4.22 shows selected 1D-NOESY spectra of **G4** recorded at -20°C .

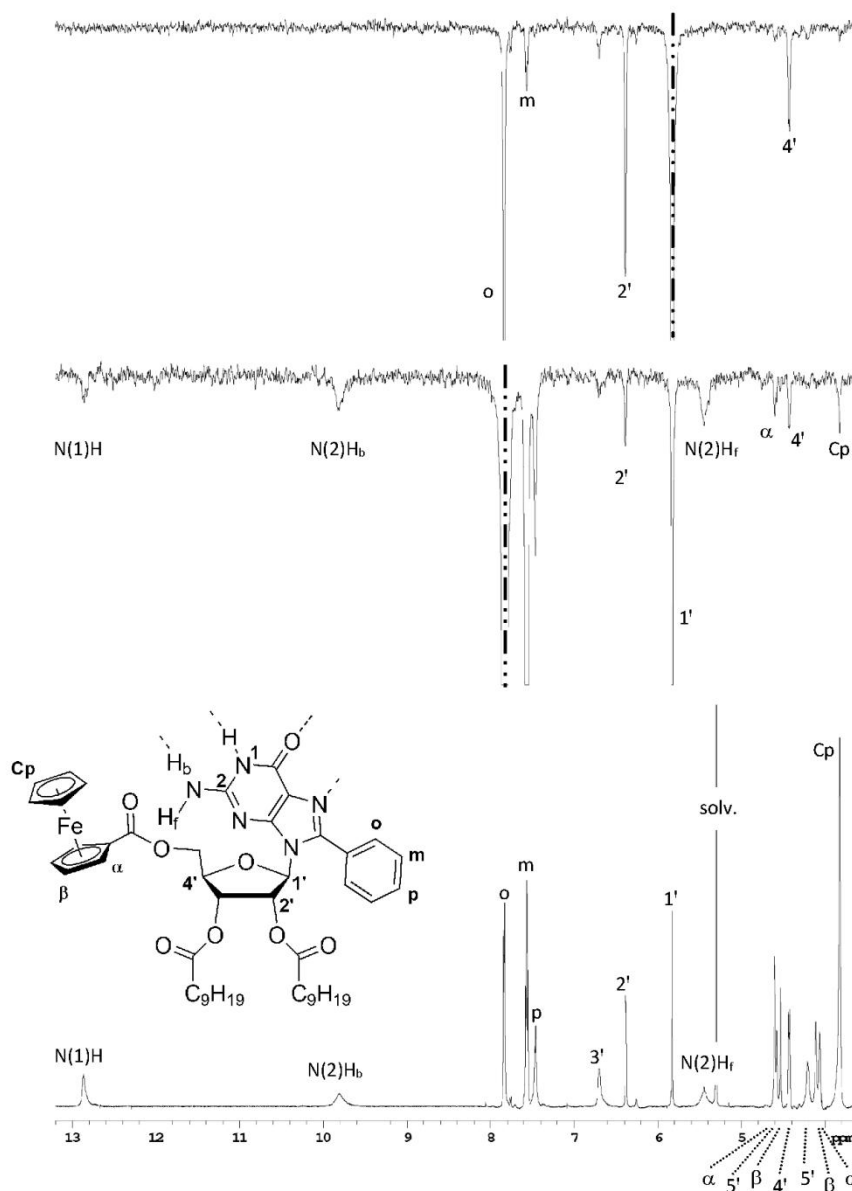


Figure 4.22 a) Downfield portion of the ^1H -NMR spectrum of **G4** at -20°C in CD_2Cl_2 and signals assignment (diastereotopic protons were not assigned); b) NOESY-1D spectrum of the same sample upon irradiation at 7.83 ppm (“o” protons); c) NOESY-1D spectrum of the same sample upon irradiation at 5.82 ppm ($1'$ proton), In each NOE spectrum were used 512 coadded transients, a recycle delay of 0.6 sec, a mixing time of 0.6 sec and a 50Hz shaped pulse. Irradiated frequencies are indicated by a dashed line.

The interaction between “orto” and $\text{H}1'$ protons, already strong at r.t., and the absence of any correlation between $\text{H}5'/\text{H}5''$ and phenyl protons point to an exclusive syn conformation for **G4**, as depicted in Figure 4.22. In addition, the orto protons show contact with both exocyclic amino and ferrocene protons (Figure 4.22b). As these proximities can only be intermolecular, they can be easily accounted for by the G_4 structure sketched in Figure 4.23, while they are incompatible with G-ribbon aggregates.

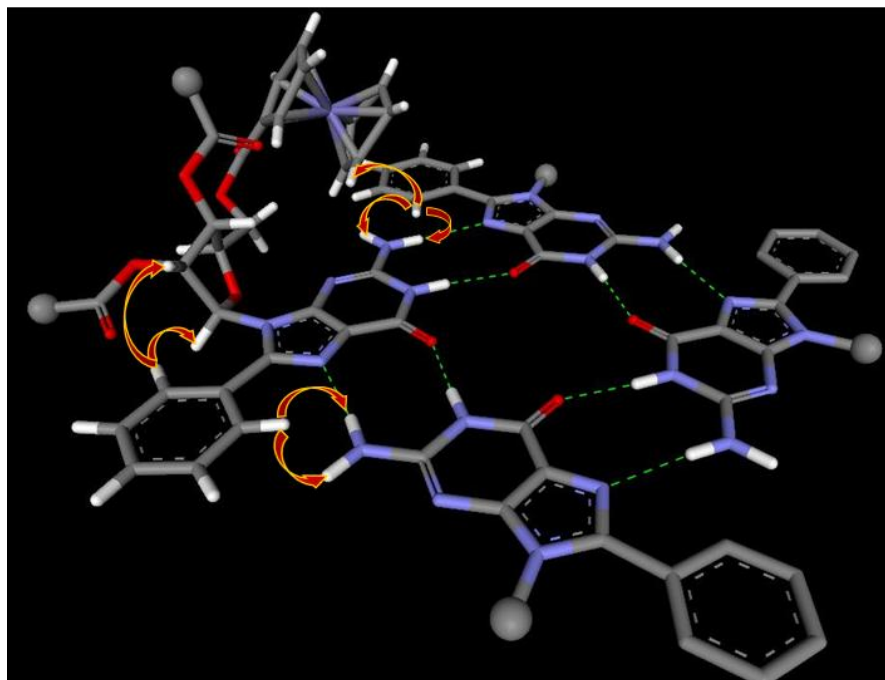


Figure 4.23 Proposed model for the isolated G_4 formed by **G4**. Arrows indicate selected NOEs. Some atoms are omitted for clarity.

Derivative **G5** shows a different behavior. In Figure 4.24 are reported a series of $^1\text{H-NMR}$ spectra of **G5** in CD_2Cl_2 at different temperatures. While the imino signal behaves analogously to what shown above for **G4**, the amino signal starts to appear only at -20°C in the form of two separate signals, a downfield (9.38 ppm) and an upfield one (5.5 ppm ca., partially hidden under the residual solvent signal). Besides, imino (12.38 ppm) and amino (9.98 ppm) signals of a second assembled species (1:6 ratio with respect to the major one) become visible.

If compared to the case of **G4** under the same conditions, the lower temperature required for the appearance of amino signals of **G5** suggests a lower dynamic stability for its aggregates.

For the major aggregate of **G5**, NOE correlations are in phase with diagonal peaks, analogously to what observed for **G4**. Selective 1D-NOE experiments (Figure 4.25) show a spatial proximity between H1' or H2' and cyclopentadienyl protons (Figure 4.25b, c), suggesting a syn conformation around the glycosidic bond for the major species. In addition, irradiation of cyclopentadienyl α proton (Figure 4.25b) shows an intermolecular NOE contact with exocyclic amino protons: we therefore assign the isolated G_4 structure to the major species. As on lowering temperature no other new signal appears in the sugar/ferrocene region of the spectrum, one could rule out that the minor species consists of the diastereomeric anti conformer. No clear evidence could be obtained on the architecture of the minor species. Nonetheless, the existence of a second type of H-bonded aggregate, possibly a dimeric species, suggests that this derivative is “confused” in its self-assembly

preferences with respect to **G4**. It should be mentioned that an analogous 8-phenoxy derivative (compound **G3**) showed in solution a behavior analogous to **G5**.

As the presence of bulky substituent at the 8 position is considered the structural feature responsible for the existence of isolated G_{4S} , it is possible to conclude that a ferrocenyl residue creates a lower steric hindrance with respect to a phenyl one.

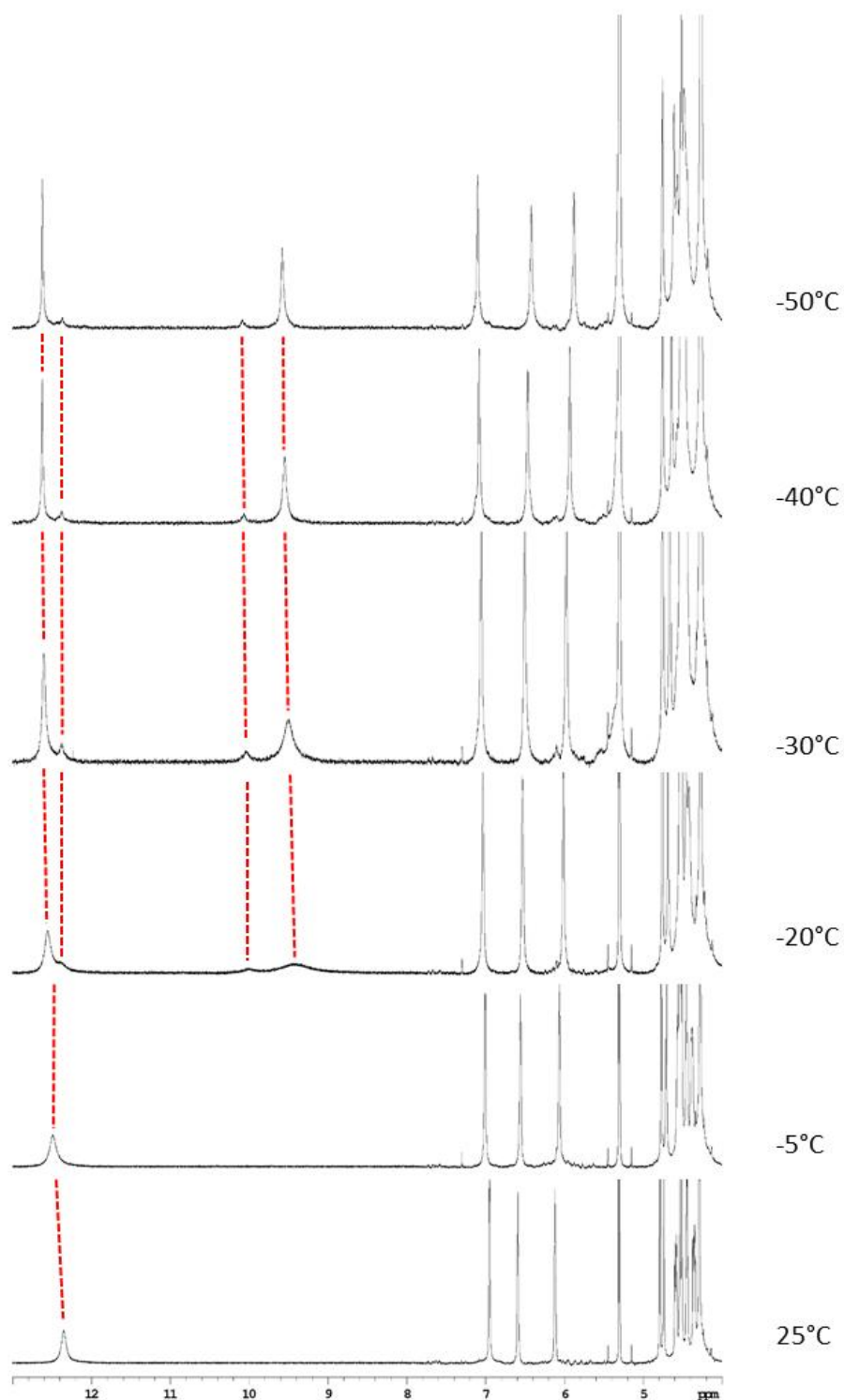


Figure 4.24 Downfield portion of the $^1\text{H-NMR}$ spectrum of pure **G5** at different temperatures in CD_2Cl_2 .

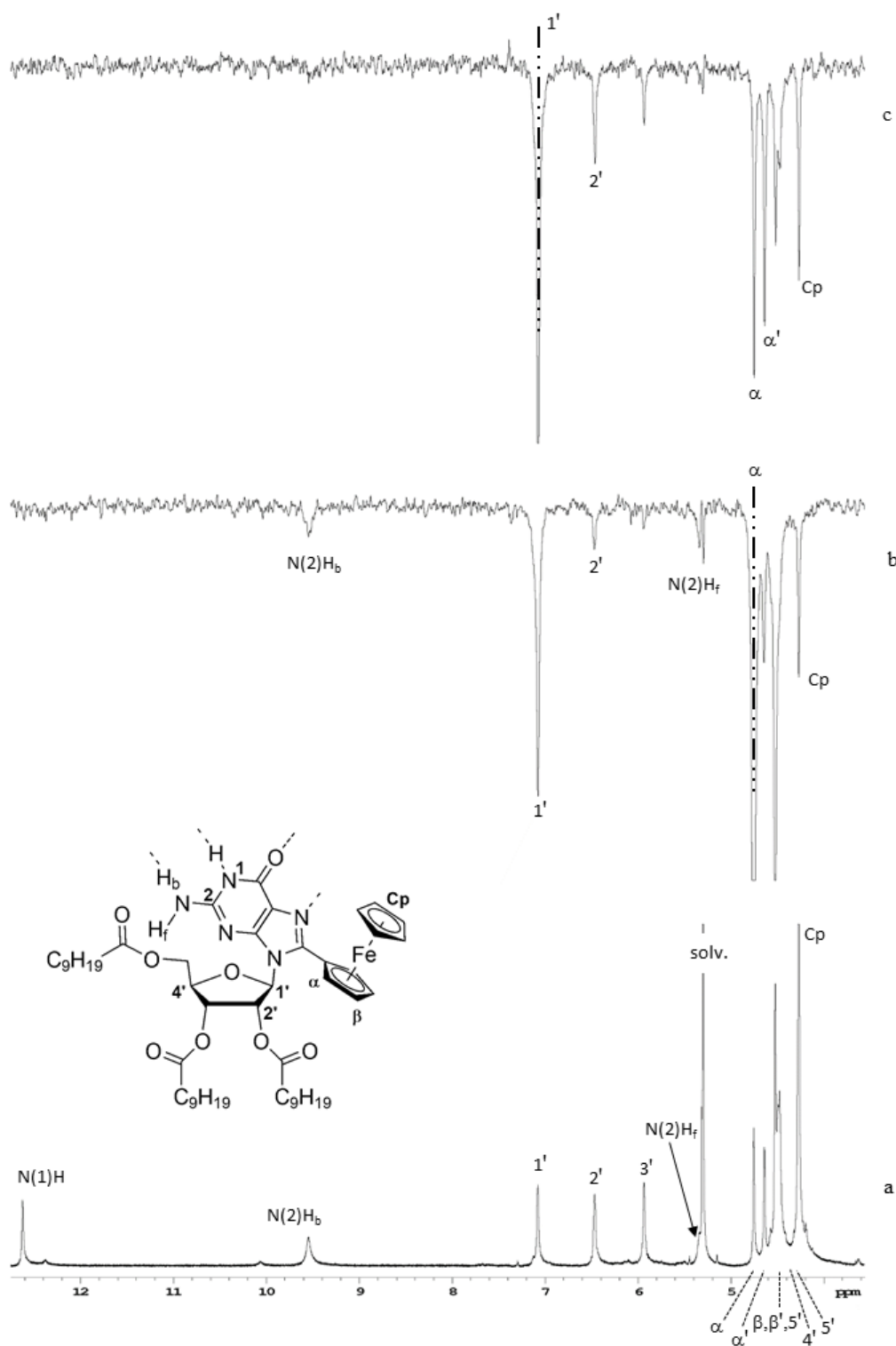


Figure 4.25 a) Downfield portion of the ¹H-NMR spectrum of **G5** at -40°C in CD₂Cl₂ and signals assignment (diastereotopic protons were not assigned); b) NOESY-1D spectrum of the same sample upon irradiation at 4.75 ppm (“α” proton); c) NOESY-1D spectrum of the same sample upon irradiation at 7.07 ppm (1' proton). In each NOE spectrum were used 512 coadded transients, a recycle delay of 0.6 sec, a mixing time of 0.6 sec and a 50Hz shaped pulse. Irradiated frequencies are indicated by a dashed line.

4.5.4 Solid-state characterization of the aggregates

To get a deeper insight on the morphology of the supramolecular structures, solid state Atomic Force Microscopy (AFM) study were performed. The samples were prepared by drop casting 150 μl of CH_2Cl_2 0.6 mg/ml solutions, containing the derivatives on the basal plane of thermally grown SiO_2/Si (230 nm SiO_2 on Si). The substrates were cleaned and functionalized with a monolayer of hexamethyldisilazane (HMDS) covalently bonded to the pending SiOH groups, prior use, in order to make the surface hydrophobic and to avoid the formation of hydrogen bond between the molecules and the surface.

Figure 4.26 shows AFM images of the packed molecules **G4** (a and c) and **G5** (b and d) under the same conditions. The crystalline architectures are extremely different, in particular **G5** grows a disordered network of entangled bundles of fibers while **G4** self-assembles in an ordered systems of aligned fibers that show an average height of 4.1 ± 0.5 nm and an average width of 32.4 ± 4 nm.

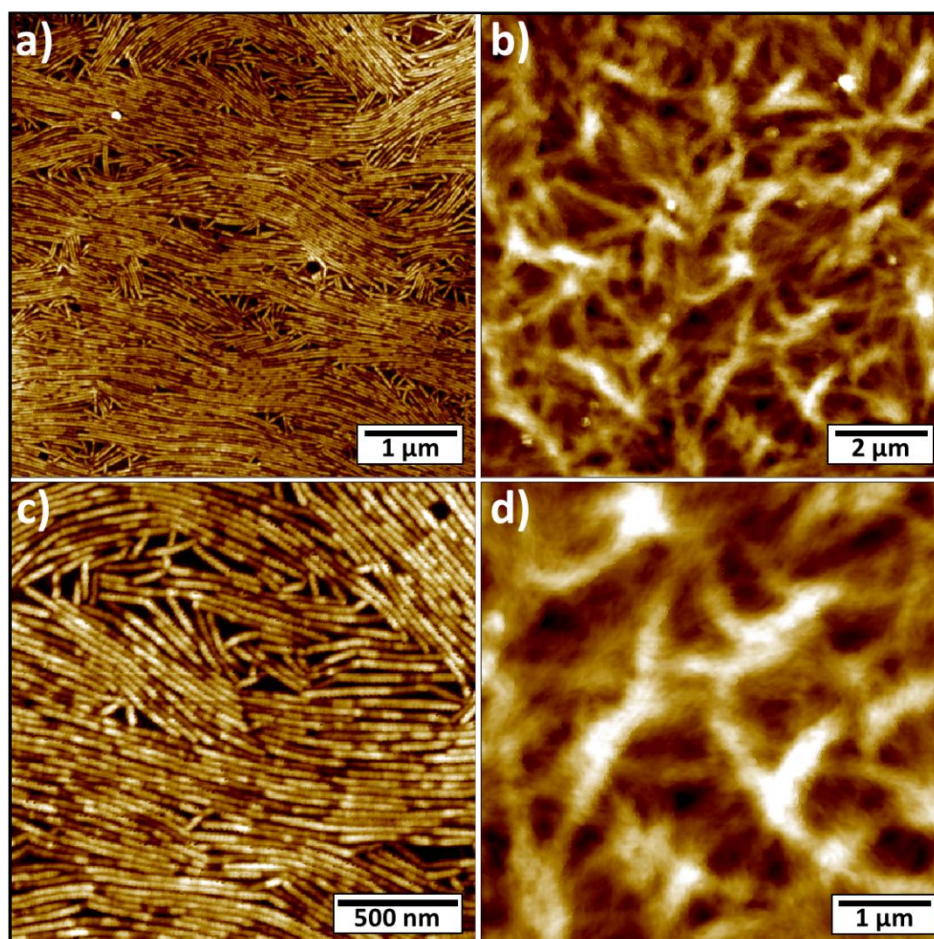


Figure 4.26 AFM images of supramolecular metal-free G4s aggregates drop cast from CH_2Cl_2 0.6 mg/ml on HMDS functionalized SiO_2 . a,c) Molecule **G4**. b,d) Molecule **G5**.

To boost the aggregation into more stable and ordered supramolecular structures, the films were then exposed to a solvent vapor annealing (SVA) in CH_2Cl_2 for 48 hours under ambient conditions. By this method it's possible to modify the morphology of the system i.e. to re-arrange the molecules into the most thermodynamically stable architectures. It is noteworthy that this method has previously been successfully used to finely tune the self-assembly of various molecular systems, including porphyrins,¹⁷ *n*-type perylene nanowires,¹⁸ *p*-type pentacene,¹⁹ and hexaperibenzacoronene (HBC) structures.²⁰

Figure 4.27 portrays the AFM images of the **G4** (a,c) and **G5** (b,d) fibers formed on the surface using SVA method. To this end, both systems look similar, appearing as bundles of entangled fibers. However, a fine analysis the architecture reveals that **G4** is more ordered over large scale (Figure 4.27 a,c, linear structure can be clearly seen the AFM image).

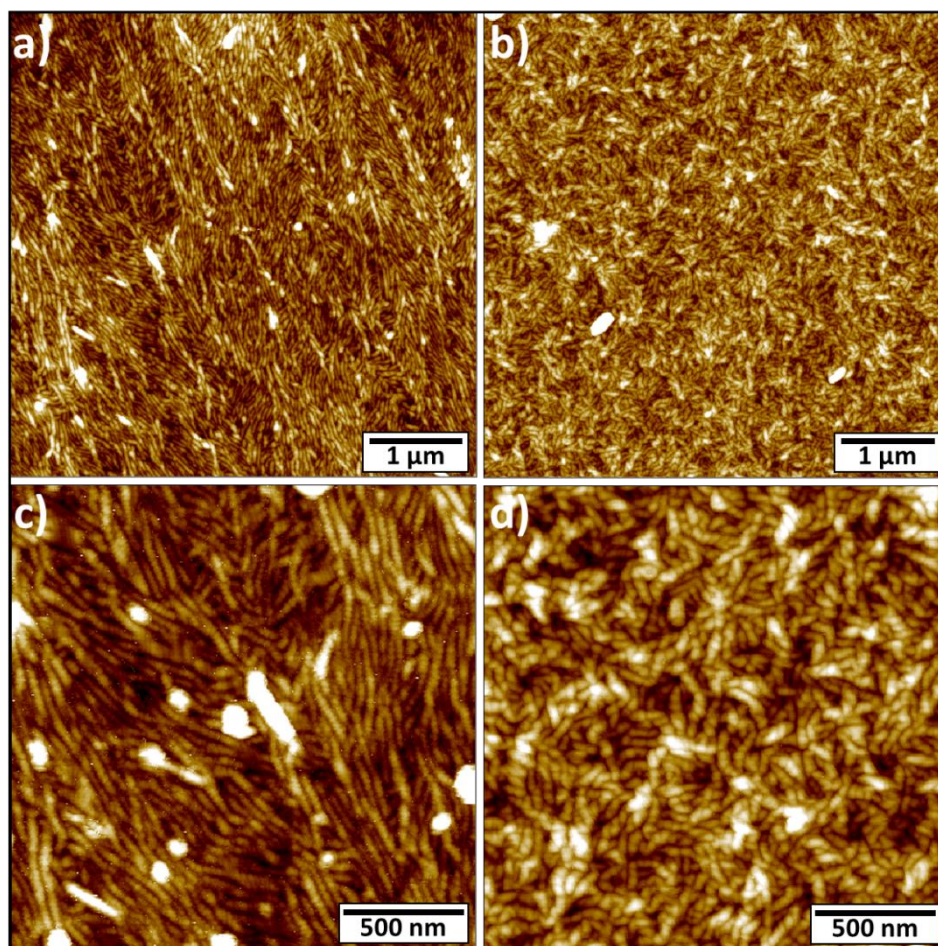


Figure 4.27 AFM images of supramolecular metal-free G4s aggregates drop cast from CH_2Cl_2 0.6 mg/ml on HMDS functionalized SiO_2 after SVA (CH_2Cl_2 for 48 hours). a,c) Molecule **G4**. b,d) Molecule **G5**.

4.6 Conclusions

In summary, by using STM at the solid/liquid interface, we have provided direct evidence on the sub-nanometer scale for the engineering of guanosine-based scaffolds. We have shown that supramolecular structures formed by ferrocene-exposing guanosines in solutions and at surfaces can be tuned by introducing sterically demanding substituents, ranging from *G*-ribbons to *G*₄ cation-free architectures. This self-assembly is governed by the formation of H-bonds between guanosines that dictates the spatial localization of ferrocenes, ultimately forming 1D conjugated arrays that may be employed as prototypes of supramolecular nanowires.

By using AFM imaging, we have monitored the self-association into SiO₂/Si substrate of two other LipoG carrying a phenyl (**G4**) and ferrocenyl (**G5**) group at the C(8) position, respectively. Derivative **G4** assembles into unprecedented *G*₄ cation-free architectures, both in CD₂Cl₂ solution and at the surface. Derivative **G5** does form isolated *G*₄ as well, but another aggregated species is present in equilibrium. Indeed, the size of ferrocenyl moiety seems not large enough to drive the self-assembly towards the exclusive existence of isolated *G*₄s in solution but its shape seems to hamper pi-stacking and hence a shift in equilibria towards (stacked) quartets in the solid state.

Our approach demonstrates that a careful molecular design of the guanosine starting building block makes it possible to steer the self-assembly towards the formation of a range of different thick films, even in the absence of templating ions. The thickness was measured at more than 10 nm according to profile recorded from the AFM images.

Unfortunately, although we were able to create an array with these guanosine derivatives, when we applied an oxidation potential, all the ferrocene groups were oxidized, making them useless as QCA. This is why we moved to another class of molecules: porphyrins, see in the next chapter.

Bibliography

- ¹ Mohamed El Garah, Rosaria C. Perone, Alejandro Santana Bonilla, Sebastien Haar, Marilena Campitiello, Rafael Gutierrez, Gianaurelio Cuniberti, Stefano Masiero, Artur Ciesielski and Paolo Samorì *Chem. Commun.* **2015**, 51, 11677-11680.
- ² a) R. Otero, M. Schock, L. M. Molina, E. Laegsgaard, I. Stensgaard, B. Hammer, F. Besenbacher, *Angew. Chem. Int. Ed.* **2005**, 44, 2270-2275; b) R. Otero, W. Xu, M. Lukas, R. E. A. Kelly, E. Laegsgaard, I. Stensgaard, J. Kjems, L. N. Kantorovich, F. Besenbacher, *Angew. Chem. Int. Ed.* **2008**, 47, 9673-9676.
- ³ A. Ciesielski, P. Samorì, *Nanoscale* **2011**, 3, 1397-1410.
- ⁴ R. Rinaldi, E. Branca, R. Cingolani, S. Masiero, G. P. Spada, G. Gottarelli, *Appl. Phys. Lett.* **2001**, 78, 3541-3543.
- ⁵ R. Rinaldi, G. Maruccio, A. Biasco, V. Arima, R. Cingolani, T. Giorgi, S. Masiero, G. P. Spada, G. Gottarelli, *Nanotechnology* **2002**, 13, 398-403.
- ⁶ G. P. Spada, S. Lena, S. Masiero, S. Pieraccini, M. Surin, P. Samorì, *Adv. Mater.* **2008**, 20, 2433-2438.
- ⁷ N. A. Wasio, R. C. Quardokus, R. P. Forrest, C. S. Lent, S. A. Corcelli, J. A. Christie, K. W. Henderson, S. A. Kandel, *Nature* **2014**, 507, 86-89.
- ⁸ Iurlo Matteo; Mengozzi, Luca, Rapino Stefania, Marcaccio Massimo; Perone Rosaria; Masiero Stefano; Cozzi Pier Giorgio; Paolucci Francesco, *Organometallics*.
- ⁹ Sessler, J. L.; Sathiosatham, M.; Doerr, K.; Lynch, V.; Abboud, K. A. *Angew. Chem. Int. Ed.* **2000**, 39, 1300-1302.
- ¹⁰ T. N. Pham, S. Masiero, G. Gottarelli, S. P. Brown, *J. Am. Chem. Soc.* **2005**, 127, 16018-16019.
- ¹¹ S. Masiero, S. Pieraccini, G. P. Spada, in *Guanine Quartets: Structure and Application*, The Royal Society of Chemistry, **2013**, 28-39.
- ¹² T. Giorgi, S. Lena, P. Mariani, M. A. Cremonini, S. Masiero, S. Pieraccini, J. P. Rabe, P. Samorì, G. P. Spada, G. Gottarelli, *J. Am. Chem. Soc.* **2003**, 125, 14741-14749.
- ¹³ *In ref 12, this signal splitting had been attributed to the existence of isolated G-quartets on the basis of the well-documented preference of 8-bromo guanosine to adopt a syn conformation around the glycosidic bond and the lack of any liquid crystalline behavior. Although G2 behaves in the same way, the present results suggest to reconsider the supramolecular behavior of G2 in solution, taking into account the existence of small ribbon-like aggregates.*

- ¹⁴ a) J. VandeVondele, M. Krack, F. Mohamed, M. Parrinello, T. Chassaing, J. Hutter, *Comput. Phys. Commun.* **2005**, 167, 103-128; b) M. Krack, M. Parrinello, *High Performance Computing in Chemistry* **2004**, 25, 29-51.
- ¹⁵ a) A. D. Becke, *J. Chem. Phys.* **1993**, 98, 1372-1377; b) A. D. Becke, *Phys. Rev. A* **1988**, 38, 3098-3100.
- ¹⁶ S. Grimme, *J. Comput. Chem.* **2006**, 27, 1787-1799.
- ¹⁷ M. El Garah, A. Santana Bonilla, A. Ciesielski, A. Gualandi, L. Mengozzi, A. Fiorani, M. Iurlo, M. Marcaccio, R. Gutierrez, S. Rapino, M. Calvaresi, F. Zerbetto, G. Cuniberti, P. G. Cozzi, F. Paolucci and P. Samorì, *Nanoscale*, **2016**, 8, 13678-13686.
- ¹⁸ G. De Luca, A. Liscio, P. Maccagnani, F. Nolde, V. Palermo, K. Müllen and P. Samorì, *Adv. Funct. Mater.* **2007**, 17, 3791-3798.
- ¹⁹ D. H. Kim, D. Y. Lee, H. S. Lee, W. H. Lee, Y. H. Kim, J. I. Han and K. Cho, *Adv. Mater.* **2007**, 19, 678-682.
- ²⁰ G. De Luca, A. Liscio, F. Nolde, L. M. Scolaro, V. Palermo, K. Müllen and P. Samorì, *Soft Matter*, **2008**, 4, 2064-2070.

V. Porphyrin-ferrocene hybrids

5.1 Introduction

Another possible strategy to control the assembly of molecules on surface and to obtain the desired disposition of molecular dots was related to the synthesis of functionalized porphyrins containing ferrocene.. The arrangement of metal-porphyrins on surfaces has been deeply studied by single molecule imaging.¹

The aim of this work is to prove the feasibility of a porphyrin bearing different ferrocene groups. We expected that in this case energetically different charged states would be available. To be a good candidate as quantum molecular cell, a hybrid porphyrin-ferrocene must have not only the appropriate electrochemical properties, but also the ability to self-assemble into an ordered linear structure, which can reproduce the architecture of a matrix cell. In addition, for a practical use it is also necessary a way to anchor the macrocycle on a solid surface.

In particular, we identified as targets, porphyrin derivatives where the ferrocene units are located at the meso positions of the porphine ring and hence in close proximity. In addition, we designed derivatives where ferrocenes were partially or fully conjugated with the aromatic macrocycle. We expect for these derivatives a multistep oxidation process, which will allow the easy obtainment of the doubly oxidized QCA cell, coupled with a stronger interaction between quantum dots. To drive the formation of 1D or 2D organized architectures, amide functional groups were planned.

5.2 Project

Analysis of literature brought us to design porphyrin derivatives with the general structure depicted in Figure 5.1: a *trans*-A₂B₂ porphyrin with two ferrocenes directly conjugated to the ring and a different type of functional group in the other two opposite meso positions.

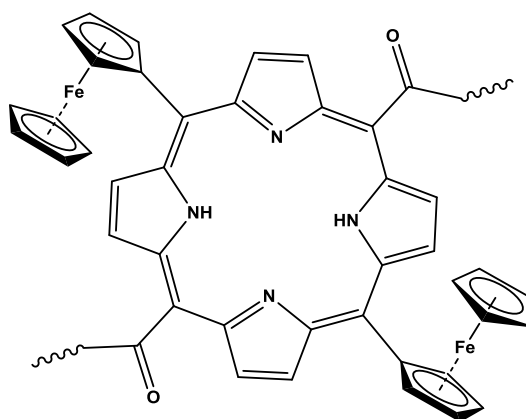
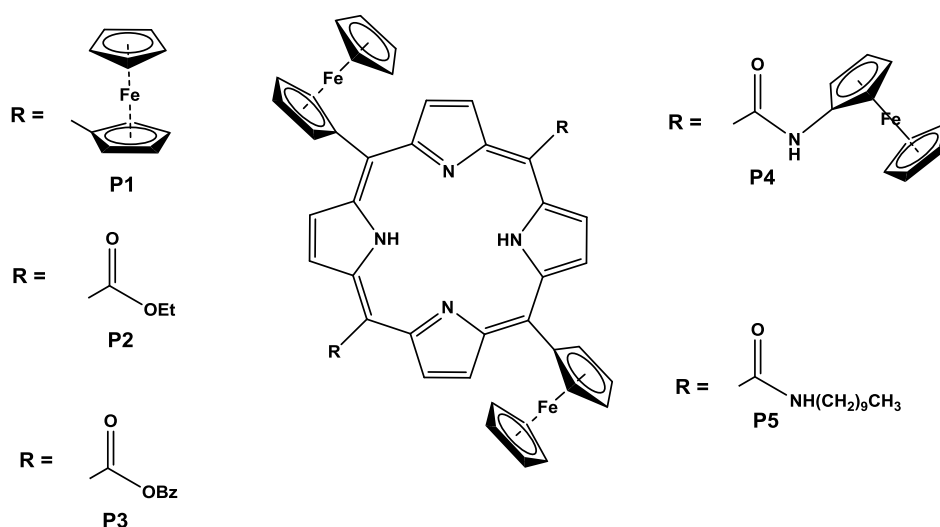


Figure 5.1 General formula of the target porphyrin.

These other two groups must be capable of ensuring the self-assembly into linear aggregates, while the anchoring of the molecule should occur through Van Der Waals interactions between the surface and the macrocycle. In particular, the amide function has been identified as a suitable group to allow the formation of hydrogen bonds between neighboring porphyrin rings, thus making the 2D aggregation possible.

In the second part of my research, we have synthesized several hybrids porphyrin-ferrocene, summarized in Scheme 5.1, carrying ferrocene residues directly connected to the porphyrin core, in order to study their electrochemical behavior and their self-assembly at surfaces.



Scheme 5.1 Porphyrin-ferrocene hybrids **P1-P5**.

P2 and **P3** are two porphyrins with ester functions, ethyl and benzyl, in the two meso positions. The goal in this case was to get a versatile molecule, usable as an half-cell with two dots: the complete cell would result be formed thanks to hydrogen bonds between the two molecules upon conversion of esters into carboxylic acids. These molecules are also intermediates for the synthesis of **P4** and **P5**.

Porphyrins **P4** and **P5** have been designed as candidate molecular unit cell and half-cell, respectively. In these derivatives, the ferrocene units are located at the meso positions of the porphyrin ring and hence in closer proximity. In addition, ferrocenes are either partially or fully conjugated with the aromatic macrocycle. The amide functional groups were introduced to drive the formation of 1D organized architectures via H-bonding, while the long aliphatic chains in **P5** have the purpose of “insulating” the expected 1D supramolecular rows of cells and, in case, favour surface adsorption.

We expect for these derivatives a multistep oxidation process, which will allow the easy obtainment of the doubly oxidized QCA cell, coupled with a stronger interaction between quantum dots.

5.3 Synthetic approaches

5.3.1 P1 (5,10,15,20-tetra ferrocenyl porphyrin)

Initially, porphyrin **P1**, known in the literature and with four ferrocenyl groups on the meso carbons was prepared (Figure 5.2), as a reference model for the other porphyrins.

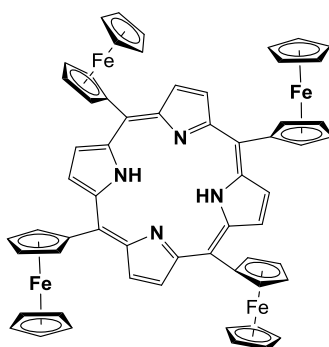
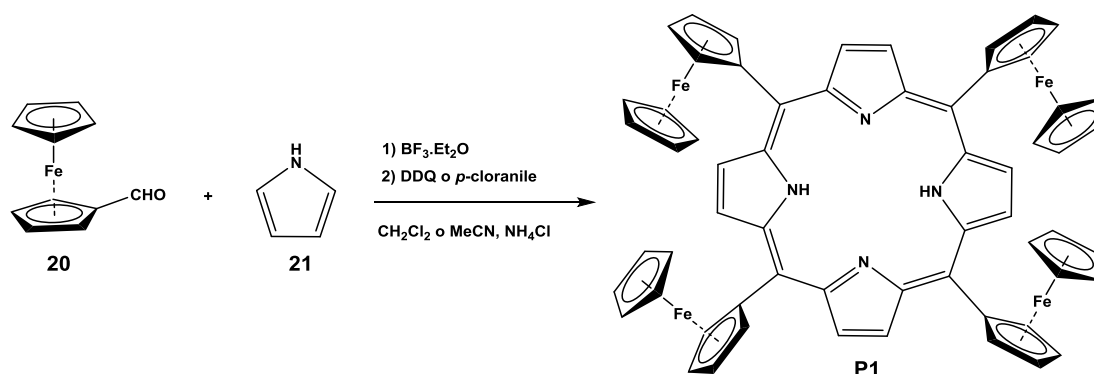


Figure 5.2 5,10,15,20-tetra ferrocenyl porphyrin.

The first attempt to obtain compound **P1** dates back to 1977 by Wollmann and Hendrickson²; after that many authors in recent years reported its synthesis^{3,4,5,6}.

The electrochemical studies of **P1** resulted in conflicting reports. Narayanan⁴ shows a single oxidation peak at 0.54 V, Venkatraman² describes two oxidation processes at 0.45 and 0.63 V, Nemykin³ reports two oxidation processes at -0.10 and +0.03 V. Currently there is no unique theory to explain the reasons for the particular electrochemical behaviour of this molecule.

We have followed two procedures for the preparation of **P1**. The first⁵ procedure uses the acid catalysed condensation between ferrocenecarboxaldehyde and pyrrole, both commercially available, and subsequent oxidation according to Lindsey's method⁷ (Scheme 5.2).

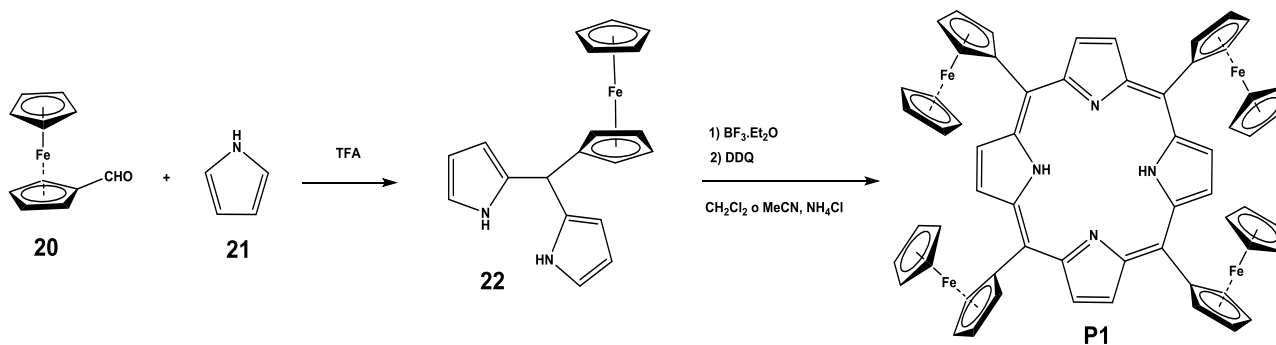


Scheme 5.2 Synthesis of **P1**.

The main difficulty was to obtain satisfactory yields; in no one of our attempts yield reached the reported 40%. We tried to change the following reaction conditions in order to define those that would guarantee higher yields:

- *Solvent*: CH_2Cl_2 has led to higher yields than MeCN. The solvent was always degassed for 30 minutes in an ultrasonic bath under argon atmosphere before use because, according to literature, this procedure may increase the final yield⁸. This operation has also been performed in the synthesis of all other porphyrins that will be presented below.
- *Catalyst*: the equivalents of $\text{BF}_3\cdot\text{Et}_2\text{O}$ were increased from 0.1 to 0.3, but this adjustment has not led to significant yield increases.
- *Oxidant*: the use of DDQ or p-chloranil have led to equivalent results.

The second procedure is based on the self condensation of meso ferrocenyl dipyrromethane **22** and subsequent oxidation, as in the Lindsey method (Scheme 5.3). The compound **22** was prepared by reaction of ferrocenecarboxaldehyde with an excess of pyrrole (40 eq) in the presence of acid catalyst, according to the general synthetic method for the preparation of meso-substituted dipyrromethanes⁹.



Scheme 5.3 Alternative synthesis of **P1**.

Two attempts have been made, employing CH_2Cl_2 or MeCN as solvent and TFA or $\text{BF}_3\cdot\text{Et}_2\text{O}$ as acid catalyst, respectively. In both cases, DDQ was used as oxidant. However, in either case results were poorer than with the first method.

Table 5.1 shows schematically the conditions used for the synthesis of compound **P1**. Conditions in the entry 1 and 3 have led to the best results.

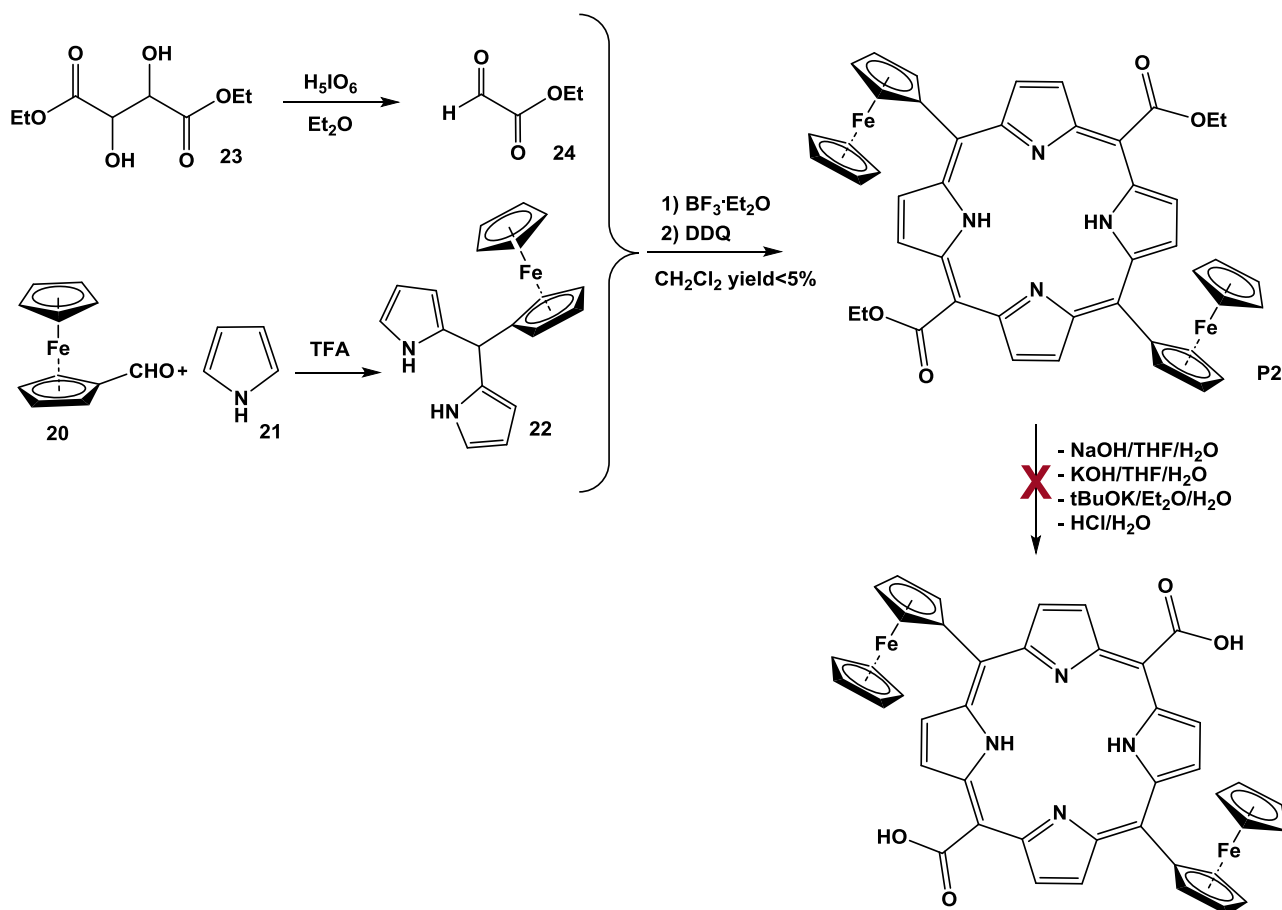
ENTRY	REAGENTS	SOLVENTS	OXIDANT	CATALYST	YIELD
1	FcCHO, pyrrole	CH ₂ Cl ₂	DDQ (0.8 equiv.)	BF ₃ ·Et ₂ O (0.33 equiv.)	<5%
2	FcCHO, pyrrole	MeCN, NH ₄ Cl	DDQ	BF ₃ ·Et ₂ O	trace
3	FcCHO, pyrrole	CH ₂ Cl ₂	<i>p</i> -chloranil (0.8 equiv.)	BF ₃ ·Et ₂ O (0.33 equiv.)	<5%
4	FcDPM	CH ₂ Cl ₂	DDQ	TFA	trace
5	FcDPM	MeCN, NH ₄ Cl	DDQ	BF ₃ ·Et ₂ O	trace

Table 5.1 Different strategies to synthesize **P1**.

5.3.2 P2 (Porf_COOEt)

The synthesis of **P2** (Scheme 5.4) starts from the oxidative degradation of diethyl tartrate with periodic acid to form ethyl glyoxylate¹⁰ followed by reaction, in the conditions of the Lindsay method, with dipyrromethane equipped with ferrocene group to form the final porphyrin. As acid catalyst was used BF₃·Et₂O (0.1 eq with respect to 1) and DDQ (0.8 eq) as oxidizing agent.

All the attempts to obtain the corresponding carboxylic acid by hydrolysis of **P2** failed, probably due to the easy decarboxylation of the former (vide infra).

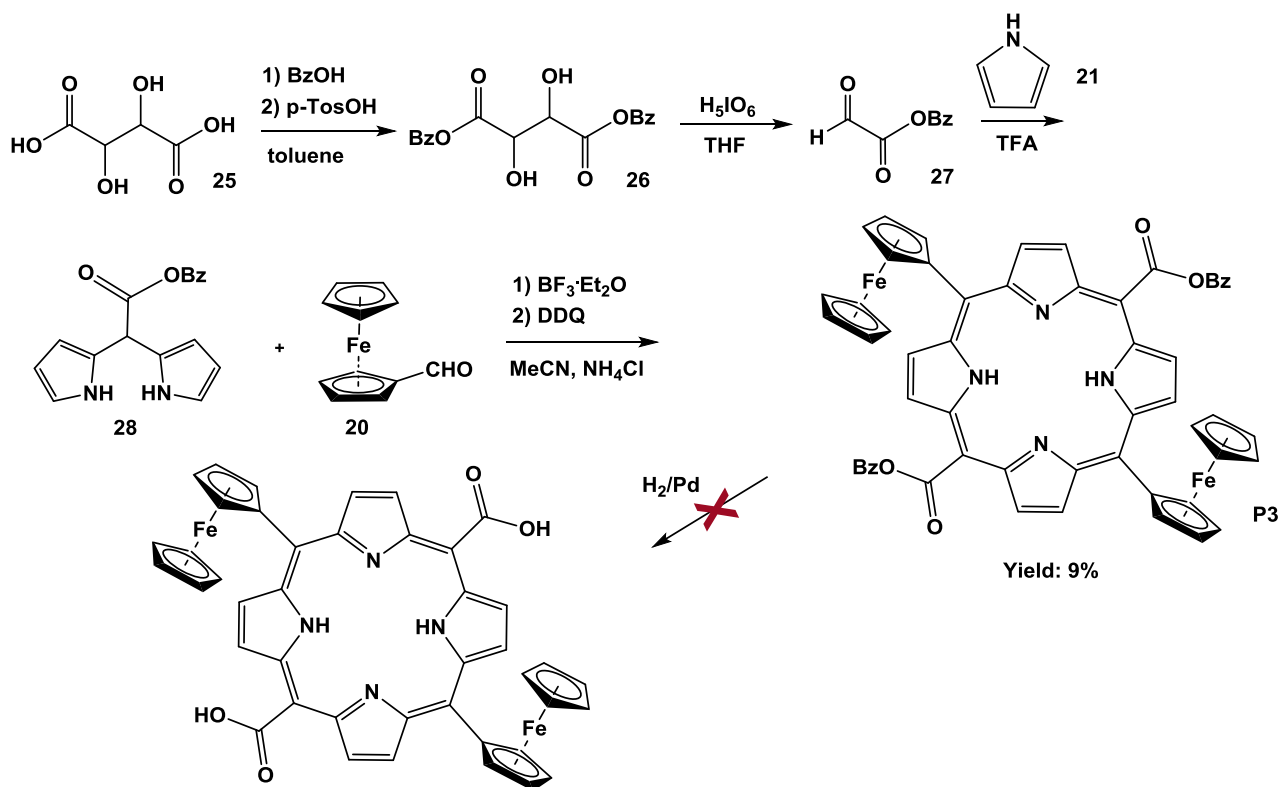
Scheme 5.4 Synthesis of **P2**.

5.3.3 **P3** (Porf_COOBz)

The synthetic path followed for the preparation of **P3** is reported in Scheme 5.5. The Fischer esterification of tartaric acid led to dibenzyl tartrate **26**, which was then subjected to oxidative cleavage with periodic acid to form benzyl glyoxylate **27**. The reaction of the aldehyde function with an excess of pyrrole in the presence of acid catalyst according to the method of Lindsey led to meso-benzyloxycarbonyl dipyrromethane **28**. The condensation between **28** and ferrocenecarboxaldehyde followed by oxidation with DDQ brought to the formation of porphyrin **P3**. Compared to the conditions described for the formation of **P2** some adjustments have been made:

- the oxidizing agent was used in excess (2 eq).
- the use of MeCN as a solvent in the presence of an excess of NH_4Cl (10 eq) at 0°C . Lindsey showed how these conditions can minimize the scrambling effect, despite of longer time of reactions and low yields of final porphyrin.¹¹

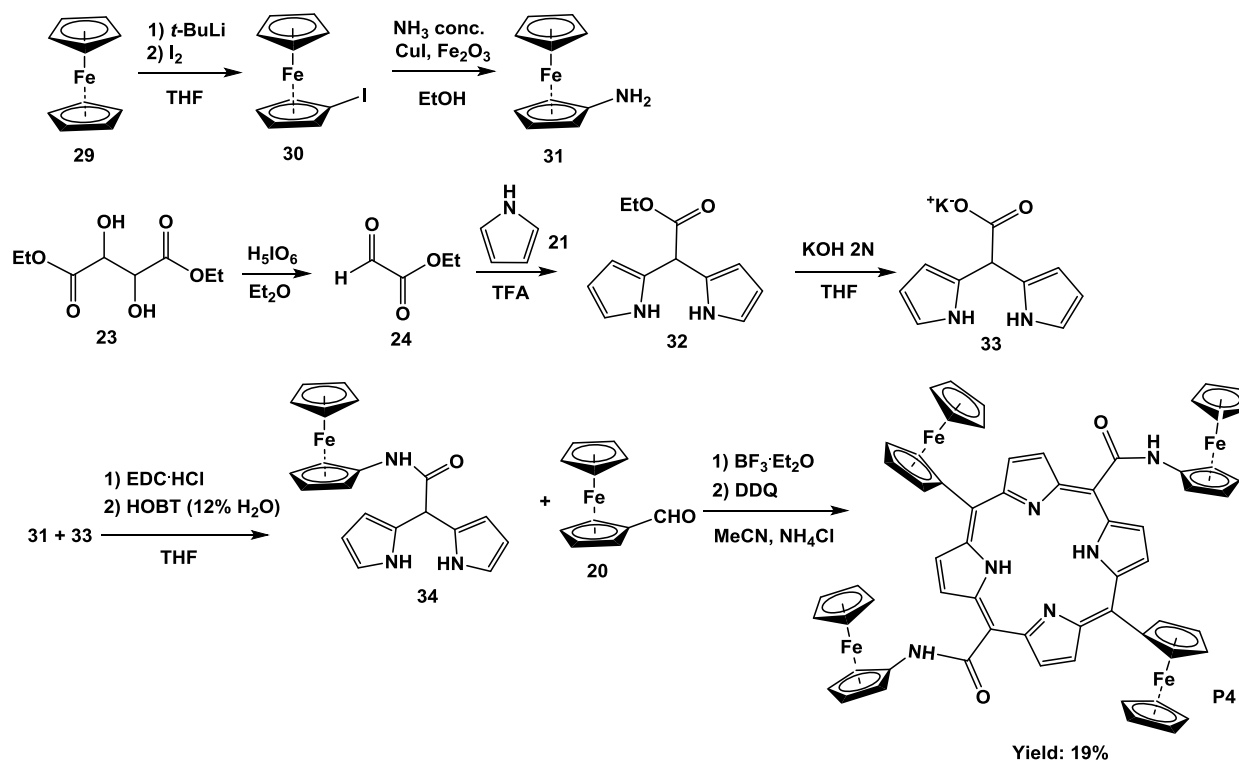
We tried the conversion of **P3** into the corresponding meso-dicarboxylic acid by catalytic hydrogenolysis, but we were unable to isolate the compound.



Scheme 5.5 Synthesis of P3.

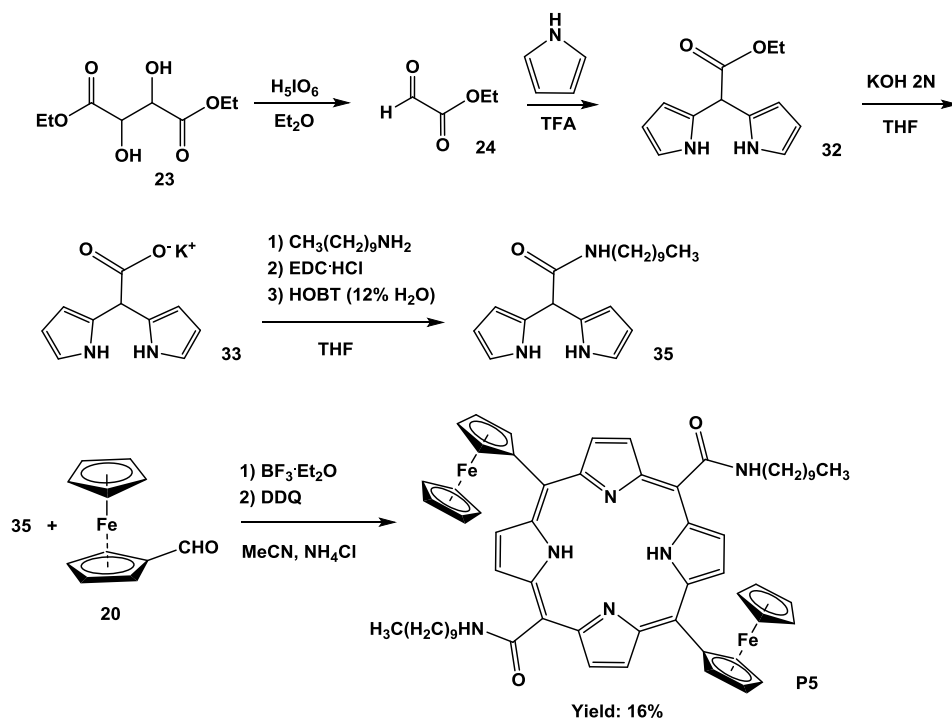
5.3.4 P4 (Porf_NHFc)

The synthesis of **P4** is reported in Scheme 5.6: ferrocene was converted into iodoferrocene¹² with *t*-BuLi and I₂. Subsequent treatment of **30** with concentrated ammonia in the presence of CuI gave aminoferrocene **31**.¹³ Ethyl glyoxylate was obtained by oxidation of diethyl tartrate with periodic acid and reacted with pyrrole to give the corresponding dipyrromethane **32**. Saponification of **32** and reaction via EDC/HOBT coupling with amino ferrocene gave dipyrromethane **34**, which could be condensed with ferrocenecarboxaldehyde to form the desired porphyrin **P4**.

Scheme 5.6 Synthesis of **P4**.

5.3.5 **P5** (Porf_NHC₁₀)

The synthesis of **P5** (Scheme 5.7) follows the same sequence of reactions as for **P4**, but decylamine was used instead of aminoferrocene.

Scheme 5.7 Synthesis of **P5**.

5.4 Electrochemical studies

The work and the characterization are still in progress. First, we report the electrochemical study in solution using cyclic voltammetry measurements, performed by the group of Professor Paolucci. Ferrocene-porphyrin molecules **P4** and **P5** were solubilized in dry dichloromethane (0.5 mM) with tetrabutylammonium hexafluorophosphate (TBAPF₆) as supporting electrolyte (0.05 mM), Cyclic voltammetry of derivative **P4** is shown in Figure 5.3.

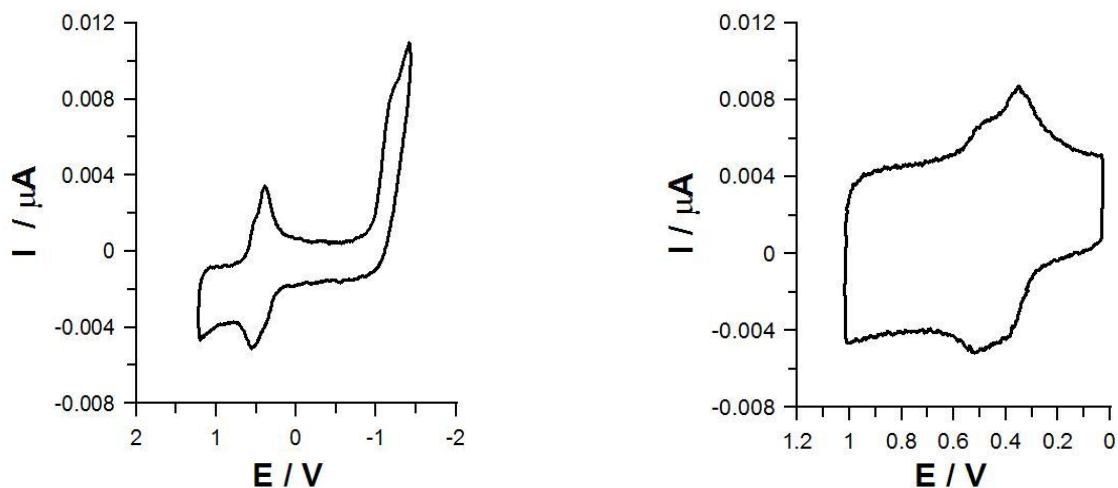


Figure 5.3 Cyclic voltammetry of **P4** 0.5 mM in 0.05 mM TBAPF₆ in DCM, potential vs SCE. Left: T = 298 K, 1 V/s. Right: T = 220 K, 10 V/s.

In this spectrum we can see two distinct oxidation peaks, which were attributed to oxidation of the two different types of ferrocene located in the molecule: one for the two directly conjugated ferrocenes and one for the other two. It is therefore possible to obtain a mixed-valence compound and this would confirm that the molecule can be used as a QCA cell. The observation of two peaks suggests that, in this case, the communication between the π Fc residues is weak.

Regarding derivative **P5** (Figure 5.4), however, cyclic voltammetry shows again two oxidation peaks, in which the second peak appears as a shoulder of the first. By reducing the temperature or the scanning speed, the second peak appears better resolved. This indicates that the two Fc residues communicate with each other from an electronic point of view and this also makes the porphyrin **P5** a good candidate for the implementation of a QCA system as an half-cell.

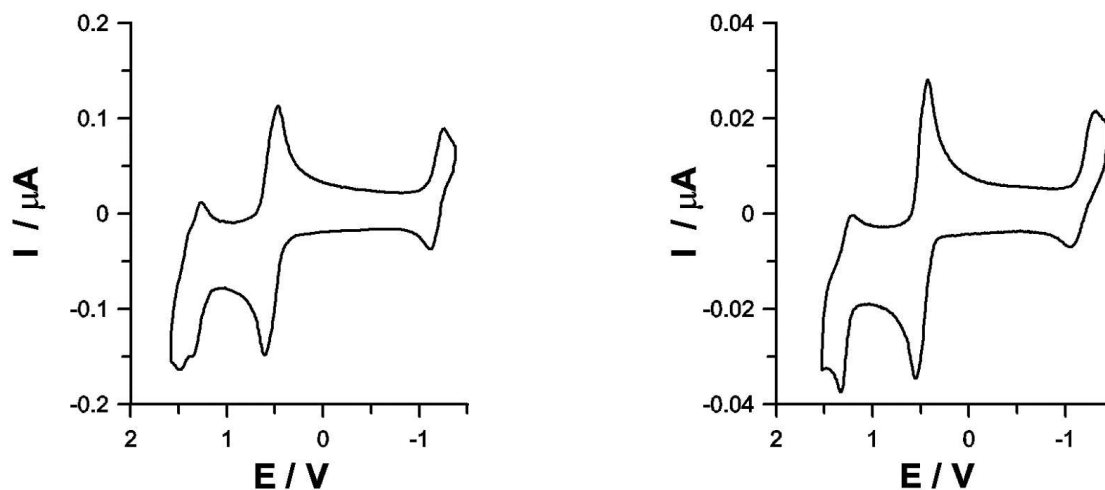


Figure 5.4 Cyclic voltammetry of **P5** 0.5 mM in 0.05 mM TBAPF₆ in DCM, potential vs SCE. Left: T = 298 K, 5 V/s. Right: T = 220 K, 1 V/s.

5.5 Organization on surfaces

Studies on the morphology of the assemblies originated by **P4** and **P5** are still in progress, but some preliminary results show the formation of extended domains of ordered structures: in Figure 5.5 is shown an UHV-STM image of the topography of **P5** dissolved in chloroform and electrospayed on a Au(111) surface.

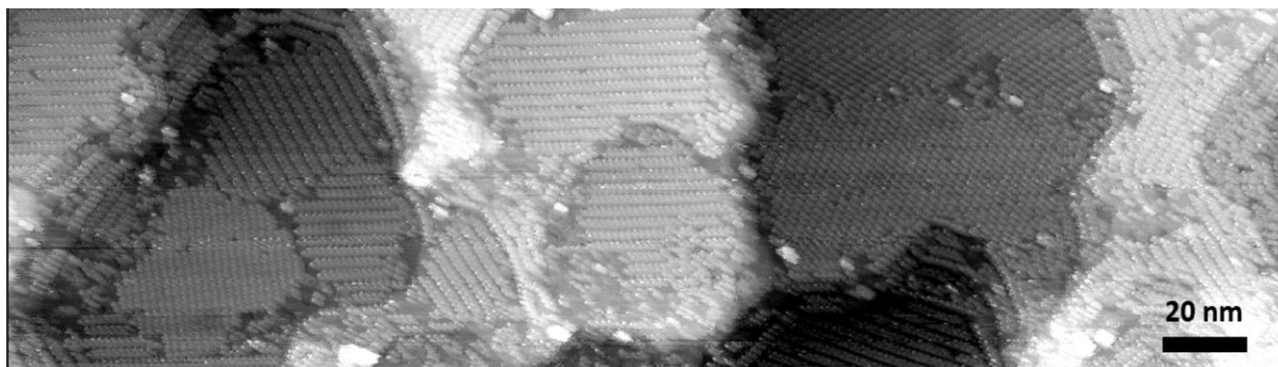


Figure 5.5 STM image (at 77K) of **P5** on Au(111) surface.

A closer look at these domains (Figure 5.6, top) reveals an ordered arrangement of ribbon-like 2D structures, with a unit cell (in red) of 3.6 x 1.5 nm and an angle of 123°. Figures 5.6 A and B refer to images acquired with two different STM tips.

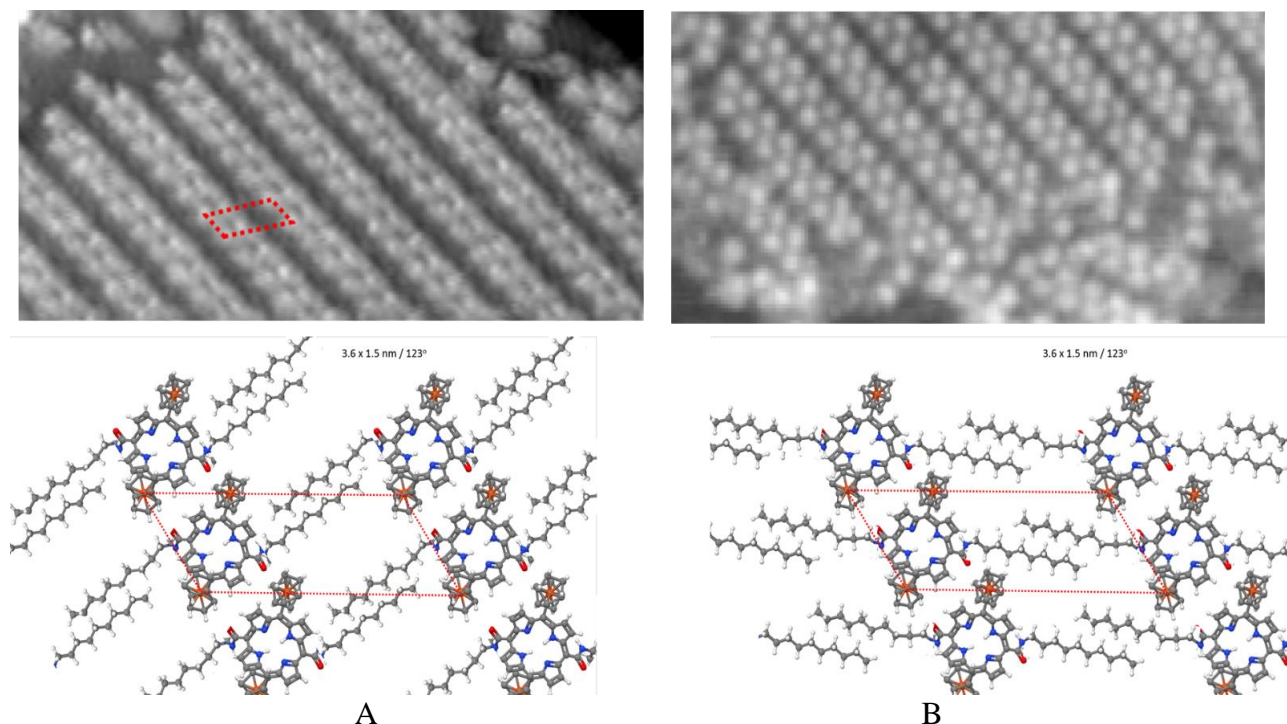
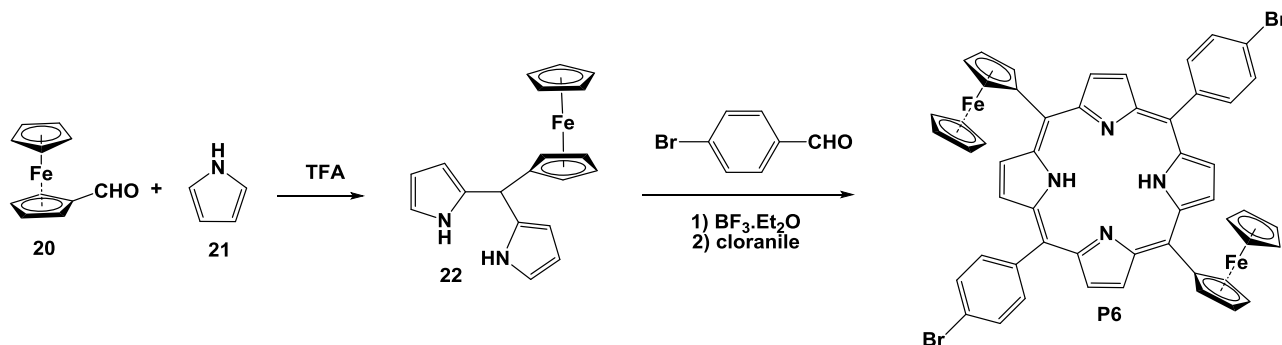


Figure 5.6 UHV-STM Topography (25pA, -2.2V) of P5 on gold.

Modelling of these images (Figure 5.6, bottom) confirms the formation of linear tapes of porphyrins, insulated by aliphatic tails. Nonetheless, the self-assembly seems controlled by lipophilic forces between aliphatic tails rather than by hydrogen bonding between amide groups. As a consequence, the orientation of the molecular units with respect to the ribbon axis is not the optimal one.

While further studies are in progress on **P4**, we decided to synthesize porphyrin **P6** (Scheme 5.8) with the aim of polymerizing via the STM¹⁴ tip the molecule deposited on a suitable surface to form, in this case, a conducting 2D polymer with the proper disposition of ferrocene units. Polymerization experiments are currently in progress.



Scheme 5.8 Synthesis of **P6**.

Bibliography

- ¹ a) J. Visser, N. Katsonis, J. Vicario, B. L. Feringa, *Langmuir* **2009**, 25, 5980; b) M. C. Lensen, J. A. A. W. Elemans, S. J. T. van Dingenen, J. W. Gerritsen, S. Speller, A. E. Rowan, R. J. M. Nolte, *Chem.–Eur. J.* **2007**, 13, 7948; c) Hulsken, R. van Hameren, J. W. Gerritsen, T. Khoury, P. Thordarson, M. J. Crossley, A. E. Rowan, R. J. M. Nolte, J. A. A. W. Elemans, S. Speller, *Nat. Nanotechnol.* **2007**, 2, 285.
- ² R. G. Wollmann, D. N. Hendrickson, *Inorganic Chemistry*, **1977**, 16, 3079-3089.
- ³ S. Venkatraman, V. Prabhuraja, R. Mishra, R. Kumar, T. K. Chandrashekar, W. Teng, K. R. Senge, *Indian J. Chem.* **2003**, 42A, 2191-2197.
- ⁴ V. N. Nemykin, C. D. Barrett, R. G. Hadt, R. I. Subbotin, A. Y. Maximov, E. V. Polshin, A. Y. Kuposov, *Dalton Trans.* **2007**, 31, 3378-3389.
- ⁵ S. J. Narayanan, S. Venkatraman, S. R. Dey, B. Sridevi, V. R. G. Anand, T. K. Chandrashekar, *Synlett.* **2000**, 12, 1834-1836.
- ⁶ N. M. Loim, N. V. Abramova, V. I. Sokolov, *Mendeleev Commun.* **1996**, 6(2), 46-47.
- ⁷ J. S. Lindsey, R. W. Wagner, *J. Org. Chem.* **1989**, 54, 828-836.
- ⁸ A. Nowak-Król, B. Koszarna, S. Y. Yoo, J. Chromiński, M. K. Węclawski, C-H. Lee, D. T. Gryko, *J. Org. Chem.* **2011**, 76, 2627-2634.
- ⁹ B. J. Littler, M. A. Miller, C-H. Hung, R. W. Wagner, D. F. O'Shea, P. D. Boyle, J. S. Lindsey, *J. Org. Chem.* **1999**, 64, 1391-1396.
- ¹⁰ M. P. Trova, P. J. F. Gauuan, A. D. Pechulis, S. M. Bubb, S. B. Bocckino, J. D. Crapo, B. J. Day, *Bioorg. Med. Chem.* **2003**, 11, 2695-2707.
- ¹¹ B. J. Littler, Y. Ciringh, J. S. Lindsey, *J. Org. Chem.* **1999**, 64, 2864-2872.
- ¹² J. C. Goeltz, C. P. Kubiak, *Organometallics.* **2011**, 30, 3908-3910.
- ¹³ A. Leonidova, T. Joshi, D. Nipkow, A. Frei, J-E. Penner, S. Konatschnig, M. Patra, G. Gasser, *Organometallics.* **2013**, 32, 2037-2040.
- ¹⁴ Okawa, Y. & Aono, M. *Nature* **2001** 409, 683–684.

VI. Supramolecular photoswitchable hydrogels

6.1 Introduction

A gel is a substance with these properties: (1) a continuous microscopic structure with macroscopic dimensions that is permanent at the time scale of an analytical experiment and (2) solid-like rheology despite being predominantly liquid.^{1,2} A gel can form a solid-like network (gel phase) which restricts the bulk flow of the liquid component (sol phase). If the solvent used to form the gel is water, the resulting gel is called a hydrogel.

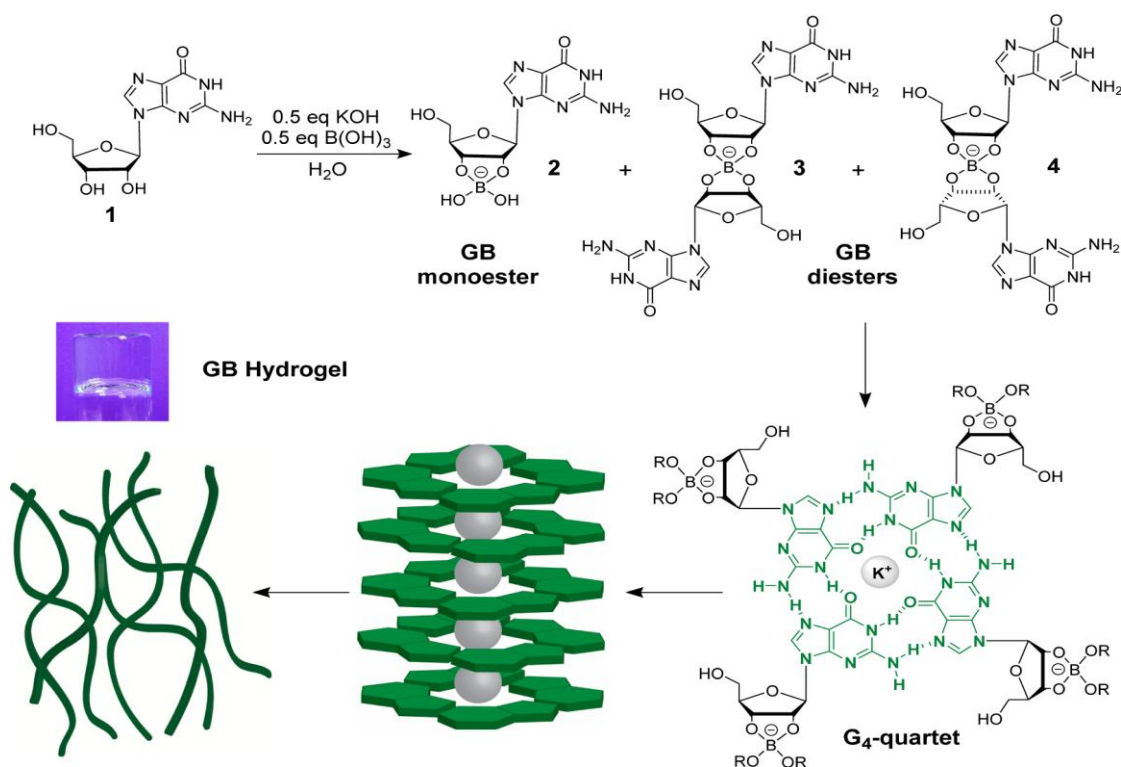
In contrast to the covalently linked networks in polymeric gels, the fibrous network of a physical gel forms through noncovalent interactions, such as ionic forces, hydrophobic interactions, π - π stacking, and hydrogen bonding. Supramolecular gels³, in which small organic molecules self-assemble to form fibers, are an example of physical gels: such materials are very attractive due to their potential biocompatibility and biodegradability.

Nucleosides and nucleic acids are examples of supramolecular gels based on natural products where self-assembly and molecular recognition of nucleobases is involved. As mentioned in Chapter 4, guanosine (G) shows unique self-assemblies, containing both a Watson-Crick edge and Hoogsteen edge, and some of the gels formed with G and its derivatives show notable promise for separations and biomedical applications.

Guanosine derivatives, for example 5'-guanosine monophosphate (5'-GMP) have been known to form gels⁴ typically via templation of G4-quartet motifs⁵ by cations such as K^+ and Na^+ , where four guanine bases form a macrocycle that is held together by hydrogen bonds and ion-ligand dipole interactions. The role of the cation is to assist the stacking of individual G4-quartets to give extended G4-wires, which ultimately form the fibers responsible of hydrogel formation. In order to obtain these guanine hydrogels, high concentrations of the nucleobase gelator (generally >0.05 M) and KCl (0.1–0.5 M) were needed. This requirement is likely because of the competition from water, that makes formation of the G4-quartet's hydrogen bonds and ion-dipole interactions challenging.

Recently, Davis and coworkers reported studies on a $G4 \cdot K^+$ hydrogel, where gelation of water by guanosine (G **1**) itself is achieved by addition of just 0.5 equiv of $KB(OH)_4$ relative to the concentration of the gelator **G 1** (Scheme 6.1).⁶ The countercation in the borate salt strongly alters the physical properties of the hydrogel. Addition of 0.5 equiv. of $KB(OH)_4$ to **G 1** (1 wt%; 36 mM) in water gave a strongest transparent gel (vial K), while the weakest system was obtained with $LiB(OH)_4$, (0.5 equiv.), obtaining a free-flowing solution (vial Li). Although the $LiB(OH)_4$ helps to dissolve **G 1** by forming borate esters (monoester **2** and diastereomeric diesters **3** and **4**), the sample

does not gel with Li^+ as cation. This is due to the fact that K^+ is far better than Li^+ at stabilizing G4-quartets.



Scheme 6.1 Proposed mechanism for gelation of water by **G 1** and $\text{KB}(\text{OH})_4$, via formation of GB borate monoester **2** and diesters **3/4**, followed by formation and stacking of $\text{G}_4 \cdot \text{M}^+$ quartets and intermolecular association of G_4 -wires.

6.2 Project

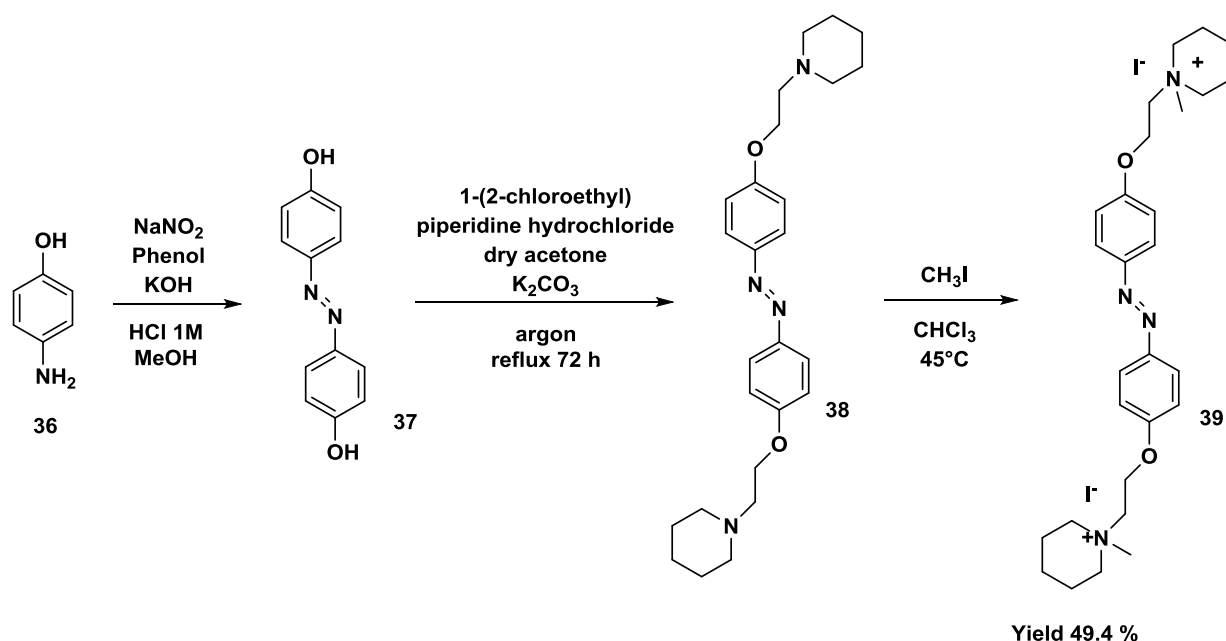
Responsive and dynamic hydrogels are clearly attractive for many applications, including sensing of biomolecules and ions, as media for cell culture, tissue engineering and targeted drug delivery.^{7,8,9,10}

During the period at the University of Maryland, in the Prof. Jeffery Davis' research group, I worked on the synthesis and characterization of specific dyes, containing azobenzene groups, in order to insert them in the guanosine hydrogels. As we know that small molecules can promote and stabilize supramolecular assemblies. For example, Sleiman's group demonstrated¹¹ that intercalators could program self-assembly of oligonucleotides into well-defined DNA nanostructures. Davis and co-workers also investigated interactions of dyes with supramolecular hydrogels made from guanosine and borate salts.¹² Both of these examples show the role of chaperones to control form and function in supramolecular assemblies, particularly those made from DNA nucleobases.

These dyes are capable, in principle, to change their conformation in a reversible way, through an external light stimulus. Thus, it could be possible to obtain photoresponsive hydrophilic gels, able to break and reform themselves in a controlled manner.

6.3 Synthesis of the AD dye

Xiang Zhou and co-workers¹³ reported the synthesis of an azobenzene derivative (Scheme 6.2) to control the movements and conformation of a G-quadruplex by irradiation. The formation and dissociation of G-quadruplex DNA was induced by interconversion of the *trans* and *cis* forms of compound **39**.



Scheme 6.2 Synthesis of compound **39**.

Compound **39** (called AD in this thesis) was synthesized by treating 4-hydroxyanilin with aqueous solution of sodium nitrite in acid condition, followed by addition of phenol in basic MeOH. Then, 4,4'-dihydroxyazobenzene (**37**) was reacted with 1-(2 chloroethyl)piperidine hydrochloride via Williamson synthesis to give compound **38**, which was subsequently transformed in the third step into the final product by exhaustive methylation.

6.4 Studies in solution

UV/Vis spectroscopy was used to characterize the isomerization of compound **39** by photoillumination. Indeed, the azobenzene group is well known to undergo *trans*-to-*cis* isomerization under UV/Vis light.

Preliminary studies were conducted in solution to investigate the photoresponsive behavior of the dye in water. Upon the irradiation of a dilute solution of **39** in H₂O (0.5 mM) at 365 nm for 10 minutes, compound **39** underwent isomerization to the *cis* form (figure 6.2, blue line), and the system reverted to a photostationary *trans* (PSS-*trans*) state after irradiation at 432 nm for 10 minutes (Figure 6.2, black line).

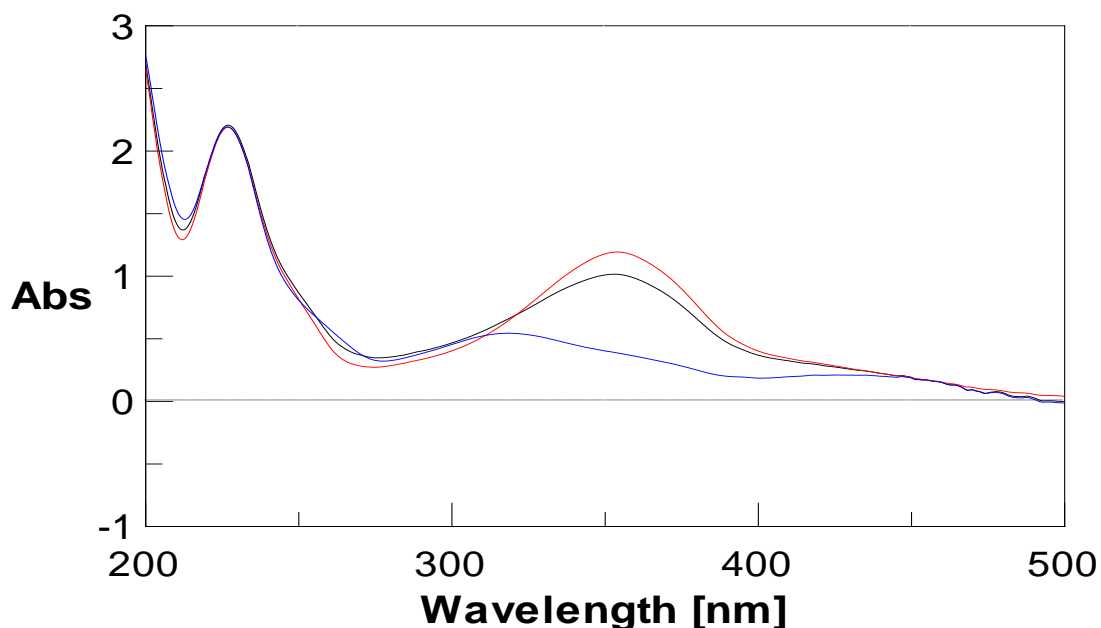


Figure 6.2 UV/Vis spectrum of compound **39** in H₂O (0.5 mM) before and after photoirradiation. Red line: all *trans* configuration under visible light. Blue line: PSS-*cis* after irradiation at 365 nm for 10 minutes. Black line: PSS *trans* after irradiation at 432 nm for 10 minutes.

In order to study the thermal back isomerization of the dye, a *cis* sample was maintained in the dark at room temperature and monitored by UV/Vis during the time. The thermal back isomerization was slow, indeed, as displayed in Figure 6.3: only after 17 hours the UV spectrum was almost superimposable to the PSS-*trans* trace (from red line to green line in Figure 6.3).

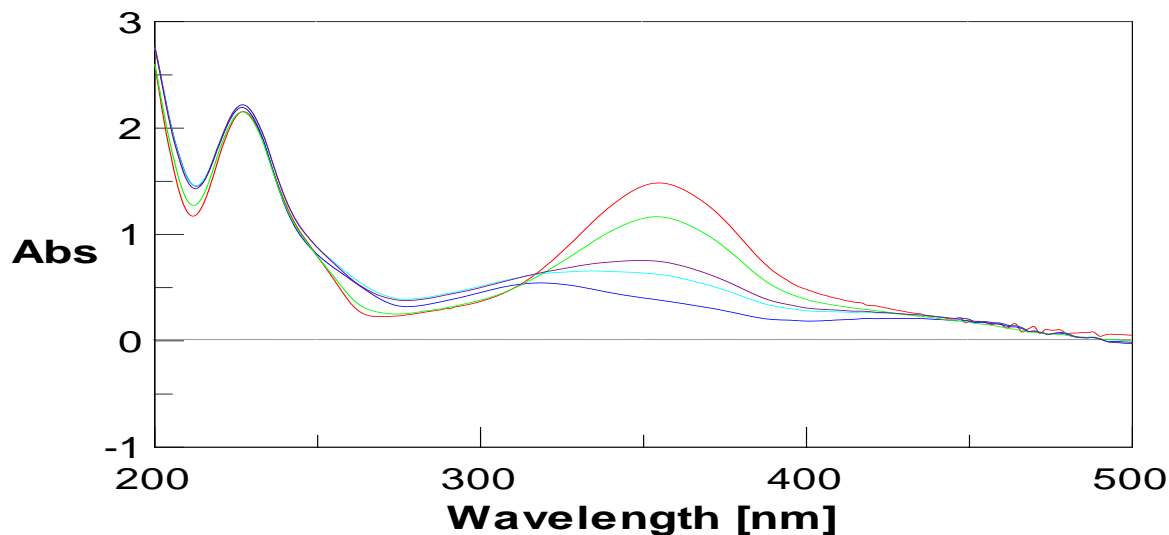


Figure 6.3: UV/Vis spectrum of trans **39** in H₂O (0.5 mM) (red line). After irradiation at 365nm for 10 minutes (blue line) compound **39** has been checked during time (after 1 h: light blue line; after 2 h: black line and after 17 h: green line).

In Figure 6.4 are reported CD spectra (top) and UV/Vis spectra (down) obtained from a water solution of 10 mM of guanosine in LiB(OH)₄ with AD dye 3 mM (red line) and spectra of the same solution without dye (blue line).

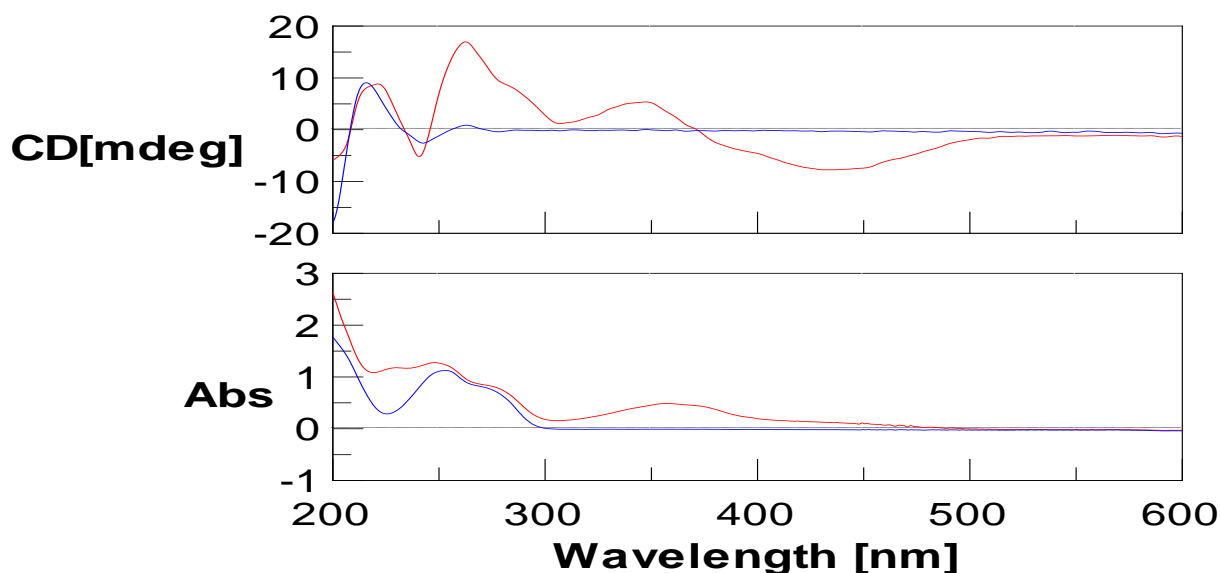


Figure 6.4 CD (top) and UV/Vis (down) spectra of a water solution of 10 mM of guanosine in LiB(OH)₄ with AD dye 3 mM (red line) and without dye (blue line).

Both the samples show an exciton signal, typical of a D₄-symmetric octamer. Interestingly, the sample with the dye shows an induced CD signal in the absorption region of the achiral dye, from

300 to 500 nm approximately. This signal suggests a dye-GB interaction, probably based on ionic forces. The same result was obtained with a solution of 10 mM of guanosine in $\text{KB}(\text{OH})_4$ (Figure 6.5).

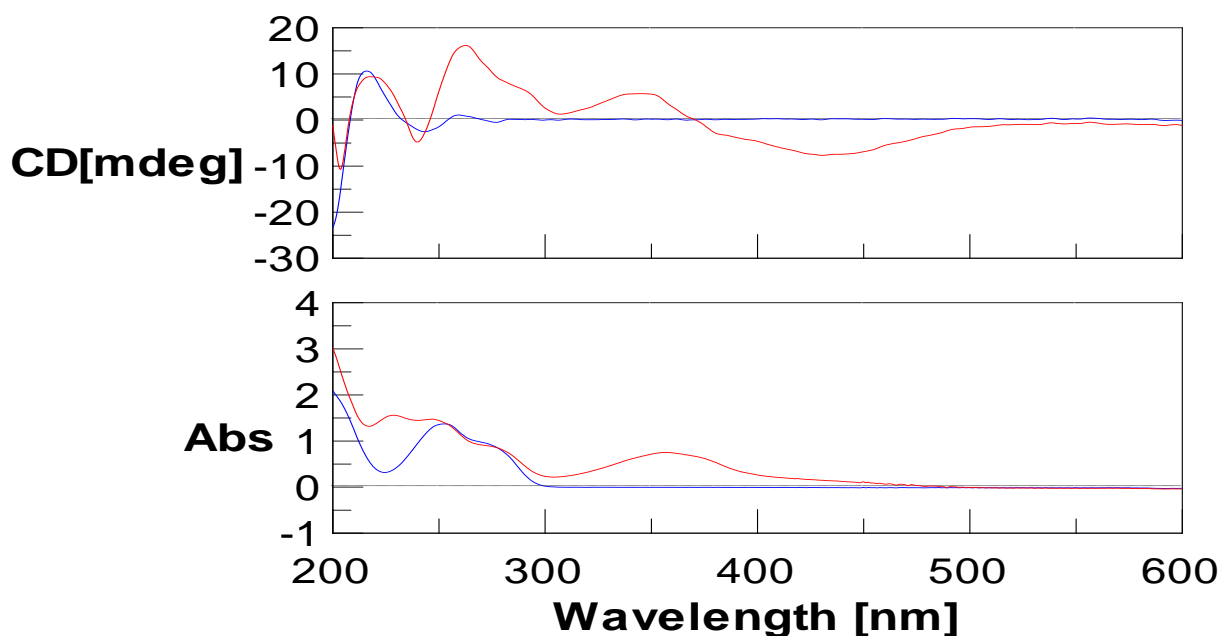


Figure 6.5 CD (top) and UV/Vis (down) spectra of a water solution of 10 mM of guanosine in $\text{KB}(\text{OH})_4$ with AD dye 3 mM (red line) and without dye (blue line).

6.5 GB hydrogels

Based on these results, I tried to synthesize guanosine-borate (GB) gel, in order to put the dye inside the gel. A GB hydrogel was prepared according to the general preparation procedure: the desired amount of guanosine was weighed into a vial, and the appropriate amount of $\text{B}(\text{OH})_3$ solution was added. The mixture was sonicated for approximately 30 s, and the appropriate amount of LiOH or KOH solution was added. The suspension was heated to 90 - 100 °C in a water bath until guanosine was dissolved, and the solution was clear. The solution was then removed from the heat and a measured amount of dye solution was transferred into the vial while warm. The vial was allowed to cool to room temperature. Gels were formed at a 2:1 ratio of G: $\text{KB}(\text{OH})_4$.⁶

I started with several concentrations of guanosine (from 50 to 100 mM) with $\text{LiB}(\text{OH})_4$ and with two different concentrations of dye, 0.5 and 1 mM. I monitored these gels during a week, while the inversion tests (by simply reversing vial containing sample) provided macroscopic evidence of strength of gels (see Table 6.1).

Entry	Guanosine	Without dye	Dye AD 0.5 mM	Dye AD 1 mM
1	G 50 mM	Liquid	Liquid	Liquid
2	G 60 mM	Liquid	Viscous liquid	Liquid
3	G 72 mM	Very weak gel	Very weak gel	Very weak gel
4	G 80 mM	Very weak gel	Very weak gel	Very weak gel
5	G 100 mM	Gel	Gel	Gel

Table 6.1 Inversion tests after a week of G:LiB(OH)₄ and different concentrations of AD dye.

Concentration of the dye 1 mM appeared too high compared to concentration of the guanosine. At the same time, G 50 mM formed a free flowing solution and, on the opposite, G 100 mM produced a strong gel. In light of this, I selected three concentrations of guanosine and two concentrations of dye, following all the samples during approximately 3 days. (Table 6.2)

Entry	GB Hydrogel	14 h	24 h	48 h	60 h
1	G 60 mM	Almost gel	Almost gel	Very weak gel	Very weak gel
2	G 60 mM + 0.25 mM dye AD	Liquid	Liquid	Viscous liquid	Viscous liquid
3	G 60 mM + 0.50 mM dye AD	Liquid	Liquid	Viscous liquid	Viscous liquid
4	G 72 mM	Almost gel	Weak gel	Weak gel	Gel
5	G 72 mM + 0.25 mM dye AD	Liquid	Liquid	Viscous liquid	Viscous liquid
6	G 72 mM + 0.50 mM dye AD	Liquid	Liquid	Very viscous liquid	Very viscous liquid
7	G 80 mM	Almost gel	Almost gel	Gel	Gel
8	G 80 mM + 0.25 mM dye AD	Liquid	Liquid	Very weak gel	Weak gel
9	G 80 mM + 0.50 mM dye AD	Liquid	Viscous liquid	Very weak gel	Weak gel

Table 6.2 Inversion tests during three days of G:LiB(OH)₄ and different concentrations of AD dye.

In addition, I used another dye (called ST in this thesis) commercially available, 4-(4-Diethylaminophenylazo)-1-(4-nitrobenzyl)pyridinium bromide (Figure 6.6). Inversion tests with this dye and G:LiB(OH)₄ are reported in the Table 6.3. Unfortunately, this dye showed poor solubility in water.

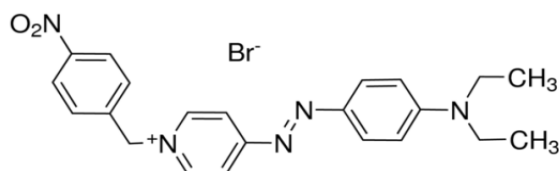


Figure 6.6 Structure of 4-(4-Diethylaminophenylazo)-1-(4-nitrobenzyl)pyridinium bromide (ST dye).

Entry	GB Hydrogel	14 h	24 h	48 h	60 h
1	G 60 mM	Liquid	Viscous liquid	Very weak gel	Very weak gel
2	G 60 mM + 0.25 mM dye ST	Liquid	Liquid	Viscous liquid	Viscous liquid
3	G 60 mM + 0.50 mM dye ST	Liquid	Liquid	Liquid	Viscous liquid
4	G 72 mM	Liquid	Weak gel	Gel	Gel
5	G 72 mM + 0.25 mM dye ST	Liquid	Liquid	Very weak gel	Gel
6	G 72 mM + 0.50 mM dye ST	Liquid	Liquid	Viscous liquid	Very weak gel
7	G 80 mM	Liquid	Almost gel	Gel	Gel
8	G 80 mM + 0.25 mM dye ST	Liquid	Viscous liquid	Almost gel	Gel
9	G 80 mM + 0.50 mM dye ST	Liquid	Liquid	Very weak gel	Gel

Table 6.3 Inversion tests during three days of G:LiB(OH)₄ and different concentrations of ST dye.

Furthermore, I prepared samples with guanosine 80 mM, $\text{KB}(\text{OH})_4$ and the two different dyes (Table 6.4)

Entry	GB Hydrogel	14 h	24 h	48 h	60 h
1	G 80 mM	Gel	Gel	Gel	Gel
2	G 80 mM + 0.25 mM dye AD	Gel	Weak gel	Weak gel	Weak gel
3	G 80 mM + 0.50 mM dye AD	Gel (less strong)	Gel (less strong)	Weak gel	Weak gel
4	G 80 mM + 0.25 mM dye ST	Liquid	Liquid	Liquid	Viscous liquid
5	G 80 mM + 0.50 mM dye ST	Very weak gel	Viscous liquid	Viscous liquid	Viscous liquid

Table 6.4 Inversion tests during three days of G: $\text{KB}(\text{OH})_4$ and different concentrations of AD and ST dyes.

Preliminary results show that both dyes make weaker gels as the concentration of the dye is increased, especially with ST dye. Potassium gels are more stable than lithium gels, as we expected, and can be used to test future dyes.

Surprisingly, most of these samples show birefringence when observed through crossed polarizers (see Figure 6.7 and Figure 6.8), regardless of the presence of dye.

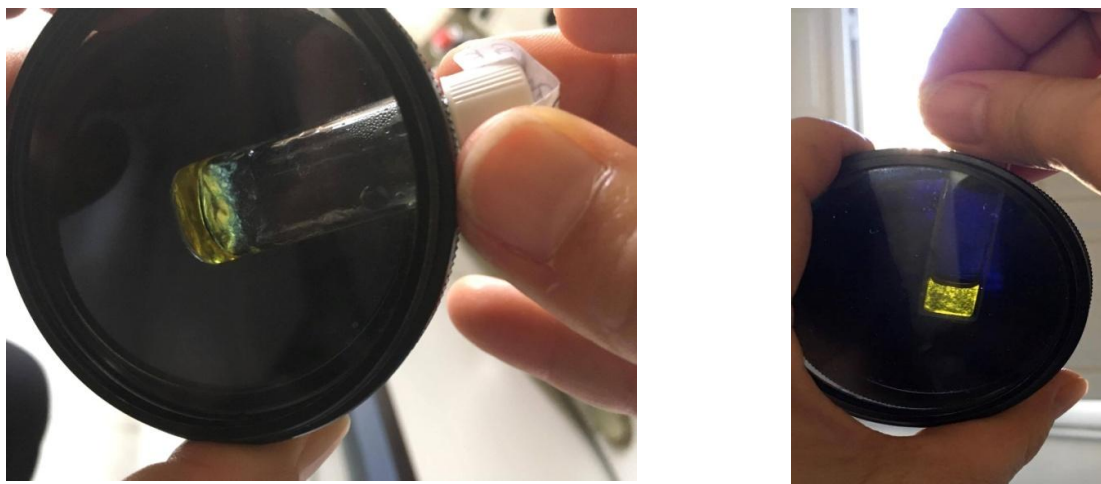


Figure 6.7 Birefringence of two sample. Left: 80 mM G:KB(OH)₄ with dye AD 0,5 mM, right: 40 mM G:KB(OH)₄ with dye AD 2,5 mM.

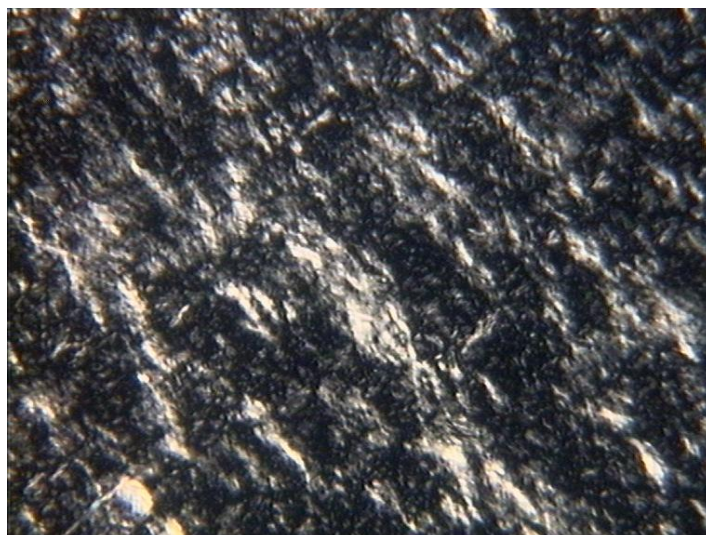


Figure 6.8 Optical microcope (crossed polarizers) birefringence of a water solution of 120 mM G:LiB(OH)₄.

These preliminary results suggest that what has always been considered a gel is actually a liquid crystalline phase, where some degree of anisotropy is present. This opens further possibilities for these materials and will be deeply investigated.

Bibliography

- ¹ Zweep, N.; van Esch, J. H. The Design of Molecular Gelators. In *Functional Molecular Gels*; **2014**; pp 1–29.
- ² Nishinari, K. Some Thoughts on The Definition of a Gel. In *Gels: Structures, Properties, and Function*; Tokita, M., Nishinari, K., Eds.; Springer, **2009**; Vol. 136, pp 87–94.
- ³ (a) Caran, K. L.; Lee, D.-C.; Weiss, R. G. Molecular Gels and their Fibrillar Networks. In *Soft Fibrillar Materials: Fabrication and Applications*; Liu, X. Y., Li, J.-L., Eds.; Wiley-VCH Verlag GmbH & Co. KGaA: Weinheim, Germany, **2013**. (b) *Molecular Gels: Materials with Self-Assembled Fibrillar Networks*; Weiss, R. G., Terech, P., Eds.; Springer: Dordrecht, The Netherlands, **2006**. (c) Raghavan, S. R.; Douglas, J. F. *Soft Matter* **2012**, 8, 8539–8546.
- ⁴ (a) Bang, I. *Biochem. Z.* **1910**, 26, 293. (b) Gellert, M.; Lipsett, M. N.; Davies, D. R. *Proc. Natl. Acad. Sci. U.S.A.* **1962**, 48, 2013. (c) Davis, J. T. *Angew. Chem., Int. Ed.* **2004**, 43, 669.
- ⁵ (a) García-Arriaga, M.; Hogley, G.; Rivera, J. R. *J. Am. Chem. Soc.* **2008**, 130, 10492. (b) Ciesielski, A.; Lena, S.; Masiero, S.; Spada, G. P.; Samorì, P. *Angew. Chem., Int. Ed.* **2010**, 49, 1963. (c) Cafferty, B. J.; Gallego, I.; Chen, M. C.; Farley, K. I.; Eritja, R.; Hud, N. V. *J. Am. Chem. Soc.* **2013**, 135, 2447.
- ⁶ Gretchen Marie Peters,[†] Luke P. Skala,[†] Taylor N. Plank,[†] Hyuntaek Oh,[‡] G. N. Manjunatha Reddy,[§] Andrew Marsh,[#] Steven P. Brown,[§] Srinivasa R. Raghavan,[‡] and Jeffery T. Davis*,[†] *J. Am. Chem. Soc.* **2015**, 137, 5819–5827.
- ⁷ Ikeda, M.; Yoshii, T.; Matsui, T.; Tanida, T.; Komatsu, H.; Hamachi, I. *J. Am. Chem. Soc.* **2011**, 133, 1670–1673.
- ⁸ Buerkle, L. E.; von Recum, H. A.; Rowan, S. J. *Chem. Sci.* **2012**, 3, 564–572.
- ⁹ Kuang, Y.; Shi, J.; Li, J.; Alberti, K. A.; Xu, Q.; Xu, B. *Angew. Chem., Int. Ed.* **2014**, 53, 8104–8107.
- ¹⁰ Liu, G.-F.; Zhang, D.; Feng, C.-L. *Angew. Chem., Int. Ed.* **2014**, 53, 7789–7793.
- ¹¹ Greschner, A. A.; Bujold, K. E.; Sleiman, H. F. *J. Am. Chem. Soc.* **2013**, 135, 11283.
- ¹² Peters, G. M.; Skala, L. P.; Plank, T. N.; Hyman, B. J.; Reddy, G. N. M.; Marsh, A.; Brown, S. P.; Davis, J. T. *J. Am. Chem. Soc.* **2014**, 136, 12596.
- ¹³ Xiaolin Wang, Jing Huang, Yangyang Zhou, Shengyong Yan, Xiaocheng Weng, Xiaojun Wu, Minggang Deng, and Xiang Zhou*, *Angew. Chem. Int. Ed.* **2010**, 49, 5305–5309.

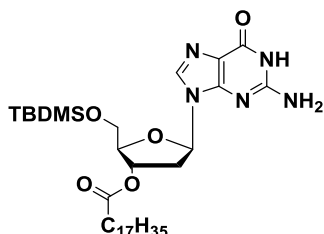
VII. Experimental part

General

All reactions requiring anhydrous conditions were carried out in oven-dried glassware under dry argon atmosphere. Macherey-Nagel Polygram silica gel plates (layer thickness 0.20 mm) were used for TLC analyses. Column chromatography was performed on Geduran silica gel 60 (40-63 μm). Reagents and solvents, including dry solvents, were purchased from Aldrich, TCI or Alfa Aesar.

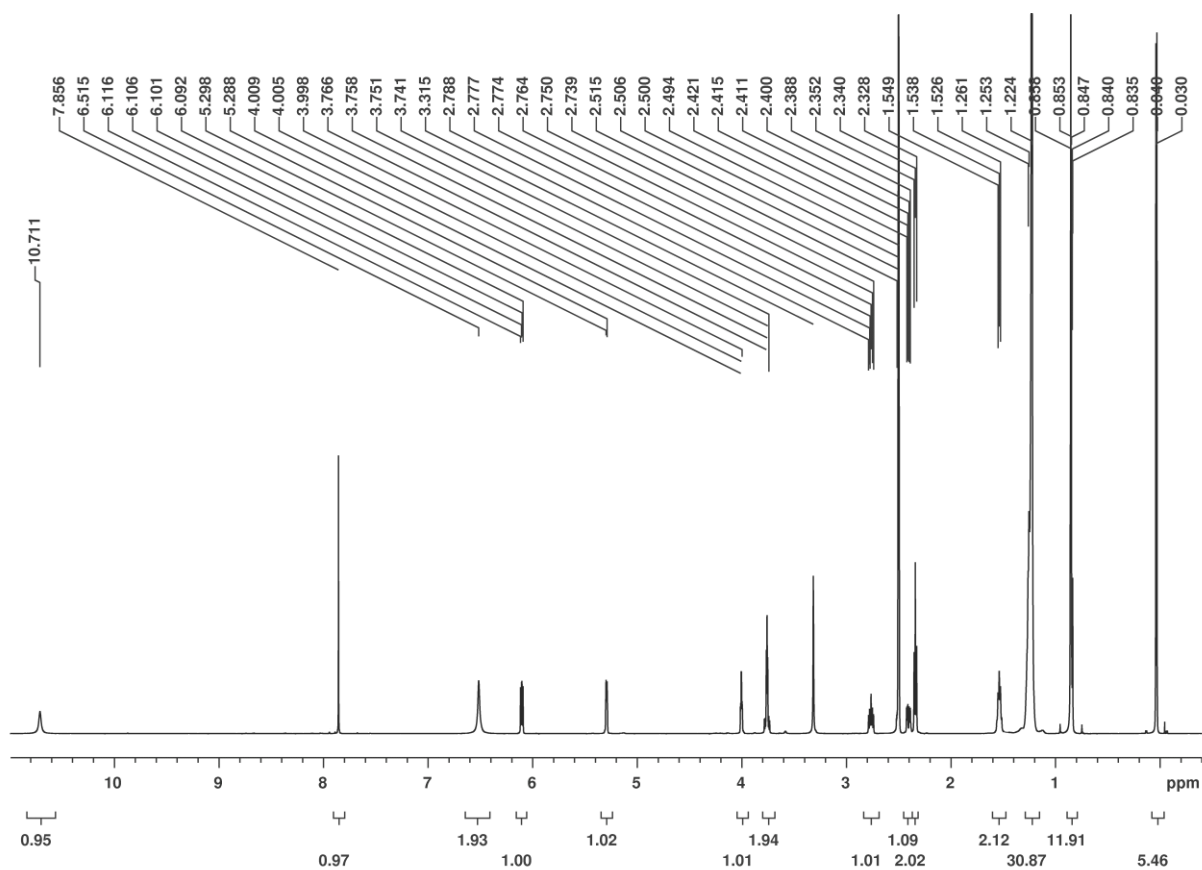
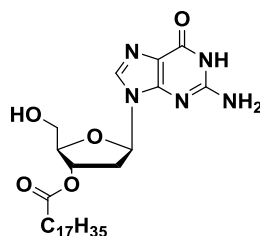
Nuclear magnetic resonance spectra were recorded on Varian (600, 400 or 200 MHz) spectrometers and referenced to the residual solvent resonance. Electrospray ionization mass spectra were obtained from methanol solutions with a Micromass ZMD 4000. CD were recorded with a Jasco J-710 spectropolarimeter (cell path length= 0.01 cm).

5'-O-tert-butylidimethylsilyl-3'-O-octadecanoyl-2'-deoxyguanosine 3:



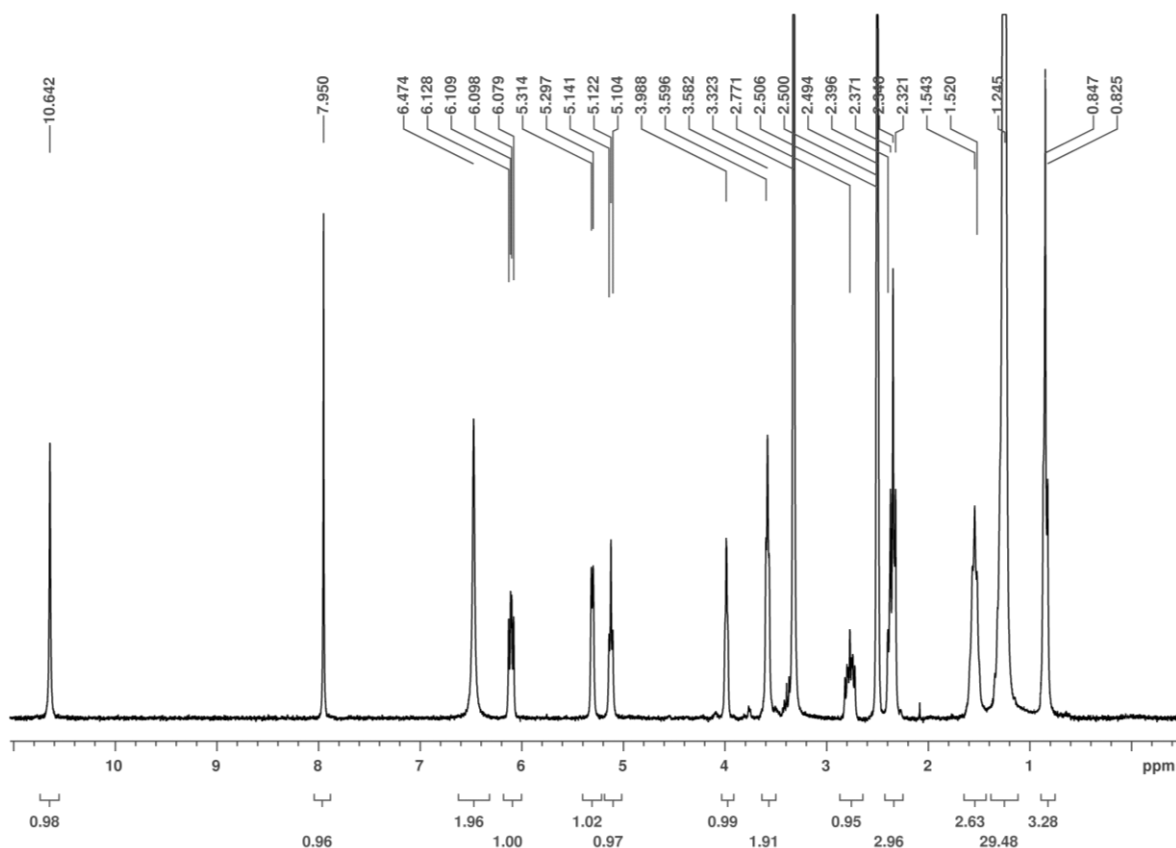
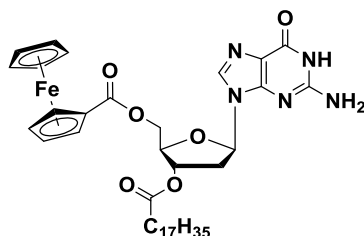
Stearic anhydride (1.14 g, 2.07 mmol) and a catalytic amount of 4-dimethylamino pyridine (DMAP) were added to a flask containing a suspension of 5'-O-tert-butylidimethylsilyl-2'-deoxyguanosine 2¹ (750 mg, 1.97 mmol, dried over P₂O₅ *in vacuo* for 2 h at 60 °C) in 30 mL of an acetonitrile - toluene mixture 1:1 and triethylamine (TEA) (288 μL , 2.07mmol). The reaction was stirred at 80° C under argon for 5 h. The solvents were removed under reduced pressure and the crude material was dissolved in dichloromethane and extracted three times with a saturated solution of NaHCO₃. The organic layer was then dried over MgSO₄. The crude material was purified by column chromatography on silica gel using ether to elute stearic acid, then with dichloromethane/ methanol (95:5) as eluent to afford the desired product as a white solid (750 mg, 1.16 mmol, yield 59%).

ESI-MS (positive mode, MeOH solution, m/z): 648.1 [M+H]⁺, 670.3 [M+Na]⁺

H-NMR (600 MHz DMSO-d₆) of **3****3'-O-octadecanoyl-2'-deoxyguanosine 4**

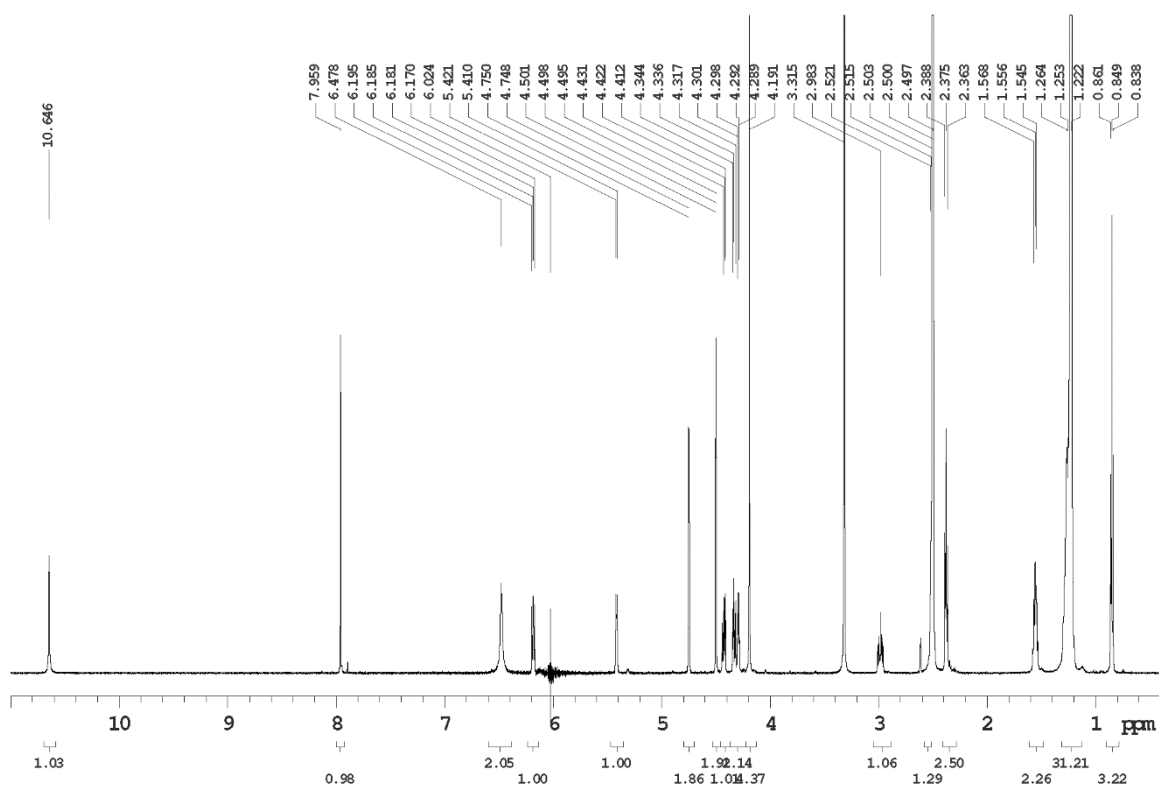
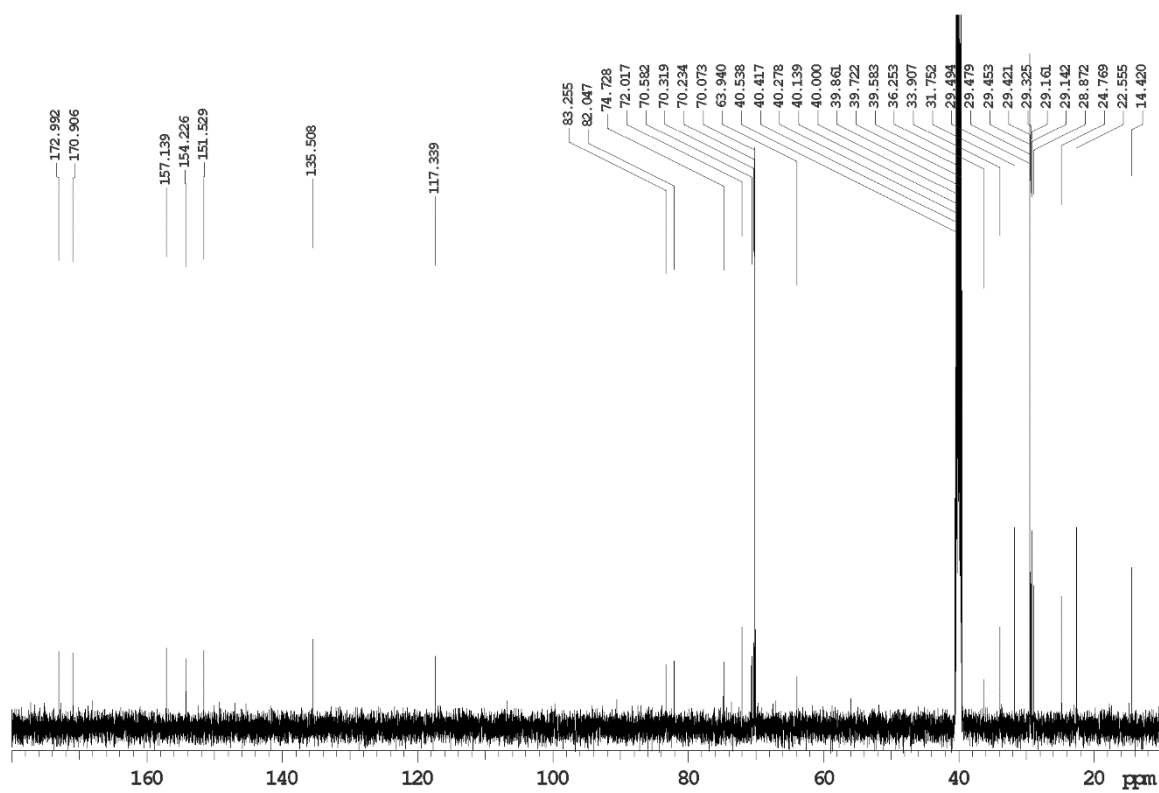
Tetrabutylammonium fluoride trihydrate (TBAF) (547 mg, 1.73 mmol) was added to a solution of 5'-*O*-*tert*-butyldimethylsilyl-3'-*O*-octadecanoyl-deoxyguanosine (750 mg, 1.16 mmol) in THF (20 mL) and the solution was stirred for 4 h at room temperature. The solvent was removed under reduced pressure and the crude material was dissolved in dichloromethane and extracted three times with water. The organic layer was then dried over MgSO₄. The crude material was purified by column chromatography on silica gel using dichloromethane /methanol (96:4) as eluent, affording the product as a white solid (460 mg, 0.85 mmol, yield 74%)

ESI-MS (positive mode, MeOH solution, *m/z*): 534.2 [M+H]⁺, 567.3 [M+Na]⁺

H-NMR (200 MHz DMSO-d₆) of **4****5'-O-ferrocenoyl-3'-O-octadecanoyl-2'-deoxyguanosine G1**

Ferrocene carboxylic acid (238 mg, 1.03 mmol) and 3'-O-decanoyl-2'-deoxyguanosine (460 mg, 0.86 mmol) were dried over P₂O₅ *in vacuo* for 2 h at 60 °C. Ferrocene carboxylic acid was then dissolved in DMF (10 mL), DCC (467 mg, 2.27 mmol) was added and the resulting solution was stirred under argon atmosphere. After 30 min. 3'-O-decanoyl-2'-deoxyguanosine and DMAP (126 mg, 1.03 mmol) were added and the solution was stirred for 4 h. The solvent was removed under reduced pressure, the crude was dissolved in dichloromethane and extracted with a sat. NaHCO₃. The organic layer was dried over MgSO₄. The reaction mixture was applied to a silica gel column packed in dichloromethane and eluted with a gradient of methanol in dichloromethane. The final product was eluted with a mixture of dichloromethane-methanol (96:4) yielding the product as a yellow solid (260 mg, 0.35 mmol, yield 40%).

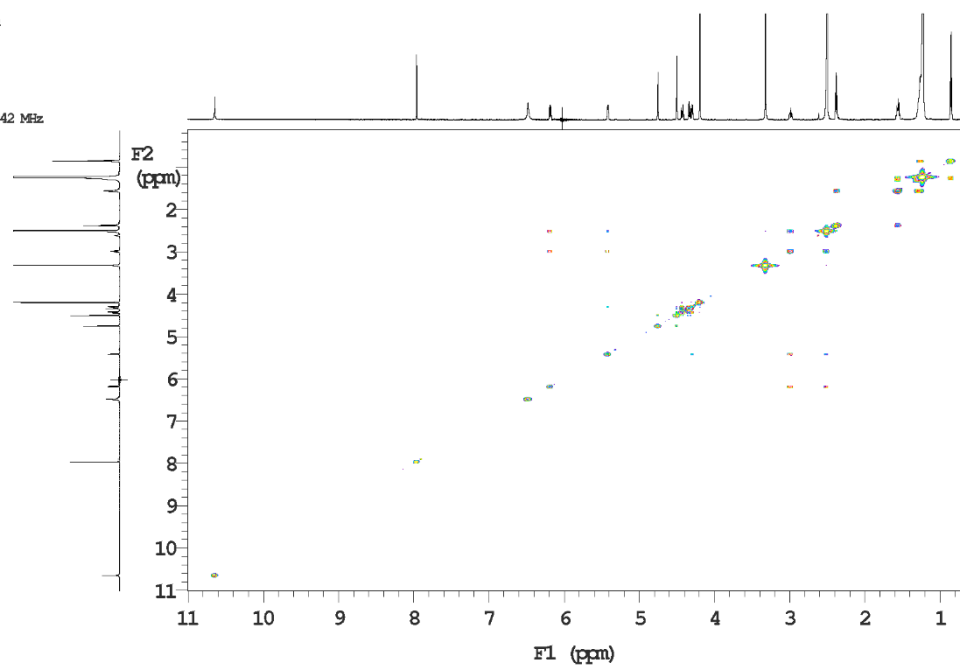
ESI-MS (positive mode, MeOH solution, *m/z*): 744.7 [M+H]⁺, 769.5 [M+Na]⁺

H-NMR (600 MHz DMSO-d₆) of **G1**¹³C-NMR (600 MHz DMSO-d₆) of **G1**

COSY spectrum (600 MHz DMSO-d₆) of G1

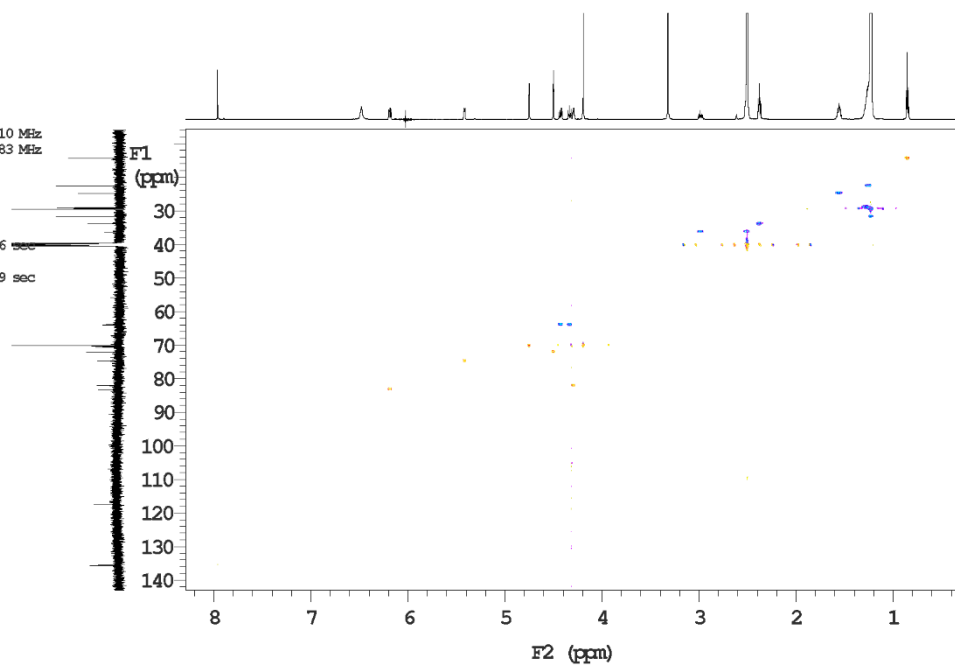
i600 std parameters

File: dg_3C18_5Fc_H_8mg_06ml_gcocy_dms0_170914

Temp. 25.0 C / 298.1 K
Operator: sangiacRelax. delay 1.000 sec
Acq. time 0.213 sec
Width 9611.9 Hz
2D Width 9611.9 Hz
4 repetitions
256 increments
OBSERVE H1, 599.7304242 MHz
DATA PROCESSING
Sine bell 0.107 sec
F1 DATA PROCESSING
Sine bell 0.027 sec
FT size 4096 x 4096
Total time 0 min 0 secHSQC spectrum (600 MHz DMSO-d₆) of G1

i600 std parameters

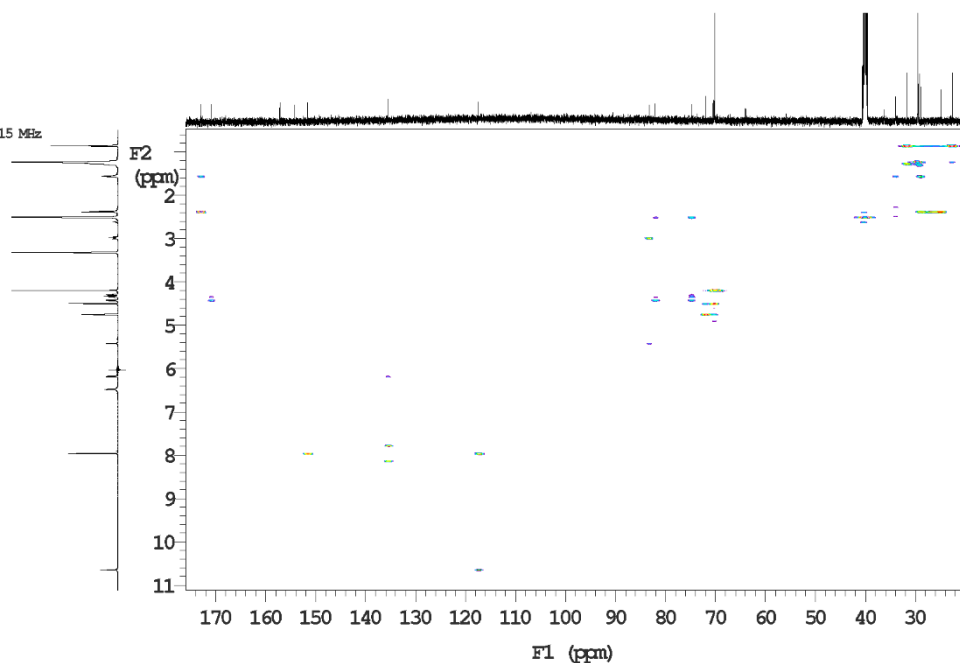
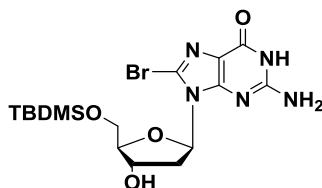
File: dg_3C18_5Fc_H_8mg_06ml_gHSQCAD_dms0_170914

Temp. 25.0 C / 298.1 K
Operator: sangiacRelax. delay 1.000 sec
Mixing 0.500 sec
Acq. time 0.230 sec
Width 9611.9 Hz
2D Width 25632.8 Hz
16 repetitions
2 x 256 increments
OBSERVE H1, 599.7304210 MHz
DECOUPLE C13, 150.8136483 MHz
Power 43 dB
on during acquisition
off during delay
W40 Triple modulated
DATA PROCESSING
Gauss apodization 0.106 sec
F1 DATA PROCESSING
Gauss apodization 0.009 sec
FT size 8192 x 2048
Total time 0 min 0 sec

HMBC spectrum (600 MHz DMSO-d₆) of **G1**

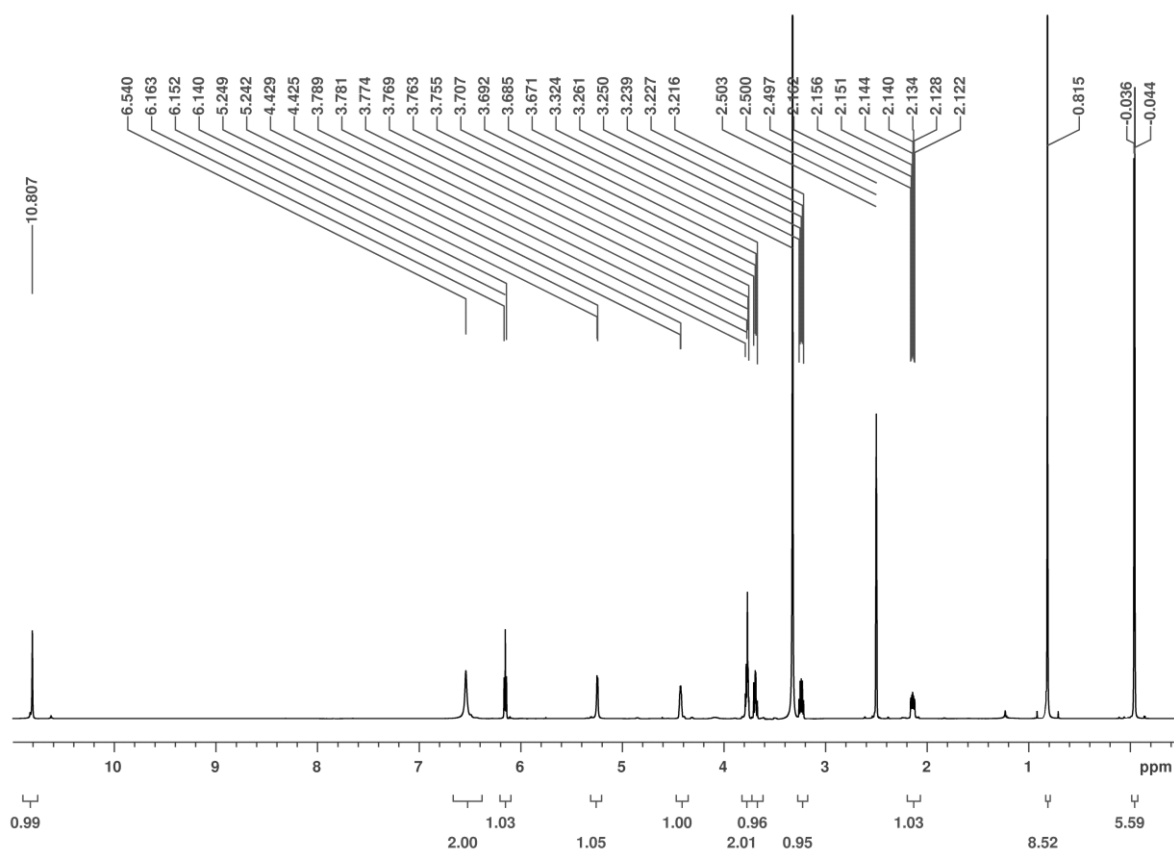
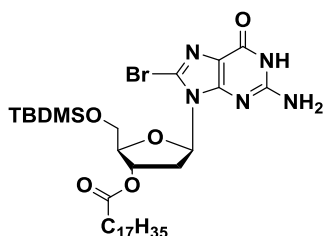
i600 std parameters

File: dg_3C18_5Fc_H_8mg_06mf_gHMBC_dmsc_170914

Temp. 25.0 C / 298.1 K
Operator: sangiacRelax. delay 1.000 sec
Mixing 0.080 sec
Acq. time 0.128 sec
Width 9611.9 Hz
2D Width 36199.1 Hz
32 repetitions
256 increments
OBSERVE HL, 599.7304215 MHz
DATA PROCESSING
Sine bell 0.064 sec
F1 DATA PROCESSING
Sine bell 0.007 sec
F1 size 4096 x 2048
Total time 0 min 0 sec**8-bromo-5'-O-*tert*-butyldimethylsilyl-2'-deoxyguanosine 6**

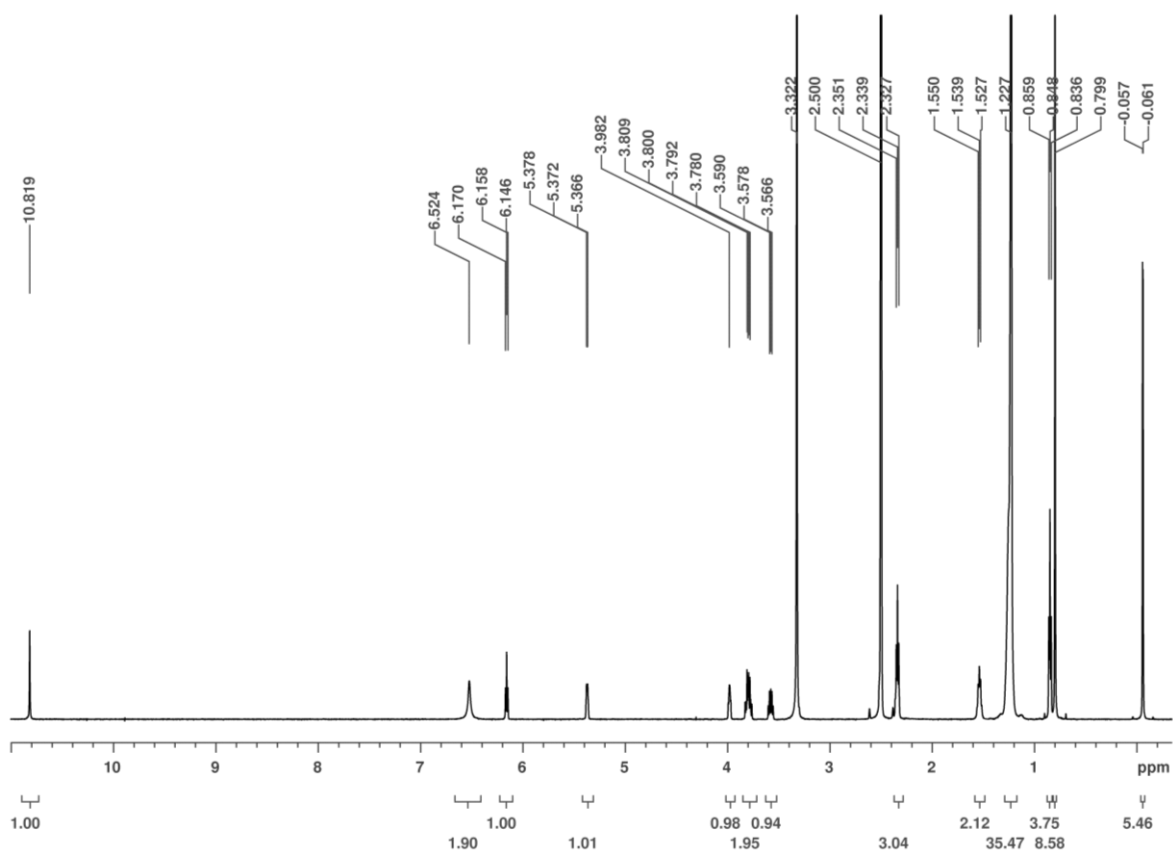
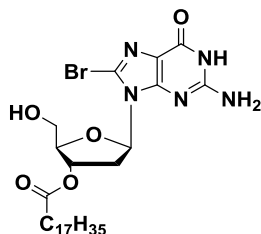
8-Bromo-2'-deoxyguanosine **5**² (740 mg, 2.14 mmol) and imidazole (326 mg, 5.35mmol) were suspended in dry DMF (10 mL) and treated with a solution of *tert*-butyldimethylsilyl chloride (355 mg, 2.35 mmol) in THF (5 mL). The reaction mixture was stirred for 2h at room temperature, concentrated, diluted in water (20 mL) and extracted with DCM (2 x 20 mL). The organic layer was dried over MgSO₄, concentrated and purified by chromatography on silica gel (CH₂Cl₂: MeOH 93:7) to provide 621mg (1.35mmol, 63%) of the title compound as a white powder.

ESI-MS (positive mode, MeOH solution, *m/z*): 461.4 [M+H]⁺, 483.4 [M+Na]⁺

H-NMR (200 MHz DMSO-d₆) of **6****8-bromo-5'-O-tert-butylidimethylsilyl-3'-O-octadecanoyl-2'-deoxyguanosine 7**

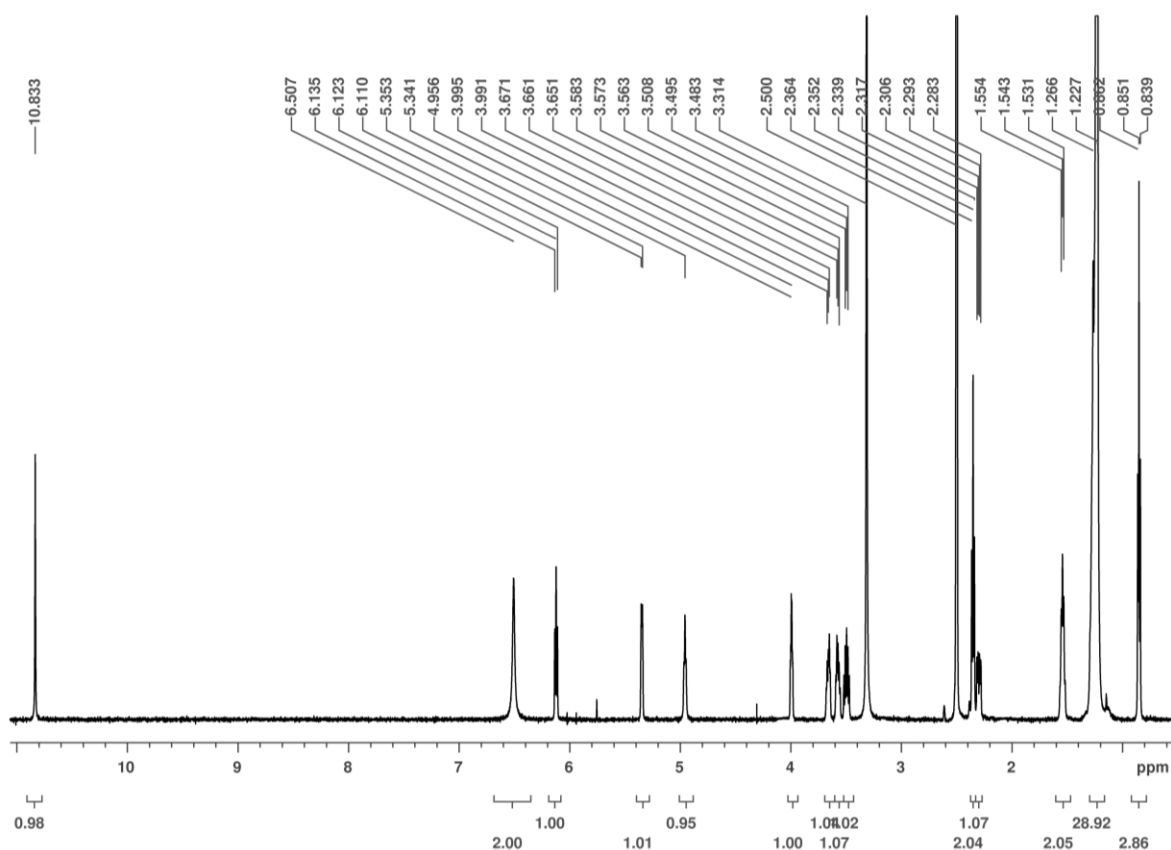
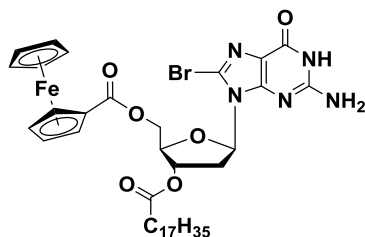
Stearic anhydride (780 mg, 1.42 mmol) and a catalytic amount of DMAP were added to a flask containing a suspension of 8-bromo-5'-O-tert-butylidimethylsilyl-2'-deoxyguanosine (621 mg, 1.35 mmol, dried in P₂O₅ in vacuo for 2 h at 60°C) in 20 mL of an acetonitrile-toluene 1:1 mixture and TEA (206 μL, 1.42 mmol). The reaction was stirred at 80° C under argon for 12 h. The solvents were removed under reduced pressure and the crude material was dissolved in dichloromethane and extracted three times with sat. NaHCO₃. The organic layer was then dried over MgSO₄. The crude material was purified by column chromatography on silica gel using DCM/methanol (95:5) as eluent affording the desired product as a white solid (560 mg, 0.77 mmol, yield 57%).

ESI-MS (positive mode, MeOH solution, m/z): 727.8 [M+H]⁺, 749.8 [M+Na]⁺

H-NMR (200 MHz DMSO-d₆) of **7****8-bromo-3'-*O*-octadecanoyl-2'-deoxyguanosine **8****

Tetrabutylammonium fluoride trihydrate (560 mg, 0,77mmol) was added to a solution of 8-bromo-5'-*O*-*tert*-butyldimethylsilyl-3'-*O*-octadecanoyl-deoxyguanosine (364 mg, 1.15 mmol) in THF (15 mL) and the solution was stirred for 4 h at room temperature. The solvent was removed under reduced pressure and the crude material was dissolved in dichloromethane and extracted three times with water. The organic layer was then dried over MgSO₄. The crude material was purified by column chromatography on silica gel using dichloromethane/methanol (96:4) as eluent, affording product **8** as a white solid (306 mg, 0.5 mmol, yield 65%)

ESI-MS (positive mode, MeOH solution, m/z): 613.6 [M+H]⁺, 635.6 [M+Na]⁺

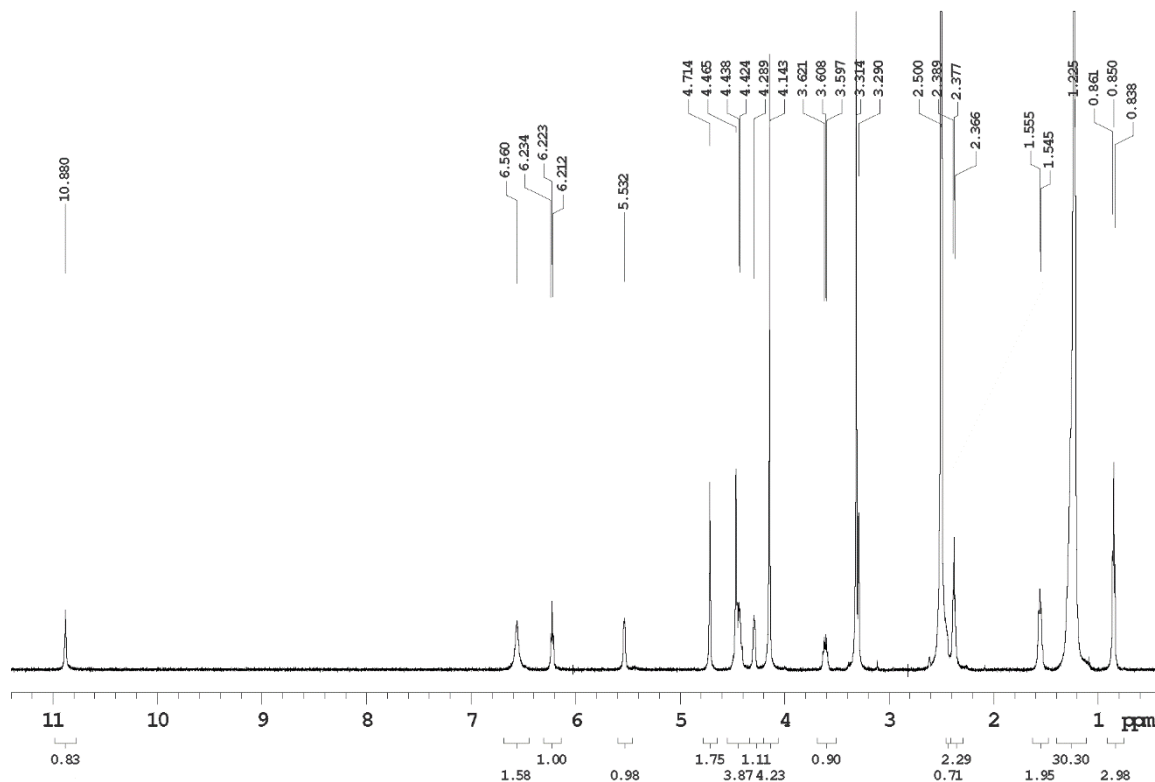
H-NMR (200 MHz DMSO-d₆) of **8****8 bromo-5'-O-ferrocenoyl-3'-O-octadecanoyl-2'-deoxyguanosine G2**

Ferrocene carboxylic acid (138 mg, 0.6 mmol) and 8-bromo-3'-O-decanoyl-2'-deoxyguanosine (306 mg, 0.5 mmol) were dried over P₂O₅ *in vacuo* for 2 h at 60°C. Ferrocene carboxylic acid was dissolved in dry THF (10 mL), Et₃N (79 μL, 0.6 mmol) was added and the resulting solution was cooled at 0° C under argon atmosphere. Methanesulfonyl-chloride (CH₃SO₂Cl 46 μL, 0.6 mmol) was added and the reaction was stirred at the same temperature for two hours. 8-Bromo-3'-O-decanoyl-2'-deoxyguanosine and DMAP (catalytic amount) were then added and the solution was stirred for 12 hours at room temperature. The solvent was removed under reduced pressure, the crude was dissolved in dichloromethane and extracted with sat. NaHCO₃. The organic layer was dried over MgSO₄. The residue was applied to a silica gel column packed in dichloromethane and eluted with a gradient of methanol in dichloromethane. The target product was eluted with a

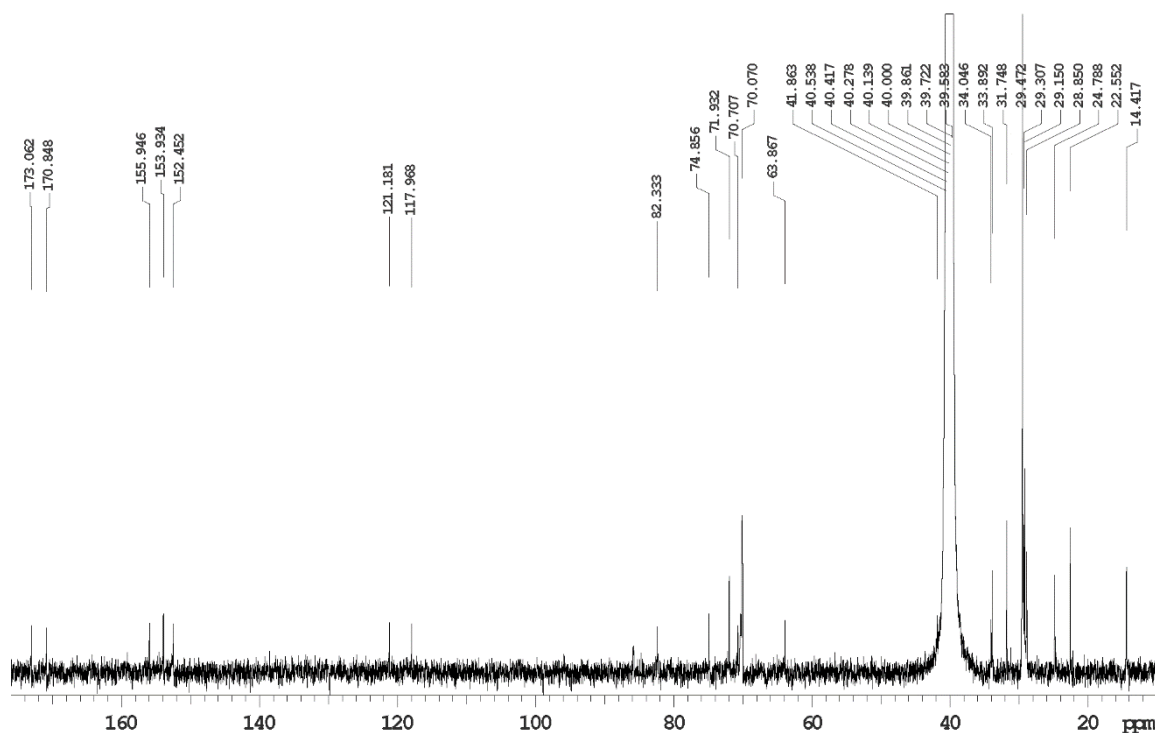
mixture of dichloromethane-methanol (97:3) and crystallized from MeOH, yielding **G2** as a yellow solid (165 mg, 0.20 mmol, yield 40%).

ESI-MS (positive mode, MeOH solution, m/z): 825.6 $[M+H]^+$, 847.6 $[M+Na]^+$

H-NMR (600 MHz DMSO- d_6) of **G2**



^{13}C -NMR (600 MHz DMSO- d_6) of **G2**



COSY-NMR (600 MHz DMSO-d₆) of G2

i600 std parameters

File: dg_8Br_3Cl8_5Fc_gCOSY_dms0_190314

Temp. 25.0 C / 298.1 K

Operator: sangiac

Relax. delay 1.000 sec

Acq. time 0.213 sec

Width 9611.9 Hz

2D Width 9611.9 Hz

8 repetitions

256 increments

OBSERVE H1, 599.7304272 MHz

DATA PROCESSING

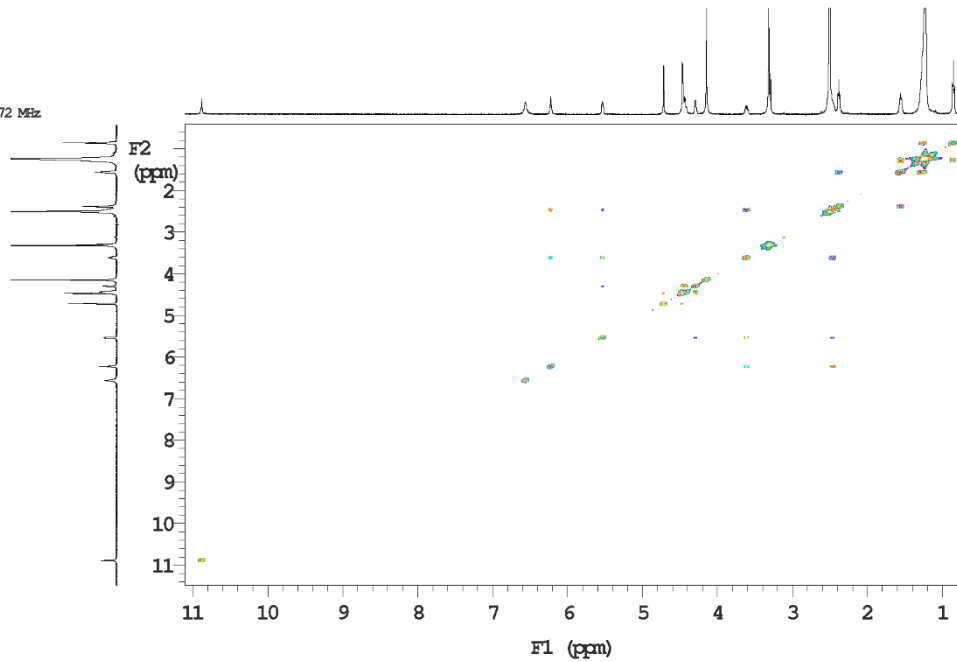
Sine ball 0.107 sec

F1 DATA PROCESSING

Sine ball 0.027 sec

FT size 4096 x 4096

Total time 0 min 0 sec

HSQC-NMR (600 MHz DMSO-d₆) of G2

i600 std parameters

File: dg_8Br_3Cl8_5Fc_gHSQCad_dms0_190314

Temp. 25.0 C / 298.1 K

Operator: sangiac

Relax. delay 1.000 sec

Mixing 0.500 sec

Acq. time 0.230 sec

Width 9611.9 Hz

2D Width 25632.8 Hz

16 repetitions

2 x 256 increments

OBSERVE H1, 599.7304205 MHz

DECOUPLE CL3, 150.8136483 MHz

Power 43 dB

on during acquisition

off during delay

W40 Triple modulated

DATA PROCESSING

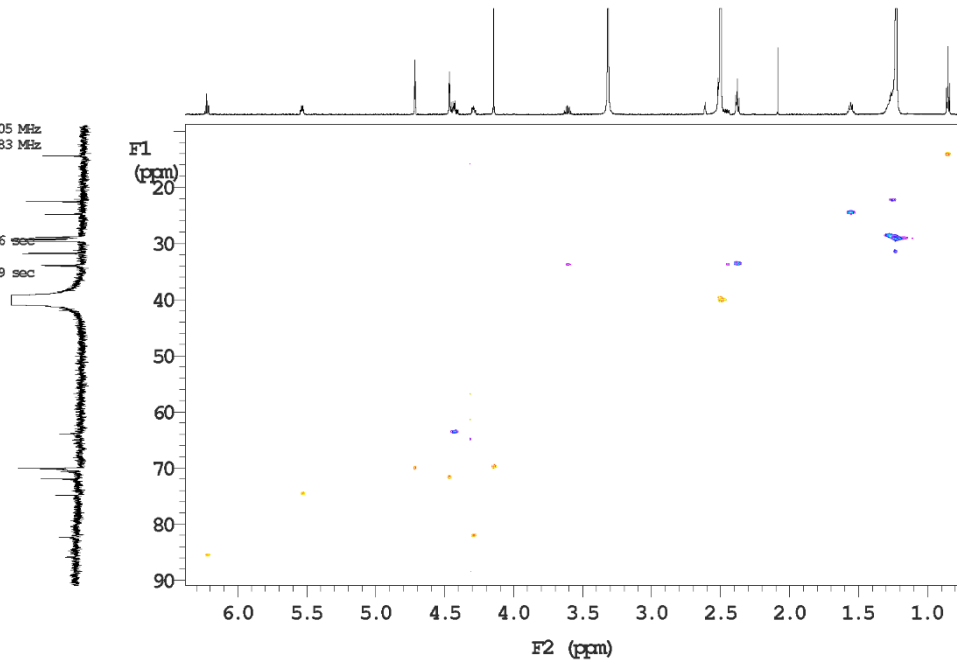
Gauss apodization 0.106 sec

F1 DATA PROCESSING

Gauss apodization 0.009 sec

FT size 8192 x 2048

Total time 0 min 0 sec



HMBC-NMR (600 MHz DMSO-d₆) of **G2**

i600 std parameters

File: d2_8Br_3Cl8_5Fc_gHMBC_dms0_190314

Temp. 25.0 C / 298.1 K
Operator: sangiacRelax. delay 1.000 sec
Mixing 0.080 sec
Acq. time 0.128 sec
Width 9611.9 Hz
2D Width 36199.1 Hz
64 repetitions
256 increments

OBSERVE HL, 599.7304224 MHz

DATA PROCESSING

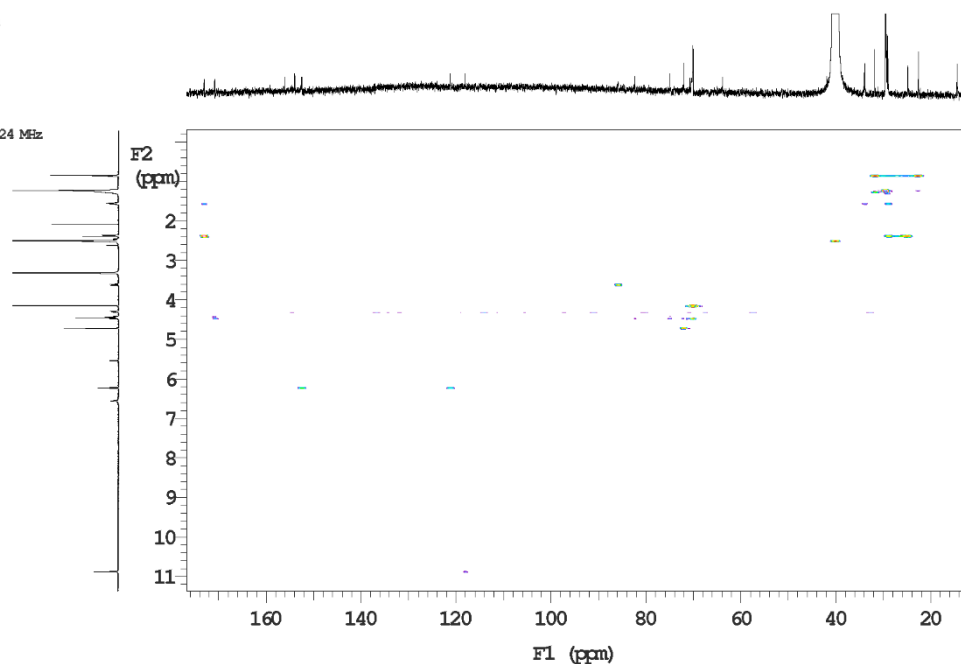
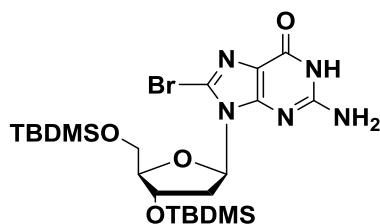
Sine bell 0.064 sec

F1 DATA PROCESSING

Sine bell 0.007 sec

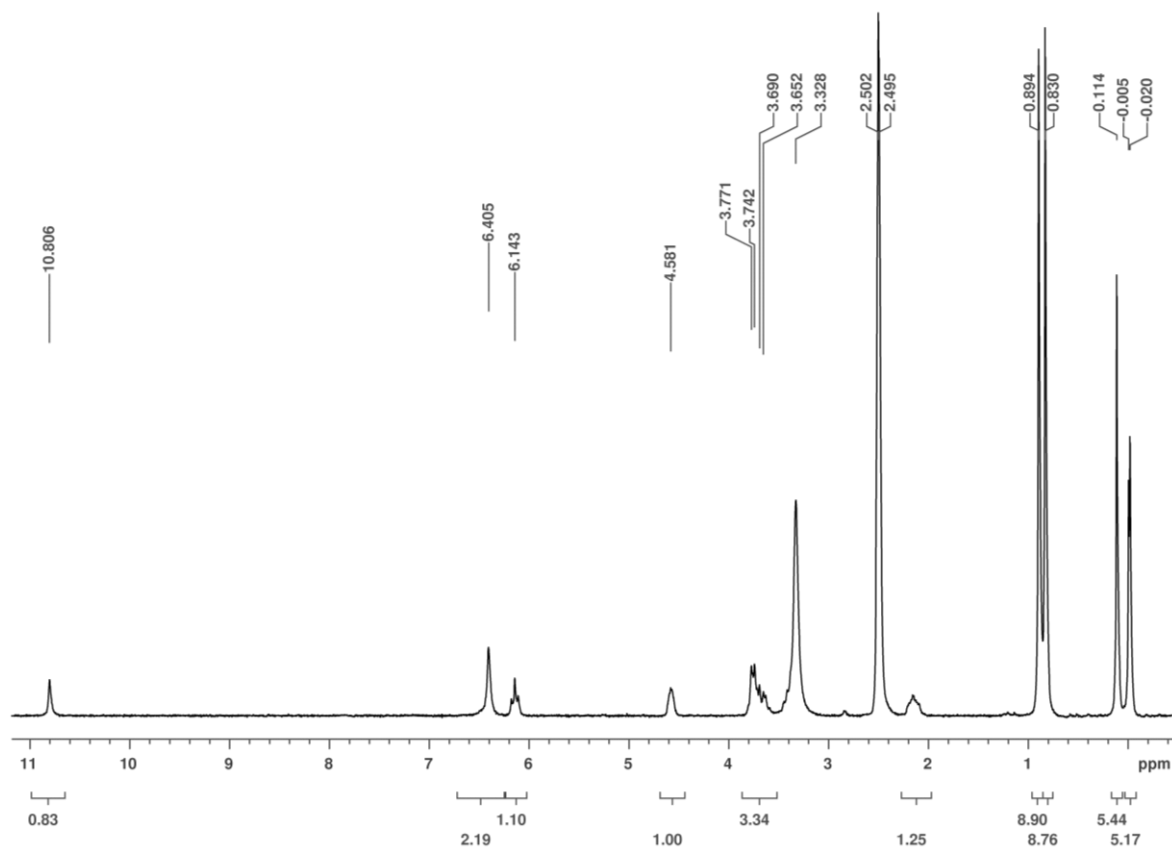
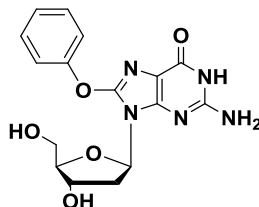
FT size 4096 x 2048

Total time 0 min 0 sec

**8-bromo-3'-5'-O-bis-(tert-butyldimethylsilyl)-2'-deoxyguanosine 9**

8-bromo-2'-deoxyguanosine **5** (266 mg, 0.74 mmol) and imidazole (1.09 g, 16 mmol) were suspended in dry DMF (20 mL). *t*-butyldimethylsilyl chloride (1.45 g, 9.6 mmol) was added and the reaction mixture was stirred for 5h at room temperature, concentrated, diluted in water (20 mL) and extracted with EtOAc (3 x 20 mL). The organic layer was dried over MgSO₄ and concentrated to provide 1.52 g (1.35 mmol, 82%) of the title compound as a white powder.

ESI-MS (positive mode, MeOH solution, *m/z*): 575.9 [M+H]⁺, 597.9 [M+Na]⁺

H-NMR (200 MHz DMSO-d₆) of **9****8-Phenoxy-2'-deoxyguanosine 10**

To a suspension of Cs₂CO₃ (4.32 g, 13.2 mmol) in dry xylene was added phenol (1.24 g 13.2 mmol) and the mixture was heated at 130° C for 1 h. 8-Bromo-3'-5'-*O*-bis-(*tert*-butyldimethylsilyl)-2'-deoxyguanosine (1.52 g, 2.65 mmol) was then added and the reaction mixture was stirred at the same temperature for 12 h. The solvent was removed under reduced pressure, the crude was dissolved in ethyl acetate and extracted with a sat. NaHCO₃. The organic layer was dried over MgSO₄. The residue was applied to a silica gel column and eluted with dichloromethane/methanol (98:2). 8-Phenoxy-3'-5'-*O*-bis-(*tert*-butyldimethylsilyl)-2'-deoxyguanosine was isolated as a white solid (500 mg, 0.85 mmol, 32 %).

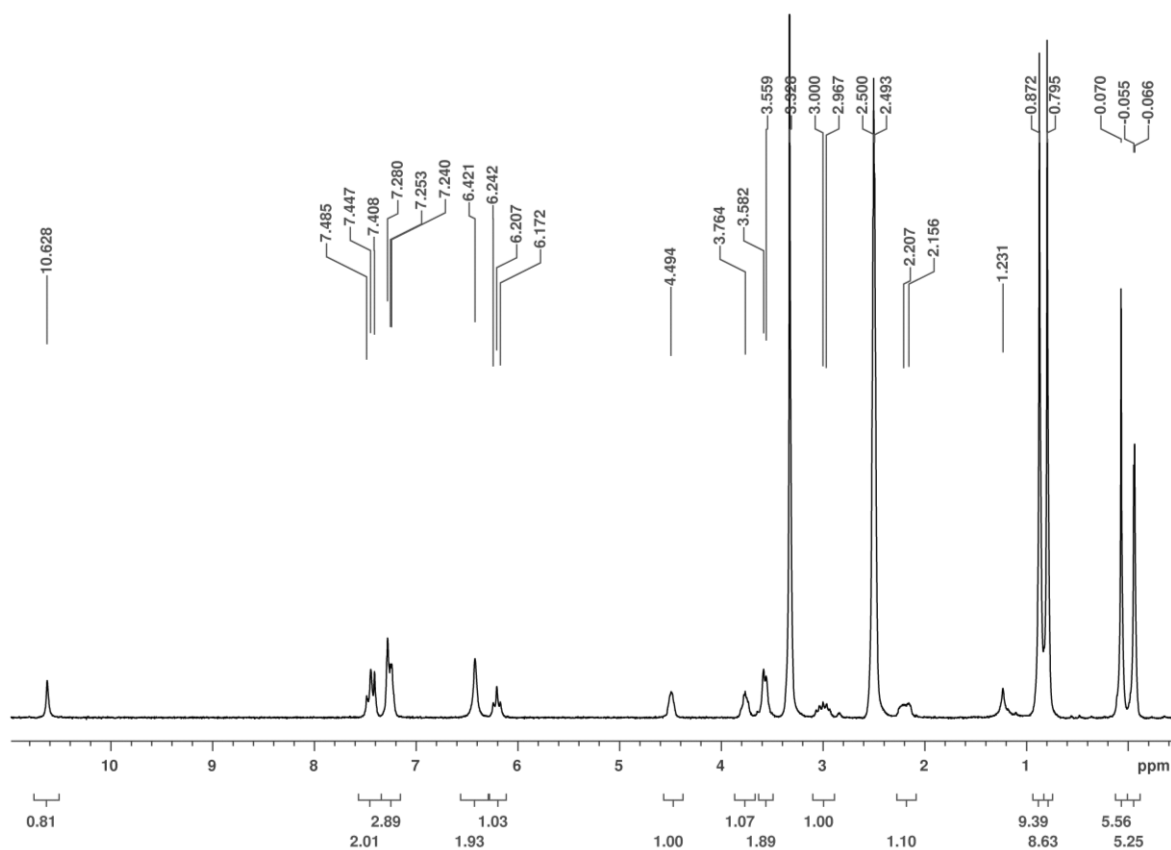
ESI-MS (positive mode, MeOH solution, *m/z*): 588.1 [M+H]⁺, 610.1 [M+Na]⁺

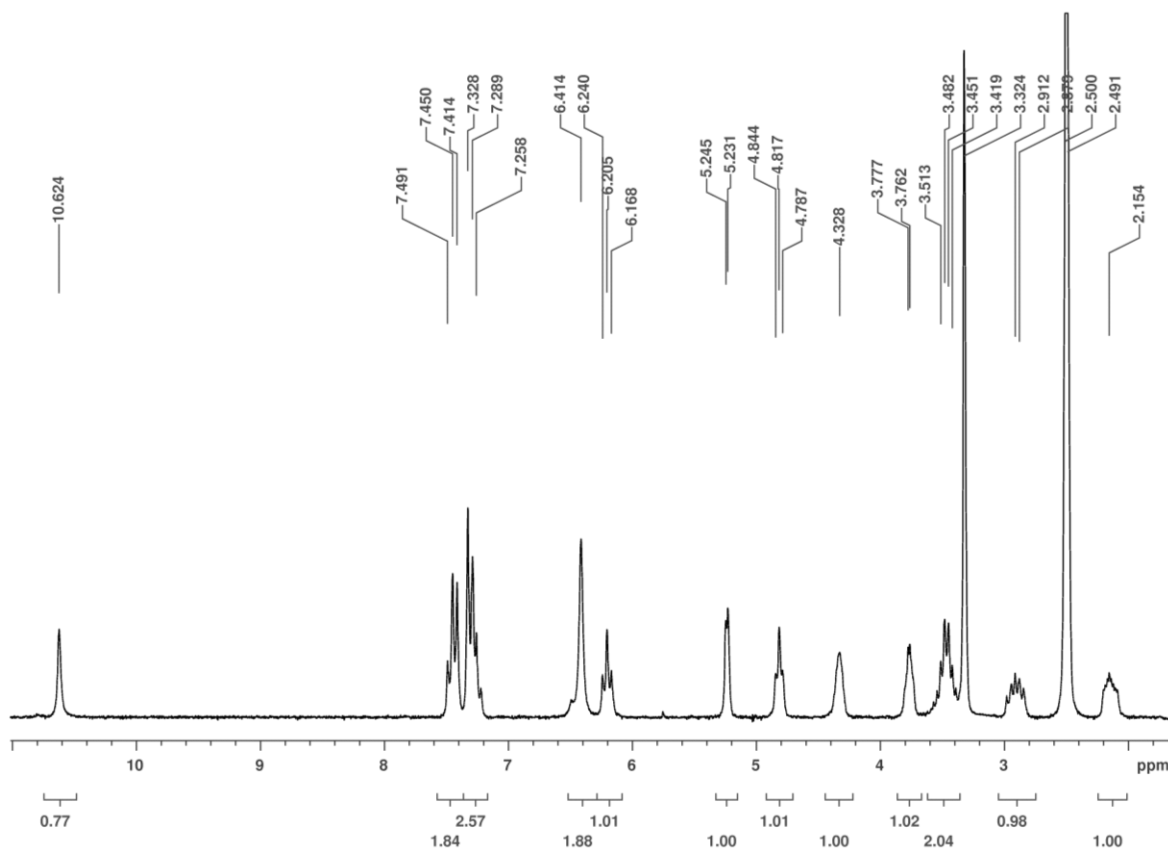
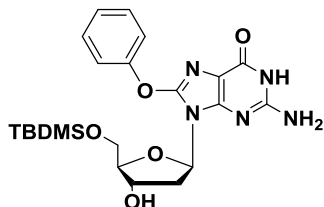
Tetrabutylammonium fluoride trihydrate (804 mg, 2.55 mmol) was added to a solution of 8-phenoxy-3'-5'-*O*-bis-(*tert*-butyldimethylsilyl)-2'-deoxyguanosine (500 mg, 0.85 mmol) in THF (15 mL) and the solution was stirred for 4 h at room temperature. The solvent was removed under

reduced pressure and the crude material was dissolved in dichloromethane and extracted three times with water. The organic layer was then dried over MgSO_4 . The crude material was purified by column chromatography on silica gel using dichloromethane /methanol (85:15) as eluent, affording 8-phenoxy-2'-deoxyguanosine **10** as a white solid (290 mg, 0.81 mmol, yield 95 %).

ESI-MS (positive mode, MeOH solution, m/z): 359.9 $[\text{M}+\text{H}]^+$

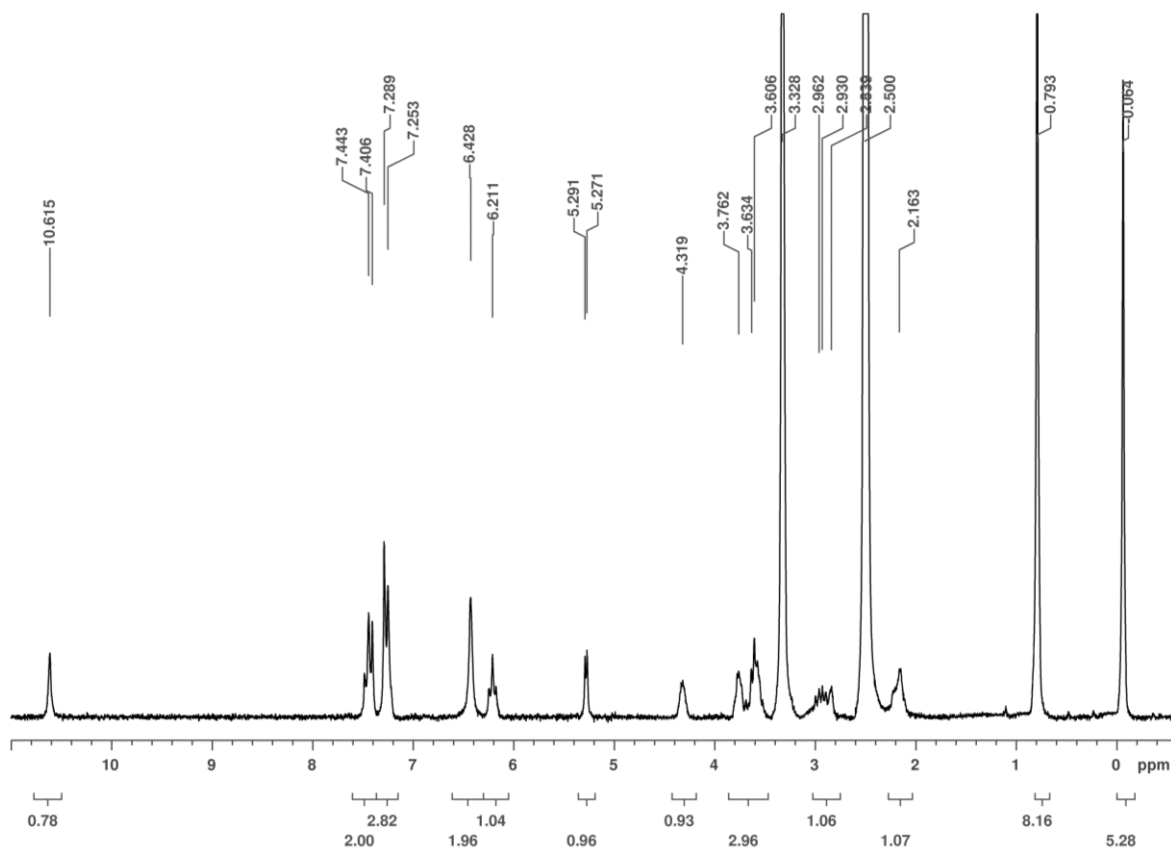
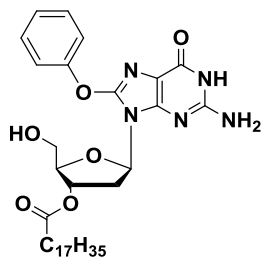
$^1\text{H-NMR}$ (200 MHz DMSO-d_6) of **10 a**



H-NMR (200 MHz DMSO-d₆) of **10****8-phenoxy-5'-O-(*tert*-butyldimethylsilyl)-2'-deoxyguanosine 11**

8-phenoxy-2'-deoxyguanosine (266 mg, 0.74 mmol) and imidazole (126 mg, 1.85 mmol) were suspended in dry DMF (10 mL) and treated with a solution of *tert*-butyldimethylsilyl chloride (112 mg 0.74 mmol) in THF (2 mL). The reaction mixture was stirred for 2 h at room temperature, concentrated, dissolved in DCM (2 x 20 mL) and extracted with sat. NaHCO₃. The organic layer was dried over MgSO₄, concentrated and purified by chromatography on silica gel (CH₂Cl₂:MeOH 9:1) to provide 320 mg (0.68 mmol, 92 %) of the title compound as a white powder.

ESI-MS (positive mode, MeOH solution, m/z): 474.1 [M+H]⁺

H-NMR (200 MHz DMSO-d₆) of **11****8-phenoxy-3'-O-octadecanoyl-2'-deoxyguanosine 12**

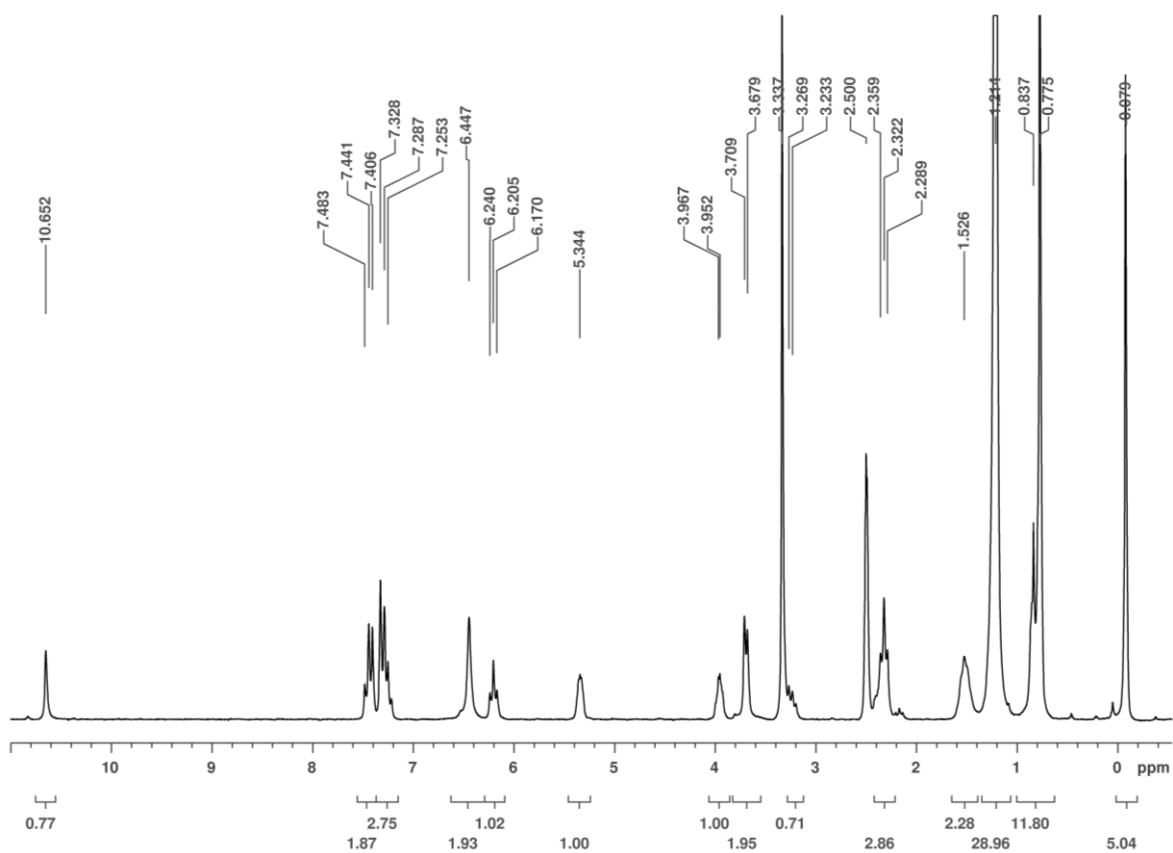
Stearic anhydride (391 mg, 0.71 mmol) and a catalytic amount of DMAP were added to a flask containing a suspension of 8-phenoxy-5'-O-(*tert*-butyldimethylsilyl)-2'-deoxyguanosine (320 mg, 0.68 mmol, dried over P₂O₅ *in vacuo* for 2 h at 60°C) in 20 mL of a 1:1 mixture of acetonitrile and toluene. TEA (102 μL, 0.71 mmol) was added and the reaction mixture was stirred at 80° C under argon for 4 h. Solvents were removed under reduced pressure and the crude material was dissolved in dichloromethane and extracted three times with sat. NaHCO₃. The organic layer was then dried over MgSO₄. The crude material was purified by column chromatography on silica gel using dichloromethane/methanol (97:3) as eluent, affording 8-phenoxy-5'-O-(*tert*-butyldimethylsilyl)-3'-O-octadecanoyl-2'-deoxyguanosine as a white solid (240 mg, 0.33 mmol, yield 48%).

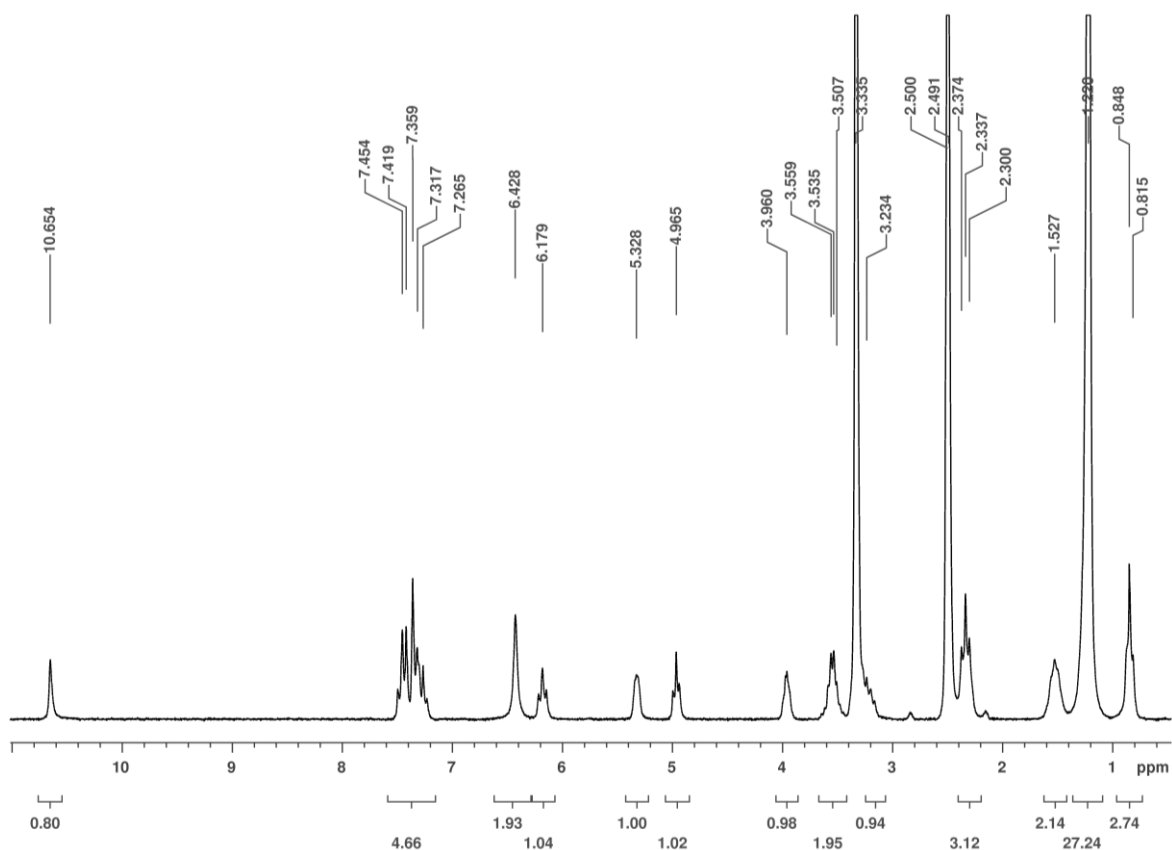
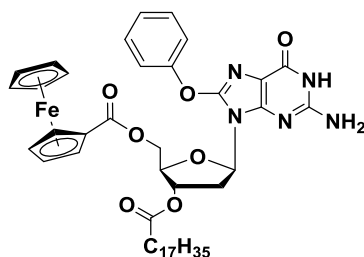
ESI-MS (positive mode, MeOH solution, *m/z*): 740.4 [M+H]⁺

Tetrabutylammonium fluoride trihydrate (170 mg, 0,54 mmol) was added to a solution of 8-phenoxy-5'-*O*-(*tert*-butyldimethylsilyl)-3'-*O*-octadecanoyl-2'-deoxyguanosine (200 mg, 0.27 mmol) in THF (5 mL) and the solution was stirred for 3 h at room temperature. The solvent was removed under reduced pressure and the crude material was dissolved in dichloromethane and extracted three times with water. The organic layer was then dried over MgSO₄. The crude material was purified by column chromatography on silica gel using dichloromethane/methanol (96:4) as eluent, affording 8-phenoxy-3'-*O*-octadecanoyl-2'-deoxyguanosine **12** as a white solid (100 mg, 0.16 mmol, yield 30 %)

ESI-MS (positive mode, MeOH solution, m/z): 626.4 [M+H]⁺, 648.3 [M+Na]⁺

H-NMR (200 MHz DMSO-d₆) of **12a**



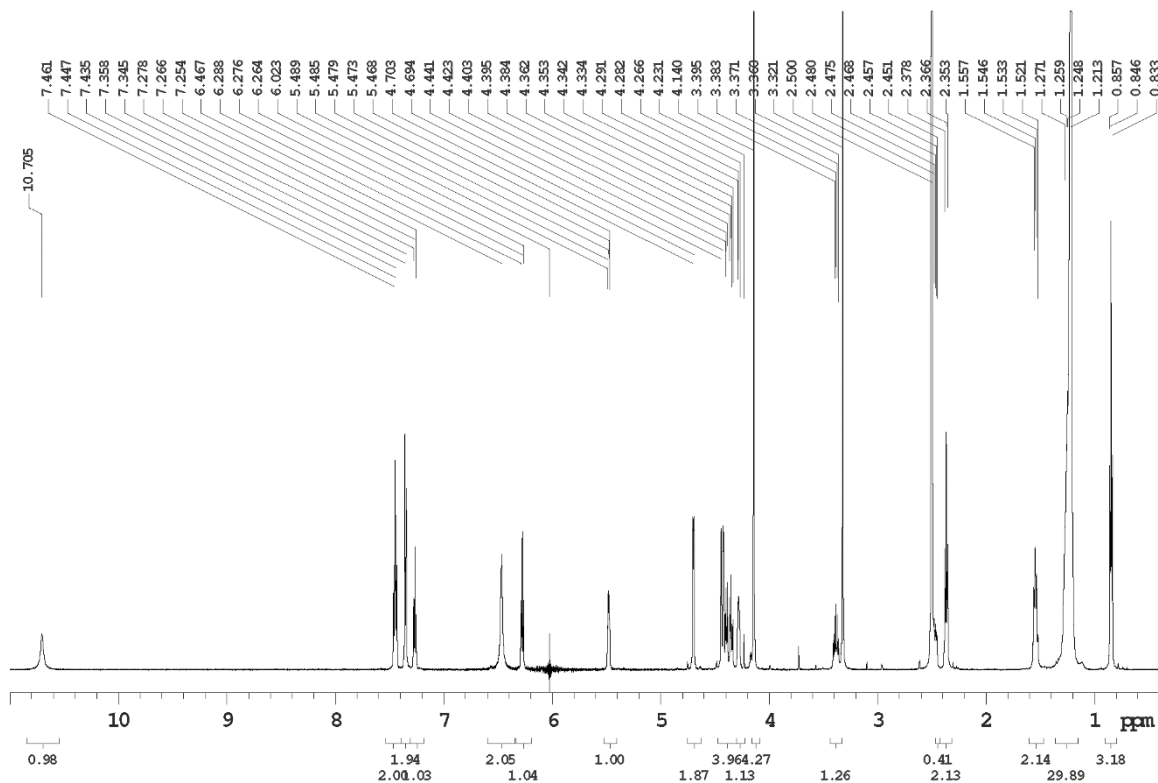
H-NMR (200 MHz DMSO-d₆) of **12****8-phenoxy-5'-O-ferrocenoyl-3'-O-octadecanoyl-2'-deoxyguanosine G3**

Ferrocene carboxylic acid (55.2 mg, 0.24 mmol) and 8-phenoxy-3'-O-decanoyl-2'-deoxyguanosine (100 mg, 0.16 mmol) were dried over P₂O₅ in vacuo for 2 h at 60°C. Ferrocene carboxylic acid was dissolved in dry THF (5 mL), Et₃N (108 μL, 0.24 mmol) was added and the resulting solution was cooled at 0°C. (18 μl, 0.24 mmol) was added and stirring was continued at the same temperature for 2 h. 8-Phenoxy-3'-O-decanoyl-2'-deoxyguanosine and DMAP (catalytic amount) were then added and the mixture was allowed to reach room temp. After 12 hours, the solvent was removed under reduced pressure, the residue was dissolved in dichloromethane and extracted with sat. NaHCO₃. The organic layer was dried over MgSO₄ and the crude reaction mixture was applied to a silica gel column packed in dichloromethane and eluted with a gradient of methanol in dichloromethane. The final product was eluted with a mixture of dichloromethane-methanol (98:2)

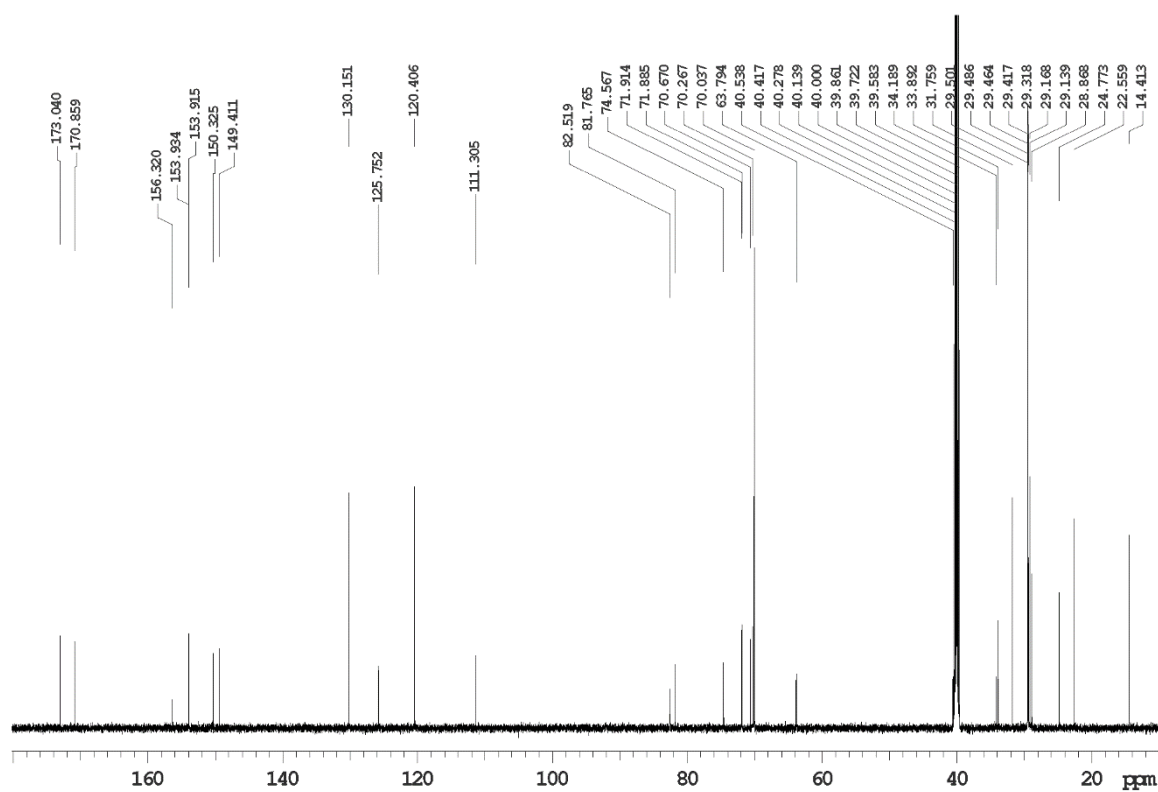
and crystallized in MeOH, affording the title product as a yellow solid (80 mg, 0.095 mmol, yield 60%).

ESI-MS (positive mode, MeOH solution, m/z): 838.3 [M+H]⁺, 860.3 [M+Na]⁺

H-NMR (600 MHz DMSO-d₆) of **G3**



C¹³-NMR (600 MHz DMSO-d₆) of **G3**



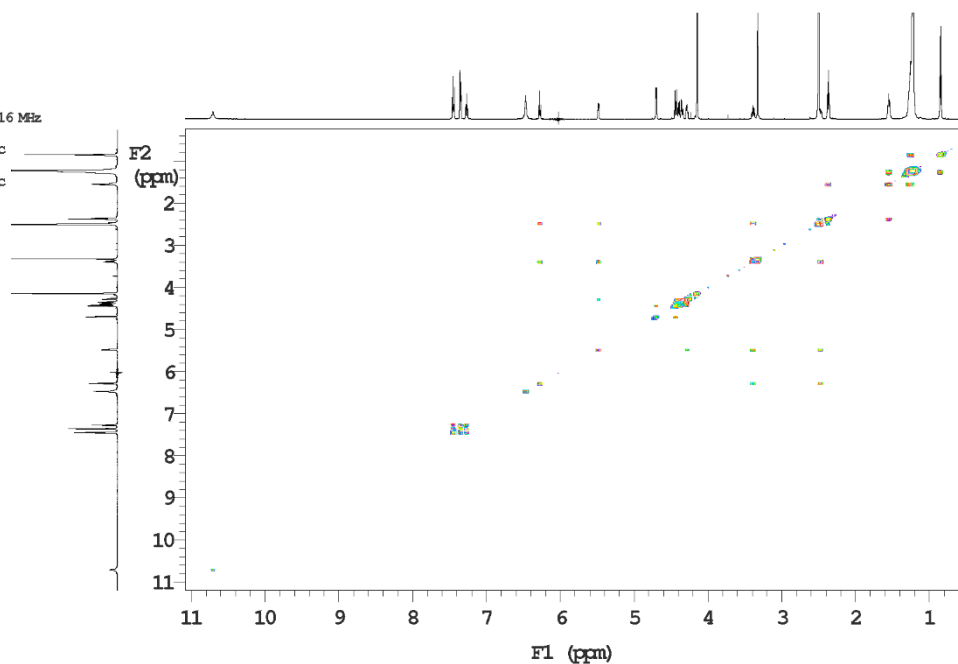
COSY-NMR (600 MHz DMSO-d₆) of G3

i600 std parameters

File: 8pho_dg_3c18_5fc_gcosy_dms0_030914

Temp. 25.0 C / 298.1 K
Operator: sangiac

Relax. delay 1.000 sec
 Acq. time 0.213 sec
 Width 9611.9 Hz
 2D Width 9611.9 Hz
 4 repetitions
 256 increments
 OBSERVE H1, 599.7304216 MHz
 DATA PROCESSING
 Sq. sine bell 0.107 sec
 F1 DATA PROCESSING
 Sq. sine bell 0.013 sec
 FT size 4096 x 4096
 Total time 0 min 0 sec

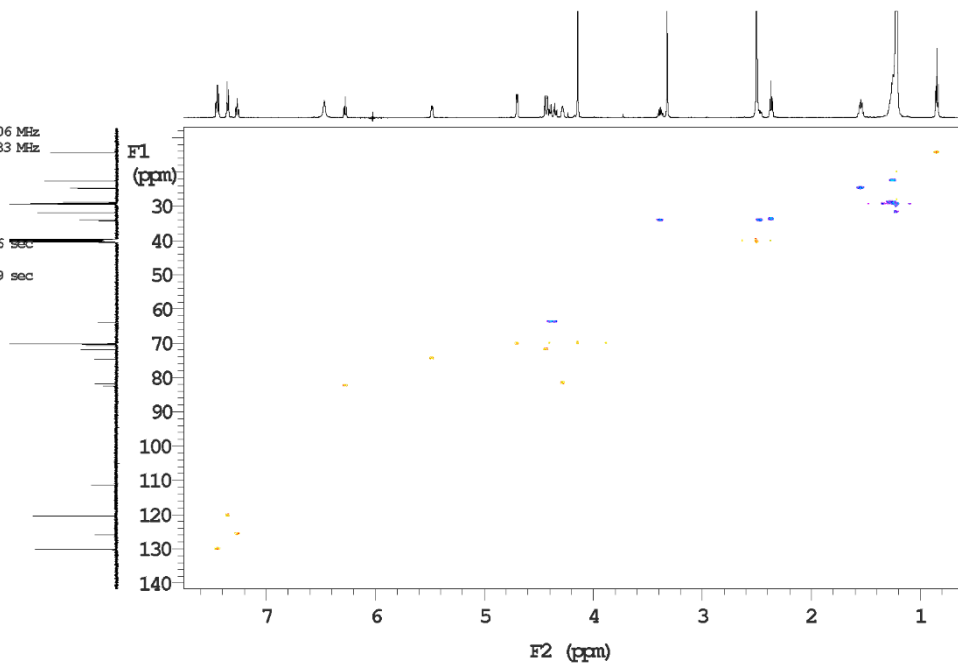
HSQC -NMR (600 MHz DMSO-d₆) of G3

i600 std parameters

File: 8pho_dg_3c18_5fc_ghsqcad_dms0_030914

Temp. 25.0 C / 298.1 K
Operator: sangiac

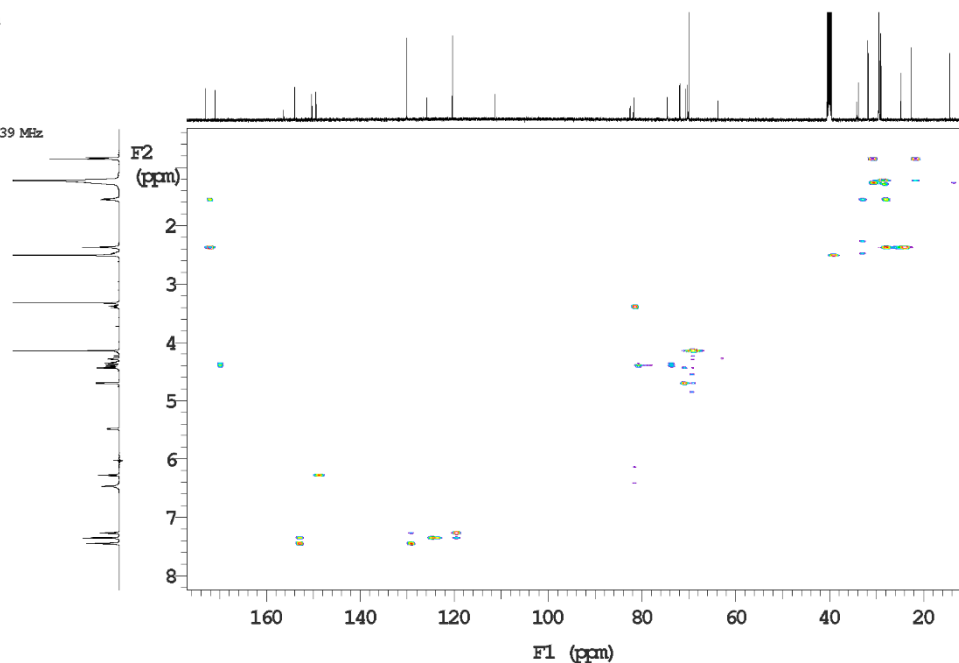
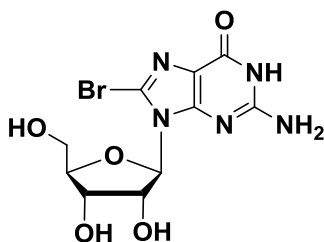
Relax. delay 1.000 sec
 Mixing 0.500 sec
 Acq. time 0.230 sec
 Width 9611.9 Hz
 2D Width 25632.8 Hz
 16 repetitions
 2 x 256 increments
 OBSERVE H1, 599.7304206 MHz
 DECOUPLE C13, 150.8136483 MHz
 Power 43 dB
 on during acquisition
 off during delay
 W40 Triple modulated
 DATA PROCESSING
 Gauss apodization 0.106 sec
 F1 DATA PROCESSING
 Gauss apodization 0.009 sec
 FT size 8192 x 2048
 Total time 0 min 0 sec



HMBC -NMR (600 MHz DMSO-d₆) of **G3**

i600 std parameters

File: 8Pho_d3_3Cl8_5Fc_gHMBC_dms0_030914

Temp. 25.0 C / 298.1 K
Operator: sangiacRelax. delay 1.000 sec
Mixing 0.080 sec
Acq. time 0.128 sec
Width 9611.9 Hz
2D Width 36199.1 Hz
32 repetitions
256 increments
OBSERVE H1, 599.7304239 MHz
DATA PROCESSING
Sine bell 0.064 sec
F1 DATA PROCESSING
Sine bell 0.007 sec
FT size 4096 x 2048
Total time 0 min 0 sec**8-Bromo guanosine 14**

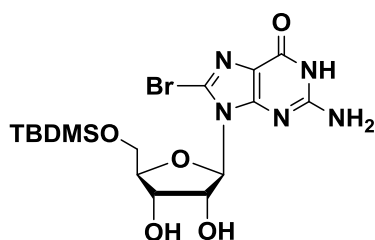
Guanosine (1.00 g, 3.53 mmol) was suspended in 60 mL of an acetonitrile/water 2:1 mixture and N-Bromosuccinimide (943 mg, 5.3 mmol, 1.5 eq) was added in three portions over 20 min. Stirring was continued until TLC (CH₂Cl₂/MeOH 8:2) revealed the disappearance of the starting material (2 h). Solvents were then removed in vacuo and the pale yellow solid thus obtained was suspended in acetone (20 mL) and stirred at r.t. for 2 h. The flask was then placed in refrigerator and left overnight at -20°C. The precipitate was filtered and washed several times with cold acetone, to afford 1.09 g, 3.02 mmol (yield 86%) of the title compound as a white solid.

ESI-MS: m/z 359.8/361.8 [M-H]⁻; 361.8/363.8 [M+H]⁺.

HR-MS: calcd. for C₁₀H₁₂BrN₅O₅, m/z 361.0022; found, m/z 361.0020.

¹H-NMR δ (dms0-d₆): 3.54 (m, 1H, H5'), 3.63 (m, 1H, H5'), 3.85 (m, 1H, H4'), 4.13 (m, 1H, H3'), 4.92 (m, 1H, OH5'), 5.01 (m, 1H, H2'), 5.08 (d, $J=5.1$, 1H, OH3'), 5.44 (d, $J=6.0$, 1H, OH2'), 5.68 (d, $J=6.0$, 1H, H1'), 6.50 (bs, 2H, NH₂), 10.81 (bs, 1H, NH) ppm.

¹³C-NMR δ (dms0-d₆): 62.46, 70.75, 70.94, 86.31, 90.14, 117.98, 121.54, 152.52, 153.90, 155.87

8-Bromo-5'-O-*tert*-butyldimethylsilyl guanosine 15

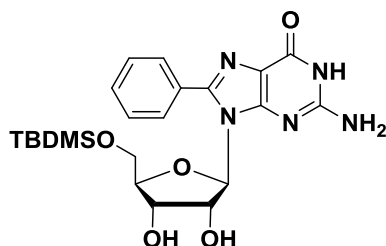
8-Bromoguanosine (1.274 g, 3.52 mmol) was dried at 50°C over P₂O₅ in vacuo for 2h and dissolved in DMF (17 mL). Imidazole (491 mg, 7.21 mmol, 2.05 eq) was then added. To the resulting mixture was added dropwise a solution of *t*-butyldimethylsilyl chloride (558 mg, 3.70 mmol, 1.05 eq.) in THF (9 mL) and stirring was continued for 2 h. As TLC (CH₂Cl₂/MeOH 8:2) revealed the presence of unreacted starting material, an extra amount of imidazole (120 mg, 1.76 mmol, 0.5 eq.) and *t*-butyldimethylsilyl chloride (266 mg, 1.76 mmol, 0.5 eq.) was added and reaction was continued for 2 h. The crude mixture was poured into water (50 mL) and the precipitate was filtered, washed with water and Et₂O and dried, to afford the product (1.04 g, 2.19 mmol, 62%) as a white solid.

RF = 0.6 (CH₂Cl₂/MeOH 8:2)

ESI-MS: *m/z* 473.9/475.9 [M-H]⁻; 475.9/477.9 [M+H]⁺.

HR-MS: calcd. for C₁₆H₂₆BrN₅O₅Si, *m/z* 475.0887; found, *m/z* 475.0889.

¹H-NMR δ(CD₃OD): -0.03 and 0.01 (s,s, 6H, SiMe₂), 0.84 (s, 9H, tBuSi), 3.83 (dd, *J*=11.4, *J*=5.7, 1H, H5'), 3.92 (dd, *J*=11.4, *J*=4.0, 1H, H5'), 3.95 (m, *J*=11.4, *J*=5.7, *J*=4.0, 1H, H4'), 4.56 (m, *J*=5.7, 1H, H3'), 5.26 (dd, *J*=5.7, *J*=4.2, 1H, H2'), 5.85 (d, *J*=4.2, 1H, H1') ppm.

8-Phenyl-5'-O-*tert*-butyldimethylsilyl guanosine 16

PdCl₂(PPh₃)₂ (59.0 mg, 0.084 mmol, 0.2 eq.) was added to a degassed solution of 8-bromo-5'-O-*tert*-butyldimethylsilylguanosine (200 mg, 0.421 mmol), phenylboronic acid (77 mg, 0.630 mmol, 1.5 eq.) and K₃PO₄ (223 mg, 1.05 mmol) in 7 mL of a 6:1 mixture of dioxane/water. The mixture was heated at 95°C for 22 h. After cooling to r.t., solvents were removed by distillation, the dark residue was suspended in 50 mL of Et₂O and filtered. The filtrate was washed with brine (40 mL) and 1N HCl (6 mL) and then dried over MgSO₄. The precipitate was washed with a CH₂Cl₂/MeOH 4:1 mixture, washings were combined with the ethereal residue and solvents were removed in vacuo.

The residue was purified by column chromatography on silica gel (CH₂Cl₂/MeOH 95:5) and the product was obtained in a 61% yield (121 mg, 0.256 mmol).

RF = 0.2 (CH₂Cl₂/MeOH 9:1)

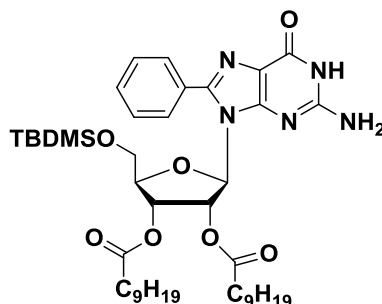
ESI-MS: *m/z*: 472.0 [M-H]⁻; 474.0 [M+H]⁺; 497.2 [M+Na]⁺.

HR-MS: calcd. for C₂₂H₃₁N₅O₅Si, *m/z* 473.2094; found, *m/z* 473.2092.

¹H-NMR δ (dms_o-d₆): 0.003 and 0.006 (s,s, 6H, SiMe₂), 0.841 (s, 9H, tBuSi), 3.74-3.84 (m, 3H, H4',H5'), 4.13 (m, 1H), 4.94 (d, *J*=6.0, 1H, OH), 5.07 (m, 1H), 5.36 (d, *J*=6.0, 1H, OH), 5.60 (d, *J*=5.5, 1H, H1'), 6.43 (bs, 2H, NH₂), 7.52-7.54 (m, 3H, ArH), 7.64-7.67 (m, 2H, ArH), 10.73 (bs, 1H, NH) ppm.

¹³C-NMR δ (dms_o-d₆): -4.81 (CH₃), -4.76 (CH₃), 18.49 (C), 26.27 (CH₃), 64.10 (C5'), 70.51 (C2'), 70.66 (C3'), 85.34 (C4'), 89.73 (C1'), 117.44 (C), 129.06 (CH, Ph), 129.51 (CH, Ph), 129.87 (CH, Ph), 130.66 (C), 147.80 (C), 152.74 (C), 153.54 (C), 157.13 (C) .

8-Phenyl-5'-O-tert-butyltrimethylsilyl-2',3'-O-didecanoyl guanosine 17



8-Phenyl-5'-O-tert-butyltrimethylsilyl guanosine (100 mg, 0.211 mmol) was dried in vacuo over P₂O₅ at 50°C for 1 h and dissolved in 15 mL of an acetonitrile/toluene 2:1 mixture. Decanoic anhydride (163 μL, 0.444 mmol, 2.10 eq.), Et₃N (64 μL, 0.444 mmol, 2.10 eq.) and a small amount of DMAP were then added and the mixture was heated at 80°C for 7 h. After cooling to r.t. MeOH (0.5 mL) was added and stirring was continued for 20 min. Solvents were removed by distillation, the residue was dissolved in CH₂Cl₂, washed with 5% NaHCO₃ and brine and dried over MgSO₄. After removal of solvents, the residue was purified by chromatography on silica gel (CH₂Cl₂/MeOH 99:1) and the product (120 mg, 0.153 mmol) was obtained as a white solid in a 72% yield.

RF = 0.36 (CH₂Cl₂/MeOH 97:3)

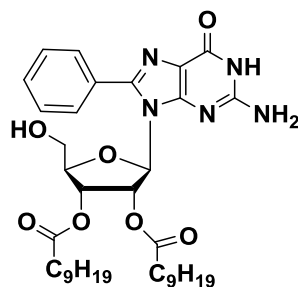
ESI-MS: *m/z*: 780.2 [M-H]⁻; 782.4 [M+H]⁺; 804.3 [M+Na]⁺.

HR-MS: calcd. for C₄₂H₆₇N₅O₇Si, *m/z* 781.4810; found, *m/z* 781.4812.

¹H-NMR δ (dms_o-d₆): 0.024 and 0.021 (s,s, 6H, SiMe₂), 0.810 (s, 9H, tBuSi), 0.843 and 0.848 (t,t, 6H, CH₃), 1.13-1.27 (m, 24H, CH₂), 1.41 and 1.49 (qi, qi, 4H, CH₂-CH₂-CO), 2.19-2.35 (m, 4H, CH₂-CO), 3.87 (m, 2H), 4.07 (m, 1H), 5.63 (m, 1H), 5.75 (d, *J*=5.0, 1H), 6.26 (m, 1H), 6.43 (bs, 2H, NH₂), 7.53-7.55 (m, 3H, ArH), 7.59-7.61 (m, 2H, ArH), 10.84 (bs, 1H, NH) ppm.

^{13}C -NMR δ (dms o - d_6 /CDCl $_3$): -4.83 (CH $_3$), -4.76 (CH $_3$), 19.01 (C), 14.12 (CH $_3$), 22.62 (CH $_2$), 24.56 (CH $_2$), 24.66 (CH $_2$), 26.35 (CH $_3$), 28.88 (CH $_2$), 29.07 (CH $_2$), 29.18 (CH $_2$), 29.18 (CH $_2$), 29.20 (CH $_2$), 29.27 (CH $_2$), 29.32 (CH $_2$), 29.40 (CH $_2$), 31.83 (CH $_2$), 33.67 (CH $_2$), 34.01 (CH $_2$), 63.50 (C5'), 71.63 (C2'), 71.79 (C3'), 85.31 (C4'), 89.36 (C1'), 119.00 (C), 129.13 (CH, Ph), 129.74 (CH, Ph), 130.58 (C), 130.71 (CH, Ph), 147.45 (C8), 152.96 (C), 153.68 (C), 158.22 (C), 172.01 (C=O), 172.30 (C=O).

8-Phenyl-2',3'-O-didecanoyl guanosine 18



To a solution of 8-phenyl-5'-O-*t*-butyldimethylsilyl-2',3'-O-didecanoyl guanosine (120 mg, 0.153 mmol) in THF (4 mL) were added 72.5 mg (0.230 mmol, 1.5 eq) of TBAF. The mixture was stirred at r.t. until tlc (CH $_2$ Cl $_2$ /MeOH 92:8) showed complete disappearance of starting material. The reaction mixture was concentrated, redissolved in CH $_2$ Cl $_2$ and washed with sat. NaHCO $_3$ (3x10 mL). The organic phase was dried over MgSO $_4$ and solvents were removed by distillation. The residue was purified on silica gel by eluting first with Et $_2$ O, then with CH $_2$ Cl $_2$ /MeOH 95:5. The product was obtained as a white solid in a 73% yield (75 mg, 0.112 mmol).

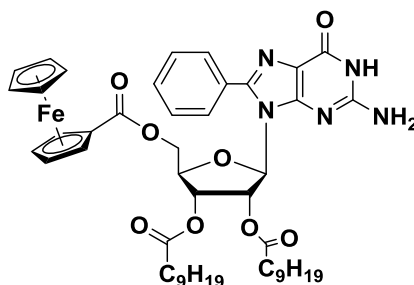
RF = 0.28 (CH $_2$ Cl $_2$ /MeOH 92:8)

ESI-MS: m/z : 666.3 [M-H] $^-$; 668.3 [M+H] $^+$; 690.3[M+Na] $^+$.

HR-MS: calcd. for C $_{36}$ H $_{53}$ N $_5$ O $_7$, m/z 667.3945; found, m/z 667.3948.

^1H -NMR δ (dms o - d_6): 0.84 and 0.85 (t,t, 6H, CH $_3$), 1.12-1.27 (m, 24H, CH $_2$), 1.40 and 1.48 (qi, qi, 4H, CH $_2$ -CH $_2$ -CO), 2.16-2.35 (m, 4H, CH $_2$ -CO), 3.64 (m, 1H, 5'H), 3.75 (m, 1H, 5'H), 4.08 (m, 1H, 4'H), 5.49 (m, 1H, 3'H), 5.78 (d, J =6.0, 1H), 5.80 (m, 1H, 2'H), 6.18 (t, 1H, OH), 6.48 (bs, 2H, NH $_2$), 7.53-7.55 (m, 3H, *m*- and *p*-ArH), 7.58-7.61 (m, 2H, *o*-ArH), 10.84 (bs, 1H, NH) ppm.

^{13}C -NMR δ (dms o - d_6): 14.03 (CH $_3$), 22.58 (CH $_2$), 24.50 (CH $_2$), 24.76 (CH $_2$), 28.95 (CH $_2$), 29.01 (CH $_2$), 29.16 (CH $_2$), 29.17 (CH $_2$), 29.19 (CH $_2$), 29.28 (CH $_2$), 29.32 (CH $_2$), 29.35 (CH $_2$), 31.76 (CH $_2$), 33.61 (CH $_2$), 33.89 (CH $_2$), 61.65 (C5'), 71.73 (C2'), 72.08 (C3'), 85.10 (C4'), 88.08 (C1'), 119.64 (C), 129.22 (CH, *m*-Ph), 129.86 (CH, *o*-Ph), 130.52 (C, Ph), 131.86 (CH, *p*-Ph), 147.36 (C8), 153.55 (C), 153.71 (C), 159.61 (C), 171.78 (C=O 2'), 172.27 (C=O 3').

8-Phenyl-5'-O-ferrocenoyl-2',3'-O-didecanoyl guanosine G4

Ferrocene carboxylic acid (77,5 mg, 0.337 mmol, 1.3 eq.) was dried in vacuo at 50°C for 1 h and dissolved in THF (9 mL). Et₃N (175 μL, 1.217 mmol, 4.7 eq.) was added and the resulting solution was cooled to 0°C. Methanesulfonyl chloride (25,5 μL, 0.311 mmol, 1.2 eq.) was added and the mixture was allowed to warm to r.t. and stirred for 2 h. A solution of vacuum-dried 8-phenyl-2',3'-O-didecanoyl guanosine (173 mg, 0.259 mmol) in THF (6 mL) was then added, followed by a catalytic amount of DMAP. Stirring was continued for 24 h, then MeOH (0.5 mL) was added and the reaction mixture was concentrated in vacuo. The residue was dissolved in CH₂Cl₂, washed with water and dried over MgSO₄. The solvent was removed by distillation and the residue was purified by chromatography on silica gel (gradient from CH₂Cl₂ to CH₂Cl₂/MeOH 99:1), affording the title compound (85 mg, 0.097 mmol) as a yellow solid in a 38% yield.

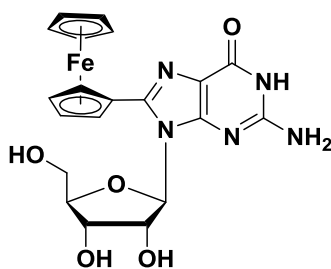
RF = 0.24 (CH₂Cl₂/MeOH 9:1)

ESI-MS: *m/z*: 878.2 [M-H]⁻

HR-MS: calcd. for C₄₇H₆₁FeN₅O₈, *m/z* 879.3870; found, *m/z* 879.3866.

¹H-NMR δ (CD₂Cl₂): 0.84-0.88 (m, 6H, CH₃), 1.20-1.33 (m, 24H, CH₂), 1.52-1.67 (m, 4H, CH₂-CH₂-CO), 2.26-2.36 (m, 4H, CH₂-CO), 3.97 (s, 5H, Fc), 4.17 (s, 1H, Fc), 4.20 (s, 1H, Fc), 4.34 (dd, *J*=12.0, 4.3, 1H, H5'), 4.41 (m, 1H, H4'), 4.61 (s, 1H, Fc), 4.62 (dd, *J*=12.0, 4.3, 1H, H5'), 4.67 (s, 1H, Fc), 5.85 (d, *J*=3.0, 1H, H1'), 6.43 (dd, *J*=3.0, 5.4, 1H, H2'), 6.48 (dd, *J*=5.4, 7.8, 1H, H3'), 7.49 (t, 1H, *J*=7.1, Ph), 7.56 (t, 2H, *J*=7.1, Ph), 7.81 (d, *J*=7.1, 2H, Ph), 12.57 (bs, 1H, NH) ppm.

¹³C-NMR δ (CD₂Cl₂): 13.96 (CH₃), 22.77 (CH₂), 24.93 (CH₂), 25.66 (CH₂), 29.15 (CH₂), 29.24 (CH₂), 29.37 (CH₂), 29.42 (CH₂), 29.46 (CH₂), 29.51 (CH₂), 29.57 (CH₂), 29.77 (CH₂), 31.96 (CH₂), 31.99 (CH₂), 33.95 (CH₂), 33.99 (CH₂), 61.72 (CH₂, C5'), 69.79 (CH, Fc), 69.96 (CH, C3'), 70.07 (CH, Fc), 70.13 (C, Fc), 71.74 (CH, Fc), 72.47 (CH, C2'), 79.92 (CH, C4'), 87.65 (CH, C1'), 117.06 (C, '), 172.50 (C, CO(3')).

8-Ferrocenylguanosine 19

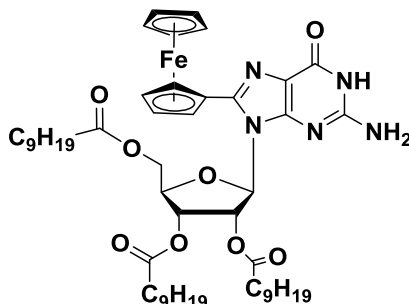
A mixture of **14** (0.300 g, 0.83 mmol), DME (12 mL), ferroceneboronic acid (0.286 g, 1.24 mmol, 1.5 eq) and NaOH (3M, 5.25 mL, 15.75 mmol) was degassed with a stream of Ar for 40 min. in an ultrasonic bath. PdCl₂(PPh₃)₂ (0.058 g, 0.1 eq) was added and the resulting solution was refluxed at 85°C under argon for 48 h. The solvent was then removed under reduce pressure, the reaction mixture was quenched with 10% HCl and the solid was filtered, washed with water and dried. The product thus obtained was used in the subsequent step without further purification.

R_f = 0.17 (DCM/MeOH 9:1)

MS-ESI: *m/z*: 467 (100) [M-H]⁻

HR-MS: calcd. for C₂₀H₂₁FeN₅O₅, *m/z* 467.0892; found, *m/z* 467.0898.

¹H-NMR δ(dms_o-d₆): 3.57 and 3.71 (m, m, 2H, H5',H5''), 3.97 (m, 1H, H4'), 4.19 (m, 1H, H3'), 5.16 (m, 1H, H2'), 5.24 (m, 1H, OH^{5'}), 5.36 (d, *J*=6.0, 1H, OH^{3'}), 5.53 (d, *J*=6.0, 1H, OH^{2'}), 6.3 (bs, 2H, NH₂), 6.65 (d, *J*=7.2, 1H, H1'), 10.71 (bs, 1H, NH) ppm.

8-Ferrocenyl-2',3',5'-O-tridecanoyl guanosine G5

Crude 8-Ferrocenylguanosine **19** (0.430 g, 1.0 eq, 0.92 mmol) was dried over P₂O₅ in vacuo for 2 h at 55 °C and then suspended in 30 mL of an acetonitrile-toluene 1:1 mixture. Decanoic anhydride (0.443 μL, 3.15 eq, 2.90 mmol) and triethylamine (0.209 μL, 3.15 eq, 2.90 mmol) were then added, followed by a catalytic amount of 4-dimethylamino pyridine. The mixture was stirred under argon for 14 h at 80°C. A second aliquot of decanoic anhydride (0.443 μL, 3.15 eq, 2.90 mmol) and TEA (0.209 μL, 3.15 eq, 2.90 mmol) was added and stirring was continued for 12 h at the same temperature.

The solvent was removed under reduced pressure, the crude was dissolved in dichloromethane and extracted with a sat. NaHCO₃ and brine. The organic layer was dried over MgSO₄. The crude

reaction mixture was then applied to a silica gel column packed in dichloromethane and eluted with a mixture of dichloromethane-methanol (from 99:1 to 95:5). The product was obtained as an orange viscous glass.

Yield: 23%

ESI-MS (positive mode, MeOH solution, m/z): 928.2 $[M-H]^+$, 930.5 $[M+H]^+$, 953.4 $[M+Na]^+$

HR-MS: calcd. for $C_{50}H_{75}FeN_5O_8$, m/z 929.4965; found, m/z 929.4964.

1H -NMR δ (dms o - d_6): 0.82-0.85 (m, 9H, CH_3), 1.17-1.24 (m, 36H, CH_2), 1.47 (m, 4H, 2 $\underline{CH_2}$ - CH_2 -CO), 1.58 (qi, $J=6.6$, 2H, $\underline{CH_2}$ - CH_2 -CO), 2.27-2.45 (m, 6H, CH_2 - $\underline{CH_2}$ -CO), 4.28 (s, 5H, Fc), 4.30 (m, 1H, $H5'$), 4.37 (m, 1H, $H4'$), 4.48 (m, 1H, $H5'$), 4.50 (bs, 2H, Fc), 4.60 (s, 1H, Fc), 4.64 (s, 1H, Fc), 5.74 (dd, $J=4.2, 6.0$, 1H, $H3'$), 6.40 (bs, 2H, NH_2), 6.58 (t, $J=6.0$, 1H, $H2'$), 6.75 (d, $J=6.0$, 1H, $H1'$), 10.77 (bs, 1H, NH) ppm.

^{13}C -NMR δ (dms o - d_6): 14.38 (CH_3), 14.41 (CH_3), 22.55 (CH_2), 24.75 (CH_2), 24.79 (CH_2), 24.91 (CH_2), 24.97 (CH_2), 28.76 (CH_2), 28.82 (CH_2), 28.96 (CH_2), 29.01 (CH_2), 29.11 (CH_2), 29.15 (CH_2), 29.21 (CH_2), 29.25 (CH_2), 29.28 (CH_2), 29.34 (CH_2), 31.73 (CH_2), 33.62 (CH_2), 33.76 (CH_2), 33.86 (CH_2), 34.15 (CH_2), 63.05 (CH_2 , $C5'$), 68.60 (CH, Fc), 68.74 (CH, Fc), 69.78 (CH, Fc), 70.00 (CH, Fc), 70.19 (CH, Fc), 70.59 (CH, $C2'$), 71.09 (CH, $C3'$), 74.47 (C, Fc), 80.06 (CH, $C4'$), 86.52 (CH, $C1'$), 117.29 (C5), 146.09 (C8), 152.56 (C4), 153.52 (C), 156.58 (C), 172.16 (CO^2), 173.12 (CO^5), 174.97 (CO) ppm.

Microscopy studies

The Atomic Force Microscopy (AFM) study of the self-assembled G4 and G5 in two dimensions was performed using Veeco Dimension 3100 running with a Nanoscope IV controller. Solutions of investigated molecules were prepared in hexane. First, the solution of each molecule was drop-casted into clean SiO_2/Si substrate and directly characterized by AFM. Second, we proceeded to use the Solvent Vapor Annealing (SVA) method. After drop-casting the molecule solution into the substrate, the system (molecule/substrate) was kept closed in a container contacting CH_2Cl_2 solution for 48 hours.

Scanning Tunneling Microscopy experiments

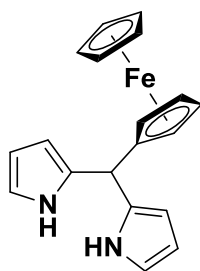
Scanning Tunneling Microscopy (STM) measurements were performed using a Veeco scanning Tunneling microscope (multimode Nanoscope III, Veeco) at the interface between a highly oriented pyrolytic graphite (HOPG) substrate and a supernatant solution, thereby mapping a maximum area of $1 \mu m \times 1 \mu m$. Solution of molecules were applied to the basal plane of the surface. For STM measurements, the substrates were glued to a magnetic disk and an electric contact was made with silver paint (Aldrich Chemicals). The STM tips were mechanically cut from a Pt/Ir wire (90/10,

diameter 0.25 mm). The raw STM data were processed through the application of background flattening and the drift was corrected using the underlying graphite lattice as a reference. The lattice was visualized by lowering the bias voltage to 20 mV and raising the current up to 65 pA. STM imaging was carried out in constant height mode without turning off the feedback loop, to avoid tip crashes. Monolayer pattern formation was achieved by applying onto freshly cleaved HOPG 4 μL of a solution. The STM images were recorded at room temperature once achieving a negligible thermal drift. Solutions of all molecules were prepared by dissolving the molecules in CHCl_3 and diluting with 1-phenyloctane to give 1 mM solution (solvent composition 99 % 1-phenyloctane + 1 % CHCl_3). All of the molecular models were minimized with MMFF and processed with QuteMol visualization software

DFT calculations

To provide a molecular understanding of three G derivatives self-assembly in 2D and shed light onto the formation and stability of supramolecular structures, we have carried out density functional theory (DFT) calculations using the hybrid Gaussian and plane-wave method (GPW), implemented in the QUICKSTEP module of the CP2K package. We used the B3LYP hybrid exchange-correlation potential, whereas the Grimme's DFT-D2 method was employed for taking into account the dispersion forces. To gain insights into the intermolecular binding mechanisms, we have focused our attention on unravelling the interplay between H-bonds, which hold the guanine cores together, and the effective metallic repulsion coming from the four iron cations present in the ferrocenes.

Meso ferrocenyl dipyrromethane 22



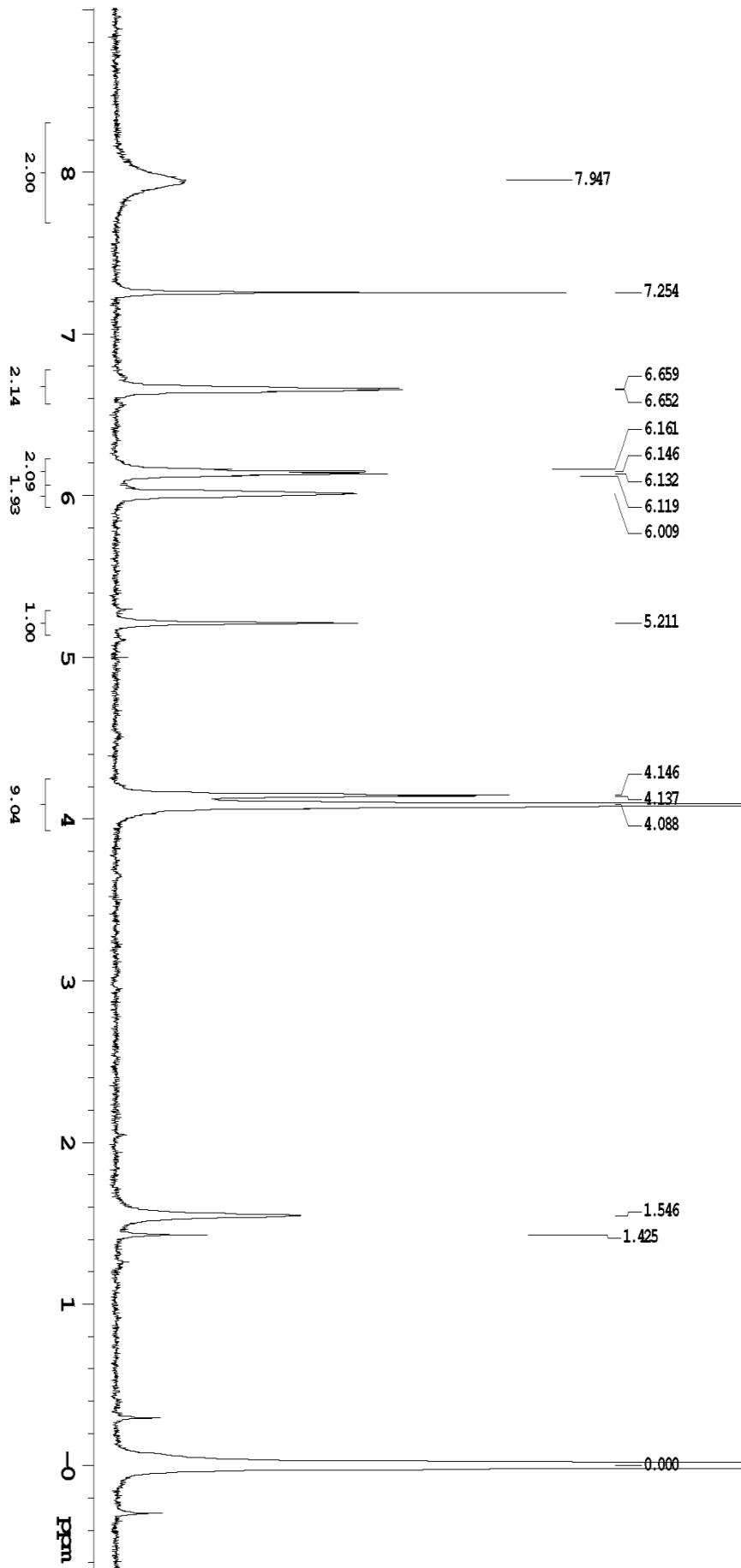
Pyrrole 38.8 mL (40 equiv, 0.56 mol) and FcCHO 3 g (0.014 mol) were added to a dry round-bottomed flask under Ar. TFA 107 μL (0.10 equiv, 0.014 mol) was then added, and the solution was stirred under Ar at room temperature for 20 min in the dark. The crude mixture was dissolved in dichloromethane and washed with 0.1 N NaOH. The organic phase was dried with MgSO_4 and the solvent was removed under vacuum at 50°C due to remove pyrrole. The orange oil was washed with cyclohexane three times and the solvent was removed under vacuum. The crude product was

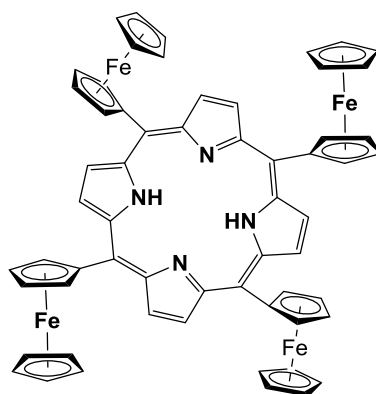
purified by column chromatography on silica gel (CyHex/EtOAc 9:1), affording the final product as a yellow solid (1.24 g, 0.00375 mol). Rf = 0.4 (CyHex/EtOAc 8:2)

Yield: 27%

ESI-MS: m/z (%): 331.09 [M+H⁺]

¹H NMR in CDCl₃:



5,10,15,20-tetra ferrocenyl porphyrin P1

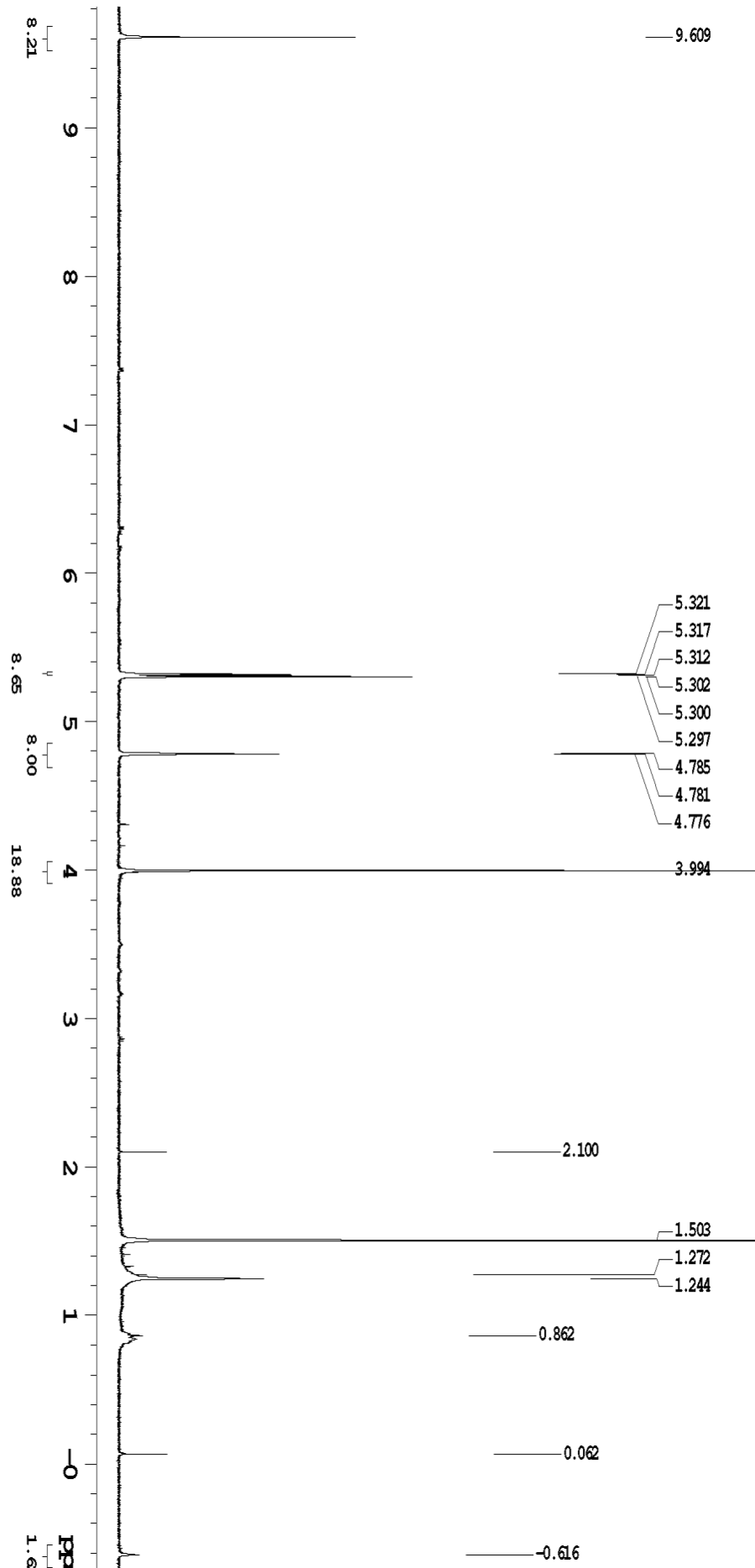
In a 3-necked flask 150 mL of anhydrous CH_2Cl_2 was degassed by bubbling argon for 30 minutes at 0°C . After removing the ice bath and under magnetic stirring 321 mg (1 eq, 0.0015 mol) of FcCHO , 114 μL (1.1 eq, 0.00165 mol) of pyrrole and 62 μL (0.33 eq, 0.0005 mol) of $\text{BF}_3\cdot\text{Et}_2\text{O}$ were added and the reaction was stirred in the dark for 20 h. Then 272 mg (0.8 eq, 0.0012 mol) of DDQ was added and the reaction was refluxed for 90 min in air at 50°C and at room temperature for further 3 h. The solvent was removed under vacuum, the solid was washed two times with CH_2Cl_2 and filtered. The crude product was purified by column chromatography on alumina (CH_2Cl_2) and then on silica gel (CH_2Cl_2), affording the final product as a purple solid (10 mg, 0.0096 mmol).

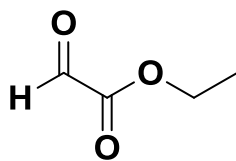
$R_f = 0.16$ (CH_2Cl_2)

Yield: 3%

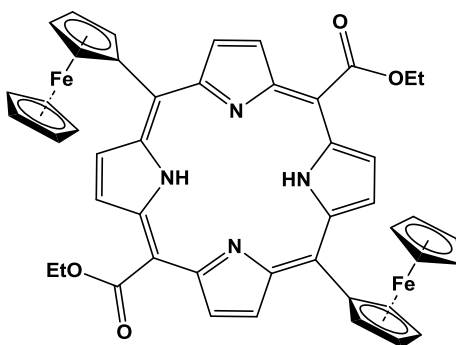
ESI-MS: m/z (%): 1047 [M+H⁺]

^1H NMR CD_2Cl_2



Ethyl glyoxylate 24

A solution of diethyl-L-tartrate (1.66 mL, 0.00971 mol) in anhydrous Et₂O (15 mL) under N₂ was cooled in an ice-water bath for 15 min and the paraperiodic acid (H₅IO₆) (2.21 g, 1 eq, 0.00971 mol) was added in portion over 45 min. The resulting milky reaction mixture was then stirred for a further 3 h, until the ether become almost clear and a white solid separated. The ether phase was decanted, dried with 4 Å molecular sieves. Evaporation of the solvent gave the crude ethyl glyoxylate in ca. 80%, which was used directly in the next step without further purifications.

5,15-Di(ferrocenyl)-10,20-di(ethoxycarbonyl)porphyrin P2

In a three-necked flask 158 mL of anhydrous CH₂Cl₂ was degassed by bubbling argon at 0°C for 30 minutes. After removing the ice bath, 371 mg (0.00364 mol) of ethyl glyoxylate, 1,24 g (1.03 eq, 0.00375 mol) of *meso*-(Ferrocenyl)dipyrromethane and 45 µL (0.1 eq, 0.000364 mol) of BF₃·Et₂O added dropwise were stirred at room temperature in the dark for 20 hours. The reaction was then opened to air and 661 mg (0.8 eq, 0.00291 mol) of DDQ were added, continuing to stir overnight.

Purification by two consecutive silica gel column chromatographies:

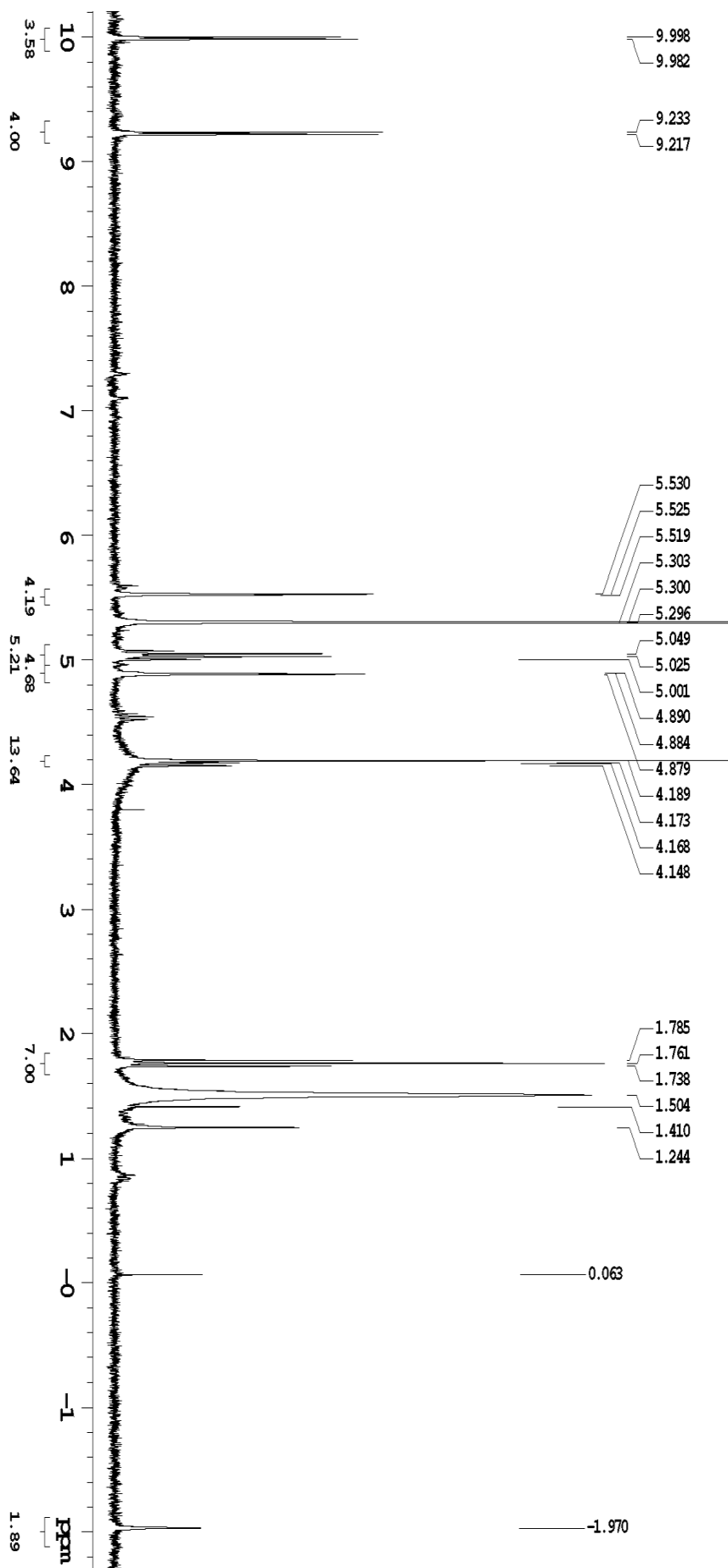
1. CH₂Cl₂
2. CH₂Cl₂:CyHex 9:1

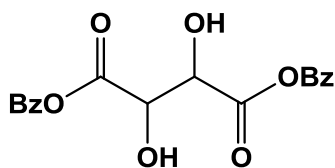
R_f = 0.3 (CH₂Cl₂)

Yield = 3%

ESI-MS: *m/z* (%) 823.16 [M+H⁺]

¹H NMR in CD₂Cl₂:



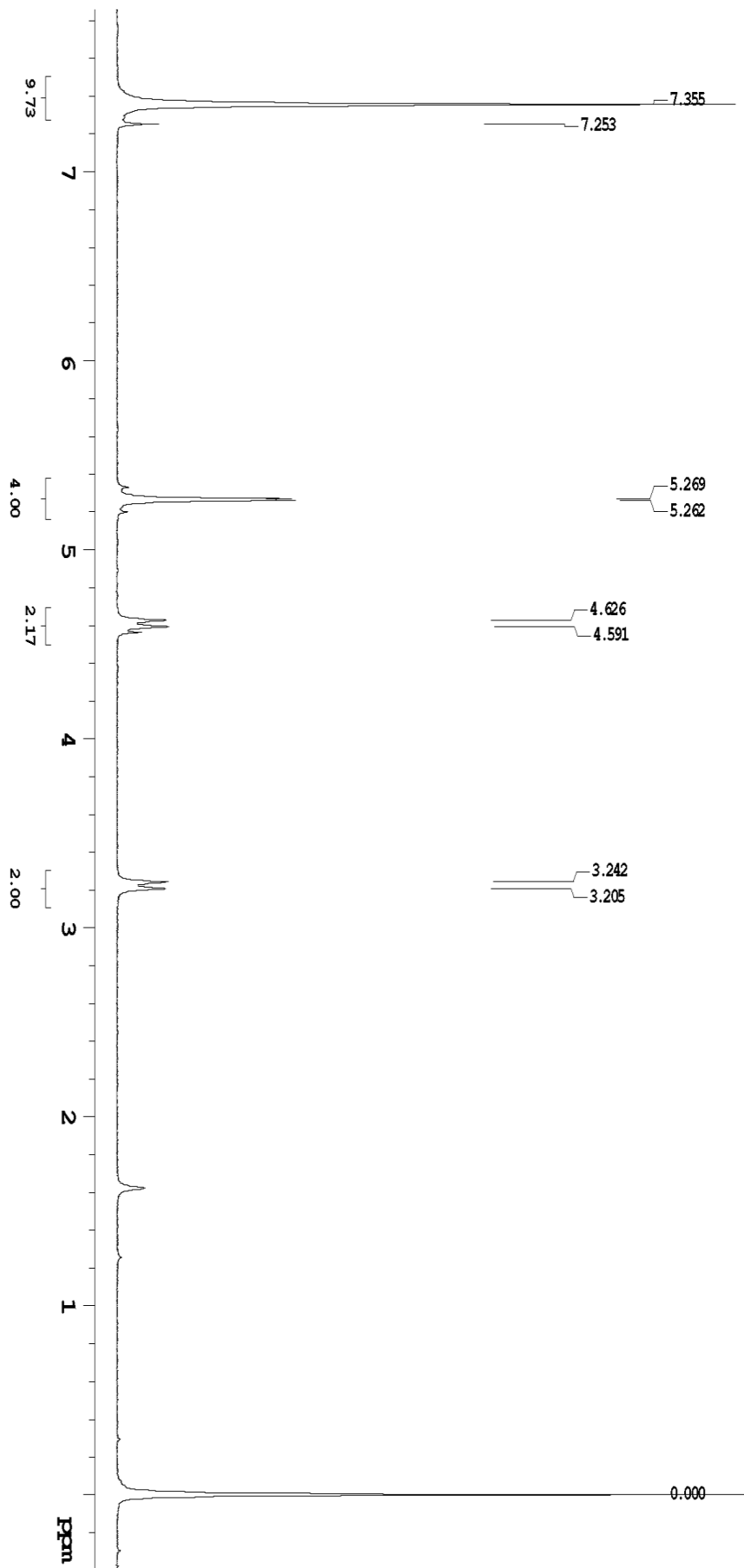
Dibenzyl-tartrate 26

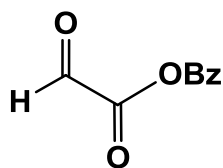
1g (0.0067 mol) of tartaric acid, 1.38 mL (1.98 eq, 0.0133 mol) of benzyl alcohol, 63 mg (0.05 eq, 0.000335 mol) of *p*-toluenesulfonic acid were stirred in a flask, using 25 mL of toluene as solvent. The Dean-Stark apparatus was used in order to collect the forming water, setting the temperature at 160°C. After 12 hours, the solution was concentrated on a rotary evaporator; the residual solid is dissolved in EtOAc and extracted with H₂O. The organic phase was dried over MgSO₄ and concentrated on a rotary evaporator. Purification by silica gel column chromatography (CyHex:EtOAc 85:15).

R_f = 0.27 (CyHex:EtOAc 7:3)

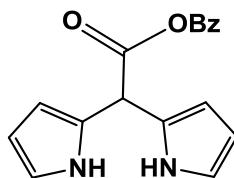
ESI-MS: *m/z* (%): 353.1 [M+Na⁺], 369.2 [M+K⁺]

¹H NMR in CDCl₃:



Benzyl glyoxylate 27

A solution of dibenzyl-tartrate (200 mg, 0.00061 mol) in THF (1.94 mL) under an argon atmosphere was cooled in an ice-water bath for 15 minutes and H_5IO_6 (138 mg, 1eq, 0.00061 mol) was added in portions over 15 minutes. The reaction was stirred for 3 hours, and sonicated repeatedly. The solvent was removed under vacuum, then the resulting solid was dissolved in EtOAc, washed with a saturated solution of NaHCO_3 and brine (x2) and dried over MgSO_4 . Evaporation of the solvent gave the crude benzyl glyoxylate in ca. 80%, which was used directly in the next step without further purifications.

meso-(Benzoyloxycarbonyl)dipyrromethane 28

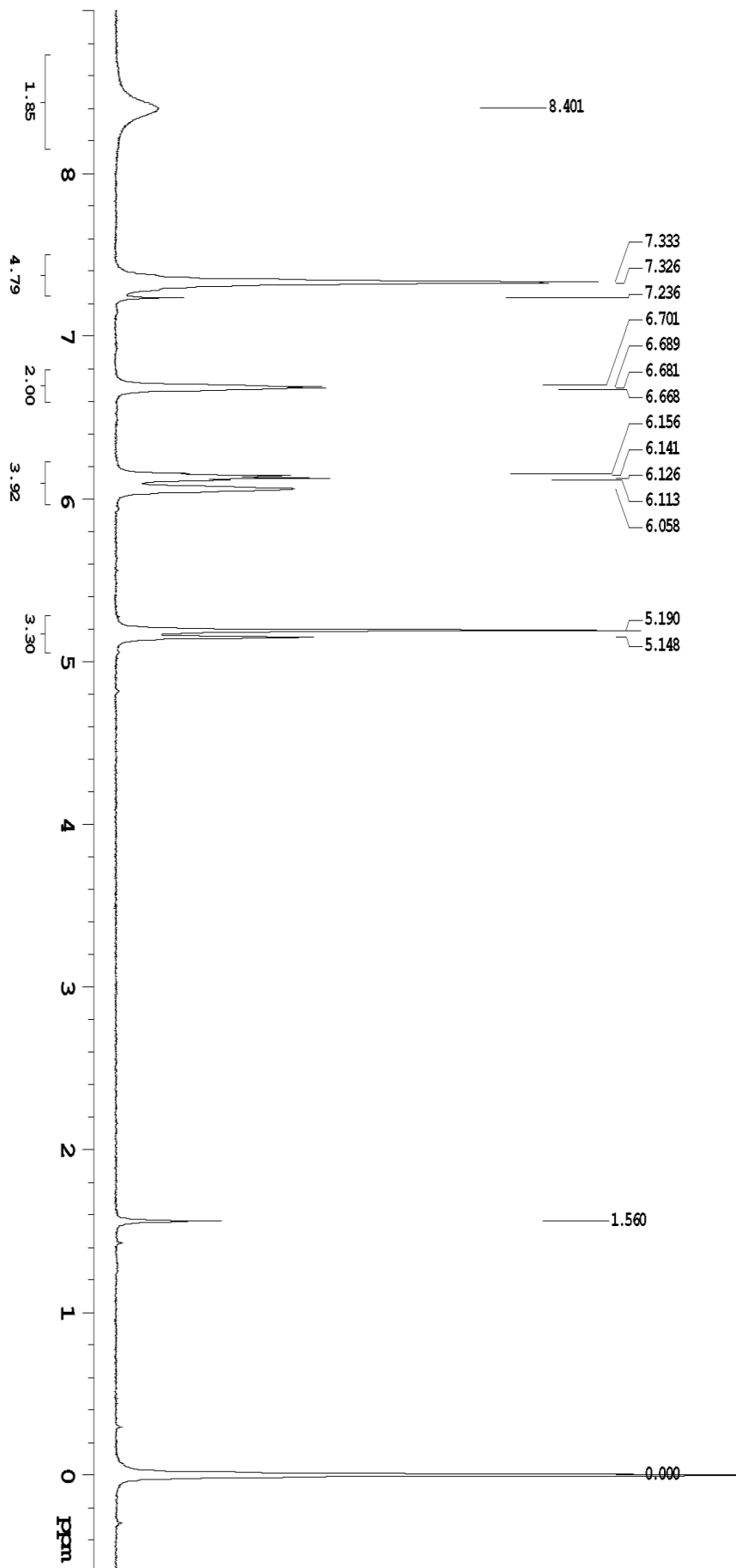
Pyrrole 2.3 mL (40 eq, 0.034 mol) and benzyl glyoxylate (140 mg, 0.00085 mol) were added to a flask and stirred under an argon atmosphere. TFA 6.5 μl (0.1 eq, 0.000085 mol) was then added, and the reaction was stirred for further 20 minutes, at room temperature in the dark. The crude mixture was dissolved in CH_2Cl_2 and washed with 0.1 N NaOH. The organic phase was dried with MgSO_4 , and the solvent was removed under vacuum at 50°C due to remove pyrrole. The resulting phase was washed with cyclohexane (x3) and the solvent was removed under vacuum. Purification by silica gel column chromatography (CyHex:EtOAc 7:3).

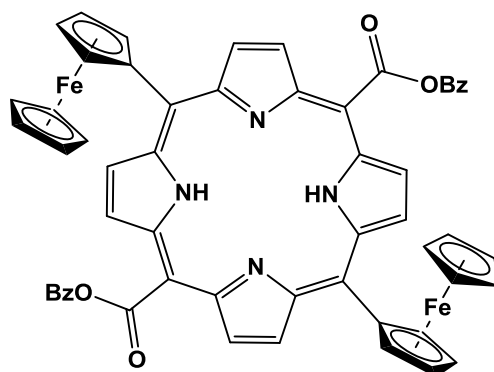
$R_f = 0.48$ (FM: CyHex:EtOAc 7:3)

Yield: 27%

ESI-MS: m/z (%): 279.1 $[\text{M}-\text{H}^+]$, 303.0 $[\text{M}+\text{Na}^+]$

^1H NMR in CDCl_3 :



5,15-Di(ferrocenyl)-10,20-di(benzyloxycarbonyl)porphyrin P3

NH_4Cl 428 mg (10eq, 0.008 mol) and CH_3CN 80 mL were added in a three-necked flask. The solvent was degassed by bubbling argon for 30 minutes at 0°C . Keeping the ice bath and under magnetic stirring, 172 mg (1 eq, 0.0008 mol) of FcCHO , 224 mg (1 eq, 0.0008 mol) of *meso*-(Benzyloxycarbonyl)dipyrromethane, 10 μL (0.1 eq, 0.00008 mol) of $\text{BF}_3\cdot\text{Et}_2\text{O}$ (dropwise) were added, and the reaction was stirred in the dark for 5 hours. Then 360 mg (2 eq, 0.0016 mol) of DDQ was added, the reaction was opened to air and the ice bath removed. After 20 hours, the solvent was removed under vacuum and the crude product was purified by two consecutive silica gel column chromatographies:

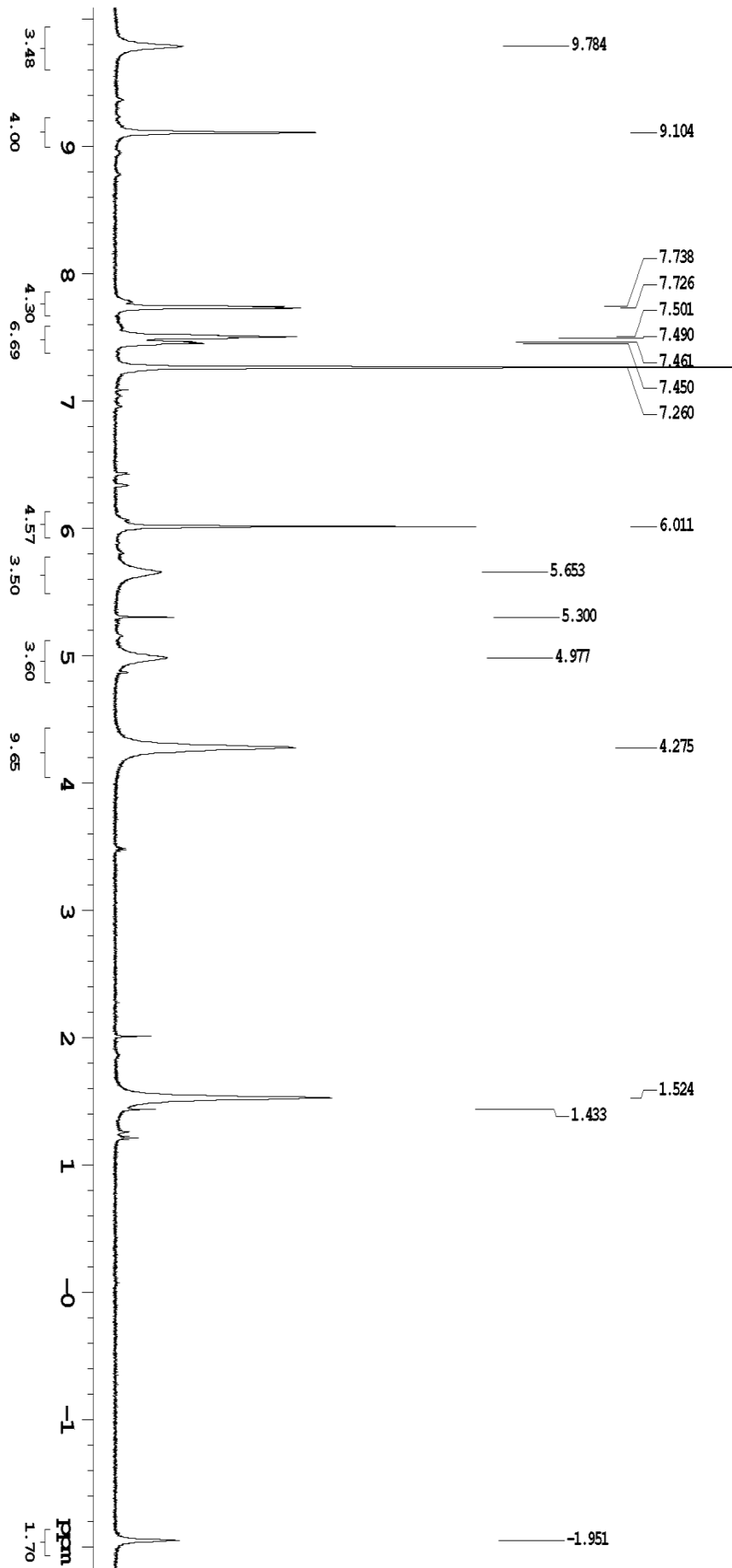
- 1) $\text{CH}_2\text{Cl}_2:\text{CH}_3\text{OH}$ 95:5.
- 2) CH_2Cl_2 .

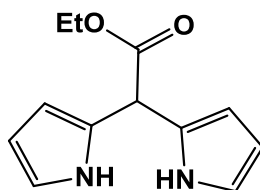
The product was then washed with Et_2O (x2), affording 34 mg (0.000036 mol) of a purple solid.

$R_f = 0.80$ (CH_2Cl_2)

Yield: 9%

^1H NMR in CDCl_3 :



meso-(Ethoxycarbonyl)dipyrromethane 32

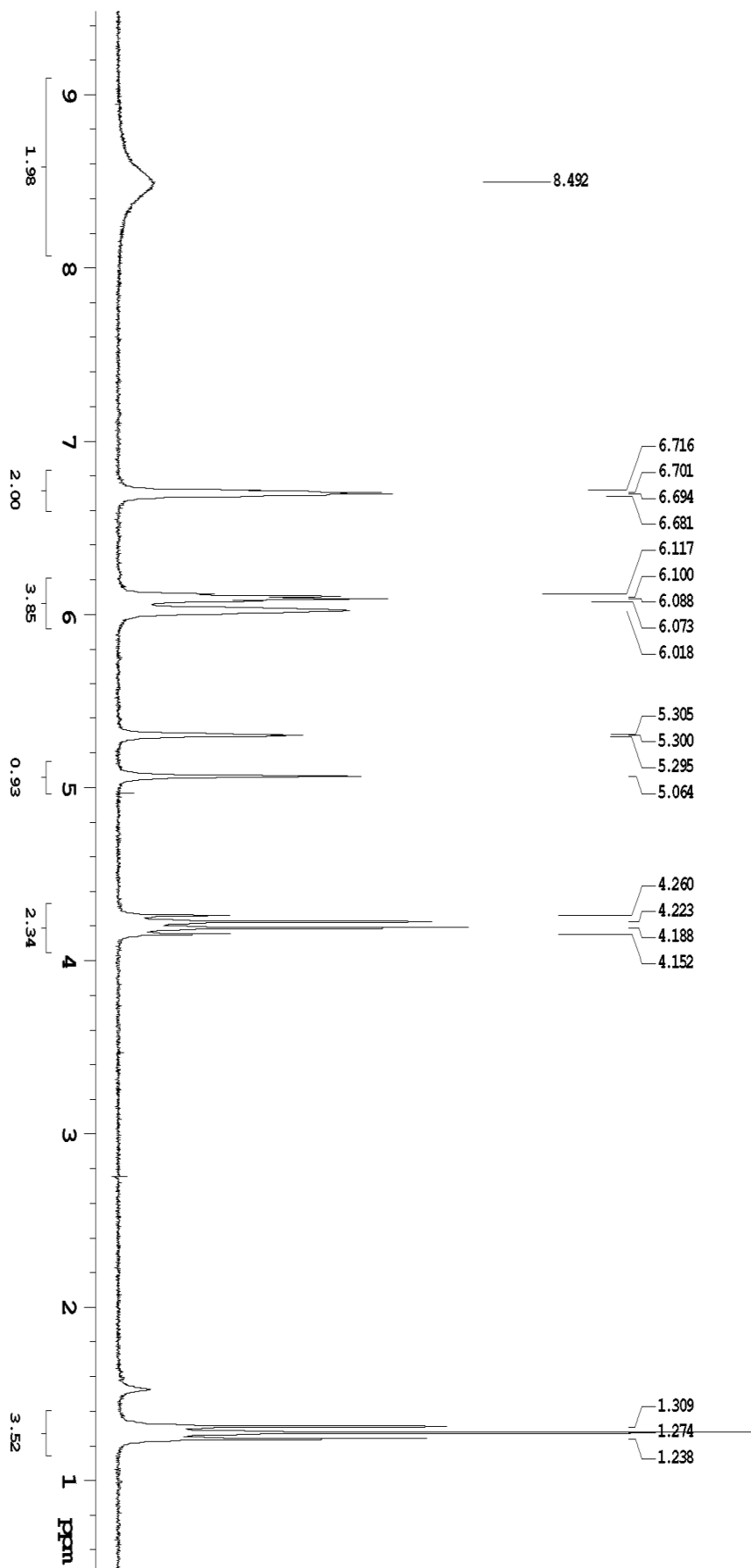
Pyrrole 43 mL (40 eq, 0.6216 mol) and ethyl glyoxlate 1.58 g (1 eq, 0.01554 mol) were added to a flask under an atmosphere of argon. TFA 0.119 ml (0.1 eq, 0.001554 mol) was then added, and the solution was stirred under an atmosphere of argon at room temperature in the dark for 20 minutes. The crude mixture was dissolved in CH₂Cl₂, and washed with NaOH 0.1N. The organic phase was dried with MgSO₄ and the solvent was removed under vacuum at 50°C due to remove pyrrole. The crude product was washed with cyclohexane (x3) and concentrated on a rotary evaporator, resulting in a dark brown oil. The oil was purified by silica gel column chromatography (CH₂Cl₂), affording 899 mg (0.0041 mol) of fuchsia crystals.

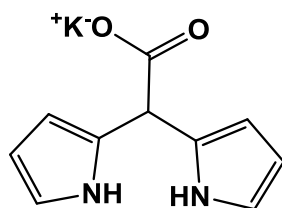
R_f = 0.33 (CH₂Cl₂)

Yield: 27%

ESI-MS: *m/z* (%): 217.2 [M-H⁺], 253.2 [M+Cl⁻], 241.2 [M+Na⁺]

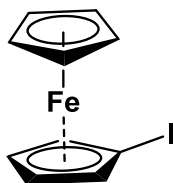
¹H NMR in CD₂Cl₂:



meso-(Carboxyl)dipyrromethane 33

1.139 g (1 eq, 0.00522 mol) of *meso*-(Ethoxycarbonyl)dipyrromethane was dissolved in THF 13.3 mL, under an atmosphere of argon. KOH 2N 5.12 mL was added, and the reaction mixture was refluxed at 75°C for 2 hours. Evaporation of the solvent gave the crude product in ca. 100%, which was used directly in the next step without further purifications.

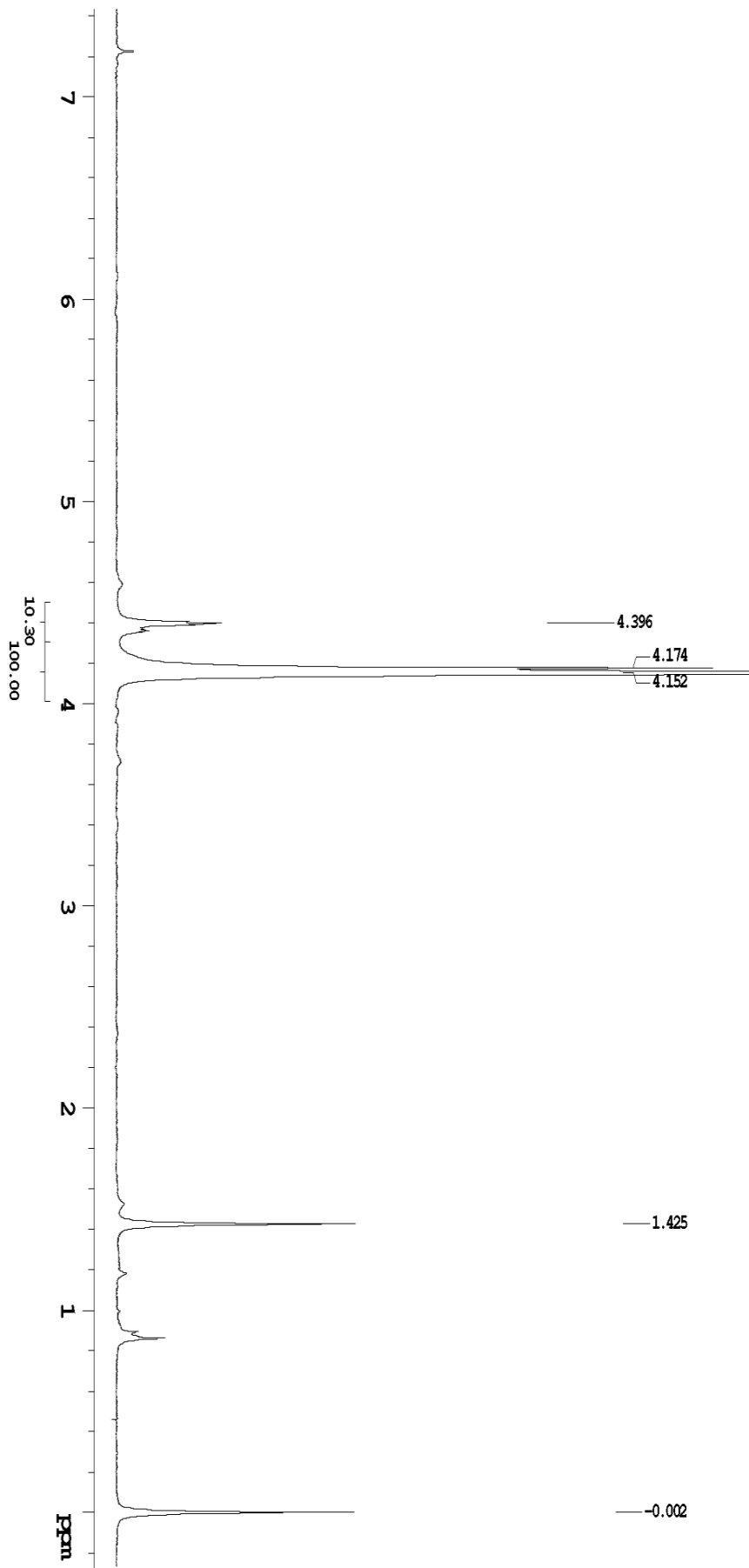
ESI-MS: m/z (%): 189.2 [M-H⁺], 145.5 [M-COO⁻]

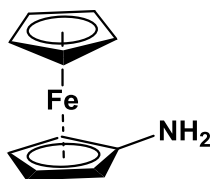
Iodoferrocene 30

Ferrocene 7.49 g (0.040 mol) previously dried at 50°C was dissolved in 50 mL of anhydrous THF in four-necked flask under an argon atmosphere. 19 mL of 1.7 M *t*BuLi in hexane was added dropwise to the flask, cooled in an ice bath over 20 minutes with efficient stirring. The reaction turned red. After additional 15 minutes, the reaction was cooled at -80°C in a dry ice/acetone bath. Solid iodine 10 g (1eq, 0.040 mol) was added in portions under argon and the flask was left in the cooling bath overnight. H₂O 1 mL + 15 mL was added, stirring for 10 minutes. The crude mixture was extracted with CyHex and the aqueous phase was washed with additional CyHex. The collected organic phases were washed with 15 mL H₂O and 15 mL (x4) of 5% Na₂S₂O₃. The organic layer was dried over MgSO₄ and filtered. The solvent was removed under vacuum and the product was dried in a vacuum pump.

Yield: 14%

¹H NMR in CDCl₃:



Aminoferrocene 31

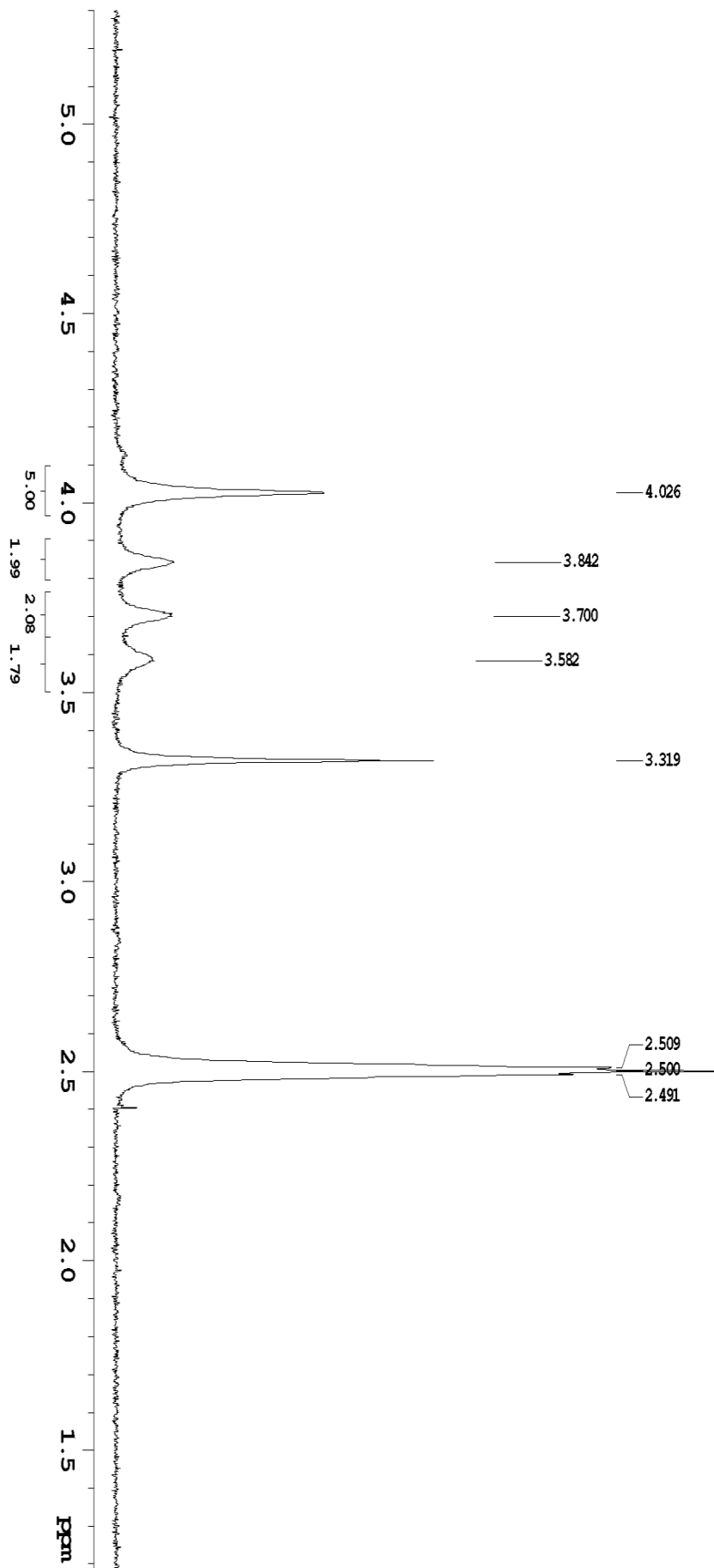
Iodoferrocene 998 mg (0.0032 mol) was dissolved in 30 mL of C₂H₅OH. 60 mg of CuI (0.1 eq, 0.00032 mol), 50 mg of Fe₂O₃ (0.1 eq, 0.00032 mol) and 300 mg of NaOH (2.3 eq, 0.0075 mol) were added to the solution. 15 mL of aqueous ammonia 13.5 N was added to the resulting red suspension, and the reaction mixture was heated to 90°C for 6 hours. The reaction mixture was cooled to room temperature and 350 mL of Et₂O was added. The organic phase was then washed with aqueous NaOH 1N (100 ml x 3), dried over MgSO₄, filtered and evaporated to dryness to obtain the crude product, purified by silica gel column chromatography (CyHex:EtOAc 1:1) to obtain 118 mg (0.00059 mol) of a yellow solid.

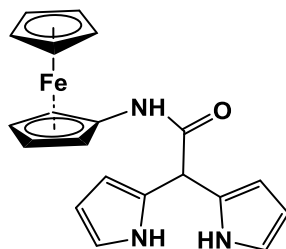
R_f = 0.28 (CyHex:EtOAc 1:1)

Yield: 18%

ESI-MS: *m/z* (%): 201.2 [M+H⁺]

¹H NMR in DMSO:



meso-(N-Ferrocenylamido)dipyrromethane 34

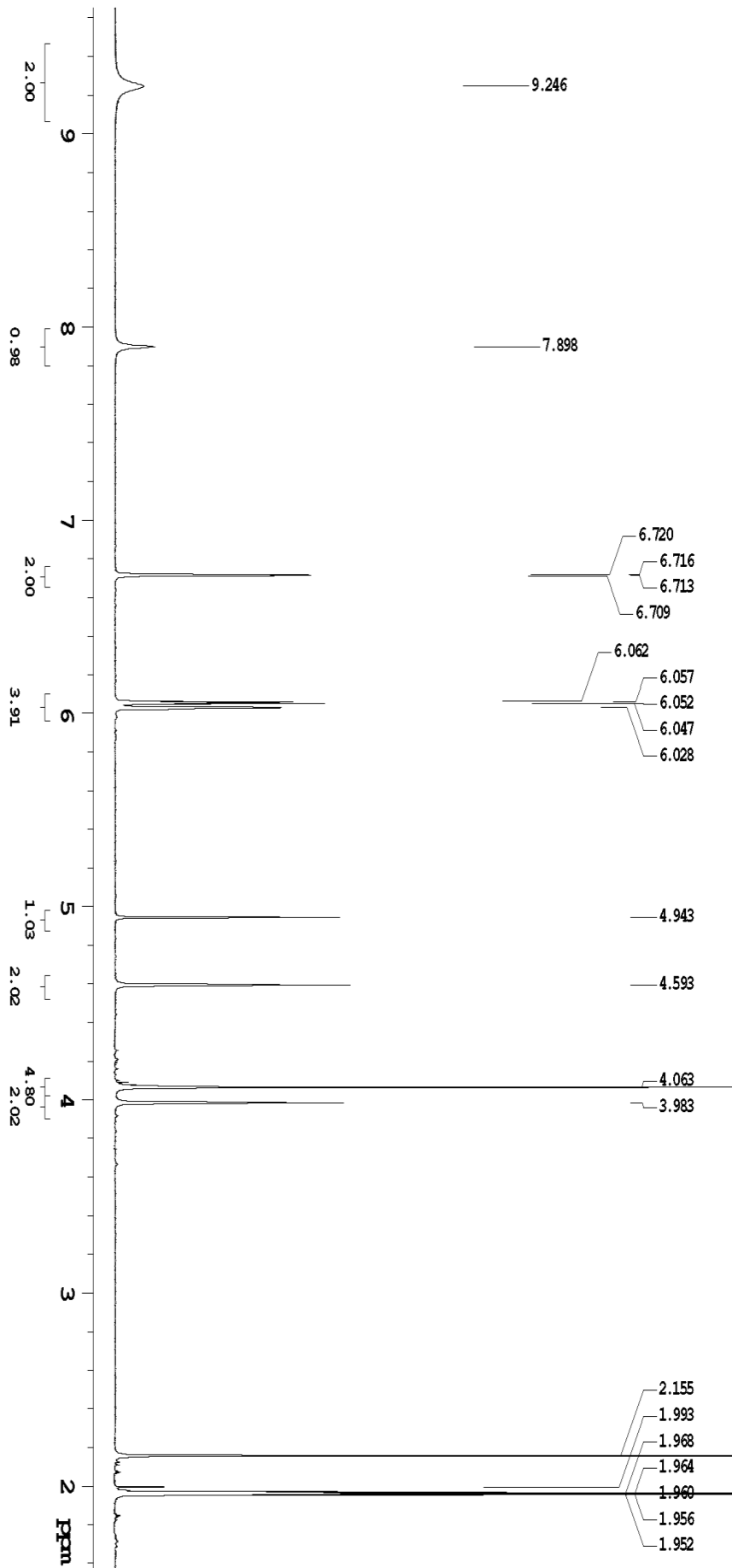
Aminoferrocene 445 mg (0.8 eq, 0.0022 mol) was dissolved in 15 mL of THF anhydrous. The resulting solution was added in a flask containing 549 mg (1 eq, 0.0028 mol) of *meso*-(carboxyl)dipyrromethane, under an argon atmosphere. Then 429 mg of HOBT (12% H₂O) (1 eq, 0.0028 mol) was added, followed by EDC·HCl 554 mg (1 eq, 0.0028 mol) in two portions. After 2 hours, the crude product was purified by silica gel column chromatography (CyHex:EtOAc 2:1), to obtain 397 mg (0.0011 mol) of a yellow solid.

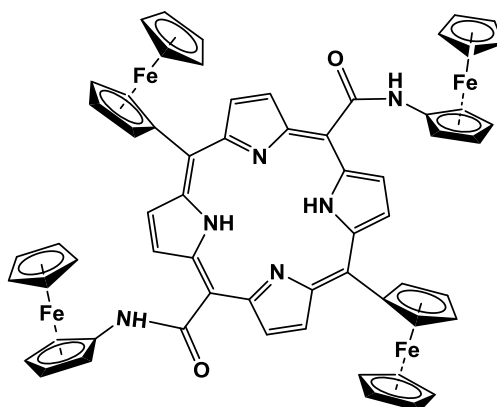
R_f = 0.50 (CyHex:EtOAc 2:1)

Yield: 48%

ESI-MS: *m/z* (%): 372.0 [M-H⁺], 408.0 [M+Cl⁻]

¹H NMR in CD₃CN:



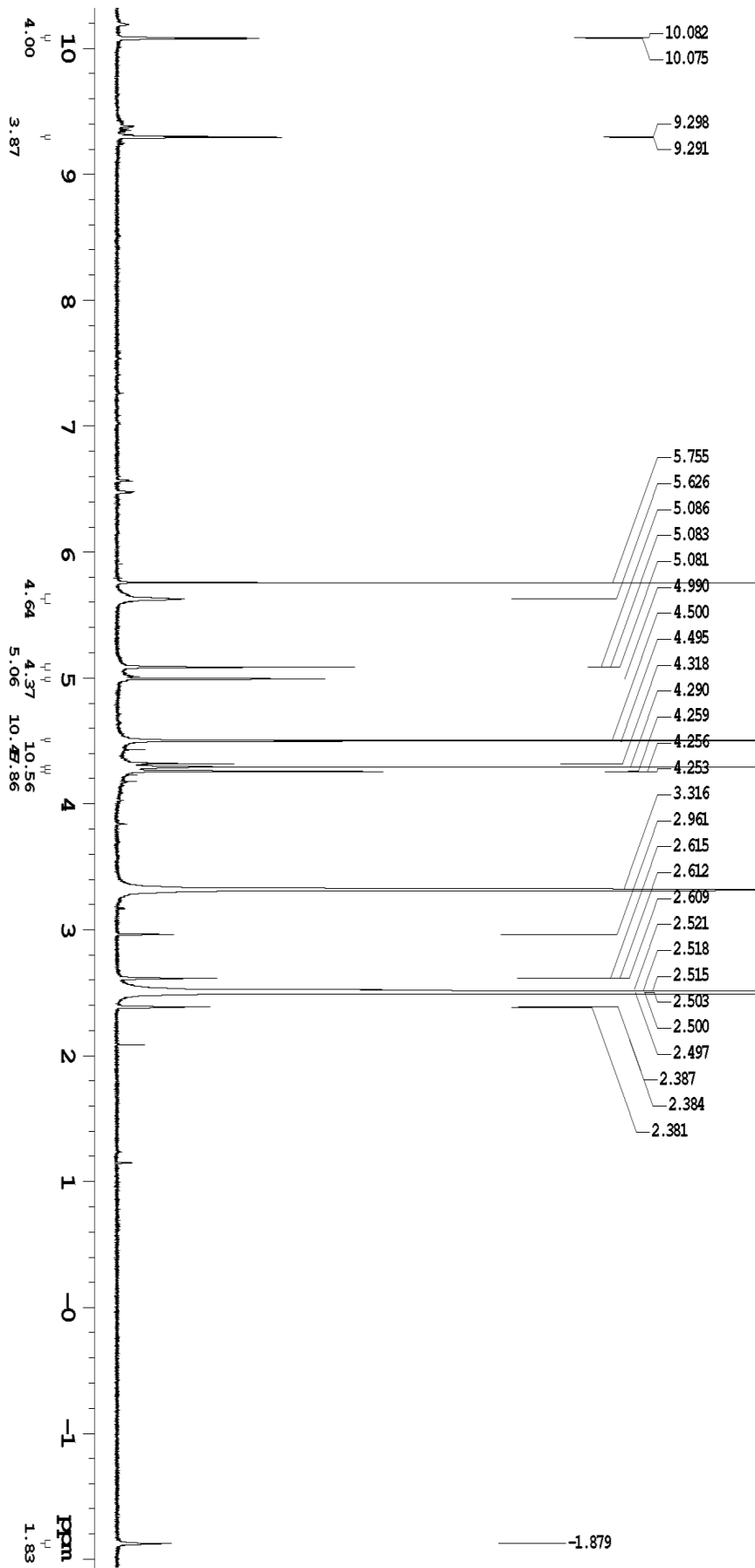
5,15-Di(ferrocenyl)-10,20-di(N-ferrocenylamido)porphyrin P4

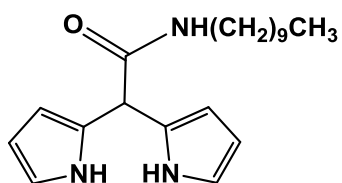
NH_4Cl 214 mg (10eq, 0.004 mol) and 40 mL of CH_3CN were added in a three-necked flask. The solvent was degassed by bubbling argon for 30 minutes at 0°C . Keeping the ice bath and under magnetic stirring, 86 mg (1 eq, 0.0004 mol) of FcCHO , 149 mg (1 eq, 0.0004 mol) of *meso*-(N-Ferrocenylamido)dipyrromethane, 5 μL (0.1 eq, 0.00004 mol) of $\text{BF}_3\cdot\text{Et}_2\text{O}$ (dropwise) were added, and the reaction was stirred in the dark for 5 hours. Then, 180 mg (2 eq, 0.0008 mol) of DDQ was added, the reaction was opened to air and the ice bath removed. After 20 hours, the solvent was removed under vacuum and the crude product was purified by a first column chromatography on alumina ($\text{CH}_2\text{Cl}_2:\text{CH}_3\text{OH}$ 7:3) followed by a silica gel column chromatography ($\text{CH}_2\text{Cl}_2:\text{CH}_3\text{OH}$ 99:1), to obtain 44 mg (0.000039 mol) of purple solid, then washed with CH_3OH .

$R_f = 0.42$ (FM: $\text{CH}_2\text{Cl}_2/\text{CH}_3\text{OH}$ 99:1)

Yield: 19%

^1H NMR in DMSO:



meso-(N-Decilamido)dipyrromethane 35

meso-(Carboxyl)dipyrromethane 992 mg (1 eq, 0.00522 mol) was dissolved in 27 mL anhydrous THF under an argon atmosphere. Then decylamine 1.04 mL (1 eq, 0.00522 mol) and HOBt (12% H₂O) 788 mg (1 eq, 0.00522 mol) were added, followed by EDC·HCl 1.00 g (1 eq, 0.00522 mol) in two portions. After 24 hours, the solvent was removed under vacuum, then the crude product was washed with Et₂O and filtered. The liquid phase was again removed under vacuum, affording a dark brown oil. Purification by two consecutive silica gel column chromatographies:

- 1) CH₂Cl₂:CH₃OH 95:5.
- 2) CyHex:EtOAc 70:30.

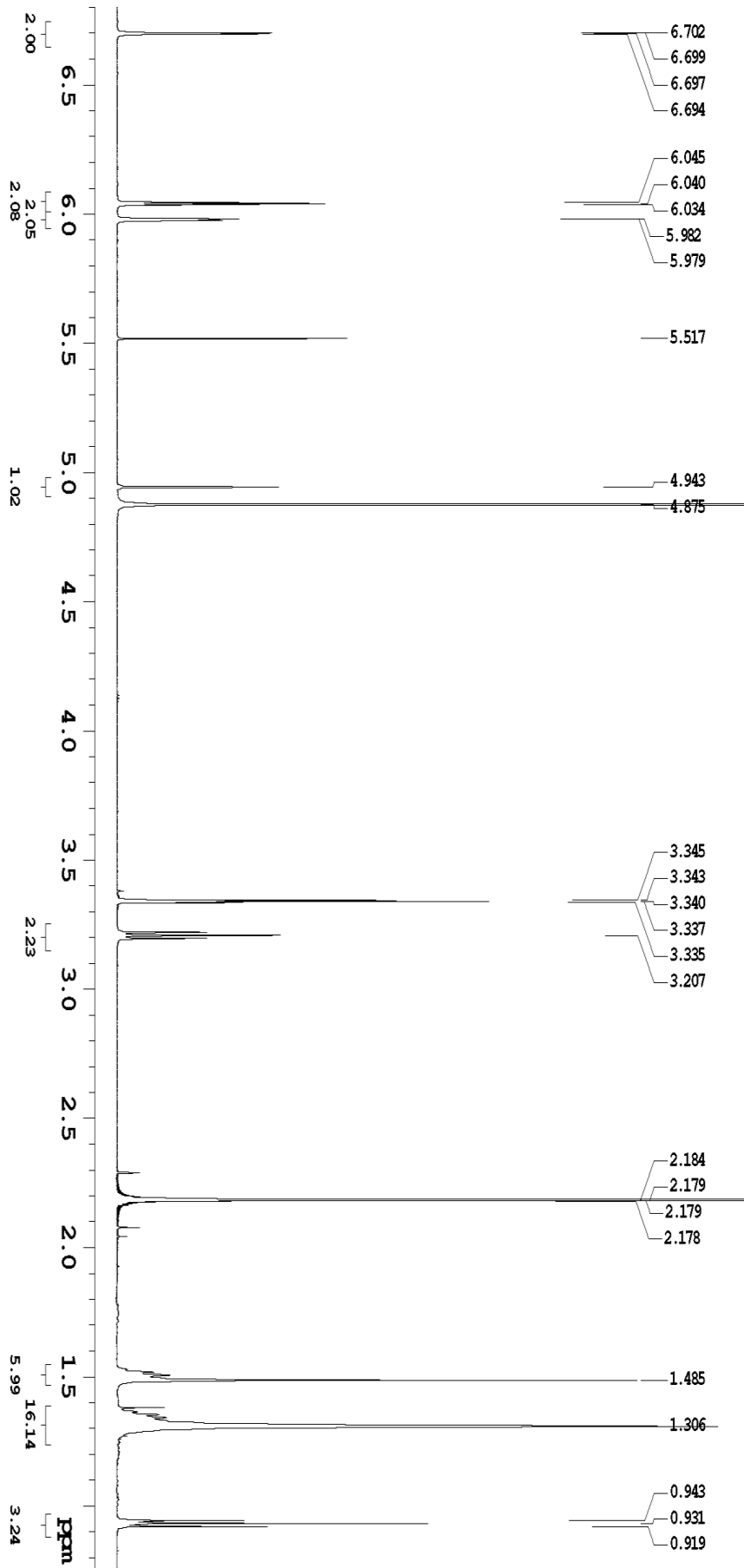
The product was then washed with Et₂O (x3) and CyHex (x1), to obtain 971 mg (0.0029 mol) of a white solid.

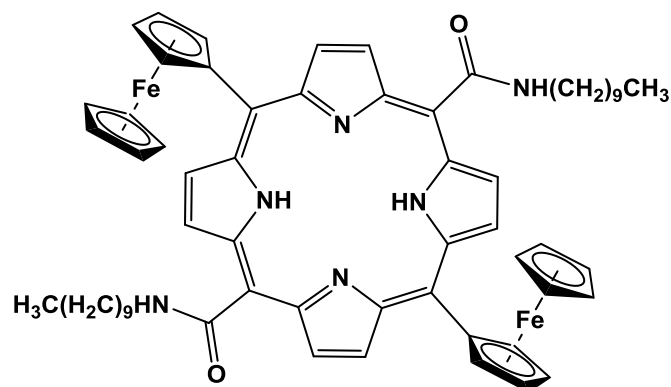
R_f = 0.30 (CyHex:EtOAc 7:3)

Yield: 56%

ESI-MS: *m/z* (%): 328.3 [M-H⁺], 364.2 [M+Cl⁻], 368.3 [M+K⁺]

¹H NMR in CD₃OD:



5,15-Di(ferrocenyl)-10,20-di(N-decylamido)porphyrin P5

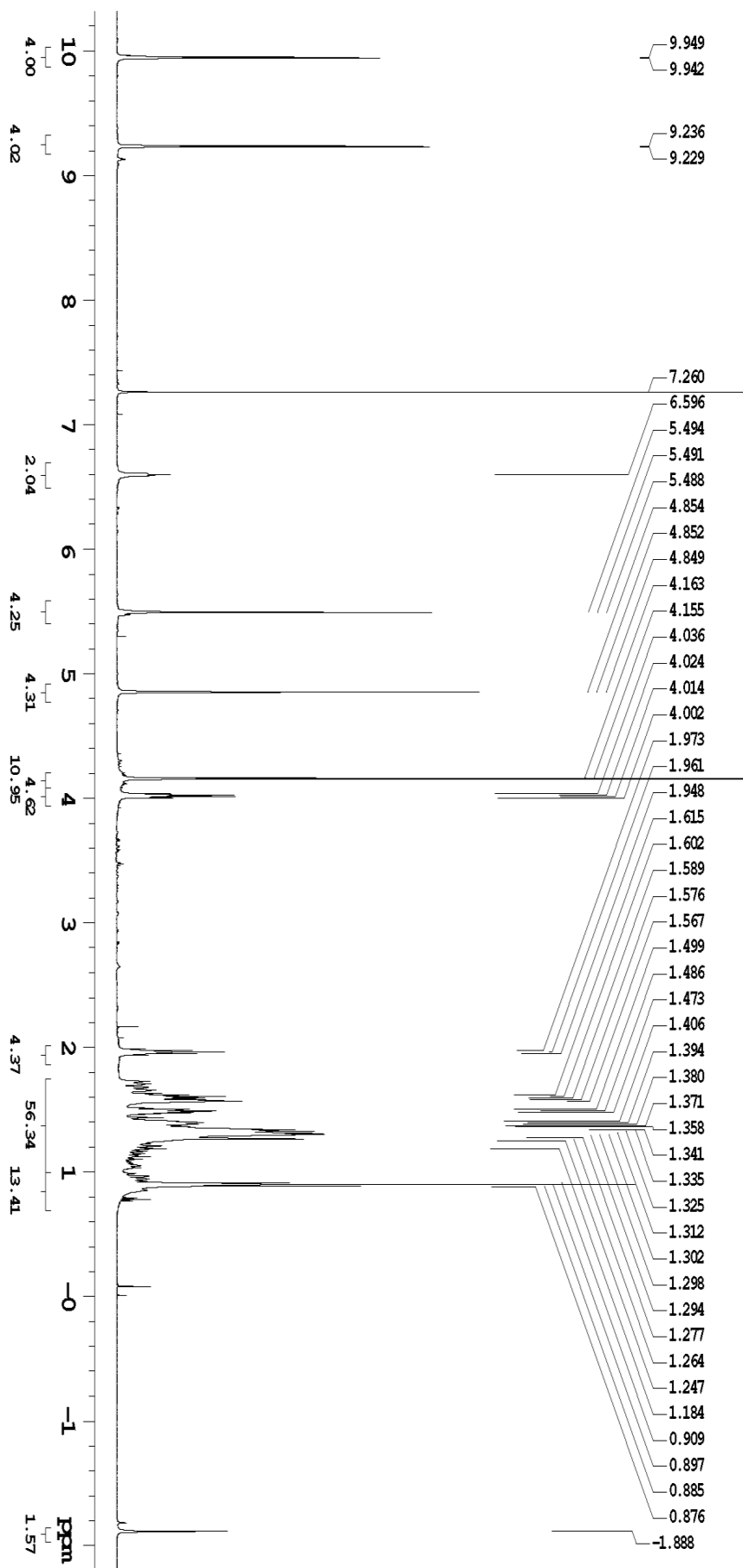
NH_4Cl 776 mg (10 eq, 0.0145 mol) and 144 mL of CH_3CN were added in a three-necked flask. The solvent was degassed by bubbling argon for 30 minutes at 0°C . Keeping the ice bath and under magnetic stirring, 310 mg (1 eq, 0.00145 mol) of FcCHO , 479 mg (1 eq, 0.00145 mol) of *meso*-(N-Decylamido)dipyrromethane, 18 μL (0.1 eq, 0.000145 mol) of $\text{BF}_3\cdot\text{Et}_2\text{O}$ (dropwise) were added, and the reaction was stirred in the dark for 48 hours. Then 658 mg (2 eq, 0.00290 mol) of DDQ was added, the reaction was refluxed for 90 minutes in air at 50°C and at room temperature for further 20 hours. The solvent was removed under vacuum and the crude product was purified by a first column chromatography on alumina (CyHex:EtOAc 80:20) followed by a silica gel column chromatography (CyHex:EtOAc 70:30). The product was then washed with Et_2O (x3) and crystallized by $\text{C}_2\text{H}_5\text{OH}$.

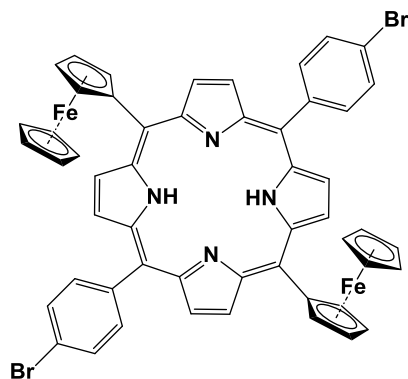
$R_f = 0.44$ (CyHex:EtOAc 70:30)

Yield: 16%

ESI-MS: m/z (%): 1045 [$\text{M}+\text{H}^+$], 1067 [$\text{M}+\text{Na}^+$], 1084 [$\text{M}+\text{K}^+$]

^1H NMR in CDCl_3 :



5,15-bis(4-bromophenyl)-10,20-ferrocenyl-porphyrin P6

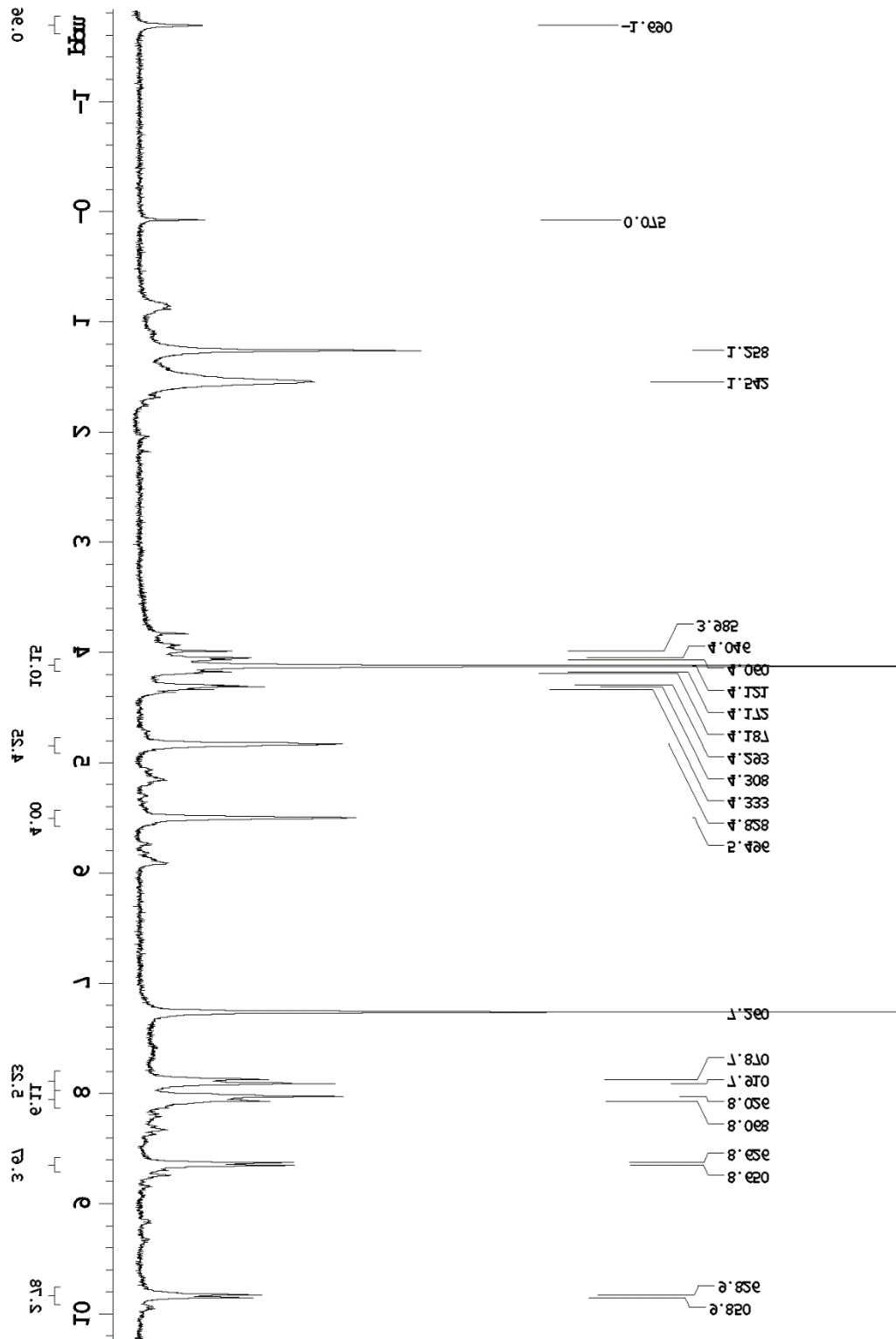
CH₂Cl₂ 45 mL and CH₃CN 225 mL were added in a three-necked flask. The solvent was degassed by bubbling argon for 30 minutes. Under magnetic stirring, 505 mg (1 eq, 2.727 mmol) of 4-bromobenzaldehyde, 900 mg (1 eq, 2.727 mmol) of FcDPM, 35.59 μL (0.273 mmol) of BF₃·Et₂O (dropwise) were added, and the reaction was stirred in the dark for 3 hours. Then, 671 mg (2.40 mmol) of cloranile was added. After 72 hours, the solvent was removed under vacuum and the crude product was purified by two consecutive silica gel column chromatographies:

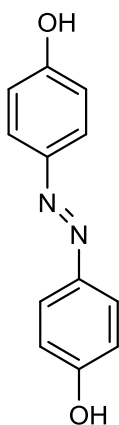
- 1) Toluene
- 2) CyHex:CH₂Cl₂:Toluene 6:2.5:1.5

The product was finally washed with CH₃CN.

Yield: 26%

¹H NMR in CDCl₃:



4,4'-Dihydroxyazobenzene 37

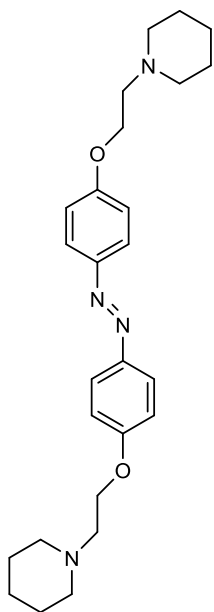
4-Hydroxyanilin (6.4 g, 0.058 mol) was dissolved in 100 mL of dilute hydrochloric acid (1 M) and cooled to 0°C. An aqueous solution of sodium nitrite (4.03 g, 0.058 mol in 20 mL of water) was added dropwise under constant stirring. The mixture is diluted by adding 200 mL of precooled methanol. In a separate batch, phenol (5.46 g, 0.058 mol) and potassium hydroxide (6.2 g, 0.11 mol) are dissolved in 40 mL of methanol and also cooled to 0°C. This phenolate solution is added dropwise under constant stirring to the first mixture. The red solution is stirred for another 2 h at 0°C before the reaction is quenched with dilute hydrochloric acid. The red solid was filtered, washed thoroughly with water, and dried. The crude material was purified by recrystallization from concentrated acetic acid.

Yield: 4.48 g, 0.021 mol, 36%.

EI-MS: m/z 214.0 (M^+).

^1H NMR: (DMSO- d_6) δ 10.05 (br, 2 H), 7.74 (d, 4 H, J) 4 Hz), 6.93 (d, 4 H, J) 4 Hz); (CDCl₃) δ 7.84 (d, 4 H, J) 4 Hz), 6.95 (d, 4 H, J) 4 Hz), 5.05 (br, 2 H).

^{13}C NMR (DMSO d_6): δ 160.3 (2), 145.6 (2), 124.4 (4), 116.1 (4).

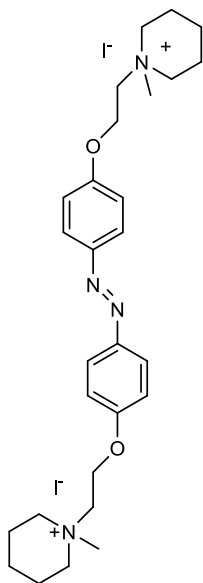
1, 2-bis (4-(2-(piperidin-1-yl) ethoxy) phenyl) diazene 38

4,4'-Dihydroxyazobenzene (0.214 g, 1 mmol) was refluxed with 1-(2-chloroethyl)piperidine hydrochloride (0.440 g, 3 mmol) in dry acetone in presence of anhydrous K_2CO_3 (0.420 g, 3 mmol) under Ar. After stirring for 50 h, the reaction mixture was allowed to cool down and added with water. Then the crude product was filtered and the resulting orange solid was obtained. The solid product was dissolved in CH_2Cl_2 and washed with water for several times, then dried with Na_2SO_4 , and concentrated to dryness. The product was further purified by silica gel column chromatography (chloroform/ methanol, 1:10) to give the desired yellow solid product (0.259 g, 59.4% yield).

1H NMR ($CDCl_3$): δ = 1.49 (m, 4 H), 1.70 (m, 8 H), 2.64 (m, 8 H), 2.90 (m, 4 H), 4.26 (m, 4 H), 7.00 (d, J = 9.0 Hz, 4 H), 7.87 ppm (d, J = 9.0 Hz, 4 H);

^{13}C NMR ($CDCl_3$): δ = 24.40, 26.17, 55.31, 58.07, 66.49, 114.97, 124.52, 147.23, 161.04 ppm. ESI-MS for $C_{26}H_{36}N_4O_2$: calcd. $(M+2H/2)^+$: 219.14864, found: 219.14984.

1, 1'-(2, 2'-(4, 4' (diazene-1, 2-diyl) bis (4, 1-phenylene)) bis (oxy) bis (ethane-2, 1-diyl) bis (1-methylpiperidinium) iodide 39



CH₃I (6 mL, 0.096 mmol) was added to a solution of compound **38** (0.190 g, 0.44 mmol) in CHCl₃ (20 mL). After stirring for 24 h at 45°C, the reaction mixture was filtered and yellow solid was obtained. The collected yellow solid was further recrystallized with methanol/ diethyl ether (1: 5) to give the desired orange solid product (0.155 g, 49.4% yield).

¹H NMR (d₆-DMSO): δ = 1.54 (m, 4 H), 1.82 (m, 8 H), 3.14 (s, 6 H), 3.44 (m, 8 H), 3.84 (m, 4 H), 4.56 (m, 4 H), 7.17 (d, J = 9.0 Hz, 4H), 7.88 ppm (d, J = 9.0 Hz, 4H); ¹³C NMR (d₆-DMSO): δ = 20.02, 21.23, 48.60, 61.56, 62.20, 116.02, 124.86, 147.27, 160.32 ppm. ESI-MS for C₂₈H₄₂N₄O₂I₂: calcd. ((M-2I+2e)/2)⁺: 233.16594, found: 233.16553.